

Effective Charges Near ^{56}Ni and Production of Anti-Nuclei Studied with Heavy-Ion Reactions

Rickard du Rietz
Department of Physics



LUND UNIVERSITY

2005

Thesis for the Degree of Doctor of Philosophy

To be presented, with the permission of the Faculty of Natural Science of Lund University, for public criticism in lecture hall B at the Department of Physics on March 3rd 2005, at 10.15.

Faculty opponent: Dr. Cyrus Baktash
Oak Ridge National Laboratory, USA

Division of Nuclear Physics
Department of Physics
Lund University
Box 118
SE-221 00 Lund
Sweden

Copyright © 2005 Rickard du Rietz
ISRN LUNFD6/(NFFR-1026)/1-152/ (2005)
ISBN 91-628-6394-0

Typeset by the author using L^AT_EX 3.14159
Printed in Sweden by Intellecta DocuSys AB, Malmö 2005

Organization LUND UNIVERSITY Department of Physics Lund University Box 118 SE-221 00 Lund SWEDEN		Document name DOCTORAL DISSERTATION	
		Date of issue January 20, 2005	
		CODEN ISRN LUNFD6/(NFFR-1026)/1-152/(2005)	
Author(s) Rickard du Rietz		Sponsoring organization	
Title and subtitle Effective Charges Near ^{56}Ni and Production of Anti-Nuclei Studied with Heavy-Ion Reactions			
Abstract This thesis presents the research performed within two different research groups using heavy-ion induced nuclear reactions. They offer the opportunity to investigate different properties of nuclear matter. The results are based on measurements using a variety of different experimental techniques. The PHENIX experiment measured the production of deuteron and anti-deuterons at mid-rapidity in gold-gold collisions at the Relativistic Heavy-Ion Collider, RHIC. The invariant yields and transverse momentum spectra are presented. The results are not in agreement with a simple coalescence model with a constant coalescence parameter B_2 . Excited states of atomic nuclei were populated using fusion-evaporation reactions. The emitted γ rays were detected in large multi-detector arrays. One experiment was in conjunction with a plunger device. Lifetimes of analogue states in the $T_z = \pm 1/2 A = 51$ mirror nuclei ^{51}Fe and ^{51}Mn were measured using the recoil distance Doppler shift (RDDS) technique. The deduced $B(E2)$ values make possible an investigation of isoscalar and isovector polarization charges. A comparison between the experimental results and large-scale shell-model calculations yields a quantitative estimate of the effective nucleon charges in the fp shell.			
Key words: Heavy-ion reactions, PHENIX, RHIC, anti-deuteron, γ ray multi-detector arrays, fusion-evaporation reactions, RDDS, mirror nuclei, lifetimes, effective charges, shell-model calculations			
Classification system and/or index terms (if any)			
Supplementary bibliographical information:		Language English	
ISSN and key title:		ISBN 91-628-6394-0	
Recipient's notes	Number of page 152	Price	
	Security classification		

Distribution by (name and address)
Rickard du Rietz, Department of Physics
Box 118, SE-221 00 Lund, SWEDEN

I, the undersigned, being the copyright owner of the above-mentioned dissertation, hereby grant to all reference sources permission to publish and disseminate the abstract of the above-mentioned dissertation.

Signature _____



Date January 20, 2005

Preface

This thesis is the result of my years as a graduate student at the Physics Department at Lund University. It compiles the work I have been involved in, which has been performed within two different research groups. Both groups perform experiments with heavy-ion induced nuclear reactions to investigate the properties of nuclear matter.

During my first years as a student I was involved in the research activities of the group for Relativistic Heavy-Ion Physics. This research group is participating in the PHENIX experiment, which is one of four experiments at the Relativistic Heavy-Ion Collider at Brookhaven National Laboratory, USA. In particular, the group is contributing to the pad chamber detectors. I have also been involved in the work with the Lund PC Farm, which has been used for various simulations to the PHENIX experiment. The analysis of data has focused on the search for deuterons and anti-deuterons produced in the heavy-ion collisions. Most of my work within this research group is discussed in my licentiate thesis, which was defended during spring 2003.

During my further studies I have been involved in the research activities of the Nuclear Structure Group, which aim to investigate properties and structures of atomic nuclei. I have participated in several experiments and is the spokesperson for an upcoming experiment in preparation. The analysis work has focused on lifetime measurements in data from the GASP03.12 experiment performed at Legnaro National Laboratory, Italy, during 2003. Based on the experimental results I have performed an unique study to probe effective nucleon charges in the fp shell.

I have previously presented parts of the results at the following occasions:

- Quark Matter Conference, Nantes, France, July, 2002.
- 12th UK Postgraduate Nuclear Physics Summer School, St. Andrews, Scotland, September, 2003.
- Svenskt Kärnfysikermöte XXIII, Stockholm, Sweden, November, 2003.
- 4th International Balkan School on Nuclear Physics, Bodrum, Turkey, September 2004.

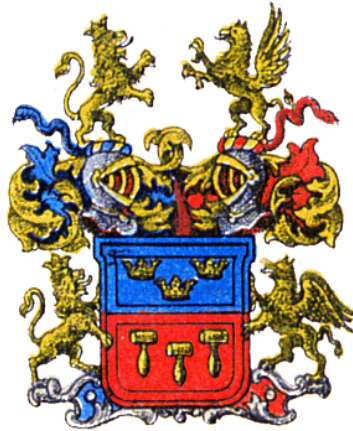
The first chapter of the thesis gives a short introduction to the nuclear shell-model and the quark-gluon plasma. It also briefly describes nuclear reactions and the reaction mechanisms that have been employed in this work.

The next chapter presents the experiments this thesis is based upon. In particular the GASP03.12 and PHENIX experiments are described. Chapter two also introduce the utilized methods for the lifetime analyses.

The analysis of deuterons and anti-deuterons is described in detail in chapter three. This analysis is one of two independent searches for deuterons and anti-deuterons performed with PHENIX.

Chapter four introduces and describes electromagnetic properties in nuclei. In particular, the phenomenon of effective charges is discussed. The chapter further describes the various analyses I have been involved in.

Lund, January 20, 2005
Rickard du Rietz



The du Rietz coat of arms with attributes.

List of Included Papers

PAPER I: **Construction and Performance of the PHENIX Pad Chambers**

K. Adcox *et al.* (PHENIX collaboration)
Nucl. Instr. and Meth. A **497** (2003) 263

PAPER II: **Deuteron and antideuteron production in Au+Au collisions at $\sqrt{S_{NN}} = 200$ GeV**

S.S. Adler *et al.* (PHENIX collaboration)
Submitted to Phys. Rev. Lett.

PAPER III: **Effective Charges in the fp Shell**

R. du Rietz *et al.*
Phys. Rev. Lett. **93** 222501 (2004)

PAPER IV: **Lifetime Measurements in the $A = 51$ Mirror Nuclei**

R. du Rietz, J. Ekman, C. Fahlander, and D. Rudolph
Proceedings of the 4th International Balkan School on Nuclear Physics, Bodrum, Turkey, September 2004. To be published in Balkan Physics Letters Special Issue

PAPER V: **A Shell-Model Study of ^{53}Fe**

R. du Rietz *et al.*
To be submitted to Phys. Rev. C

The papers are reprinted with the permission of the copyright holders:

American Physical Society
Research Road
Box 9000, Ridge
NY 11961-9000

Elsevier Science Publishers B.V.
P.O. Box 103
1000 AC Amsterdam
The Netherlands

The cooperation of the copyright holders is gratefully acknowledged.

Contents

Preface	v
List of Included Papers	vii
1 General Aspects	1
1.1 Nuclear Matter	1
1.1.1 The Nuclear Shell Model	2
1.1.2 The Quark Gluon Plasma	5
1.2 Nuclear Reactions and Collision Terminology	7
1.2.1 Fusion-Evaporation Reactions	8
1.2.2 The Spectator-Participant Model	10
2 Experiments	13
2.1 The GASP03.12 Experiment	13
2.1.1 Detectors and Experimental Set-Up	13
2.1.2 Lifetime Measurements	15
2.2 The GSFMA73 and GS2k017 Experiments	18
2.3 The PHENIX Experiment	18
2.3.1 Detector Arrangements and Data Acquisition	18
2.3.2 The Pad Chambers	21
3 Deuteron and anti-deuteron physics with PHENIX	23
3.1 The Coalescence Model	23
3.2 Data Analysis	25
3.3 Physics Results	33
4 Gamma-Ray Spectroscopy	37
4.1 Electromagnetic Properties	37
4.2 Mirror nuclei	43
4.3 Data Analysis	45
4.3.1 Effective charges in ^{51}Mn and ^{51}Fe	45
4.3.2 Excited states in ^{53}Fe	57
4.3.3 Excited states in ^{54}Ni	59
5 Conclusion and Outlook	63
6 Popularised Summary in Swedish	65

Acknowledgements	67
A Parameterization of the cross sections	69
Bibliography	71
Paper I: Construction and performance of the PHENIX pad chambers	
Paper II: Deuteron and antideuteron production in Au+Au collisions at $\sqrt{S_{NN}} = 200$ GeV	
Paper III: Effective Charges in the fp Shell	
Paper IV: Lifetime Measurements in the $A = 51$ Mirror Nuclei	
Paper V: A Shell-Model Study of ^{53}Fe	

Chapter 1

General Aspects

During the first moment of its evolution, the universe was formed through several phase transitions involving fundamental changes in the state of matter. After the first few microseconds, matter is believed to have existed in a state described as a soup of free quarks and gluons, the Quark Gluon Plasma. As the universe expanded and cooled down, more complex matter condensed out of the plasma, eventually forming atomic nuclei and finally the atoms, which are the basis for any known life form today. At present, it is believed that a Quark Gluon Plasma may exist in the universe in the core of neutron stars. While the temperature is relatively low in the stars, the density is extremely high due to immense gravitational forces. In today's laboratory nucleus-nucleus collisions are used to ignite nuclear matter that form highly excited systems. With advanced and complex detector equipment the constituents and evolution of such reactions are investigated, which allows to probe fundamental properties and changes of nuclear matter in the course of the evolution of the universe.

1.1 Nuclear Matter

Nuclear matter has been studied ever since Rutherford's famous scattering experiment revealed that the atom consists of a small, positively charged nucleus, surrounded by electrons. A few years after this discovery it was realized that the nucleus itself consisted of nucleons (protons and neutrons) and later experiments revealed that even the nucleons had an internal structure, namely the quarks. The quarks are combined in groups of two or three forming the hadrons, which consists of mesons (two quarks) and baryons (three quarks). The transition from ordinary nuclear matter to quark matter (or vice-versa) is predicted to behave like a thermodynamical phase transition, analogous to the transition from water to steam during boiling. A schematic phase diagram for nuclear matter is sketched in Fig. 1.1 that shows temperature vs net baryon density for an extended volume of nuclear matter in thermal equilibrium. The indicated trajectory illustrates an avenue for probing quark matter using high-energy nucleus-nucleus collisions, where conditions may approximate those of the early universe.

Nucleus-nucleus collisions are also employed to investigate properties of nuclear matter near its ground state (as indicated in Fig. 1.1). Such studies allow to probe

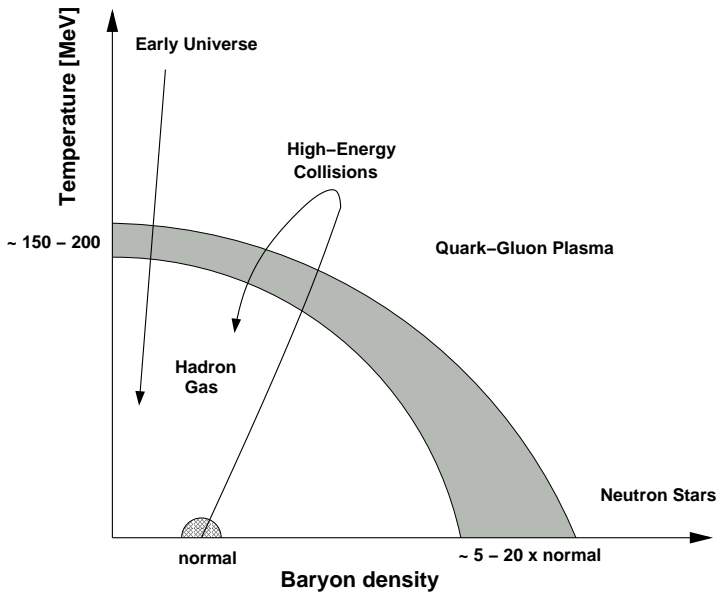


Figure 1.1: *Phase diagram of nuclear matter. Temperature is plotted vs net baryon density for an extended volume of nuclear matter in thermal equilibrium.*

parameters used to describe a nucleus: its mass, nuclear radius, angular momentum, electromagnetic moments, energies of excited states, etc. This in turn offers a possibility to investigate the properties of the force acting between the nucleons. However, to obtain an understanding and deeper knowledge of nuclear properties it is, like in any other regime in Fig 1.1, important to perform comparisons of experimental data to theoretical calculations and simulations. Thus it is required to formulate a theoretical model that accounts for the nuclear force between nucleons, which can be used to describe a nuclear system. One such nuclear model is the *nuclear shell model* [1, 2], which successfully describes near-spherical nuclei and serves as a base for other, more complex models.

1.1.1 The Nuclear Shell Model

In the nuclear shell model, the nucleons (protons and neutrons) are assumed to move in bound orbitals. Each orbital is assigned a set of quantum numbers and has a well determined energy, angular momentum, and parity associated with it. As the nucleons are fermions (half-integer spin) the Pauli principle permits no more than two nucleons (of each type) to occupy the same state, i.e. have identical sets of quantum numbers. This results in a finite number of particles occupying a given energy level and a nucleus is predicted to have a shell structure. When a shell with particular energy, angular momentum, and parity is filled, any additional particle of that type

must be put into a different shell at a higher energy. The concept of closed (filled) shells is supported from experimental data, which indicates that closed shells occur at proton or neutron numbers of 2, 8, 20, 28, 50, 82, and 126, the so-called magic numbers.

A nucleus consist of a given number of individual nucleons. The properties of the nuclear system can be described from the solutions to the Schrödinger wave equation. Due to mathematical difficulties solving this full many-body problem the Schrödinger wave equation cannot be solved analytically for a given Hamiltonian, but must be solved using numerical methods. Assuming only a two-body nucleon interaction¹, the Hamiltonian for such an A -nucleon system can be written as

$$\mathcal{H} = \sum_{i=1}^A \left(-\frac{\hbar^2}{2m} \nabla_i^2 \right) + \frac{1}{2} \sum_{i \neq j}^A V_{ij}(\vec{r}), \quad (1.1)$$

where the first term is the kinetic energy of the particle motion and $V_{ij}(\vec{r})$ is the two-body potential representing the interaction between the nucleons i and j . As the nuclear force affecting the nucleons is not fully understood, the nucleon-nucleon interaction is commonly approximated with an average nuclear potential. This potential should represent the average interaction of all the other nucleons exerted on any one of the nucleons in the nucleus. Usually, a spherically symmetric potential is selected, which allows to separate the Schrödinger equation into a radial part and an angular part, where the latter is independent of the central potential $V(r)$. Hence, the angular part can be solved directly and the solution can be expressed as the *spherical harmonics*, $Y_{\ell m_\ell}(\theta, \phi)$. The introduced quantum number $\ell = 0, 1, 2, \dots$ in $Y_{\ell m_\ell}(\theta, \phi)$ is related to the orbital angular momentum and its projection onto the quantization axis is given by $m_\ell = 0, \pm 1, \pm 2, \dots, \pm \ell$. Each ℓ -value can be represented as a nuclear orbital (level) denoted as s, p, d, f, g, \dots . Due to the restriction on m_ℓ there are exactly $2\ell + 1$ possible $Y_{\ell m_\ell}(\theta, \phi)$ solutions for each level. Thus a $2\ell + 1$ folded degeneracy is introduced, which together with the intrinsic spin, allows for an occupancy of $2(2\ell + 1)$ nucleons in one orbital. In combination with the solution to the radial part, using the potential representing the nucleon-nucleon interaction, the levels are separated in energy and a shell structure is obtained. The choice of the shell model potential should thus be of such form that experimentally observed shell structures are reproduced.

One first attempt to introduce a potential representing the average interaction is the spherical harmonic oscillator potential. Comparison with experimental data reveals, however, that only the magic numbers of 2, 8, and 20 are reproduced in the obtained shell structure. To obtain a better agreement with observed data a more realistic potential describing the average interaction with the other nucleons is introduced. Such a potential mimics the nuclear matter or charge distribution and is expressed using a spherical Woods-Saxon form written as

$$V_{WS}(r) = \frac{-V_0}{1 + \exp\left(\frac{r-R}{a}\right)}, \quad (1.2)$$

which is sketched in Fig. 1.2. r is the distance of the nucleons with respect to the center of the nucleus and R is the radius of the nucleus given by $R = r_0 A^{1/3}$ fm

¹In reality, however, there is evidence to suggest that the nucleons interact not only through two-body forces, but through three-body forces as well.

($r_0 \approx 1.2$ fm). The depth of the well, V_0 , is proportional to the density of nucleons and is of the order of 50 MeV. The parameter $a \approx 0.57$ fm is related to the surface diffuseness, d , which is the distance over which the potential changes from 90% to 10% of V_0 (see Fig. 1.2).

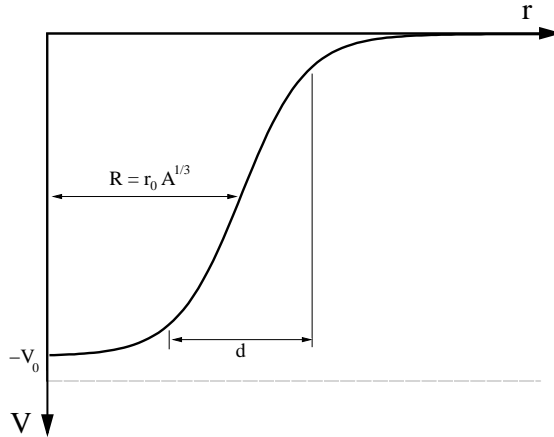


Figure 1.2: The form of a Woods-Saxon potential often used in shell model calculations. The skin diffuseness, d , is defined as the distance from 90% to 10% of the total potential depth.

The level structure predicted by the shell model using the Woods-Saxon potential is illustrated in Fig. 1.3(a). It is found that neither the spherical harmonic oscillator potential, nor the Woods-Saxon potential produces energy eigenvalues with closed shells for all the magic numbers. This is, however, accounted for by adding yet another term to Eq. 1.2, which allows for even further separation of the energy levels. The introduced term, referred to as the *spin-orbit* interaction, couples the orbital angular momentum with the intrinsic spin to form a total angular momentum \vec{j} with an associated quantum number j . Due to the two orientations of the nucleon spin the spin-orbit interaction splits the degeneracy of an energy level at a given ℓ -value ($\ell > 0$) into two new levels with different energies and total angular momentum quantum number $j = \ell \pm 1/2$. Furthermore, the ℓ -value determines the parity of the level such that an even (odd) ℓ -value corresponds to positive (negative) parity. Figure 1.3(b) shows the energy level structure calculated using the spin-orbit interaction added to the Woods-Saxon potential. The energy levels are denoted with quantum numbers $n\ell j$ and as seen the experimental observed magic numbers are well reproduced.

The described nuclear shell model is employed as a first attempt to predict the properties of nuclei in or near their ground states. Regardless of its simplicity it is found to predict many nuclear properties very well. However, in the above approach it is assumed that the nucleus can be viewed as a spherical system, which is not the case for all nuclear systems. Some nuclei are deformed in their ground states and nuclei that are spherical, in their ground state, may reveal a deformation in an excited state. Hence, for such a scenario the spherical shell model fails to predict the nuclear properties and thus other models are introduced to account for these phenomena.

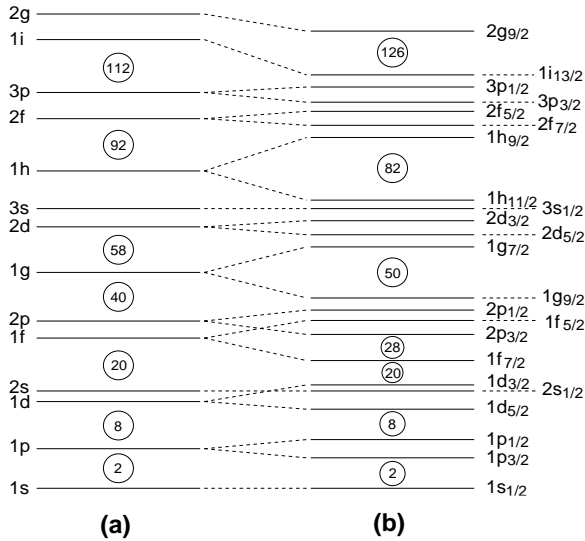


Figure 1.3: The energy levels predicted by the shell model using a Woods-Saxon form on the nuclear potential. Panel (a) shows the obtained level structure without any spin-orbit interaction added to the potential whereas panel (b) shows the results including ls coupling. The observed magic numbers are nicely reproduced for the latter case.

Such models are, e.g., the Nilsson model, in which deformation is introduced, and the Cranking model that treats rotating deformed nuclei.

Relevant parts of the present thesis discuss nuclear properties using a perspective based on large-scale shell-model calculations. In particular nuclei distributing their valence nucleons, i.e. nucleons outside a closed shell, in the fp shell have been investigated. The calculations employed an inert ^{40}Ca core, representing the $N = Z = 20$ shell closure, and the valence nucleons distributed in the full fp shell, which contains the $1f_{7/2}$ orbit below and the $2p_{3/2}$, $1f_{5/2}$, and $2p_{1/2}$ orbits above the $N = Z = 28$ shell closure. A more detailed description of the shell-model calculations is found in Ref. [3].

1.1.2 The Quark Gluon Plasma

The properties and structures of nuclei are predicted using theoretical models (e.g. the nuclear shell model), where nucleons are used as building blocks to describe the nuclei. However, the nucleons have an internal structure, quarks, which are supposed to be the fundamental constituents of nuclear matter. The quarks are affected by the strong force, which in the standard model is described by Quantum Chromo Dynamics, QCD.

The quarks are fermions and in this model they are assigned an electrical as well as a color charge. In nature only color neutral objects are allowed, which indicates that there can exist no free quarks. Instead they combine together in the form of hadrons.

The hadrons are combinations of either three quarks or anti-quarks (qqq or $\bar{q}\bar{q}\bar{q}$), as in baryons², or of one quark and one anti-quark ($q\bar{q}$), as in mesons³. Without the color charge a hadron like Δ^{++} , which consists of three upquarks (u), should have been forbidden as the quarks have to obey the Pauli exclusion principle. However, such a combination of three u quarks may be formed using three different color charges, which creates a color neutral object. The color charge is denoted red, blue, and green with the corresponding anti-colors.

The gluons, which carry color but no electric charge, are the exchange particles of the strong force. As they carry color they couple not only to the quarks, but also to each other. As a result the effective color charge will be screened at short distances. In QCD, the strength of the strong force affecting the quarks and gluons becomes relatively weak for short distances but increases rapidly for larger separations (> 1 fm). Hence, for nuclear matter close to its ground state, quarks and gluons are confined to the hadrons, whereas at large baryon densities and high temperatures the theory predicts that they are no longer confined [4, 5]. Instead they may be free to move within the whole system, forming a state of matter referred to as the Quark-Gluon Plasma, QGP. Today relativistic nucleus-nucleus collisions are used to create conditions with extreme temperatures and densities where normal nuclear matter may undergo a phase transition towards a QGP (see Fig. 1.1). The space-time evolution of such a phase transition created in a relativistic heavy-ion collision is sketched in Fig. 1.4 [4]. In this picture the collision between the nuclei occur at $(z, t) = (0, 0)$, where z is the position coordinate along the beam axis and t the time coordinate. The remnants

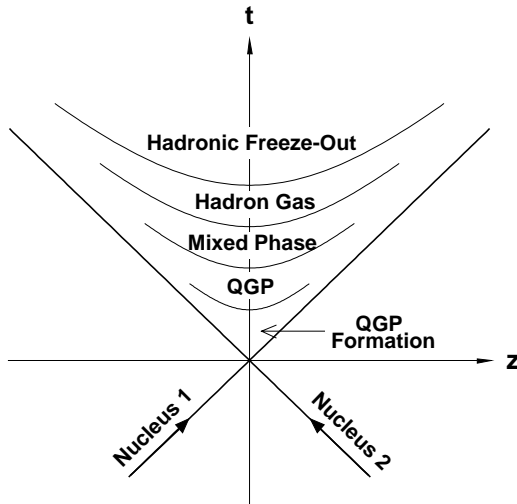


Figure 1.4: *Space-time evolution of a nucleus-nucleus collision where a QGP is formed.*

²The proton and the neutron are examples of baryons.

³For example the π mesons or the K mesons.

of the incoming nuclei fly away from the central region leaving behind a system of strongly interacting matter, which expands both longitudinally and transversely. If a phase transition to a QGP occurs the quarks and gluons become deconfined. The system will remain in this state until the expansion has reduced the temperature and baryon density enough to form hadrons and to become stable. Directly after this mixed phase the system exists in the form of a hadron gas, where the density and temperature is still too high for the hadrons to escape without further interactions. Eventually, at some point during the expansion, the interactions between the hadrons will cease and the system reaches thermal freeze-out.

The hadrons emitted from the collision reflect the properties of the system at the final freeze-out. Interesting parameters such as temperature, source size, etc. can be determined from the hadronic spectra. The time of freeze-out may differ for different particle species, and thus give rise to different source radii and temperatures. The temperature of a system is a measure of the kinetic energy of its constituent. As a large fraction of the longitudinal momentum stems from the longitudinal expansion, and therefore is of non-thermal origin, one usually determines the temperature from the transverse momentum of the emitted particles, p_T . A rough estimate is $T \sim \langle p_T \rangle$. The dimensions of the particle emitting source can be determined by intensity interferometry. This method, often referred to as Hanbury-Brown-Twiss (HBT) correlations, measures the correlation between two identical particles (e.g. $\pi^+\pi^+$) emitted from the source [6]. From this information it is in principle possible to determine both the longitudinal and transverse size of the source. The time evolution of the system and the associated expansion complicate the HBT interpretation and the temperature measurements.

Unfortunately, there is no unambiguous signal that validates if a phase transition and a formation of a Quark-Gluon Plasma has occurred. Most of the expected signals from a produced plasma can also be found in hadronic scenarios under certain conditions. Thus to conclude if a plasma has been produced in a collision, several signals have to be observed in the same event sample. A detailed discussion and description of the ideas behind some of the most promising signatures can be found in Ref. [5].

1.2 Nuclear Reactions and Collision Terminology

Particle accelerators are used to provide beams of atomic nuclei with velocities almost up to the speed of light. When these energetic particles collide with another atomic nucleus there is a nuclear reaction. This reaction may produce a system that allows to probe and study the fundamental properties and changes of nuclear matter. In order to create a system that undergoes a phase transition to a QGP, it is necessary to form the system with extremely high temperature and density. This can be achieved by colliding heavy nuclei at relativistic energies, where a large amount of the energy is deposited in a small volume of the system. Studies of fundamental properties of nuclear matter at or near its ground state are also performed using heavy-ion collisions. In this case the energies of the accelerated ions are non-relativistic, and range up till about 10% of the speed of light.

The collisions are induced by either steering the beam onto a stationary target (*fixed target* experiments) or by letting two beams coming from opposite directions cross each other (*collider* experiments). An advantage of collider experiments is that

all the beam energy is available for particle production, whereas in a fixed target experiment a large fraction of the energy is consumed by moving the center-of-mass. A fixed target experiment, however, allows for much easier focusing of the beam towards the stationary target compared to a collider experiment, which is very sensitive to the relative position of the two beams. The GASP03.12 and PHENIX experiments, which are described in chapter 2, represent a fixed target and a collider experiment, respectively. Both these experiments utilized heavy ion collisions transform the initial constituents into an excited system of nuclear matter. There are several different reaction mechanisms that may occur in such a collision, and depending on the beam energy and the centrality of the collision some mechanisms are more or less likely to occur. The sections below briefly describe the different reaction mechanisms, which dominate in the two experiments of the present thesis. In the GASP03.12 experiment a fusion-evaporation reaction is employed, whereas the relativistic collisions in PHENIX can be described using the spectator-participant model.

1.2.1 Fusion-Evaporation Reactions

The investigation of the properties of nuclear matter around its ground state requires a reaction mechanism that populates the nucleus of interest in an excited state. This can be achieved by a *fusion-evaporation reaction*, in which the nucleus is produced in an excited state with a certain angular momentum and excitation energy. The time evolution and the different stages of a fusion-evaporation reaction is schematically illustrated in Fig. 1.5 [7]. The incoming projectile collides with a target nucleus and the incident energy is shared among many of the involved nucleons. The projectile and target nuclei fuse together and form an excited and often rotating intermediate state referred to as a compound nucleus. The rotation frequency, and thus the angular momentum, of the compound nucleus depends on the collision centrality, which is characterized by the impact parameter, b , introduced in the participant-spectator model (cf. section 1.2.2).

Once the excited compound nucleus is formed there are many channels available for its decay. It may undergo fission or multi-fragmentation and thus split up into two or several constituents. Another possibility is that the highly excited compound nucleus decays through particle evaporation, in which light particles (protons, neutrons, and α particles) are emitted from the system. This allows the nuclear system to reduce its excitation energy and different residual nuclei are formed. At some stage the particle evaporation is hampered because the excitation energy of the system is not sufficient for yet another particle to be emitted. Instead the residual nucleus decreases in excitation energy via electromagnetic radiation and thus decay by emitting γ rays. Electromagnetic properties and radiation in nuclei is discussed further in section 4.1. The decay occurs at first through emission of statistical γ rays from the nuclear continuum and overgoes to emission of discrete γ rays until it reaches the ground state. These discrete γ rays carry information on the structure of the nucleus. They are detected in experiments and they allow the study of the properties of nuclear matter.

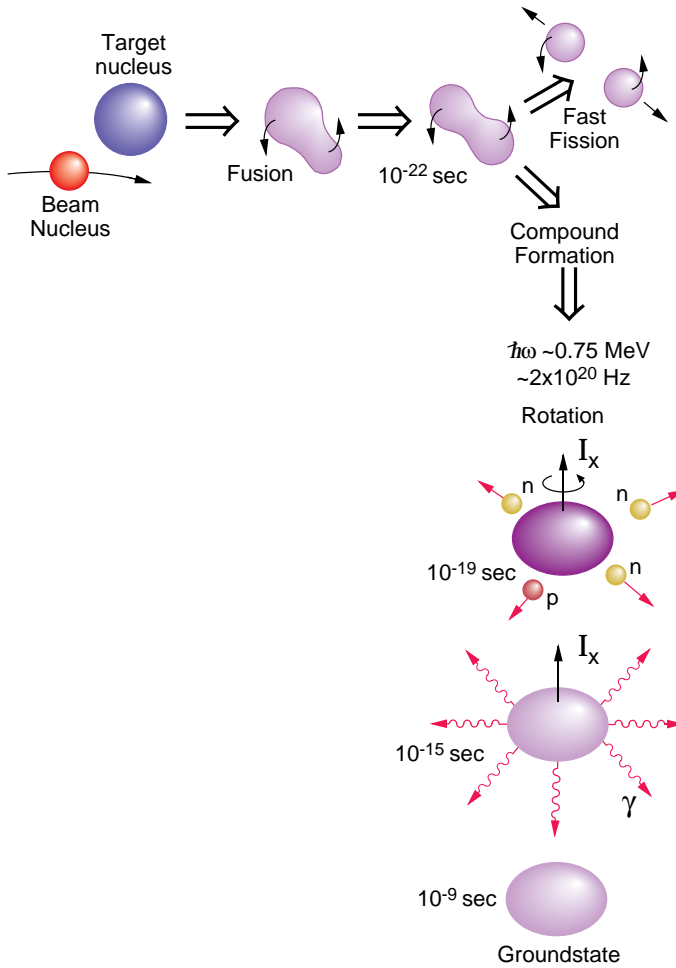
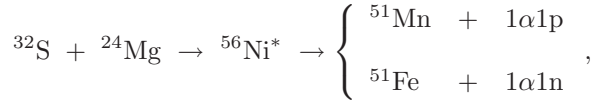


Figure 1.5: *Schematic illustration of the timescale in a nuclear fusion-evaporation reaction. Initially a target nucleus fuses together with an incoming beam nucleus and forms a nuclear compound system. The latter decays through particle evaporation and γ ray emission towards the ground state of the final nuclear product. Taken from Ref. [7].*

In the fusion-evaporation reactions employed in the present thesis the intermediate compound nucleus is extremely proton rich. Thus one would expect that most of the particles emitted in the evaporation process are protons or α -particles, which would create a residual nucleus located closer to the line of stability. However, due to the Coulomb barrier affecting the charge particles, the decay probability of neutron emission is still relatively high. This offers a possibility to study nuclei far from stability on the proton rich side of the nuclear chart. In such an experiment there will of course be several final residual nuclei, depending on the number of particles

evaporated. Examples of such reaction channels in a fusion-evaporation reaction are the two mirror nuclei ^{51}Fe and ^{51}Mn analysed in section 4.3.1. They were produced in a reaction using a ^{32}S beam colliding with a ^{24}Mg stationary target forming a ^{56}Ni compound nucleus. The reaction can be written as



where the * indicates the excited compound nucleus. It decays through particle emission and the two mirror nuclei can be found in the one- α -one-proton ($1\alpha 1\text{p}$) and one- α -one-neutron ($1\alpha 1\text{n}$) reaction channel, respectively. The decay continues as the two mirror nuclei emit γ rays, which are detected in the detector system and processed for further analysis.

1.2.2 The Spectator-Participant Model

In nucleus-nucleus collisions at relativistic energies, a hot and dense fireball of nuclear matter is produced and the collision geometry is described with the *spectator-participant model* [8], which is sketched in Fig. 1.6. In this picture the overlapping parts of the nuclei form a hot and dense region (participant region) while the remainders of the nuclei continues to move more or less undisturbed by the collision. The nucleons in the overlapping region are called the participants and the remaining nucleons are called spectators.

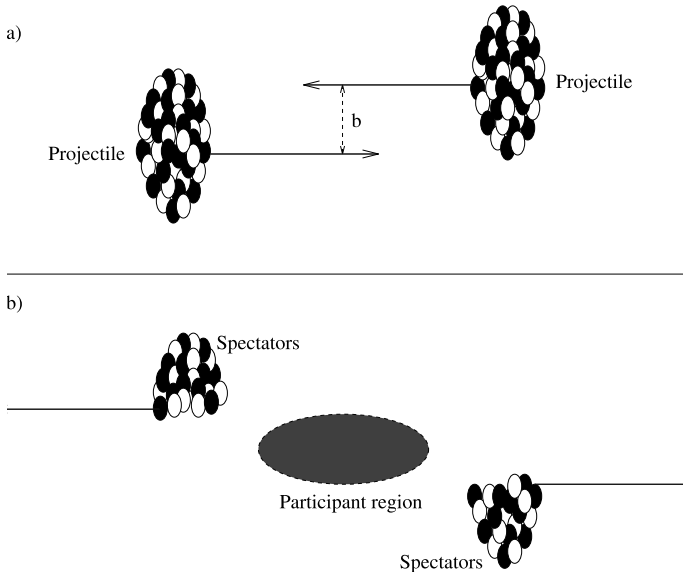


Figure 1.6: *Schematic illustration of the participant-spectator model in the centre-of-mass system. Panel (a) and (b) illustrates two heavy nuclei just before and after the collision, respectively.*

By introducing the impact parameter, b , the collision centrality can be quantified, which later is used to characterize the collisions in different event classes. The impact parameter is defined as the transverse distance between the centers of the two nuclei (see Fig. 1.6a) and values of b decide whether a collision is central⁴ or peripheral⁵. It is not possible to directly measure the impact parameter in a collision and instead measurements of other quantities are used to determine the collision geometry. These quantities, for example, the number of produced particles and transverse energy, are strongly correlated to the number of participants in the collision, which allows to experimentally estimate the impact parameter. The energy transformed into particle production gives rise to a very high particle multiplicity, and it is possible to treat the system statistically. If one assumes that thermal equilibrium is reached, a thermodynamical model can be used to describe the system and thermodynamical variables (temperature, pressure etc.) may be calculated.

The momentum components, p_x , p_y , and p_z , of a particle are used to calculate quantities such as the transverse momentum, p_T , and the azimuthal angle, ϕ . The transverse momentum, which is the momentum component perpendicular to the beam direction, and the azimuthal angle are determined from the x and y components of the particle momentum as

$$p_T = \sqrt{p_x^2 + p_y^2} \quad (1.3)$$

and

$$\phi = \arctan \frac{p_y}{p_x}. \quad (1.4)$$

Using the transverse momentum the transverse mass, m_T , is defined by

$$m_T = \sqrt{m_0^2 + p_T^2}, \quad (1.5)$$

where the speed of light is set to be unity and m_0 is the rest mass of the particle. The corresponding transformations to p_x , p_y , and p_z using the above quantities can be written as

$$\begin{aligned} p_x &= p_T \cdot \cos(\phi) \\ p_y &= p_T \cdot \sin(\phi) \\ p_z &= m_T \cdot \sinh(y) \end{aligned} \quad (1.6)$$

y is called the rapidity of the particle. It is measured along the beam direction and can be expressed in terms of the total energy of the particle and the longitudinal momentum component along the beam direction, p_z , as

$$y = \frac{1}{2} \ln \left(\frac{E + p_z}{E - p_z} \right). \quad (1.7)$$

An important feature of rapidity is that it is boost invariant and thus additive under a Lorentz transformation. This means that the shape of the rapidity distribution of particles from a moving source does not depend on the velocity of the source.

⁴ b is close to zero

⁵ b is slightly smaller than the sum of the two nuclei radii

Furthermore, the rapidity, in combination with the transverse mass, can be used to calculate the total energy, E , of a particle according to

$$E = m_T \cosh(y). \quad (1.8)$$

A frequently used approximation to the rapidity is the pseudorapidity, η , defined as

$$\eta = -\ln \left(\tan \frac{\theta}{2} \right), \quad (1.9)$$

where θ is the polar emission angle, i.e. the angle between the particle momentum \vec{p} and the beam axis. The relation between the pseudorapidity and the rapidity is given by

$$\sinh \eta = \sinh(y) \cdot \frac{m_T}{p_T}, \quad (1.10)$$

where the transverse momentum and transverse mass are defined as in Eq. 1.3 and Eq. 1.5, respectively.

In heavy-ion collision terminology other important quantities are the invariant cross-sections. Using the above derived expressions the invariant differential cross-section of a particle can be written as

$$E \cdot \frac{d^3 N}{dp_x dp_y dp_z} = \frac{d^3 N}{p_T dy dp_T d\phi}, \quad (1.11)$$

where $dp_x dp_y dp_z = p_T m_T \cosh(y) \cdot dy dp_T d\phi$. From the right-hand side of Eq. 1.11 the invariance under Lorentz boosts along the beam axis is evident from the invariance of dy . The cross-section is normalized to the total number of events, N_{evt} . For an average over several events, there is azimuthal symmetry and thus no ϕ dependence. Hence, the invariant cross-section can be written as

$$\frac{d^2 N}{2\pi N_{evt} p_T dy dp_T}. \quad (1.12)$$

This work is partly based on measurements of invariant cross-section for deuterons and anti-deuterons at relativistic energies using the PHENIX detector. The data analysis of these measurements are presented in chapter 3.

Chapter 2

Experiments

The properties of nuclear matter can be studied in data obtained from experiments utilizing nucleus-nucleus collisions. To detect and probe the constituents and the evolution of such collisions requires advanced detector technology, which is often developed and constructed within world wide collaborations. The size and economical cost of a detector system is strongly correlated to the physical motivation for the experiment. The smaller constituents that are to be probed the larger and more complex detector systems are required.

The present thesis employ four experiments: GASP03.12 performed at Legnaro National Laboratory (LNL), GSFMA73 performed at Argonne National Laboratory (ANL), GS2k017 performed at Lawrence Berkley National Laboratory (LBNL), and the PHENIX experiment performed at the Relativistic Heavy Ion Collider (RHIC) at Brookhaven National Laboratory (BNL). In particular, the thesis is based on data from the GASP03.12 and the PHENIX experiment.

2.1 The GASP03.12 Experiment

The GASP03.12 experiment was performed at LNL in collaboration with five European institutes¹. The primary goal was to determine effective charges in the fp shell via lifetime measurements in the mass $A = 51$ mirror nuclei ^{51}Fe and ^{51}Mn . The experiment utilized a heavy-ion fusion evaporation reaction with a ^{32}S beam at 95 MeV on a fixed ^{24}Mg target. The produced γ rays were detected in the GASP spectrometer [9], which was used in combination with the Cologne plunger device [10] to perform the lifetime measurements.

2.1.1 Detectors and Experimental Set-Up

GASP (GAMMA-ray SPectrometer) comprises 40 Hyper-Pure Germanium (HPGe) detectors with anti-Compton shields and a 4π calorimeter of 80 BGO² crystals. The detectors are divided in two hemispheres, which are closed to a sphere during the

¹Participants from Lund, Cologne, Keele, Padova, and Legnaro.

² $\text{Bi}_4\text{Ge}_3\text{O}_{12}$

experiment. One such hemisphere is shown in Fig. 2.1. The figure shows the experimental set-up for the GASP03.12 experiment using the Cologne plunger device, BGO inner ball, and the HPGe detectors.

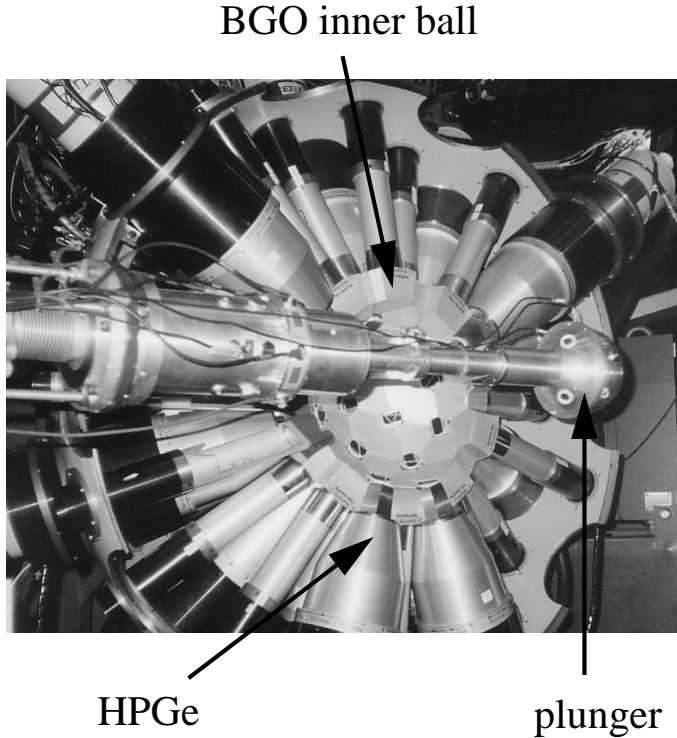


Figure 2.1: *One hemisphere of the GASP detector array with the Cologne plunger device, BGO inner ball, and the HPGe detectors. The beam enters from the left.*

The HPGe detectors are placed 27 cm from the target position and distributed in eleven rings ranging from 31.7° to 148.3° relative to the beam axis. In the offline analysis some of the detector rings are combined, which results in seven rings situated at average angles of 34.6° , 59.4° , 72.0° , 90.0° , 108.0° , 120.6° and 145.4° . The configuration of GASP including the BGO inner ball corresponds to a total photo peak efficiency of about 3% at 1332 keV. However, the efficiency almost doubles to 5.8% if the BGO inner ball is removed and the HPGe detectors are positioned closer to the target. This second configuration is utilized in experimental situations where the most important feature is the total efficiency. In the GASP03.12 experiment the GASP detector array was used in its standard configuration with both the HPGe detectors and the BGO inner ball.

The BGO elements surrounding the HPGe detectors work as anti-Compton shields. They are used as veto detectors to perform suppression of the background arising from Compton scattering. If a γ ray is Compton scattered out of the HPGe detector only a fraction of its energy is recorded and the event should be neglected. The scattered

γ ray can be detected in the surrounding BGO material, which allows to veto such events and thus suppress the background. However, it is possible that a γ ray deposits all its energy in the HPGe detector and at the same time a second γ ray is detected in a BGO crystal, which vetoes the event. Such a scenario, which happens more frequently for events with large γ ray multiplicity, is prevented by the cover of the front of the surrounding BGO material with Heavimet absorbers, which should make sure that the BGO shield only fires on scattered radiation from the HPGe detectors.

Ancillary detector systems

Additional detector systems can be used in conjunction with the GASP array in order to obtain cleaner spectra, which may, for example, offer a possibility to identify γ ray transitions of a specific residual nucleus. A few of the standard systems available at LNL are:

- **ISIS:** A detector array of 40 silicon $\Delta E - E$ telescopes used to detect light charged particles produced in the reactions.
- **N-Ring:** A neutron detector array consisting of six individual detectors, which replaces the 6 most forward elements of the BGO inner ball.
- **CAMEL:** A Recoil Mass Separator placed downstream in the target hall.

However, none of the above ancillary detector systems were used in the GASP03.12 experiment set-up. Instead the lifetime measurements were performed using the Cologne plunger device (see Fig. 2.1), which replaced the standard target chamber and was connected directly to the beam line. It consists of a small reaction chamber in which a target and a stopper foil are placed. The holder for the stopper foil is mobile that allows to vary the target-stopper distance, which is the basic requirement for the present lifetime analysis. In section 2.1.2 the principle of the lifetime measurements are discussed in more detail. During the experiment the target-stopper distance was varied over 21 distances, which in the offline analysis is combined into nine effective distances.

Data Handling

The produced signals from the BGO crystals and the HPGe detectors are fed into the GASP Data Acquisition System (DAQ), which allows to set an event trigger. For the current experiment events with at least one BGO crystal and two HPGe detectors firing in coincidence were accepted by the trigger. The signals for an accepted event were sampled and processed further and eventually stored on disk. The stored data was used in the offline analysis to extract the lifetimes of the analogue $27/2^-$ states in the $A = 51$ mirror pair.

2.1.2 Lifetime Measurements

Nuclear lifetimes of excited states range from more than 10^{15} years to below 10^{-20} s for very short-lived states. Therefore, a variety of different lifetime measurement techniques exist. The most straight forward technique is to use electronic modules

(e.g. Time-to-Amplitude-Converter) to extract nuclear lifetime in coincidence measurements of the respective radiation. This method, however, is limited to the time resolution of the detector system and can be used for $\tau > 1$ ns. Lifetimes in the picosecond region can be determined using Doppler-shift methods, which is the focus of the present thesis. In particular, it employs the Recoil Distance Doppler Shift method in the analysis of the GASP03.12 experiment.

Recoil Distance Doppler Shift Technique (RDDS)

The RDDS method is a standard technique to measure lifetimes of excited states in the picosecond region. Using a plunger device, the recoiling nuclei from a thin target foil are stopped at different distances in a stopper foil. Hence, γ rays are emitted either during the flight of the recoils or when the recoils are stopped in the stopper. The principle is illustrated as in Fig. 2.2. The energy of γ rays emitted in flight, γ_F ,

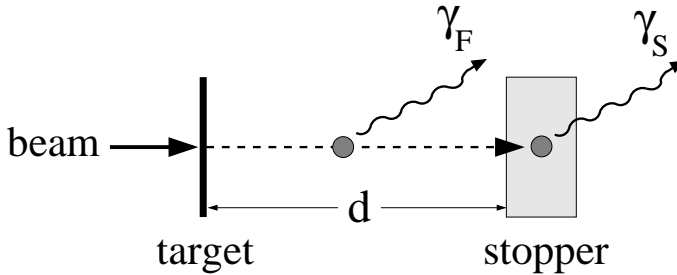


Figure 2.2: Schematic view of the plunger principle where produced recoils in a thin target foil are stopped in a stopper. Changing the target-stopper distance, d , changes the relative intensities of decays in flight, $I_{\gamma,F}$, and at rest, $I_{\gamma,S}$.

is subject to a Doppler shift while the energy of γ rays emitted from the stopper, γ_S , is unshifted. Thus, detecting γ rays at an angle θ , with respect to the recoil direction, allows to distinguish between γ_F and γ_S . The intensity of the transition de-populating an excited nuclear state is therefore distributed in a flight peak and a stopped peak, I_F and I_S , respectively. These intensities are given by

$$I_F = I_0(1 - e^{-t/\tau}) \quad \text{and} \quad I_S = I_0 e^{-t/\tau}. \quad (2.1)$$

Here, τ is the lifetime of the excited state and $t = d/v_r$ is the flight time corresponding to the target-stopper distance, d , and the recoil velocity, v_r . The fraction of the γ ray intensity in the stopped components, $F(t)$, shows an exponential dependence as

$$F(t) \equiv \frac{I_S}{I_S + I_F} = e^{-t/\tau}, \quad (2.2)$$

which gives the lifetime of the excited nuclear state.

In the above derivation it is assumed that the excited state is populated promptly, i.e., the state is not fed through upper levels that also have finite lifetimes. In such a case the determined lifetime will correspond to an effective lifetime of the excited

state. Thus, such feedings need to be accounted for, which can be done by least square fitting of the experimental data to several exponentials. Another method, developed to account for this problem, is the Differential Decay Curve Method [11, 12].

Differential Decay Curve Method (DDCM)

The DDCM technique also employs intensities of flight and stopped components of the transitions to derive the lifetime of an excited state. Consider two γ rays emitted in a nuclear decay sequence as illustrated in Fig. 2.3. τ_1 and τ_2 are the corresponding lifetimes for the two states. The intensity of the flight and stopped component for the

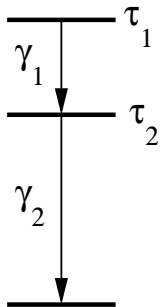


Figure 2.3: Illustration of γ ray decay of two excited states with lifetime τ_1 and τ_2 , respectively.

first transition are I_{F1} and I_{S1} , respectively, which allows to derive the corresponding intensities for the second transition as

$$I_{F2} = I_{F1}(1 - e^{-t/\tau_2}) \quad \text{and} \quad I_{S2} = I_{F1}e^{-t/\tau_2} + I_{S1}. \quad (2.3)$$

The I_{F2} and I_{S2} intensities are measured for γ rays in coincidence with the flight component of the first transition. Therefore, $I_{S1} = 0$ in Eq. 2.3 and the lifetime of the second excited state is given by

$$\tau_2 = \frac{I_{S2}}{\dot{I}_{F2}}, \quad (2.4)$$

where \dot{I}_{F2} is the first order derivative of the intensity for the flight component. Using this method allows to determine the lifetime from the observed coincidence intensities for each of the target-stopper distances. Furthermore, the use of coincidences eliminates any contributions of possible side-feeding and thus gives the real lifetime of the nuclear state.

The present thesis attempted to employ the DDCM method in the analysis of the ^{53}Fe nucleus (cf. section 4.3.2). The determined intensities of the flight and stopped components are used as input parameters to the NAPATAU³ software [13]. This software performs fits of the given input parameters and provides all computing necessary to extract the lifetime of interest. However, it was found that the lifetime

³DDCM analysis software, which has been developed at the University of Cologne

of the states of interest cannot be determined using this software with the provided intensities. Due to the small amount of statistics and the difficulties with background subtraction, in particularly for the flight components, it was impossible to obtain good fits. Instead, the standard RDDS technique was utilized.

2.2 The GSFMA73 and GS2k017 Experiments

The GSFMA73 and GS2k017 experiments were performed under nearly identical conditions. Both experiments utilize a $^{32}\text{S} + ^{28}\text{Si}$ fusion-evaporation reaction with a 130 MeV ^{32}S beam. The detector set-up consisted of the Gammasphere array [14] for detection of the emitted γ rays, the 4π CsI-array Microball [15] for detection of evaporated charge particles and the Neutron Shell [16] to detect neutrons. The event trigger was set to accept events with at least four detected γ rays or one neutron and at least three detected γ rays. Recorded raw data was processed through various offline analysis packages as described in section 4.3. More details on the experimental conditions and set-up can be found in, for example, Ref. [3, 17].

2.3 The PHENIX Experiment

The PHENIX experiment [18, 19] has been designed to investigate nuclear matter created in ultra-relativistic nuclear collisions. It is one of four⁴ large detector systems operating at the Relativistic Heavy Ion Collider, which accelerates beams of nuclei ranging from protons to gold. The detector system is divided into several subsystems, which are constructed, maintained, and developed by a world wide collaboration consisting of about 500 physicists and engineers.

The primary goal of PHENIX is to detect signs of the Quark-Gluon Plasma and to characterize its physical properties. Hence, PHENIX offers to probe the nuclear system at different stages of its evolution, i.e., from the initial collision to the final hadronization. Many quantities related to proposed QGP signatures can be studied. For instance, the initial stages of the collision can be characterized by measuring direct photons and lepton pairs whereas information of the freeze-out is probed by looking at, for example, coalescence probabilities of various nuclei and anti-nuclei.

This thesis presents an analysis on light nuclei (deuterons and anti-deuterons) produced at RHIC during its second year of running. The analysis is based on data from PHENIX and a detailed description is found in chapter 3.

2.3.1 Detector Arrangements and Data Acquisition

The PHENIX detector consists of two central spectrometer arms (East and West), two muon spectrometers (North and South), and three global detector systems. A sketch of the experimental layout, as of the second year of running, is shown in Fig. 2.4. A brief description of the design and functionality of the different subsystems is given below.

⁴The others being BRAHMS, PHOBOS, and STAR

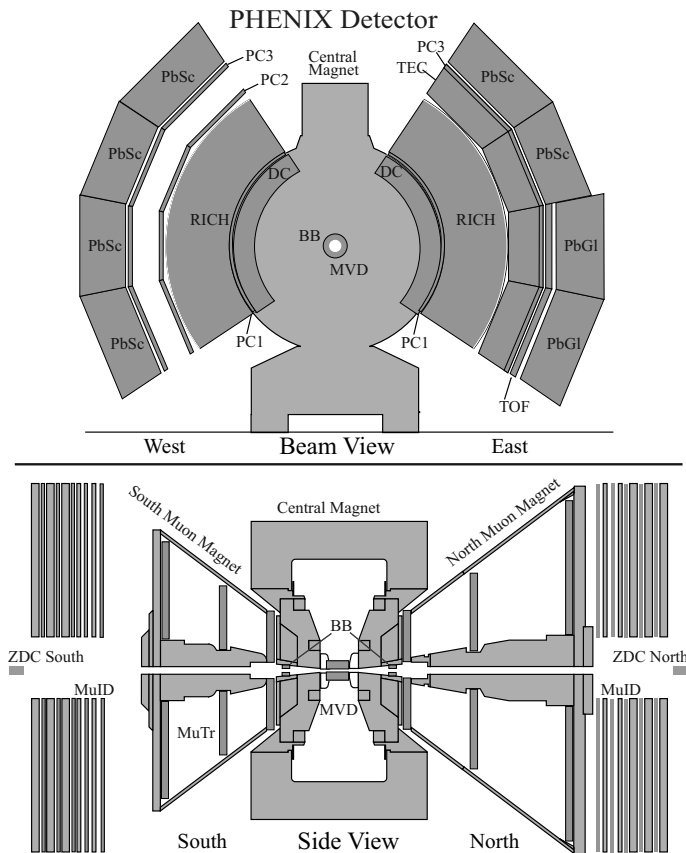


Figure 2.4: *The experimental layout of the PHENIX detector for 2002, viewed along the beam axis (top) and from the side (bottom).*

Central Arm Spectrometers

The central arm spectrometers (Fig. 2.4) are designed to perform momentum measurements, charge particle tracking, identification of various particle species, and to measure photon and electron energies. It covers the pseudorapidity interval $\Delta\eta = \pm 0.35$ and is divided into two arms (East and West), each with an azimuthal (ϕ) coverage of 90° . The spectrometer arms surround a **Central Magnet** that provides an axial field parallel to the beam. The particle tracking is performed using three detector systems;

- **Drift Chambers (DC):** Perform high resolution p_T measurements and provide precise tracking of charged particles traversing the spectrometers.
- **Pad Chambers (PC):** Pixel-based multi-wire proportional chambers that perform space coordinate measurements for charged particle trajectories. Described in more detail in section 2.3.2.

- **Time Expansion Chamber (TEC)**: Provides tracking in the $r - \phi$ plane and improves the momentum resolution for high p_T particles. It measures the energy deposition (dE/dx) along the tracks, which contributes to electron-pion separation.

The primary particle identification, energy measurements, and flight-time measurements are carried out with other subsystems:

- **Ring Imaging CHerenkov (RICH)**: The primary detectors for electron identification, which provides good electron-pion discrimination.
- **Time-Of-Flight (TOF)**: Performs high-resolution flight-time measurements (time resolution around 80 ps) used for particle identification of charged hadrons.
- **ElectroMagnetic Calorimeters (PbSc/PbGl)**: Provide photon identification and perform measurements of particle energy and flight time. The calorimeter is divided into two sectors of lead-glass (PbGl) Cherenkov calorimeters and six sectors of lead-scintillator (PbSc) sampling calorimeters.

Muon Spectrometers

To detect dimuons emerging from vector meson decay (J/Ψ , Ψ' , Υ etc.) PHENIX has designed two forward muon spectrometers, which detect muons with full azimuthal acceptance. Each consist of a

- **Muon Tracker (MuTr)**: Consists of multi-plane drift chambers for high precision particle tracking.
- **Muon Identifier (MuId)**: Composed of alternating layers of steel absorbers and low resolution tracking chambers. This combination provides a discrimination of pions, since they are stopped in the steel absorbers.

Each spectrometer is supplied with a radial magnetic field from the **Muon Magnets**.

Detectors for Global Observation

Important properties of the collision (centrality, collision vertex position etc.) are carried out by three different detector systems placed close to the beam axis:

- **Zero-Degree Calorimeters (ZDC)**: Measure the energy deposited from spectator neutrons emitted along the beam direction. They serves as a centrality trigger and can be used to monitor luminosity and to determine the position of the collision vertex.
- **Multiplicity Vertex Detector (MVD)**: Provides measurements of collision vertex position and event multiplicity. It has not been fully operational during the two first years of data taking.
- **Beam-Beam Counters (BBC)**: Composed of an array of Cherenkov counters arranged in a cluster around the beam pipe. The BBC produce a signal for the primary interaction trigger but are also used to determine the collision vertex position and provide the start time for time-of-flight measurements.

In the offline analysis, the combined information from the BBC and the ZDC is used to determine the collision centrality, which is used for event selection.

Data Handling

The detector signals are sampled and recorded with Front-End-Modules (FEM), which store signals in analogue or digital memories. At every beam crossing some detectors produce data used as input for the level-1 trigger (LVL1). If the trigger is accepted data in the FEM are transmitted by optical fibers to Data Collection Modules (DCM). To minimize the dead time, the Data Acquisition system (DAQ) can buffer five accepted LVL1 events, which allows the DAQ system to continuously record and transfer signals. The accepted data fragments are processed in the DCM to perform zero suppression, error checking, and data reformatting. The output is sent to an Event Builder (EvB), where the final stage of the event assembly takes place. The EvB provides an environment for the level-2 trigger (LVL2), which can further enrich the sample of accepted events. Finally, the data are recorded to disk for storage.

The raw data files are used as input to a reconstruction chain producing Data Summary Tapes (DST), which contain a variety of information; global event characteristics (vertex position), individual particle properties (momenta, charge), particle hit coordinates (x, y and z) for a specific detector, etc. The reconstruction occurs within an offline framework, where information from different subsystems is combined to reconstruct, for example, particle tracks or particle momenta. The DST are processed through a second offline framework to reduce redundant information. The new format, the so-called microDST, is used for various physics analyses.

2.3.2 The Pad Chambers

The central arm spectrometers comprise three different layers of pad chambers located at radial distances 2.5 m (PC1), 4.2 m (PC2), and 4.9 m (PC3) from the beam axis. They cover around ± 0.35 units of pseudorapidity and 90° in azimuth angle in each spectrometer arm. Each detector is a pixel-based multi-wire proportional chamber, has a very high detection efficiency, and is designed to fulfill the following roles:

- Provide reliable track information with accurate coordinates in the beam direction and good position resolution in the other directions.
- Provide redundancy for the drift chamber measurements.
- Define entry and exit coordinates of the particle identification subsystems.
- Provide fast position information to be used in the LVL2 trigger.

Readout and Performance of the Chambers

To achieve good spatial resolution, high detection efficiency, and reliable pattern recognition the chambers are constructed as multi-wire proportional chambers with one cathode plane finely segmented in small pads. The signals are read out by readout cards placed directly on the backplane of a chamber. Each card handles a group of 48 different pads. To reduce the number of readout channels, each pad is segmented in nine rectangular copper electrodes, so-called pixels. The pixel-pads are arranged in an interleaved pattern as illustrated in Fig. 2.5. The size of the pixels are chosen to collect an equal amount of charge on each pixel, hence the center pixels, which are located above the anode wires, are designed somewhat smaller. One center pixel and

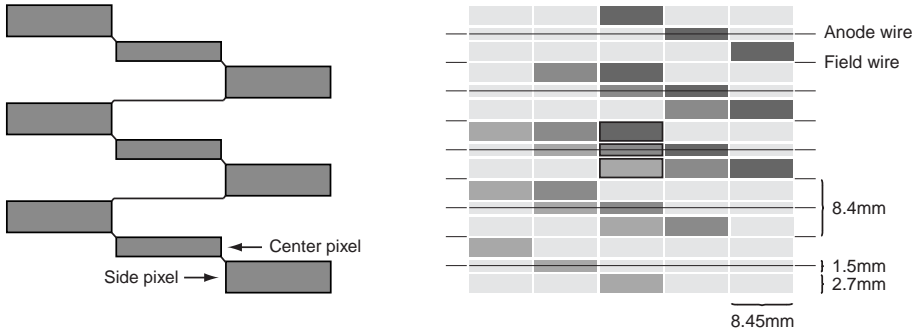


Figure 2.5: A pad consists of nine pixels (left). The pixel layout showing three fired pads combined to form one fired cell (right). Values are for PC1.

two side pixels, from different but adjacent pads, are used in conjunction to form a cell. A valid hit in a cell, and thus the detector chamber, is obtained if all three pads corresponding to a cell fires in coincidence. An individual pad fires if the collected charge exceed a pre-set discriminator threshold. The pixel pattern gives each cell a unique set of pad numbers and thus the location of the fired cell can be determined.

Before installation, each pad chamber type was tested extensively with cosmic rays to verify the charge gain on the anode wires and investigate the efficiency and position resolution. The experimental set-up and measurements are described in more detail in section 6 of PAPER I. An estimate of the charge gain on the anode wires was made for one pad chamber of each type. The chambers had no wire readout installed, but for a few wires the signal was extracted and the pulse height distribution was recorded on a multichannel analyzer. The charge gain was determined by dividing the charge corresponding to the peak with the number of electrons liberated by a minimum ionizing particle. For the used gas mixture (50% ethane and 50% argon) this was calculated to be 95 electrons/cm using tabulated values for the average energy needed to liberate an electron-ion pair [20].

The operating voltage was chosen on the basis of the different measurements and the values were set to 1700 V for PC1, 1840 V for PC2 and 1880 V for PC3, which gives a high efficiency and the voltages are safely below the onset of sparking.

Chapter 3

Deuteron and anti-deuteron physics with PHENIX

In high-energy heavy-ion experiments the measurements of hadronic spectra provide valuable information about the final freeze-out of the system. Such measurements have been performed utilizing the PHENIX detector at RHIC during its second year of operation. Analysis of light nuclei, in particular deuterons and anti-deuterons, produced in $\sqrt{s_{NN}} = 200$ GeV Au+Au collisions is presented in the sections below. This analysis is one of two independent searches for deuterons and anti-deuterons within the PHENIX collaboration. The two analyses have been processed in parallel with slightly different approaches and the difference was used for the estimation of systematic errors. The combined results of the two analyses can be found in PAPER II.

Deuterons may arise as fragments from the remaining beam nuclei, but the possibility for these fragments to survive into the central region is negligible at RHIC. Instead the observed deuterons and anti-deuterons must have been formed by either direct production of deuteron/anti-deuteron pairs or more likely by coalescence of nucleon pairs. To describe the production mechanism of the deuterons and anti-deuterons, a coalescence model is introduced.

3.1 The Coalescence Model

In the coalescence model [21, 22] a deuteron (anti-deuteron) is formed if a proton (anti-proton) and a neutron (anti-neutron) are close enough in both momentum and configuration space to fuse together. Assuming that neutrons and protons have the same momentum distributions, the invariant deuteron (anti-deuteron) cross-section in the coalescence model is related to the primordial nucleon cross-sections by

$$E_d \cdot \frac{d^3 n_d}{dp_d^3} = B_2 \left(E_p \cdot \frac{d^3 n_p}{dp_p^3} \right)^2, \quad (3.1)$$

where $p_d = 2p_p$. B_2 is the coalescence parameter, which reflects the volume of the particle-emitting source. Thus, the coalescence parameter can be determined via the ratio of the yield of deuterons and the yield of protons squared.

Consider a distribution of protons and neutrons within a nuclear volume, V , as sketched in Fig. 3.1.

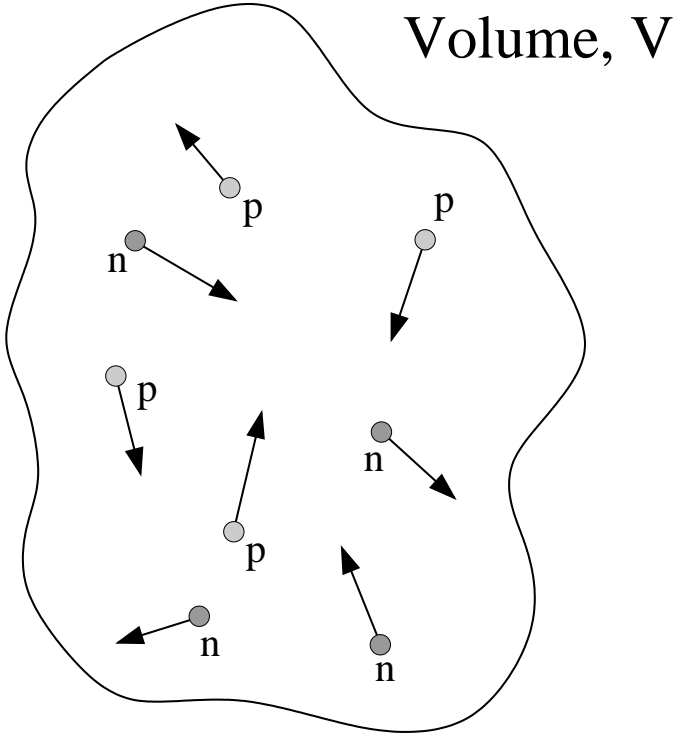


Figure 3.1: Protons and neutrons distributed over a small volume, V .

The distribution function in phase space is defined as

$$f(\vec{r}, \vec{p}) = \frac{d^6 n_p}{dp_x dp_y dp_z dx dy dz} \cdot (2\pi\hbar)^3, \quad (3.2)$$

where dn is the number of particles in a small cell ($dp_x dp_y dp_z dx dy dz$) centered around a point (p_x, p_y, p_z, x, y, z) in phase space. Assuming that protons and neutrons are uniformly distributed within the volume V , the distribution function can be written

$$f(\vec{r}, \vec{p}) = \frac{d^3 n}{dp^3} \cdot \frac{(2\pi\hbar)^3}{V}. \quad (3.3)$$

The two nucleons are supposed to bind together and form a deuteron by coalescence. In such a scenario, the deuteron density can be expressed with the distribution function (Eq. 3.3) of protons and neutrons as

$$\frac{1}{2s_d + 1} \left(\frac{d^3 n_d}{dp_d^3} \cdot \frac{(2\pi\hbar)^3}{V} \right) = \frac{1}{2s_p + 1} \left(\frac{d^3 n_p}{dp_p^3} \cdot \frac{(2\pi\hbar)^3}{V} \right) \frac{1}{2s_n + 1} \left(\frac{d^3 n_n}{dp_n^3} \cdot \frac{(2\pi\hbar)^3}{V} \right),$$

where s_d , s_p , and s_n are the spins of the deuteron, proton, and neutron, respectively [23]. The resulting deuteron momentum, p_d , is the sum of the proton and

neutron momentum, i.e., $p_d = p_p + p_n \approx 2p_p$. Assuming the same momentum distribution for the two nucleons, i.e., $\frac{d^3 n_p}{dp_p^3} = \frac{d^3 n_n}{dp_n^3}$, the deuteron density can be expressed as

$$\frac{d^3 n_d}{dp_d^3} = \frac{3}{4} \frac{(2\pi\hbar)^3}{V} \cdot \left(\frac{d^3 n_p}{dp_p^3} \right)^2, \quad (3.4)$$

which can be related to the invariant deuteron yield by

$$E_d \cdot \frac{d^3 n_d}{dp_d^3} = \frac{E_d}{E_p^2} \cdot \frac{3}{4} \frac{(2\pi\hbar)^3}{V} \cdot \left(E_p \cdot \frac{d^3 n_p}{dp_p^3} \right)^2. \quad (3.5)$$

By comparing Eq. 3.1 with Eq. 3.5 it is seen that the coalescence parameter can be written as

$$B_2 = \frac{E_d}{E_p^2} \cdot \frac{3}{4} \frac{(2\pi\hbar)^3}{V}, \quad (3.6)$$

which can be used to estimate the volume of the source. In a simple model, where one assumes that the protons and neutrons are uniformly distributed over a spherical volume with radius R and where p_T is small ($p_T < m$), the relation between B_2 and R is given by

$$B_2 \approx \frac{m_d}{m_p^2} \cdot \frac{9}{2} \frac{\pi^2 \hbar^3}{c^2 R^3} \quad (3.7)$$

3.2 Data Analysis

A study of deuteron and anti-deuteron production in Au+Au collisions at RHIC has been performed using data from the PHENIX experiment. Data was taken during the second year of running at $\sqrt{s_{NN}} = 200$ GeV with most of the detector subsystems in operation. To identify deuterons and anti-deuterons, the following detector systems in the east central tracking arm were used:

- Drift Chamber (DC)
- Two layers of Pad Chambers (PC1 and PC3)
- Time-of-Flight detector (TOF)

In addition, information from the Beam-Beam Counters (BBC) and Zero-Degree Calorimeters (ZDC) were used for triggering and event selection. The total event sample consists of about 20 million minimum bias events, where each event is required to have a vertex of $|z_{vertex}| < 20$ cm from the nominal crossing point.

Below is a description of the analysis work providing the event and track selection cuts, particle identification, correction simulations, and some results.

Event and track selection cuts

Deuterons (anti-deuterons) were identified with the particle-identification capabilities of the central tracking arm through the flight time measured with the TOF. Due to the low yield of deuterons (anti-deuterons) compared with other hadrons, stricter cuts on the tracks were required to be able to extract and determine a clear signal.

A first selection of tracks was done by requiring a drift chamber track to have an associated hit in the first layer of pad chambers (PC1). In order to define further cuts and investigate how these affect the signal, only a fraction (≈ 3 million minimum bias events) of the total event sample was used. These cuts are described below and once determined they were applied to the full data sample in order to extract the signal of the deuterons (anti-deuterons).

TOF Association

As the particle identification was performed using the TOF wall, the first restriction on the event sample was to include only events with a recorded hit in the TOF detector. To reduce the number of wrongly reconstructed particle trajectories a momentum dependent track selection cut, $F_{TOF}(p_T)$, was introduced. This was derived from calculating the distance, R , between the the intercept of the projected track with the TOF wall (x_{TRK} , y_{TRK} , z_{TRK}) and the position of the associated TOF hit (x_{TOF} , y_{TOF} , z_{TOF}), determined by the TOF itself. The distance was calculated for different p_T -bins in the interval $0.4 < p_T < 5.0$ GeV/c. Figure 3.2 shows the distribution of R for $1.0 < p_T < 1.1$ GeV/c. The distribution for each bin was fitted

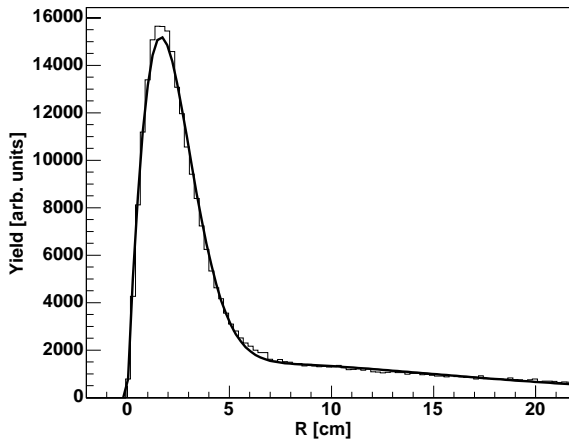


Figure 3.2: *Distribution of R for tracks with $1.0 < p_T < 1.1$ GeV/c fitted with a function $f(R)$ as described in the text.*

with a function $f(R)$ written as

$$f(R) = A \cdot R \cdot e^{-B(R+C \cdot R^2)} + D \cdot R \cdot e^{-E \cdot R}. \quad (3.8)$$

The first term represents the peak of extrapolated tracks that are correctly associated to a TOF hit whereas the second term correspond to the background arising from wrongly associated tracks. The track selection cut was set for each momentum interval such that the signal equals half the background. This allows to derive $F_{TOF}(p_T)$. Only tracks with $R \leq F_{TOF}(p_T)$ were accepted in the final analysis.

PC3 Association

Utilizing the two layers of pad chambers in the east arm spectrometer (PC1 and PC3) allows to extrapolate the particle trajectory to the primary vertex. The z coordinate of the extrapolated track (z_{pc_vertex}) was compared with the event z vertex (z_{vertex}) from the BBC, which provides a cut associated with PC3.

Constructing a straight line with the pad chamber coordinates ($x_{PC1}, y_{PC1}, z_{PC1}$ and $x_{PC3}, y_{PC3}, z_{PC3}$), the z_{pc_vertex} is calculated by extrapolating the line to $r = 0$, where $r = \sqrt{x^2 + y^2}$, i.e.,

$$z_{pc_vertex} = \frac{z_{PC1} \cdot \sqrt{x_{PC3}^2 + y_{PC3}^2} - PC3 \cdot \sqrt{x_{PC1}^2 + y_{PC1}^2}}{\sqrt{x_{PC3}^2 + y_{PC3}^2} - \sqrt{x_{PC1}^2 + y_{PC1}^2}}. \quad (3.9)$$

The difference between the two vertices ($\Delta z_{vertex} = z_{pc_vertex} - z_{vertex}$) was calculated and plotted for a set of different p_T -bins in the range $0.4 < p_T < 5.0$ GeV/c. The distribution for each bin was fitted to the sum of two gaussians that corresponds to the peak of the distribution and the background, respectively. This allows to derive a momentum dependent selection cut, $F_{PC3}(p_T)$, which was set at 2σ of the gaussian equivalent to the signal. Only tracks with $\Delta z_{vertex} \leq F_{PC3}(p_T)$ were used in the final analysis.

Energy loss

The measured energy loss in the TOF wall, ΔE , was used to introduce an energy loss cut, ΔE_{cut} , which was parameterized as

$$\Delta E_{cut} = \frac{A}{\beta^2} + B, \quad (3.10)$$

where β is the particle velocity. The parameters A and B were determined from a scatter plot of the energy loss measured in the TOF vs. $1/\beta^2$. To simplify the selection of the parameters the expected mean energy loss was calculated according to the Bethe-Bloch formula [24]

$$-\frac{dE}{dx} = K \cdot \rho \cdot \frac{Z}{A} \cdot \frac{z^2}{\beta^2} \left[2 \cdot \ln \left(\frac{2m_e c^2 (\beta\gamma)^2}{I^2} \right) - 2\beta^2 \right] \quad (3.11)$$

using $K = 0.1535$ MeVcm²/g, $z = 1$ for a singly charged particle, and the electron mass $m_e c^2 = 511$ keV. The values for the absorbing material in the TOF were $\rho = 1$ g/cm³, $\frac{Z}{A} = 0.5$, and $I = 64.7$ eV with a thickness of $dx = 1.5$ cm. With the expected mean energy loss included in the scatter plot, the parameters were set to generate a lower limit. Hence, only tracks with $\Delta E \geq \Delta E_{cut}$ were used in the final analysis.

Effect of applying the cuts

The effect of consecutively applying the different cuts to reduce the background in the deuteron mass spectrum is illustrated in Fig. 3.3. Mass spectra are obtained using the drift chamber information in conjunction with information from the TOF wall as described in section 3.2. Figure 3.3a shows the obtained mass spectrum for all

drift chamber tracks associated with a hit in the first layer of pad chambers (PC1). Panel b, c, and d illustrates the improvement of the mass spectrum after applying each of the described cuts by first applying the TOF association (b) followed by the PC3 association (c) and finally the energy loss cut (d). It is seen that the signal-to-background ratio improves to about 2:1 after the final cuts have been applied.

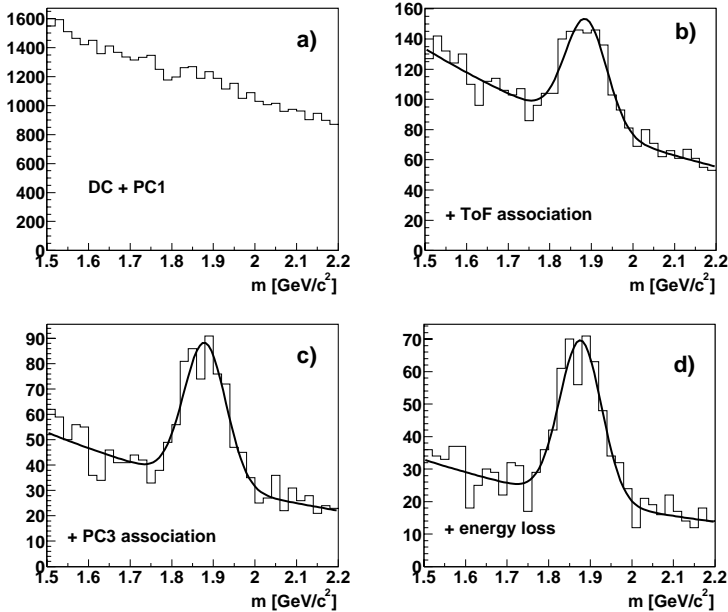


Figure 3.3: *Reconstructed mass spectra for deuterons after consecutively applying different track quality cuts as described in the text. The background is clearly reduced after the final cuts have been applied. The signal-to-background ratio improves to about 2:1. The solid curves show fits to data.*

Particle Identification and Raw Yields

The cuts described in the previous section are applied to the total event sample and tracks surviving the cuts are used in the analysis. Flight times measured in the TOF are used in combination with flight lengths and reconstructed momenta to obtain mass spectra and to identify particles. An illustration of the excellent particle identification capabilities of the tracking system is shown in Fig. 3.4. Plotted is $q \cdot (1 - \beta)$ as a function of $1/p$, where $\beta = v/c$, p is the total reconstructed momentum, and q is the charge in elementary units. Bands of pions (π^+ , π^-), kaons (K^+ , K^-), protons (p), anti-protons (\bar{p}), deuterons, and anti-deuterons are clearly seen in the figure.

The mass, m , of a particle is calculated from the reconstructed momentum, p , and

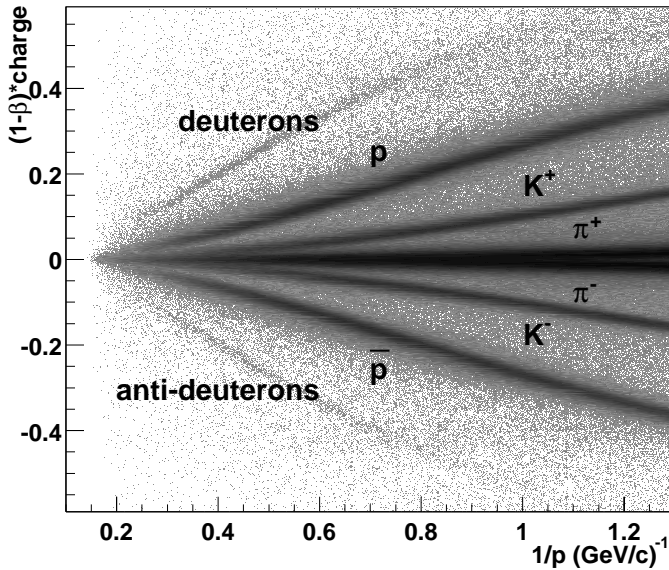


Figure 3.4: Illustration of the excellent particle identification capabilities from time-of-flight measurements. Bands of different particle species are marked.

the flight time, t , measured by the TOF according to

$$m = \frac{p}{c} \cdot \sqrt{\left(\frac{tc}{L}\right)^2 - 1}, \quad (3.12)$$

where L the flight length. To extract the yield of deuterons and anti-deuterons, the mass spectra were constructed for different bins in p_T . The distributions were fitted to a gaussian with an exponential background as

$$f(M_{fit}) = Cbe^{-bm} + \frac{N}{\sqrt{2\pi}\sigma} \cdot e^{-\frac{(m-M_{fit})^2}{2\sigma^2}}, \quad (3.13)$$

where b , C , N , M_{fit} , and σ are free parameters. N gives the yield of deuterons (anti-deuterons) in the momentum bin, M_{fit} is the fitted mass, and σ is the width of the mass distribution. The values of M_{fit} and the extracted raw yields, N_{RAW} for the different p_T -bins are listed in Table 3.1.

Table 3.1: *Extracted values of the raw yields and masses for deuterons and anti-deuterons for different p_T -bins. The tabulated mass of a deuteron is $1875.6 \text{ MeV}/c^2$.*

p_T [Gev/c]	deuterons		anti-deuterons	
	N_{RAW}	M_{fit} [MeV/ c^2]	N_{RAW}	M_{fit} [MeV/ c^2]
1.0-1.5	1065.8±79.7	1868±4	472.7±49.0	1862±5
1.5-2.0	1046.3±46.3	1864±2	518.1±35.9	1860±3
2.0-2.5	750.4±37.1	1872±2	382.2±30.1	1856±4
2.5-3.0	404.1±30.6	1884±4	186.8±25.2	1861±8
3.0-3.5	172.4±24.6	1877±8	54.8±12.4	1845±7

Corrections and simulations

The corrections needed to convert the raw particle yield to the normalized invariant distributions are obtained from simulations. Simulated events are processed through a GEANT-based Monte Carlo simulation package developed for PHENIX (PISA). This simulation package includes particle decay (if applicable), multiple Coulomb scattering, hadronic and electromagnetic interactions, and the acceptance, efficiency, and resolution of the detector. A shortcoming of GEANT is that no hadronic interactions of deuterons or anti-deuterons are implemented. Thus, the performed single-particle corrections do not account for this effect, and the corrections for hadronic interactions have been studied separately. This is discussed below.

The multiplicity dependent part of the efficiency corrections has been investigated by embedding simulated particles in real events and checking whether it gets reconstructed or not. This investigation was performed by other members within the PHENIX collaboration.

Single-particle corrections

Single-particle corrections were done using two event samples, each comprising one million events with one particle type (deuteron or anti-deuteron) per event. The particles were generated with a flat distribution in rapidity covering the full azimuthal angle ($0 \leq \phi \leq 360^\circ$) and with $0.5 \leq p_T \leq 8.0 \text{ GeV}/c$. The events were processed through PISA and the correction factors (C) were obtained by comparing the number of reconstructed deuterons (N_{rec}) in a given p_T -bin with the number of generated deuterons (N_{gen}) in the same bin. The correction factors used to convert the raw yields were calculated for the same p_T -bins as for the data. The numbers are listed in Table 3.2.

Hadronic Interaction

Since hadronic processes for nuclei are not implemented in GEANT, stand-alone calculations are performed to determine the corrections for the hadronic interactions of deuterons and anti-deuterons. The calculations are based on the accessible detector material, which a particle encounters while traversing from the primary vertex position to the TOF wall. From the path lengths, l_i , and densities, n_i , of the different

Table 3.2: Correction factors for deuterons and anti-deuterons. The error given for C is the statistical error.

p_T [Gev/c]	deuterons			anti-deuterons		
	N_{gen}	N_{rec}	C	N_{gen}	N_{rec}	C
1.0 - 1.5	66408	724	91.7±3.4	66306	774	85.7±3.1
1.5 - 2.0	46765	646	72.4±2.9	46852	671	69.8±2.7
2.0 - 2.5	40048	651	61.5±2.4	39680	680	58.4±2.2
2.5 - 3.0	37265	639	58.3±2.3	37287	691	54.0±2.1
3.0 - 3.5	36288	693	52.4±2.0	36388	687	53.0±2.0

materials the probability that a particle should survive without suffering any hadronic interaction is calculated as

$$\exp\left(-\sum_i \sigma_i n_i l_i\right), \quad (3.14)$$

where σ_i are the corresponding cross sections. The inelastic cross section for deuteron and anti-deuteron induced interactions is parameterized using the proton (neutron) and anti-proton (anti-neutron) cross sections. This parameterization is discussed in Appendix A.

Using the parameterization, the hadronic interaction probabilities are calculated for (anti-)protons and (anti-)deuterons. The calculations for (anti-)protons are compared with the interaction probabilities obtained from GEANT simulations, which indicated similar results. Hence, the mean of the methods is used as the final nucleon interaction probabilities, and the difference gives an estimate of the systematic error.

Finally, the hadronic interaction probabilities for deuterons and anti-deuterons are determined using the ratio of the interaction probabilities of (anti-)deuterons to those of (anti-)protons. The ratios are applied to the final nucleon interaction probabilities, which gives the interaction probabilities $\approx 10.0(15)\%$ and $\approx 15.0(35)\%$ for deuterons and anti-deuterons, respectively.

Secondary deuterons

Deuterons can be produced in secondary (knock-out) reactions between the produced particles and the surrounding detector material or the beam pipes. This background source is investigated using an event sample of around one thousand central HIJING events. The simulated events, which contained no primary deuterons, are fed through PISA and the output is analysed as follows:

The particles detected in the TOF wall are identified and all deuterons are selected. Since the event sample contained no primary deuterons, the detected deuterons must have been produced in secondary reactions. From the particle kinematics, a secondary vertex position and the momentum distribution of the deuterons is calculated. It was found that a large fraction of the secondary deuterons were produced in the TOF wall itself. These are, however, not to be considered as a problem as they are not reconstructed as deuterons within the reconstruction code. Instead, the investigation focuses on secondary deuterons produced close to the primary vertex. This is achieved by only selecting particles with a secondary vertex $|x| < 20$ cm and $|y| < 20$ cm.

The yields of selected secondary deuterons are calculated for different bins in p_T . The obtained p_T distribution is normalized to the number of events and extrapolated to higher momenta, which provide a comparison with normalized raw data yields. The result is illustrated in Fig. 3.5. However, the simulations utilized only central

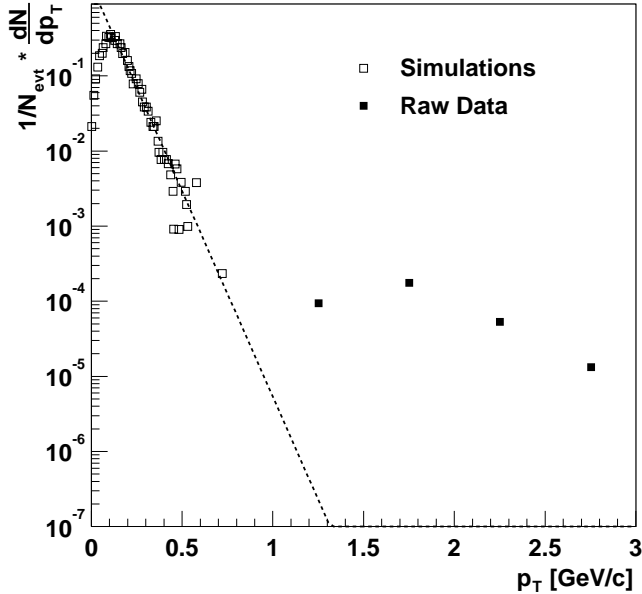


Figure 3.5: Secondary deuterons from simulated events compared to extracted raw yields in data. The dashed line shows an extrapolation of simulated data to higher p_T .

events with a full coverage of the azimuthal angle, ϕ , whereas the raw data yields are extracted for minimum bias events using the TOF acceptance in ϕ . These factors will increase the relative relation between the simulations and the measured data. Therefore, it can be concluded that secondary deuterons are negligible for $p_T > 1.0$, which is the lower limit for the first measured data point.

The production of secondary anti-deuterons can be neglected as any detected anti-deuteron must have been produced in the primary collision.

3.3 Physics Results

Following the analysis procedure described above, this section presents some physics results obtained using an event sample of 19.3 million minimum bias events. These results are combined with those of the second (anti-)deuteron analysis performed within the PHENIX collaboration, and the summarized results are presented in PAPER II.

The invariant yields of deuterons and anti-deuterons are extracted from the measured raw yields by applying the corrections discussed in the previous section. For the present results, however, there are no multiplicity dependent corrections included. The invariant yield, normalized to the number of events, N_{evt} , can be written as

$$\frac{d^2 N}{2\pi N_{evt} p_T dy dp_T}, \quad (3.15)$$

where the dy dependence is included in the single-particle corrections, dp_T are the widths of the used p_T -bins and the value of p_T is equal to the center of each p_T -bin, respectively. The values of the normalized yields are listed in Table 3.3. The

Table 3.3: *Normalized invariant yields of deuterons and anti-deuterons.*

p_T [GeV/c]	deuterons	anti-deuterons
	$d^2 N/2\pi p_T dy dp_T$ [GeV/c] $^{-2}$	$d^2 N/2\pi p_T dy dp_T$ [GeV/c] $^{-2}$
1.0 - 1.5	$(1.19 \pm 0.10) \cdot 10^{-3}$	$(5.23 \pm 0.57) \cdot 10^{-4}$
1.5 - 2.0	$(6.61 \pm 0.37) \cdot 10^{-4}$	$(3.34 \pm 0.26) \cdot 10^{-4}$
2.0 - 2.5	$(3.13 \pm 0.19) \cdot 10^{-4}$	$(1.60 \pm 0.14) \cdot 10^{-4}$
2.5 - 3.0	$(1.31 \pm 0.11) \cdot 10^{-4}$	$(5.92 \pm 0.82) \cdot 10^{-5}$
3.0 - 3.5	$(4.24 \pm 0.62) \cdot 10^{-5}$	$(1.44 \pm 0.33) \cdot 10^{-5}$

invariant spectra are fitted by an exponential in m_T , which allows to determine the temperature parameter, T , as the inverse slopes. Using the extracted fit parameters the spectra are extrapolated to lower and higher transverse momentum. Figure 3.6 shows the exponential fits to the spectra, including the extrapolation. The fits give temperature parameters of $T = 463(16)$ MeV and $T = 442(19)$ MeV for deuterons and anti-deuterons, respectively.

The extrapolation of the fits can be used to calculate the rapidity density, dN/dy , and the mean transverse momenta, $\langle p_T \rangle$. The rapidity density is calculated by integrating the (anti-)deuteron yields over p_T as

$$\frac{dN}{dy} = 2\pi \int_0^\infty p_T f(p_T) dp_T, \quad (3.16)$$

where $f(p_T)$ is the invariant yield as a function of p_T expressed as

$$f(p_T) = \frac{d^2 N}{2\pi p_T dy dp_T}. \quad (3.17)$$

In a similar manner, $\langle p_T \rangle$ is calculated as the ratio of two integrals as

$$\langle p_T \rangle = \frac{\int_0^\infty p_T^2 f(p_T) dp_T}{\int_0^\infty p_T f(p_T) dp_T} \quad (3.18)$$

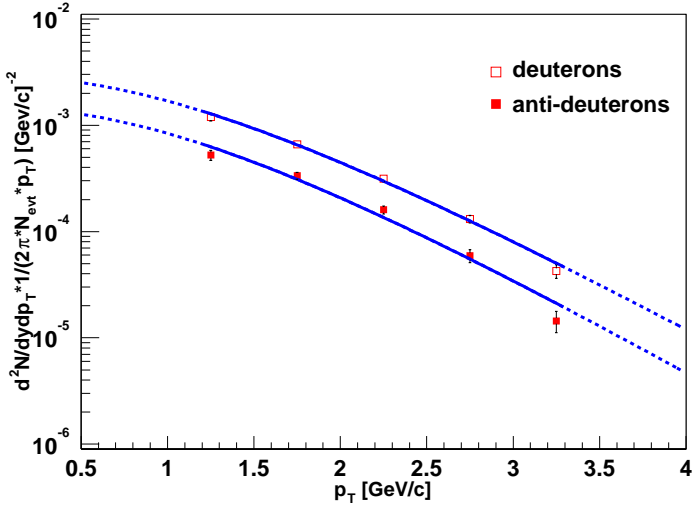


Figure 3.6: *Exponential fits in p_t and m_T to the normalized invariant deuteron and anti-deuteron spectra. Dashed lines show the extrapolation of the fits.*

Using the fitted function in m_T , the values of dN/dy and $\langle p_T \rangle$ were calculated as described above. The result is presented in Table 3.4.

Table 3.4: *Values of dN/dy and $\langle p_T \rangle$ for deuterons and anti-deuterons.*

	dN/dy	$\langle p_T \rangle$ [GeV/c]
deuterons	0.0200(6)	1.41(4)
anti-deuterons	0.0090(3)	1.37(5)

The centrality dependence of the invariant p_T -spectra is investigated by dividing the minimum bias events into different centrality classes. For each centrality class, the raw yields are extracted and converted to normalized yields. The final yields are compared and it is concluded that the yield of deuterons and anti-deuterons increases with centrality.

The Coalescence parameter (B_2)

As discussed in section 3.1, the invariant (anti-)deuteron yields can be related to the invariant (anti-)proton yields with the coalescence parameter, B_2 , as

$$B_2 = \frac{E_d \cdot \frac{d^3n_d}{dp_d^3}}{\left(E_p \cdot \frac{d^3n_p}{dp_p^3}\right)^2}, \quad (3.19)$$

where $p_d = 2p_p$. Thus, the B_2 value is calculated taking the ratio of the invariant (anti-)deuteron spectra to the square of the invariant (anti-)proton spectra. However, (anti-)protons produced from weak decays, e.g., Λ ($\bar{\Lambda}$), have to be taken into account in the study of the coalescence parameter. The Λ ($\bar{\Lambda}$) has a lifetime that corresponds to a few cm. Hence, (anti-)protons from such decays will not contribute in the coalescence of a (anti-)deuteron. Therefore, the utilized (anti-)proton spectrum need to be corrected for this feed-down effect, which will lead to a substantial increase in the coalescence parameter. The final analysis employ feed-down corrected spectra. However, at the time of the present investigation no feed-down corrections had been applied to the (anti-)proton spectra.

The study of the coalescence parameter employs the extracted invariant deuteron (anti-deuteron) spectrum and the proton (anti-proton) spectra obtained from another PHENIX analysis [25]. Figure 3.7 shows the coalescence parameter as a function of transverse momentum. The coalescence parameter increases with transverse momen-

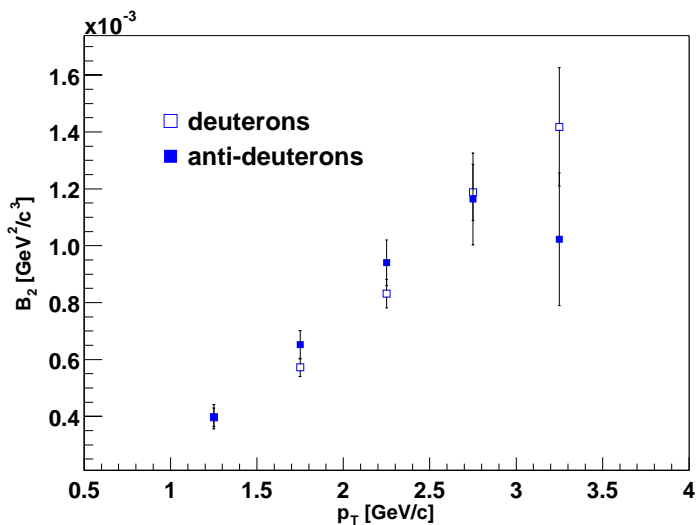


Figure 3.7: Coalescence parameter as a function of transverse momentum for deuterons (anti-deuterons). Note that the employed proton (anti-proton) spectra are not corrected for the feed-down effect.

tum, which can be seen as a sign of collective transverse expansion [26]. It is known that the p_T -dependence of B_2 is related to the density profile as well as the expansion velocity of the source. Assuming that the nucleons before freeze-out are uniformly distributed within a (static) sphere with radius R , B_2 can be related to R according to Eq. 3.7. The increase of B_2 with p_T is inconsistent with such a simple model and indicates a decreasing source size with increasing p_T . This is in qualitative agreement with results from HBT and indicates an expanding source.

Chapter 4

Gamma-Ray Spectroscopy

Measurements of discrete γ rays, emitted from the late stages in a heavy-ion fusion-evaporation reaction, allow to study the properties of atomic nuclei in their ground states and excited states. In particular, gamma-ray spectroscopy offers a possibility to probe electromagnetic properties that can be predicted from various theoretical models. Hence, from comparison between experimental data and theoretical calculations conclusions on fundamental effects in nuclei can be drawn.

Lifetimes of excited states and related electromagnetic properties have been determined from the analysis of data from the GASP03.12 experiment. Comparison with large-scale shell-model calculations provide valuable information on core polarization effects and a quantitative estimate of effective transition operators.

4.1 Electromagnetic Properties

The description of electromagnetic properties in nuclei is covered in many text books on nuclear physics, for example Ref. [27, 28, 29]. Hence, this section only discuss briefly some of the topics relevant for the present thesis.

The classical theory of radiation fields are transferred into the quantum domain through replacement of the classical multipole moments with appropriate multipole operators, $\mathcal{M}(\sigma L)$. These operators describe the change of a nucleus from its initial state, ψ_i , to its final state, ψ_f . The character of the radiation field, which can be of either electric or magnetic nature, is denoted σ and the multipole order of the radiation is denoted L . An electromagnetic transition with a multipole of order L carries an angular momentum of $L\hbar$ per photon¹.

Consider a multipole transition from an initial excited nuclear state to a final nuclear state, $\psi_i \rightarrow \psi_f$. The properties of the states are described in terms of angular momentum \vec{J}_i, \vec{J}_f and parity π_i, π_f . In the γ -ray transition, the photon is emitted with an angular momentum \vec{L} such as to conserve angular momentum

$$\vec{J}_i = \vec{J}_f + \vec{L}. \quad (4.1)$$

¹Such as $L = 1$ for a dipole transition, $L = 2$ for a quadrupole transition, and so on.

Hence, the angular momentum selection rules for a γ decay can be written

$$|J_i - J_f| \leq L \leq J_i + J_f \quad (\text{no } L = 0), \quad (4.2)$$

where L is the multipolarity of the transition. A given transition thus comprises a mixture of several components where the lowest permitted multipole transition usually dominates. Monopole γ -ray transitions ($L = 0$) are forbidden because a photon has an intrinsic angular momentum of $1\hbar$. Thus no γ decay can occur for $0^{\pi_i} \rightarrow 0^{\pi_f}$ transitions. Instead, these transitions proceed through internal conversion, in which the excitation energy is released by ejecting an electron in an atomic orbital.

The character of the radiation field is determined by the relative parity of the nuclear states in combination with the multipolarity. The parity selection rules for the character of the multipole transition are

$$\begin{aligned} \pi_i \neq \pi_f & \quad L \text{ odd} \rightarrow \text{electric, } L \text{ even} \rightarrow \text{magnetic,} \\ \pi_i = \pi_f & \quad L \text{ even} \rightarrow \text{electric, } L \text{ odd} \rightarrow \text{magnetic.} \end{aligned} \quad (4.3)$$

The transition probability, $\lambda(\sigma L)$, for γ -ray emission of multipolarity L and character σ is expressed by

$$\lambda(\sigma L, J_i \rightarrow J_f) = \frac{8\pi(L+1)}{\hbar L[(2L+1)!!]^2} \left(\frac{E_\gamma}{\hbar c}\right)^{2L+1} B(\sigma L, J_i \rightarrow J_f), \quad (4.4)$$

where the quantity $B(\sigma L)$ is the so-called reduced transition probability. Note that the transition probability depends on the γ -ray energy, E_γ , while the reduced transition probability contains no energy dependence. $B(\sigma L)$ can be expressed as

$$B(\sigma L, J_i \rightarrow J_f) = \frac{1}{2J_i + 1} |\langle \psi_f | \mathcal{M}(\sigma L) | \psi_i \rangle|^2, \quad (4.5)$$

in which $\langle \psi_f | \mathcal{M}(\sigma L) | \psi_i \rangle$ is the reduced matrix element. For a nucleus with A nucleons the multipole operator become the sum over all single particle operators. The electric and magnetic operators are written as

$$\mathcal{M}(EL) = \sum_{i=1}^A e_i r_i^L Y_{Lm_L}, \quad (4.6)$$

$$\mathcal{M}(ML) = \sum_{i=1}^A \mu_N \left(\frac{2}{L+1} g_l^i l_i + g_s^i s_i \right) \cdot [\nabla(r_i^L Y_{Lm_L})], \quad (4.7)$$

where r_i is the orbital radius for particle i and Y_{Lm_L} is the corresponding spherical harmonic function [27]. The single-particle operators are derived for a particle with charge e_i and a magnetic moment determined by the gyromagnetic factors g_l^i and g_s^i . For free nucleons the g -factors are found empirically to be $g_l^p = 1$, $g_l^n = 0$ and $g_s^p = 5.59$, $g_s^n = -3.83$ for protons and neutrons, respectively.

For a γ decay, $\psi_i \rightarrow \psi_f$, the lifetime of the initial state, τ_i , can be written as

$$\tau_i = \frac{1}{\lambda_{tot}(J_i \rightarrow J_f)}, \quad (4.8)$$

where λ_{tot} is the total transition probability given as a sum over all possible multipole components:

$$\lambda_{tot}(J_i \rightarrow J_f) = \sum_{j,k} \lambda(\sigma_j L_k, J_i \rightarrow J_f). \quad (4.9)$$

In most cases, however, the lowest multipole order dominate the transition and the contribution from other components can be neglected. A common exception are mixed $E2/M1$ transitions. The degree of mixing between the two lowest multipolarity components is given by the mixing ratio

$$\delta(\sigma_2 L_2 / \sigma_1 L_1) = \sqrt{\frac{\lambda(\sigma_2 L_2)}{\lambda(\sigma_1 L_1)}}. \quad (4.10)$$

The γ decay of an excited nuclear state has so far been considered to take place via a γ -ray transition into one final state. However, in many cases the depopulation of the initial state can occur via several branches into different final states. The total transition rate, of course, would be the sum of the individual transition probabilities. The contribution of each transition to the sum is determined by the branching ratio, b_r , which is the relative transition probability written as

$$b_r = \frac{\lambda_{tot}(\sigma L)}{\lambda_{TOT}}, \quad (4.11)$$

where $\lambda_{tot}(\sigma L)$ is the total transition rate for one of the γ -ray transitions and λ_{TOT} is the total transition rate for all transitions.

From experimentally determined lifetimes the reduced transition probabilities for the multipole transitions to the final states can be determined using Eq. 4.4 if the corresponding branching ratio and any possible mixing of different multipole components are known. The reduced transition probability for an electric quadrupole transition, for example, can be determined from experimental data via

$$B(E2; J_i \rightarrow J_i - 2) = b_r \cdot \frac{816.2}{\tau_i E_\gamma^5}, \quad (4.12)$$

where τ_i is the lifetime of the initial state in ps, and E_γ the energy of the transition in MeV.

The number of nucleons that participate in the transition is related to the configuration of the relevant nuclear states. In the extreme single-particle case, where only one nucleon contributes to the transition, Weisskopf gives estimates of the reduced transition probabilities as

$$B^W(EL) = \frac{1}{4\pi} \left(\frac{3}{L+3} \right)^2 (1.2A^{1/3})^{2L}, \quad (4.13)$$

$$B^W(ML) = \frac{10}{\pi} \left(\frac{3}{L+2} \right)^2 (1.2A^{1/3})^{2L-2}, \quad (4.14)$$

where $B^W(EL)$ and $B^W(ML)$ are expressed in the units $e^2 \text{fm}^{2L}$ and $\mu_n^2 \text{fm}^{2L-2}$, respectively [27]. Using these relations, the Weisskopf estimates for the lifetime of an initial nuclear state can be determined for the extreme case of a pure single-particle transition. They are illustrated in Fig. 4.1.

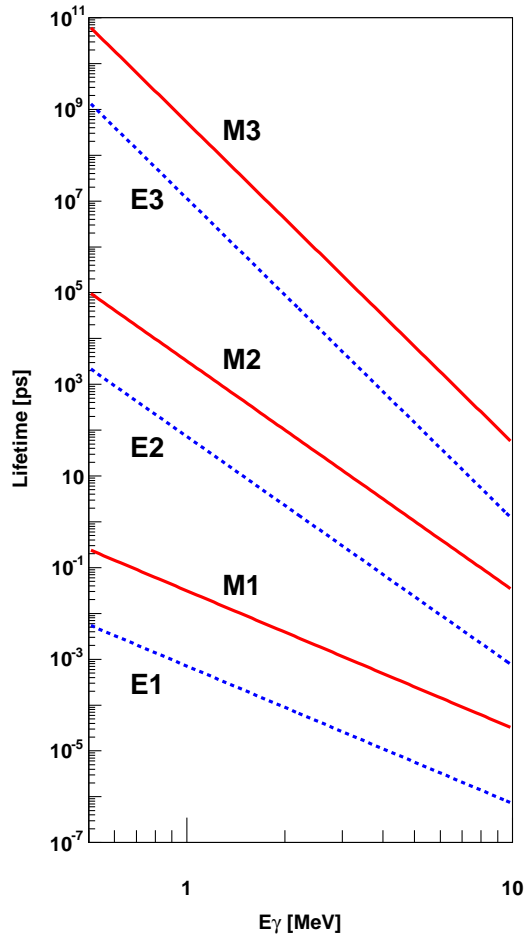


Figure 4.1: *Lifetime of an excited state as a function of the transition energy to the final state. Different lines correspond to different multipolarity and character of the emitted γ ray.*

The Weisskopf estimate for the excited $27/2^-$ states in the $A = 51$ mirror nuclei can be derived. The excited states decays via an $E2$ transition with energy of $E_\gamma = 777$ keV and $E_\gamma = 704$ keV for ^{51}Fe and ^{51}Mn , respectively. The corresponding Weisskopf estimates for the lifetimes are determined to be $\tau_{Fe} = 257$ ps and $\tau_{Mn} = 418$ ps. However, the measured lifetimes are much smaller (cf. section 4.3.1) than the Weisskopf estimates and consequently $B(E2)_{exp} > B^W(E2)$. If the experimentally measured values are much greater than the Weisskopf estimates it may indicate that the transition is of collective nature.

Reduced transition probabilities can be estimated from theoretical models accord-

ing to Eq. 4.5, in which the transition operators given in Eq. 4.6 and Eq. 4.7 are employed. The models cannot, however, treat the full many-body quantum problem of a given nucleus with A nucleons. Therefore, in shell-model calculations one defines an inert core and thus limits the calculations to the remaining valence nucleons, which are restricted to move only in a given number of valence shells. The valence nucleons involved in the transition are assumed to be independent of the nuclear core. This, however, may not be valid, since they may polarize and couple to the core. The polarization effect can be compared to the tidal waves caused on the surface of the earth by the orbiting moon. Figure 4.2 illustrates the effect for a single nucleon outside a spherical core.

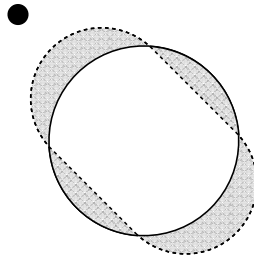


Figure 4.2: *Illustration of how a single nucleon located outside a spherical core polarizes the core.*

To account for such core polarization effects, the empirical g -factors and the bare nucleon charges are replaced in the calculations with effective g -factors and effective nucleon charges.

Effective Charges

We thus introduce an effective charge for the protons, ε_p , and neutrons, ε_n , respectively. For a nucleon i , the single-particle electric quadrupole operator becomes (cf. Eq. 4.6)

$$\mathcal{M}(E2) = \varepsilon_i r_i^2 Y_{20}, \quad (4.15)$$

where ε_i denote the introduced effective nucleon charge. The reduced $E2$ -transition probabilities are now written as the sum over all particles according to (cf. Eq. 4.5)

$$B(E2; J_i \rightarrow J_f) = \frac{1}{2J_i + 1} |\langle J_f || \sum_{i=1}^A \varepsilon_i r_i^2 Y_{20} || J_i \rangle|^2. \quad (4.16)$$

In the harmonic oscillator $\langle r^2 \rangle$ is given by

$$\langle r^2 \rangle = \frac{\hbar}{m\omega} \left(N + \frac{3}{2} \right) = b_0^2 A^{1/3} \left(N + \frac{3}{2} \right), \quad (4.17)$$

where N is the harmonic oscillator principle quantum number. In large-scale shell-model calculations, using harmonic oscillator wave functions, the parameter b_0 is commonly set to $b_0 = 1.01$ [30, 31]. Changing b_0 thus provides an easy way to vary the nucleon radius in the calculations.

The effective charges contain the bare charges plus a contribution from the polarization, e_{pol} . When the particle is bound in a harmonic oscillator potential the polarization charge is expressed as (cf. Ref. [27])

$$e_{pol} = \frac{Z}{A}e, \quad (4.18)$$

which gives effective nucleon charges $\varepsilon_p = 1.5 e$ and $\varepsilon_n = 0.5 e$ for protons and neutrons, respectively, in the case of $N = Z$ nuclei. However, here no distinction is made between protons and neutrons.

The polarization charge consists of an isoscalar, $e_{pol}^{(0)}$, and an isovector, $e_{pol}^{(1)}$, component such that

$$e_{pol} = e_{pol}^{(0)} + e_{pol}^{(1)} \cdot 2t_z, \quad (4.19)$$

where $t_z = -1/2$ and $t_z = +1/2$ corresponds to the proton and neutron, respectively. Accordingly, the effective proton and effective neutron charges can be written as

$$\begin{aligned} \varepsilon_p &= 1 + e_{pol}^{(0)} - e_{pol}^{(1)}, \\ \varepsilon_n &= e_{pol}^{(0)} + e_{pol}^{(1)}. \end{aligned} \quad (4.20)$$

Thus a single neutron will polarize the charged core more strongly than a single proton (cf. Ref. [27]).

The isoscalar and isovector components of the polarization charge arise from the coupling of the valence nucleons to the corresponding modes of the so-called giant quadrupole resonance (GQR), which is an excited vibrational state of the core. Depending on the relative phase of the oscillation of the protons and neutrons an isoscalar or an isovector mode of the GQR is generated. In the isoscalar mode the protons and

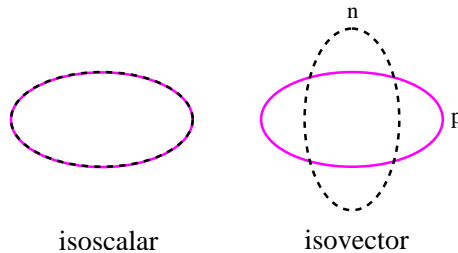


Figure 4.3: *Illustration of isoscalar (left) and isovector (right) giant quadrupole resonance modes. Protons (solid) and neutrons (dashed) are oscillating in phase and out of phase, respectively.*

neutrons oscillates with the same phase, and in the isovector mode they are out of phase [29]. The two different modes are sketched in Fig. 4.3.

According to Bohr and Mottelson [29] the total polarization charge can be written as

$$e_{pol} = e \left(\frac{Z}{A} - 0.32 \frac{N-Z}{A} + \left(0.32 - 0.3 \frac{N-Z}{A} \right) \cdot 2t_z \right), \quad (4.21)$$

where the isoscalar and isovector components thus are given as

$$\begin{aligned} e_{pol}^{(0)} &= e \left(\frac{Z}{A} - 0.32 \frac{N-Z}{A} \right), \\ e_{pol}^{(1)} &= e \left(0.32 - 0.3 \frac{N-Z}{A} \right). \end{aligned} \quad (4.22)$$

The corresponding isoscalar and isovector components of the polarization charge for a $N = Z$ nucleus are $e_{pol}^{(0)} = 0.5 e$ and $e_{pol}^{(1)} = 0.32 e$. The effective nucleon charges along the $N = Z$ line are thus expected to be $\varepsilon_p = 1.18 e$ and $\varepsilon_n = 0.82 e$ for protons and neutrons, respectively.

It is of general interest to determine the effective nucleon charges from experimental data to perform comparisons with theoretical estimations. From this it may be possible to draw conclusion of, for example, the dependency on the polarization charges in terms of isospin or the number of valence particles. A detailed description of an unique study of the $A = 51$ mirror pair, where a quantitative measurement of effective charges is performed, can be found in section 4.3.1.

4.2 Mirror nuclei

Effective nucleon charges are introduced to nuclear models to account for core polarization effects. To probe and determine effective charges experimentally are not only an interesting but also a quite challenging task. One way to access and pin down the effective charges are detailed studies of so called mirror nuclei, which are pairs of nuclei with the number of protons and neutrons interchanged. The observed differences between the two mirror nuclei are expected to arise mainly from the Coulomb force, which directly affects only the positively charged protons. If this force is neglected, the properties of the two mirror nuclei are expected to be identical as the protons and neutrons can be treated as two different quantum states of the same particle, the nucleon. In this picture an isospin quantum number, t , is introduced to describe the nucleon wave function, which allows to distinguish a proton from a neutron. A single nucleon has $t = 1/2$ with two possible directions in isospin space, $t_z = -1/2$ and $t_z = +1/2$, for the proton and neutron, respectively. For a system of several nucleons the total isospin quantum number, T , can enact all values in steps of one such as

$$\frac{1}{2}|N - Z| \leq T \leq \frac{1}{2}(N + Z) \quad (4.23)$$

where N and Z are the number of neutrons and protons, respectively. The projection of the total isospin, T_z , is the sum of the projections of the individual nucleons. Thus for a many-nucleon system T_z can be written as

$$T_z = \frac{1}{2}(N - Z) \quad (4.24)$$

where mirror nuclei are described as a, for example, $T_z = \pm 1/2$ mirror pair. An example of a $T_z = \pm 1/2$ mirror pair are the $A = 51$ nuclei. ^{51}Fe has 26 protons and 25 neutrons, while ^{51}Mn has 25 protons and 26 neutrons.

The nuclear force affecting the nucleons inside the nucleus can to first order be described with a two-body interaction. The possible combinations that arise are pp , nn , or pn interactions, where p represent the proton and n the neutron. In a two-nucleon system the possible total isospin is either $T = 1$ or $T = 0$, which correspond to an isospin triplet state (containing a pp , pn , or nn pair) and an isospin singlet state (containing a pn pair), respectively. It has been found that the pp interaction is very nearly the same as the nn interaction under the assumption that the Coulomb force is neglected. Also the interaction of a pn pair, in the same isospin state as the pp or nn pair ($T = 1$), is equal to that of the pp and nn pair. The pn pair may also be found in an isospin state ($T = 0$) that has no counterpart in the pp or nn system, because it is forbidden due to the Pauli exclusion principle. In such an isospin state the pn interaction is found to be stronger than that of the pp or nn pairs. The equality of the pp , nn , and, pn interactions in the $T = 1$ isospin state is known as charge independence of the nuclear force. With charge symmetry of the nuclear force is meant that only the pp and nn interactions are the same.

The dependency of the nuclear force may be studied using excited states in mirror nuclei, which are expected to reveal identical energy level structures assuming isospin symmetry and charge independence. However, the isospin symmetry is certainly broken by the Coulomb interaction between protons, and thus small differences in the level structure are expected. Furthermore, also (small) violations of the charge symmetry and the charge independence of the nuclear force give rise to fluctuations in the energy level structures. These effects can be investigated by looking at energy differences of "mirror states" in a pair of mirror nuclei. A more detailed description and investigation of Coulomb effects and studies of Mirror Energy Differences (MED) in mirror nuclei can be found in Ref. [3].

Together with significant theoretical effort the interpretation and understanding of Coulomb effects in mirror nuclei has increased substantially during recent years. However, almost all experimental studies of mirror nuclei have been limited to comparisons of excitation energies using MED values. This is mainly due to experimental difficulties of producing and detect the neutron deficient mirror partner with enough statistics to allow for more detailed spectroscopic measurements such as lifetimes of excited states. Such measurements in may provide useful information on, for example, effective transition operators when comparing the measured quantities with theoretical models. With improved experimental techniques these scenarios have started to become achievable during the last few years. Studies of spectroscopic quantities such as lifetimes of excited states and related electromagnetic properties of mirror nuclei can nowadays be looked upon. One example of investigating electromagnetic properties in mirror nuclei is the study of the $A = 51$ $T_z = \pm 1/2$ mirror pair, $^{51}_{26}\text{Fe}_{25}$ and $^{51}_{25}\text{Mn}_{26}$. In this study the lifetimes of the excited $27/2^-$ states are determined and used to probe the effective nucleon charges in the fp -shell. The data analysis in combination with theoretical simulations are described in detailed in section 4.3.1 and PAPER III. Bellow follows only a short description of the principle idea.

The level schemes of ^{51}Fe and ^{51}Mn are very similar as expected from the isospin formalism described above. Both nuclei can be described with their valence nucleons outside the $N = Z = 20$ shell closure distributed in the $1f_{7/2}$ orbitals. Within this re-

stricted configuration space there is only one possibility to align six (five) protons and five (six) neutrons for ^{51}Fe (^{51}Mn) to obtain the excited state with spin $27/2^-$. One other possibility to achieve this spin state would be to allow for particle excitations to the upper fp -shell ($2p_{3/2}$, $1f_{5/2}$, and $2p_{1/2}$ orbits). These excited $27/2^-$ states may mix with the the yrast $27/2^-$ state. However, large-scale shell-model calculations indicate that the mixing is small. The wave functions of the $27/2^-$ states can be used in simulations to calculate the reduced transition probabilities. By combining the theoretical simulations with the experimental values the effective nucleon charges are determined.

4.3 Data Analysis

Recorded raw data files are processed through various offline analysis packages before any physics analysis starts. This allows to perform redundancy checks, detector calibrations, data reformatting, and to sort data in various spectra and matrices for further processing. The number of packages employed strongly depends on the raw data structure and the physics aim. The most basic steps and their features in the process chain are:

- **Compression:** Removes unnecessary and incomplete data, i.e., data that do not contain all requested required signals or miss essential information.
- **Pre-sorting:** Perform alignment of time and energy signals for the various detectors utilized. This provides particle identification, from ancillary detector systems, and definition of prompt and delayed γ -ray transitions. The detectors are energy and efficiency calibrated and appropriate particle conditions are set before data is re-written to file.
- **Sorting:** Pre-sorted data is used to generate spectra and to create, for example, $\gamma\gamma$ matrices or $\gamma\gamma\gamma$ correlation cubes, which are used in the analysis.

A more detailed discussion on some of these steps can be found in, for example, Ref. [3, 17]. The final analysis is generally based on the output from the sorting phase, which allows to create and investigate spectra of various kinds. Further requirements can be introduced using different gate conditions on the data, thus generating specific spectra. For instance, $\gamma\gamma$ matrices and $\gamma\gamma\gamma$ cubes allow to perform coincidence spectroscopy, which can be used to select a specific nucleus, cascade, or transition.

4.3.1 Effective charges in ^{51}Mn and ^{51}Fe

An analysis of the $A = 51$ mirror nuclei has been performed based on data from the GASP03.12 experiment using the heavy-ion fusion-evaporation reaction $^{32}\text{S} + ^{24}\text{Mg}$ with a beam energy of 95 MeV. The ^{24}Mg target was mounted inside the Cologne plunger device in front of a stretched gold stopper foil and data were taken at target-stopper distances ranging from electric contact to 4.0 mm. The mirror nuclei ^{51}Fe and ^{51}Mn were produced via the evaporation of one α -particle and one neutron ($1\alpha 1n$ channel) and one α -particle and one proton ($1\alpha 1p$ channel), respectively. The $A = 51$ mirror pair has well established level schemes [32, 33, 34], which are shown in Fig. 4.4.

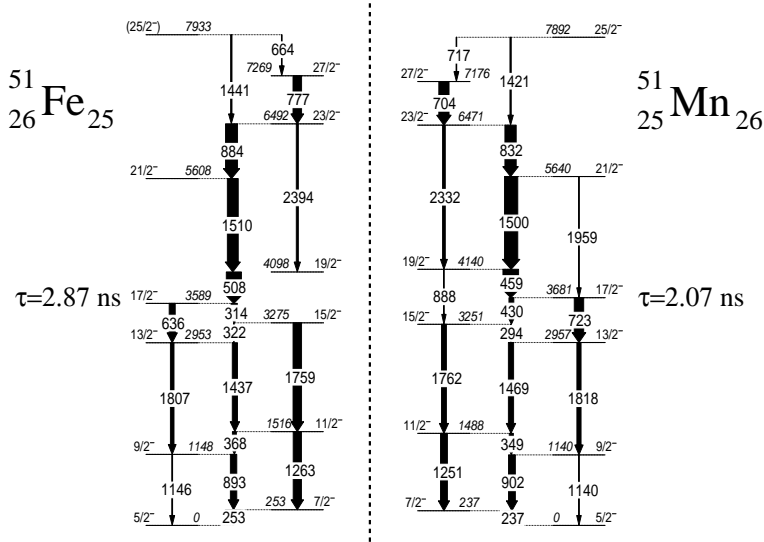


Figure 4.4: Level schemes of the $A = 51$ mirror nuclei [32, 33, 34]. Energy labels are in keV and the widths of the arrows correspond to the relative intensities of the transitions.

Data handling and experimental results

At first, the detectors are energy calibrated using ^{56}Co , ^{133}Ba , and ^{152}Eu standard calibration sources. Secondly, for each measured distance the time signals of the individual Ge detectors are aligned. During the same procedure detectors with corrupt or missing signals are masked out for further analysis. From the aligned Ge times the γ -ray transitions are assigned as being prompt or delayed by using a two-dimensional gate in a Ge-time vs Ge-energy matrix. With this gate condition set to assure that γ rays emitted from the $A = 51$ nuclei are within the gate, bad detectors excluded, and all calibrations done, the raw data was sorted. Data files acquired with the same conditions and at the same distances were added together. In total 21 files, corresponding to 21 distances, were created.

For each distance the events were sorted into $\gamma\gamma$ coincidence matrices with γ rays detected in one given detector ring placed along one axis and γ rays detected anywhere in the array along the second axis of the matrix. The γ rays were required to be detected in one of the seven detector rings and have an energy in the interval $0 < E_\gamma < 4096$ keV. Furthermore, to reduce the contribution from, for instance, Coulomb excitation in the gold stopper or random coincidences, a restriction on the total multiplicity of γ rays, M_γ , was used. The total multiplicity is the sum of the γ rays detected in the Ge-detectors and the BGO-elements. Only events with $M_\gamma > 6$ were used to create the $\gamma\gamma$ matrices. Spectra are obtained using the $\gamma\gamma$ matrices by an energy gate on one of the axis and projecting the coincidence spectrum on

the other axis. The width and placement of the energy gate can be determined by looking at the total projection, i.e., the projection of the full coincidence matrix on one axis. Figure 4.5 shows (a) the total projection and (b) a spectrum gated on the 237 keV transition in ^{51}Mn using all detector rings for data taken at a target-stopper distance of $1200\ \mu\text{m}$. Due to the relatively long distance Doppler shifted components can be observed for some of the transitions in the gated ^{51}Mn spectrum. The figure

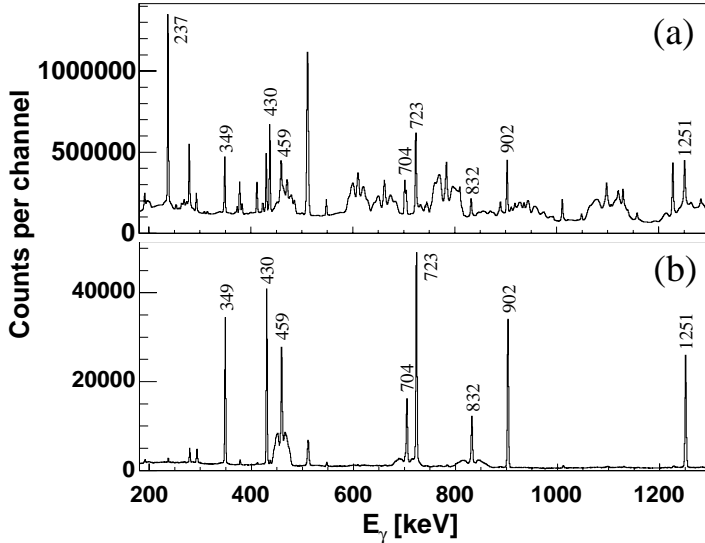


Figure 4.5: (a) The total projection and (b) a spectrum in coincidence with the 237 keV transition in ^{51}Mn (b) for data taken at a target-stopper distance of $1200\ \mu\text{m}$. Energy labels of the peaks are in keV and correspond to transitions in ^{51}Mn .

illustrates the effect of using γ rays in coincidence to obtain a clean spectrum, which later can be used in the analysis work. However, the quality of the resulting spectrum strongly depends on the gate conditions, i.e., how the peak and the background is selected. The exact setting of the energy gate might need to be reworked several times to optimize the result. This is done for all distances and detector rings and clean spectra gated on different transitions in ^{51}Mn and ^{51}Fe were collected.

Each target-stopper distance can be converted into a corresponding flight time using the velocity of the recoiling nucleus. The velocity can be derived from the shifted and unshifted Doppler components using

$$E_\gamma = E_0 \frac{\sqrt{1 - \beta^2}}{1 - \beta \cos \theta}, \quad (4.25)$$

where E_γ and E_0 are the measured energies of the two components, respectively, θ the angle to the detector with respect to the beam axis and β the recoil velocity in terms of the speed of light. Due to the symmetric geometry of the detector system the angle of the most forward, θ_f , and the most backward, θ_b , detector rings are situated

such that $\cos\theta_f = -\cos\theta_b = \cos\theta$. This allows to derive the recoil velocity using the two most outward detector rings as

$$\beta = \frac{\Delta E}{2E_0 \cos\theta}, \quad (4.26)$$

where a second order Taylor expansion of Eq. 4.25 has been used. ΔE is the energy difference between the shifted component measured in the forward and backward detector ring and E_0 the measured energy of the unshifted component.

The recoil velocity was determined using the intense 1500 keV $21/2^- \rightarrow 19/2^-$ transition obtained in coincidence with the 237 keV ground-state transition in ^{51}Mn . The velocities range from 3.7% to 4.1% of the speed of light for the three different targets used during the experiment. The variation in velocity can be explained by the fact that the three targets had slightly different thicknesses, which will give rise to somewhat different velocities. The respective individual recoil velocity for each target-distance combination is later used in the analysis for the conversion of the target-stopper distance to flight time.

The method used to determine the lifetimes of the $27/2^-$ states in the $A = 51$ mirror pair is based on very specific features of their decay schemes. They consist of essentially three regimes: the transitions below the isomeric $17/2^-$ states, those feeding into the long-lived (~ 100 ps) $27/2^-$ states, and the short-lived states in between (see Fig. 4.4). Due to the isomeric $17/2^-$ states low-lying transitions are essentially always emitted from stopped residues independently of the target-stopper distance used. Thus for spectra taken in coincidence with these low-lying transitions it is possible to apply the RDDS method to the transitions between the $27/2^-$ and the $17/2^-$ states. To avoid that Doppler shifted and unshifted components interfere only the two most forward and two most backward detector rings are used, for which the two components of the coincident transitions are well separated. This interference effect is mostly observed for the larger target-stopper distances, because more and more γ -rays are emitted in-flight than as stopped. Figure 4.6 illustrates how the target-stopper distance affects the intensities of the stopped and Doppler shifted components. The spectra are obtained by gating on the low-energy 253 keV $7/2^- \rightarrow 5/2^-$ transition in ^{51}Fe for distances of 400 μm (Fig. 4.6a) and 1200 μm (Fig. 4.6b). For the short distance (400 μm) the four transitions at 636, 777, 884, and 893 keV in ^{51}Fe are clearly seen as stopped peaks. When increasing the distance to 2000 μm the stopped components of the two transitions at 777 and 884 keV are significantly reduced and Doppler shifted 'wings' arise on each side of the stopped peaks. The 636 and 893 keV transitions are still observed as stopped peaks, because they are situated below the isomeric $17/2^-$ state and the flight distance is still rather short with respect to its lifetime.

The lifetime analysis for the $27/2^-$ states in the $A = 51$ mirror pair employ the same analysis method for both nuclei. This method was developed using data only originating from the ^{51}Mn nucleus due to the large amount of statistics compared to the very weakly populated mirror nucleus ^{51}Fe . The large amount of statistics in the ^{51}Mn case also allows for a detailed investigation of possible systematic errors and to achieve proper normalization coefficients for each distance. The latter are required for a normalization of the measuring times and beam currents between the different distances. Several methods were investigated in detail to obtain a good set of normalization coefficients. Some of these methods were:

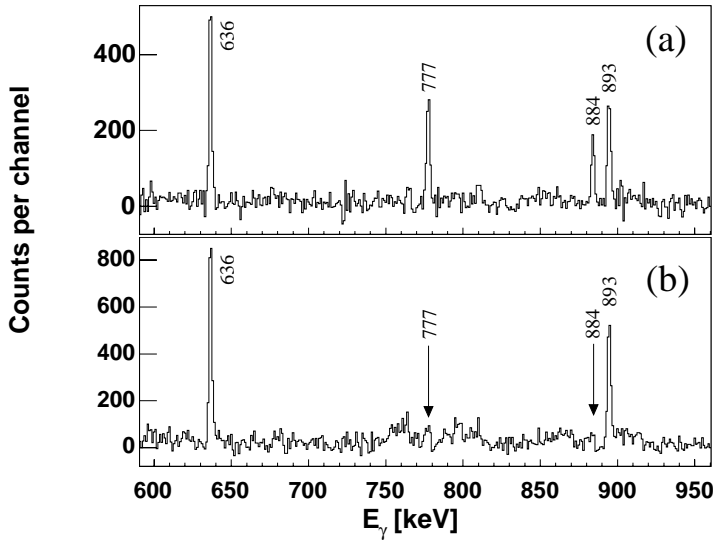


Figure 4.6: Spectra taken in coincidence with the $7/2^- \rightarrow 5/2^-$ 253 keV transition in ^{51}Fe for the two most forward and two most backward detector rings of GASP. Panel (a) shows spectra obtained with target-stopper distance 400 μm and panel (b) for the distance 1200 μm . Energy labels of the peaks are in keV.

- The intensity of the unshifted 237 keV transition in ^{51}Mn and correct the value for the decay from the known lifetime of the $17/2^-$ state.
- The intensities of the shifted and unshifted components of the transition itself.
- The intensities of the shifted and unshifted components for the 832 keV transition taken in coincidence with the 237 keV transition in ^{51}Mn .
- The intensities of the shifted and unshifted components for the 459 keV transition taken in coincidence with the 237 keV transition in ^{51}Mn .
- Only detectors situated at 90° with respect to the beam axis.
- Transitions from other nuclei, for example, ^{53}Fe .
- The number of counts in the total projection.

Because of, for example, difficulties with background subtraction, the influence in spectra from β -decaying nuclei, the limited amount of statistics for selected transitions, etc. the investigated methods were more or less applicable. It was found that the most appropriate normalization coefficients were obtained using the 459 or 832 keV transitions. Hence, further analysis employ the coefficients obtained using the combined intensities of the shifted and unshifted Doppler components for both the 459 and 832 keV transitions. The intensities for these transitions observed in

all detector rings were summed up in spectra taken in coincidence with the 237 keV ground-state transition in ^{51}Mn and then used as normalization coefficients. As the relative statistics of ^{51}Mn and ^{51}Fe in the collected data are expected to be the same for different distances the same normalization coefficients can be used for both nuclei.

Due to the special features of the $A = 51$ decay schemes the lifetime of the $27/2^-$ states in the mirror pair can in principle be extracted analysing any of the transitions located between the $27/2^-$ and $17/2^-$ states. Nevertheless, to eliminate contributions from possible side feeding an analysis of the 704 keV and the 777 keV $27/2^- \rightarrow 23/2^-$ transitions for ^{51}Mn and ^{51}Fe , respectively, is preferred. To perform an analysis of the very weakly populated ^{51}Fe nucleus the measured distances needed to be combined into nine effective distances: 6.5(1), 17.7(1), 42.7(7), 125(3), 404(11), 701(16), 1198(29), 1984(60), and 4000(100) μm . This merge was done using the extracted normalization coefficients as weighting factors and the effect on the result using nine distances compared to all 21 distances was investigated using the ^{51}Mn sample, for which each individual distance can be used in the analysis.

For ^{51}Mn it was found that an analysis of the 704 keV transition was hampered due to Doppler shifted components of the 723 keV $17/2^- \rightarrow 13/2^-$ and 717 keV $25/2^- \rightarrow 27/2^-$ transitions as well as background radiation at 701 keV from the decay of the $19/2^-$ isomer in ^{53}Fe . Instead the analysis was performed using the 459 and 832 keV transitions in spectra obtained in coincidence with the 237 keV ground-state transition. To account for the side feeding their decay curves were fitted with a short ($\tau < 10$ ps) and a long lifetime component. The analysis of the two transitions was carried out in parallel for each measured distance and individual detector rings. The results were found to be consistent with each other. The final result was obtained as the weighted mean of the results from the individual detector rings using only the 832 keV transition as the amount of side feeding is expected to be less for this transition compared to the 459 keV transition.

The analysis of ^{51}Fe was performed using the 777 keV transition for nine effective distances where the data points were fitted with an exponential to extract the lifetime. To increase the statistics, spectra in coincidence with the 253, 314, and 636 keV transitions from the two most forward and the two most backward detector rings were summed. Since a stopped component of the 777 keV line was absent in the spectrum taken at the largest distance it was excluded from the analysis. Figure 4.7 illustrates the decay curves of the 777 keV $27/2^- \rightarrow 23/2^-$ transition in ^{51}Fe and the $23/2^- \rightarrow 21/2^-$ 832 keV transition in ^{51}Mn .

The resulting lifetimes of the $27/2^-$ states in ^{51}Mn and ^{51}Fe with the corresponding $B(E2; 27/2^- \rightarrow 23/2^-)$ values are listed in Table 4.1. The $B(E2)$ values are derived from Eq. 4.12 using the extracted lifetimes and $E_\gamma = 704.4(5)$ keV and $E_\gamma = 777.1(5)$ keV for ^{51}Mn and ^{51}Fe , respectively. The ratio, R , between the $B(E2)$ values of the mirror transitions in ^{51}Fe and ^{51}Mn is $R = 0.884(22)$. The error ratio is merely statistical. The systematic uncertainty in the lifetimes is related to the normalization and the exact determination of the yield of the stopped component at large distances. Other contributions are the possible short-lived ($\tau < 1$ ps, cf. [34]) feeding into the $27/2^-$ state, and combining the results from individual detector rings and the 21 single distances used in the measurement into nine effective distances, which is necessary for the analysis of the very weakly populated mirror nucleus ^{51}Fe .

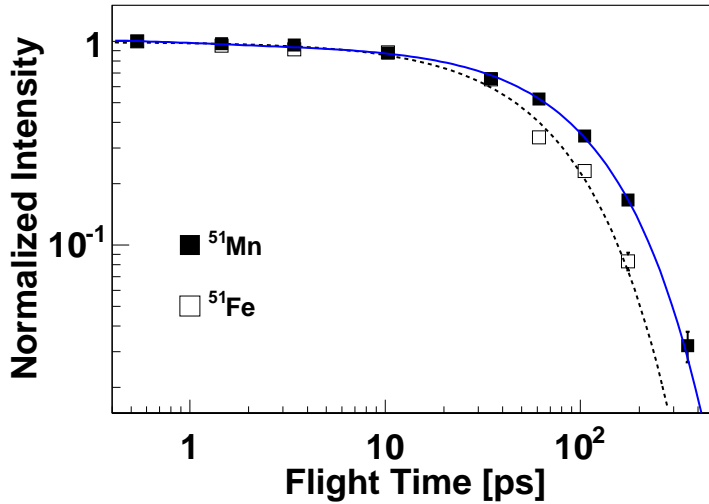


Figure 4.7: Decay curves for the 832 keV transition in ^{51}Mn (solid) and the 777 keV transition in ^{51}Fe (dashed) for nine effective flight distances.

Table 4.1: Values for the extracted lifetimes and the corresponding $B(E2)$ values for the $27/2^-$ states in the mirror nuclei ^{51}Mn and ^{51}Fe .

	Lifetime [ps]	$B(E2)$ [$e^2\text{fm}^4$]	$B(E2)$ [W.u.]
^{51}Mn	$100.7 \pm 1.2 \pm 3$	46.7(14)	4.16(12)
^{51}Fe	$69.7 \pm 1.6 \pm 3$	41.3(24)	3.68(21)

Calculations performed to determine the effective charges

To study the consequences of the lifetime results on polarization charges large-scale shell-model calculations were performed using the shell-model code ANTOINE [30, 31]. The calculations employ the full fp space containing the $1f_{7/2}$ orbit below and the $2p_{3/2}$, $1f_{5/2}$, and $2p_{1/2}$ orbits above the $N = Z = 28$ shell closure. The configuration space was truncated to only allow for excitations of up to five particles across the shell closure. This configuration space provides predictions more or less indistinguishable from calculations using the full fp space [35]. Three interactions have been studied in detail: The standard KB3G [35] interaction without any Coulomb interaction, the KB3G interaction with theoretical harmonic-oscillator Coulomb matrix elements (Coulomb HO), and the KB3G interaction with the $1f_{7/2}$ Coulomb matrix elements replaced with the experimental values from the $A = 42$ mirror pair (Coulomb A42).

The investigation of the effective charges utilizes three input parameters to the simulations; the isoscalar and isovector polarization charges, $e_{pol}^{(0)}$ and $e_{pol}^{(1)}$, and the harmonic oscillator parameter, b_0 (cf. section 4.1). As the simulations aim to repro-

duce the two experimental $B(E2)$ -values and their ratio simultaneously the study is carried out utilizing an iterative process for different combinations of the three parameters. The method to determine the effective charges using the Coulomb A42 interaction is described in detail in the following. The same method is employed for calculations using the other interactions.

Assuming identical orbital radii, i.e., the same b_0 for ^{51}Mn and ^{51}Fe the $B(E2)$ -values for the $27/2^- \rightarrow 23/2^-$ mirror transitions were calculated. The harmonic oscillator parameter was set to $b_0 = 1.01$ in all calculations while the polarization charges were varied over different intervals. For a given isoscalar value calculations were performed with the isovector parameter varied in the region $0.0 < e_{pol}^{(1)} < 1.0$. For each calculation the ratio, R , between the resulting $B(E2)_{\text{Fe}}$ and $B(E2)_{\text{Mn}}$ values is determined and plotted versus the isovector parameter. The values are fitted to a third degree polynomial and compared to the $B(E2)$ -ratio derived from the experimental results, $R_{exp} = 0.884(22)$. Fig. 4.8 illustrates the isovector polarization charge as a function of the $B(E2)$ -ratio from the shell-model calculations, when the isoscalar polarization charge is set to $e_{pol}^{(0)} = 0.5$.

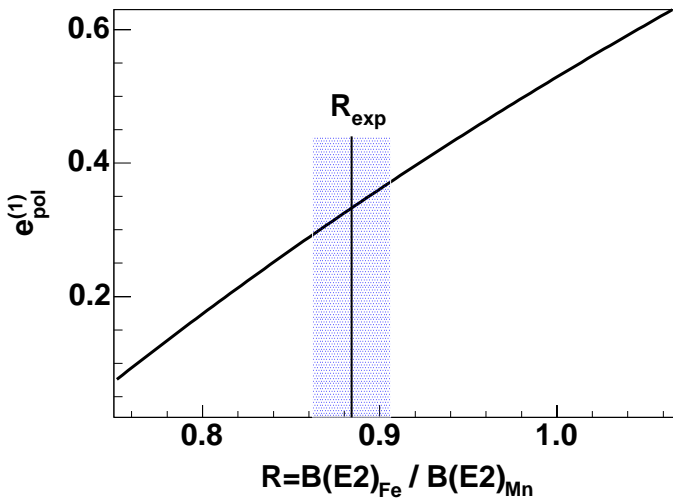


Figure 4.8: The isovector component as function of the $B(E2)$ -ratio from shell-model calculations using the Coulomb A42 interaction with $b_0 = 1.01$ and $e_{pol}^{(0)} = 0.5$. The experimental ratio is illustrated with the vertical line at $R_{exp} = 0.884(22)$.

Thus, the isovector component can be derived for a given isoscalar component. These polarization charges experimental $B(E2)$ -ratio but not necessary the absolute $B(E2)$ -values for ^{51}Fe and ^{51}Mn . To find a solution that simultaneously reproduces the absolute $B(E2)$ -values and their ratio the harmonic oscillator parameter is ad-

justed according to (cf. Eq. 4.16 and Eq. 4.17)

$$b_0 = 1.01 \left(\frac{B(E2)_{exp}}{B(E2)_{the}} \right)^{1/4}. \quad (4.27)$$

A change of b_0 will affect the absolute $B(E2)$ -values, but keep their ratio as the orbital radii are assumed to be identical for the two members of the mirror system. Thus a simulation performed with the adjusted b_0 parameter and the corresponding polarization charges will reproduce the experimental $B(E2)$ -values and their ratio simultaneously. Table 4.2 lists values of the isoscalar and isovector polarization charges with the resulting $B(E2)$ -values using $b_0 = 1.01$. These values do not reproduce the experimental values but can be used to determine the adjustment of b_0 according to Eq. 4.27. The corresponding b_0 values required to reproduce the absolute values are also listed in Table 4.2.

Table 4.2: Polarization charges employed in shell-model calculations with the resulting $B(E2)$ -values for calculations performed with the Coulomb A42 interaction and harmonic oscillator parameter $b_0 = 1.01$. A change to the b_0 values in the last row of the table are required to reproduce the experimental $B(E2)$ -values (cf. Table 4.1).

$e_{pol}^{(0)}$	0.300	0.400	0.500	0.600	0.700
$e_{pol}^{(1)}$	0.365	0.348	0.331	0.314	0.297
$B(E2)_{Fe}$	27.93	35.35	43.64	52.80	62.83
$B(E2)_{Mn}$	31.63	40.03	49.42	59.80	71.17
b_0	1.113	1.049	0.995	0.949	0.909

Based on the adjusted b_0 parameter and the corresponding polarization charges a dependence between the three parameters is derived for which the individual $B(E2)$ values are reproduced. The isoscalar and isovector polarization charges are plotted versus the harmonic oscillator parameter and fitted by second degree polynomials. Figure 4.9 illustrates this dependence for the Coulomb A42 interaction. From this dependence a combination of the three parameters is determined for each b_0 -value that, when employed in the shell-model calculations, would reproduce the experimental values and their ratio simultaneously.

As discussed in previous sections the harmonic oscillator parameter is commonly set to $b_0 = 1.01$ (cf. Eq. 4.17), which leads to an isoscalar and isovector polarization charge of $e_{pol}^{(0)} = 0.47$ and $e_{pol}^{(1)} = 0.34$ using the Coulomb A42 interaction. Using Eq. 4.20 the corresponding effective charges are 1.13 and 0.81 for the proton and neutron, respectively.

The dependence between the three parameters was derived for the other interactions as well. Figure 4.10 illustrates this dependence for two different sets of Coulomb matrix elements and one set without any Coulomb interaction. In all three cases the nuclear interactions are based on the KB3G interaction. From Fig. 4.10 it is seen that the isoscalar component is more sensitive to changes in b_0 , i.e., the nuclear radii, than the isovector component. This is because the effective proton and neutron

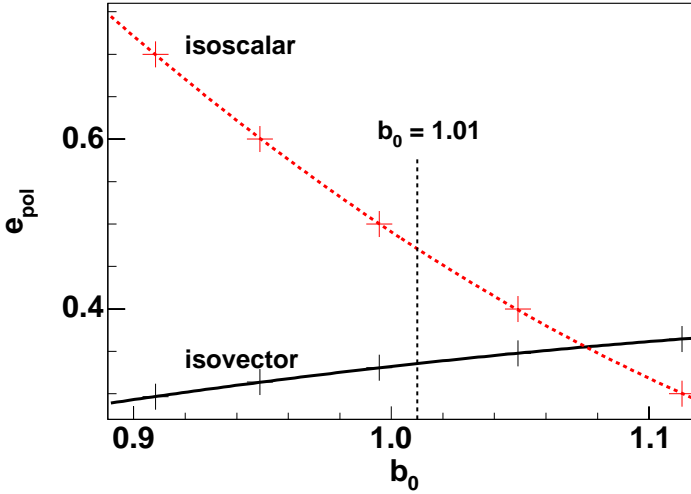


Figure 4.9: *Dependence of the three parameters b_0 and the isoscalar and isovector polarization charges for the Coulomb $A42$ interaction. A given combination of the three parameters reproduces the experimental $B(E2; 27/2^- \rightarrow 23/2^-)$ values in the $A = 51$ mirror nuclei and their ratio.*

charges are affected by the isoscalar part equally while the isovector part affects the effective charges with opposite sign. On the other hand, the isoscalar part is rather independent of the choice of $1f_{7/2}$ Coulomb matrix elements, whereas the isovector part shows a stronger dependence.

Table 4.3 lists the extracted isoscalar and isovector polarization charges for three different KB3G interactions using the harmonic oscillator parameter $b_0 = 1.01$. For comparison a calculation with the FPD6 [36] interaction is included. Using the experi-

Table 4.3: *Isoscalar and isovector polarization charges, which simultaneously reproduce the $B(E2; 27/2^- \rightarrow 23/2^-)$ values in the $A = 51$ mirror nuclei, for different shell-model calculations using $b_0 = 1.01$*

	no Coulomb	Coulomb HO	Coulomb A42	FPD6
$e_{pol}^{(0)}$	0.466(3)	0.466(3)	0.471(2)	0.632
$e_{pol}^{(1)}$	0.316(26)	0.310(37)	0.336(37)	0.315

mental $B(E2)$ -values and their errors, the uncertainties in $e_{pol}^{(0)}$ and $e_{pol}^{(1)}$ are determined by reproducing the maximum (minimum) $B(E2; 27/2^- \rightarrow 23/2^-)$ value in ^{51}Mn and minimum (maximum) $B(E2; 27/2^- \rightarrow 23/2^-)$ value in ^{51}Fe , respectively. Due to the time-consuming calculations no uncertainty for the extracted polarization charges was

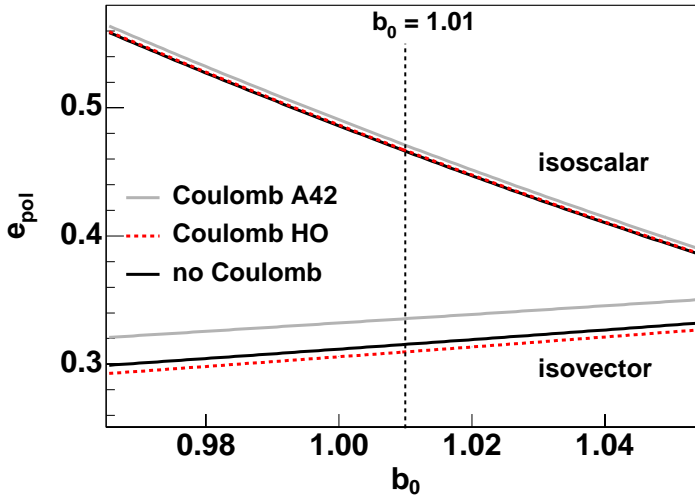


Figure 4.10: Polarization charges, necessary to reproduce the $B(E2; 27/2^- \rightarrow 23/2^-)$ values in the $A = 51$ mirror nuclei, as a function of b_0 for three different shell-model calculations.

estimated for FPD6, but it is expected to be in the same order of magnitude as the calculations performed with the KB3G interaction.

The results in Table 4.3 are in very good agreement with Eq. 4.21, which for $N = Z$ nuclei gives $e_{pol}^{(0)} = 0.5$ and $e_{pol}^{(1)} = 0.32$. The corresponding effective charges obtained using Eq. 4.20 gives $\varepsilon_p \sim 1.15 e$ and $\varepsilon_n \sim 0.80 e$ for the proton and neutron, respectively. As mentioned above, an increase of the nuclear radii for the two mirror nuclei will result in smaller effective charges to preserve the reduced $E2$ -transition probabilities.

Depending on the interaction used in the shell-model calculations somewhat different results are obtained (cf. Table 4.3). However, an observation is that calculations performed with Coulomb interaction (Coulomb HO and Coulomb A42) results in polarization charges smaller and larger than the results from the calculation without any Coulomb interaction. This phenomenon is seen in the isovector polarization charge in Fig 4.10. An investigation, utilizing several shell-model calculations, has been performed to try and understand the origin of this effect. The two different sets of Coulomb matrix elements are listed in Table 4.4.

Table 4.4: Values of the $1f_{7/2}$ Coulomb matrix elements in MeV used in shell-model calculations for two different interactions.

	$J = 0$	$J = 2$	$J = 4$	$J = 6$
Coulomb HO	-1.527	-0.666	0.127	0.426
Coulomb A42	-1.527	-0.754	0.115	0.479

The calculations were carried out using the same iteration method as described above. A "dummy" interaction was customized by manipulating the Coulomb A42 interaction such that only one of the four Coulomb matrix elements listed in Table 4.4 differed from the Coulomb HO interaction. In this way the effect of each individual Coulomb matrix element can be studied. It was found that mainly the $J = 6$ matrix element is responsible for the above mentioned phenomenon.

The polarization charges above are extracted under the assumption that the orbital radii of the two mirror nuclei are identical (b_0 is the same for both members). However, it is reasonable to assume that the Coulomb interaction pushes the proton wave functions towards larger radii with respect to the neutron wave functions. Thus, the radius of ^{51}Fe could be slightly larger than the radius of ^{51}Mn , while on the other hand shell-model calculations indicate that mostly neutrons (protons) are active in the $B(E2)$ transitions in ^{51}Fe (^{51}Mn). A detailed investigation of the effective charges taking radial effects into account is certainly interesting but requires more experimental data to account for the extra degree of freedom.

A simple study of the polarization charges assuming different radii for the two mirror nuclei has been performed. The harmonic oscillator parameter was fixed to $b_0 = 1.01$ for ^{51}Mn while it was varied in the interval $0.99 < b_0 < 1.03$ for ^{51}Fe . The derivation of the isovector and isoscalar components employed the same method as described previously. Due to the time consuming shell-model calculations this investigation was performed only with the Coulomb A42 interaction. Figure 4.11 illustrates the dependence of the two polarization charges when changing b_0 for ^{51}Fe while keeping the value for ^{51}Mn fixed at $b_0 = 1.01$. The figure isovector component

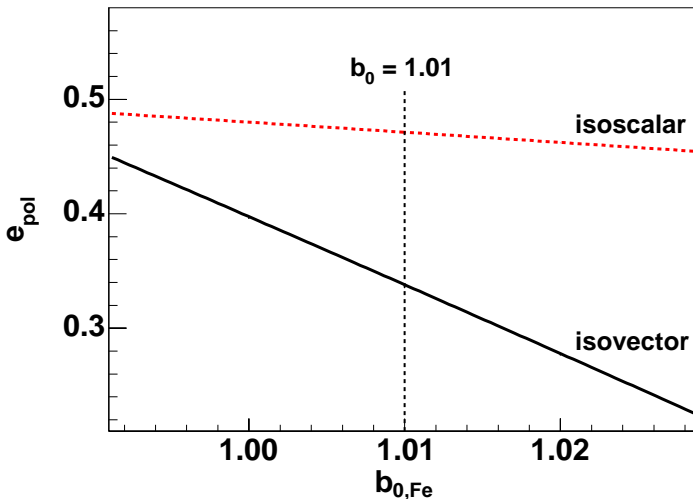


Figure 4.11: Polarization charges necessary to reproduce the $B(E2; 27/2^- \rightarrow 23/2^-)$ values in the $A = 51$ mirror nuclei, using a fixed radius for ^{51}Mn ($b_0 = 1.01$) and varying the radius for ^{51}Fe , $b_{0,\text{Fe}}$. The results are based on shell-model calculations using the Coulomb A42 interaction.

is more sensitive than the isoscalar component. This is the opposite as compared to the situation illustrated in Fig. 4.10 where the nuclear radius of both mirror nuclei was changed simultaneously. In the present scenario, however, the isovector part can compensate for different nuclear radii as it affects the effective proton and neutron charges with opposite signs.

4.3.2 Excited states in ^{53}Fe

A detailed analysis of excited states in $^{53}\text{Fe}_{27}$ has been performed using data from three experiments: the GSFMA73 experiment, the GS2k017 experiment, and the GASP03.12 experiment. From the obtained results, a largely extended level scheme was constructed and the lifetime of a few of the newly observed excited states were measured. Part of the ^{53}Fe level scheme is illustrated in Fig. 4.12. The full extended level scheme can be found in PAPER V.

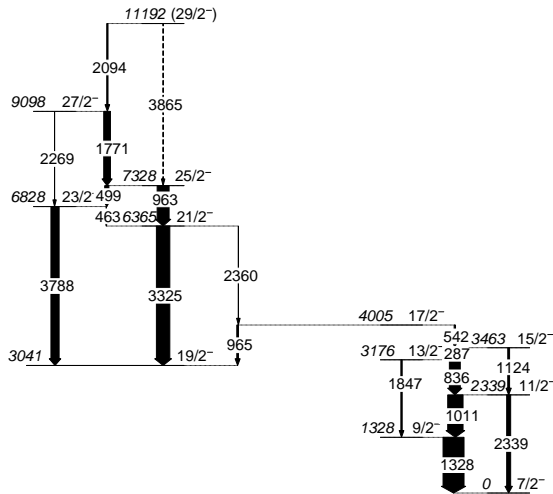


Figure 4.12: *Relevant part of the level scheme of ^{53}Fe . Energy labels are in keV and the widths of the arrows correspond to the relative intensities of the transitions.*

Data handling and experimental results

The details of the data handling and the analysis of the two Gammasphere experiments have been described earlier in, for example, Ref. [3, 17, 37]. A summary of the analysis and the experimental results in form of the extended level scheme is found in PAPER V. The basic data handling of the GASP03.12 experiment was performed as described in section 4.3.1. The sorting of events into $\gamma\gamma$ coincidence matrices, the determination of the intensities of the relevant shifted and unshifted 963 keV and 3325 keV transitions (cf. Fig. 4.12), and the merge into 14 effective flight times used in the analysis are described in PAPER V.

The lifetimes of the first excited $21/2^-$ and $25/2^-$ states in ^{53}Fe were determined using standard RDDS technique (cf 2.1.2). Hence, using the stopped components for the 963 keV $25/2^- \rightarrow 21/2^-$ and the 3325 keV $21/2^- \rightarrow 19/2^-$ transitions, the result is $\tau = 26.2(32)$ ps and $\tau < 4$ ps for the $25/2^-$ state and the $21/2^-$ state, respectively. A more detailed description of the RDDS analysis can be found in PAPER V. Note the difference between the $A = 51$ and $A = 53$ analyses, which both utilize the RDDS technique but for spectra obtained in coincidence with transitions below and above the state of interest, respectively.

Shell-Model Interpretation

The excited states in ^{53}Fe were compared to large-scale shell-model calculations that employ the full fp shell and were performed using the shell-model ANTOINE (cf. section 4.3.1). At first, the influence on the result due to the number of allowed particle excitations, t , from the $1f_{7/2}$ shell to the upper fp shell was investigated. Figure 4.13 shows the resulting energy levels from calculations using the KB3G interaction with theoretical harmonic-oscillator Coulomb matrix elements for $t = 0, 1, \dots, 5$. Allowing

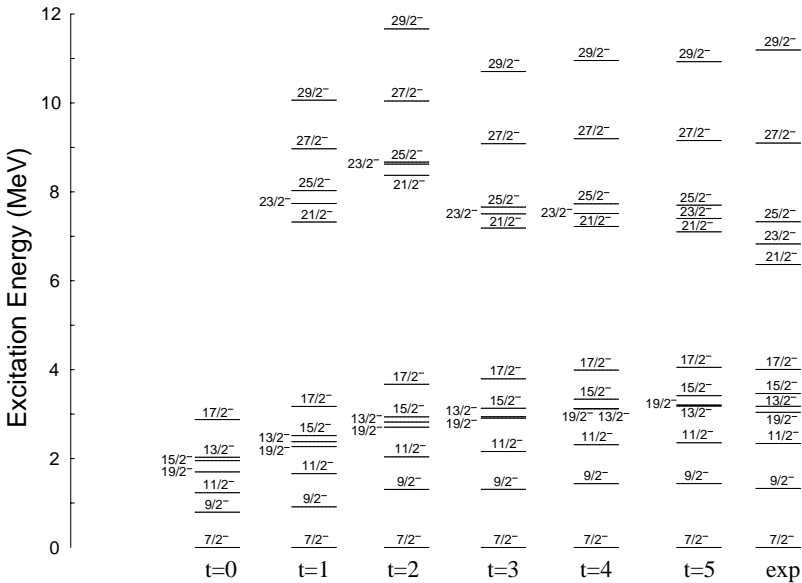


Figure 4.13: Calculated energy levels of ^{53}Fe allowing for t nucleons to be excited from the $1f_{7/2}$ shell to the upper fp shell. The experimental energy levels are included for comparison.

for only a few particle excitations it is clear that the calculated level scheme is suppressed with respect to the experimental level scheme. However, with increasing number of particle excitations the calculated energy levels converge towards the observed

energies and the experimental level sequence is better reproduced.

Further calculations were performed using four different interactions. The calculated level energies and their electromagnetic properties are compared to the experimental results. Also an investigation on effective g -factors, using effective charges as derived in section 4.3.1, was performed. A more detailed description of the calculations and the results can be found in PAPER V.

4.3.3 Excited states in ^{54}Ni

Based on the known level scheme of $^{54}\text{Fe}_{28}$ [38, 39] one expects to observe a long-lived 10^+ state followed by a five-step γ -ray cascade in the mirror nucleus $^{54}\text{Ni}_{26}$. Figure 4.14a illustrates the relevant part of the ^{54}Fe level scheme with the isomeric 10^+ state. The state has a lifetime of $\tau = 525(10)$ ns and decays via the 146 keV $E2-$ and the 3578 keV $E4-$ transitions. Simple shell-model calculations utilizing the full fp shell, but limited to allow for only two particle excitations across the $N = Z = 28$ shell closure, have been performed to estimate the lifetime of the corresponding 10^+ state in ^{54}Ni . The calculations for ^{54}Ni include same $E4$ strengths as experimentally known in ^{54}Fe . From the resulting $B(E2)$ values the lifetime of the 10^+ state is calculated as function of the $E2$ transition energy using Eq. 4.12. Figure 4.14b shows the estimated lifetime of the 10^+ state in ^{54}Ni as function of the $10^+ \rightarrow 8^+$ $E2$ transition energy.

Hence, measurements of the $10^+ \rightarrow 8^+$ $E2$ and the $10^+ \rightarrow 6^+$ $E4$ transitions in ^{54}Ni will serve as a consistency check of the nuclear shell model. In particular, a comparison with experimental data for ^{54}Fe allows for a similar study on effective charges as discussed in section 4.3.1, which may provide additional information on this phenomenon. The effective charges for the $A = 54$ mirror pair can be determined using the known lifetime and the branching ratio of the 10^+ isomer in ^{54}Fe and the corresponding, so far unknown, properties of the mirror state in ^{54}Ni . Furthermore, it is also of interest to study the Mirror Energy Differences for the $A = 54$ nuclei and compare them to the $A = 42$ nuclei ($^{42}\text{Ti}_{20}$ and $^{42}\text{Ca}_{22}$). The present analysis aims to identify and determine the level scheme structure for ^{54}Ni with focus at and around the expected isomeric 10^+ state. Lower lying excited states (2^+ , 4^+ , 6^+) have been observed in an Euroball experiment but are not yet published [40].

The present analysis is based on combined data from the GSFMA73 and GS2k017 experiments (cf. section 2.2). The ^{54}Ni nuclei are populated through the very weak $1\alpha 2n$ reaction channel. Hence, the analysis requires the detection of two correlated neutrons. In order to obtain reasonably high statistics but still a clean $1\alpha 2n$ -spectrum, extremely good and efficient neutron discrimination is needed. Problems with false two-neutron events, which arise due to neutron scattering, also need to be taken into consideration as they contaminate the $2n$ -gated spectra. Neutrons are distinguished between γ rays using different gate conditions, which allow to define whether a neutron or a γ ray hit a specific detector module. The neutron gate conditions have been reworked several times to optimize the result for the present analysis. A more detailed description of the particle identification and the different spectra used in the neutron discrimination process can be found in Ref. [41]. Due to the relatively low two-neutron detection efficiency one can expect to observe ^{54}Ni also in the $1\alpha 1n$ -gated spectra. Therefore, both the $1\alpha 1n$ - and the $1\alpha 2n$ -gated data sets are used in the analysis and sorted into $\gamma\gamma$ -matrices.

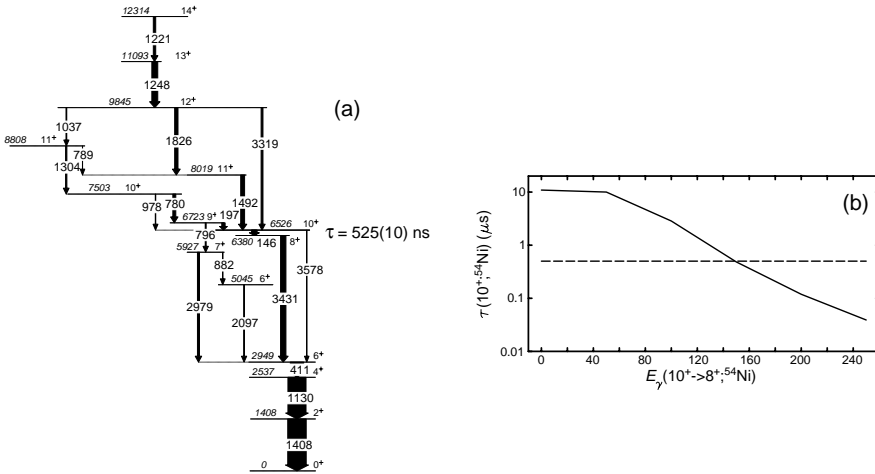


Figure 4.14: (a) Relevant part of the level scheme of ^{54}Fe . The lifetime of the 10^+ state is indicated. Energy labels are in keV and the widths of the arrows correspond the relative intensities of the transitions. (b) The lifetime of the corresponding 10^+ state in ^{54}Ni as function of the $10^+ \rightarrow 8^+$ E2 transition energy.

In order to fine tune the analysis the detected γ rays are assigned as being prompt, delayed, or isomeric. This allows to split up the constructed matrices into prompt, delayed, and isomeric parts, respectively. Isomeric γ rays are emitted once the residual nuclei are stopped whereas prompt and delayed γ rays arise from transitions when the nuclei are still in flight. To distinguish between prompt and delayed γ rays, the latter are defined using time gates next to the prompt time peak. The present reaction is believed to populate ^{54}Ni just above the proposed isomeric 10^+ state. Lower lying transitions are most likely to be found among the isomeric γ rays, whereas transitions above the 10^+ state shall be found as prompt γ rays. It can be concluded, with available statistics, that no transition corresponding to ^{54}Ni is seen in spectra comprising delayed or isomeric γ -rays. This indicates that the lifetime of the 10^+ state is longer than the corresponding state in ^{54}Fe , as the known γ -ray energies for the $6^+ \rightarrow 4^+ \rightarrow 2^+ \rightarrow 0^+$ cascade [40] are not at all observed. Hence, the continued analysis focuses on data with prompt γ -rays.

The prompt spectrum showed a promising peak at around 191 keV, which may correspond to the 197 keV $9^+ \rightarrow 10^+$ transition in ^{54}Fe . From the proposed similarities with the ^{54}Fe level scheme (cf. Fig. 4.14), one then also expects to see one peak around 780 keV and one peak around 1305 keV in coincidence with this 191 keV transition. In a spectrum obtained in coincidence with the 191 keV transition, four

peaks at 752, 1032, 1061, and 1098 keV are observed. It can, however, be concluded that these four peaks arise from ^{65}Ga [42]. The prompt $1\alpha 2n$ -gated spectrum and the spectrum obtained in coincidence with the 191 keV transition is shown in Fig. 4.15. The spectra clearly show the peaks from ^{65}Ga . There is also a tiny fraction of ^{51}Mn leaking through.

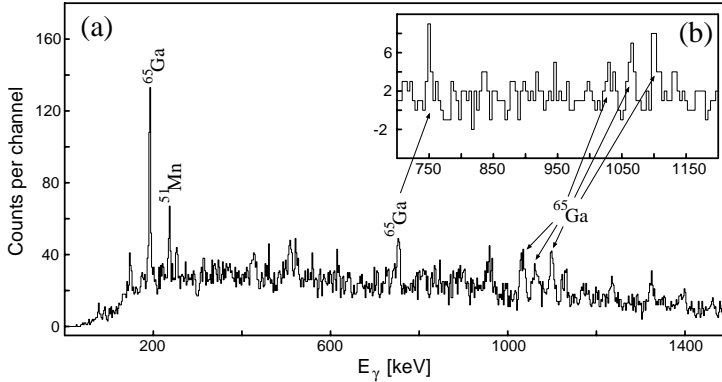


Figure 4.15: (a) The total projection of the prompt $1\alpha 2n$ -gated spectrum. (b) The spectrum in coincidence with the 191 keV line is inserted at the top. The lines from ^{65}Ga nuclei at 752, 1032, 1061 and 1098 keV are clearly seen in the coincidence spectrum.

The peaks corresponding to ^{65}Ga arise from a contamination in the ^{28}Si targets. To prevent them to oxidize, they were placed in a sealed container comprising argon atmosphere. However, instead of contamination from oxidation in air, ^{40}Ar atoms diffused into the target. Thus fusion-evaporation reactions with the ^{32}S beam on ^{40}Ar are possible, producing ^{72}Se as the compound nucleus. The ^{65}Ga nuclei are populated in the $1\alpha 2n1p$ -channel, but because of the finite proton and neutron detection efficiency it is also seen in the $1\alpha 1n$ - and $1\alpha 2n$ -spectra.

To reduce the amount of ^{65}Ga in the $1\alpha 2n$ -spectra a restriction on the total number of γ rays, M_γ , is introduced. M_γ is the sum of γ -rays detected in the Ge-detectors and in the BGO-elements. Through comparison of two $1\alpha 2n$ -gated spectra with $M_\gamma \leq 5$ and $M_\gamma \geq 7$, respectively, it is found that the amount of ^{65}Ga is significantly higher in the latter case. Hence, to remove the contamination of ^{65}Ga , the two spectra were normalized to the strong 191 keV transition in ^{65}Ga and the spectrum obtained with $M_\gamma \geq 7$ was subtracted from the spectrum obtained with $M_\gamma \leq 5$. The resulting spectrum is found to be much cleaner. This spectrum is believed to reflect the primary reaction, in which peaks from the ^{54}Ni nuclei are expected to be present. By studying this spectrum, which is shown in Fig. 4.16, peaks at 1040 keV and 1327 keV can be observed. They belong to the $^{32}\text{S} + ^{28}\text{Si}$ reaction, but unfortunately not to ^{54}Ni . They are known transitions in ^{53}Co [43], which is the $1\alpha 2n1p$ reaction channel.

It is concluded that no peaks arising from the ^{54}Ni nuclei can be observed with good accuracy in any of the, so far, produced spectra. It is believed that due to the

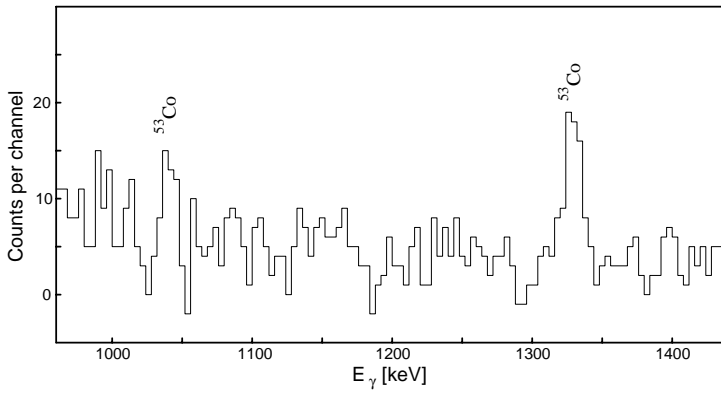


Figure 4.16: *The resulting spectrum obtained by subtracting two spectra as described in text. The reduced amount of ⁶⁵Ga and the two peaks at 1040 and 1327 keV, corresponding to known transitions in ⁵³Co, are clearly seen.*

long lifetime of the proposed 10^+ state one would not get enough γ -rays from either above or below the isomer, to fire the event trigger.

Chapter 5

Conclusion and Outlook

The first part of the present thesis discusses the first measurements of deuterons and anti-deuterons produced in $\sqrt{s_{NN}} = 200$ GeV gold-gold collisions at RHIC, performed within the PHENIX experiment. Invariant yields and transverse momentum spectra are presented. In combination with measured (anti-)proton spectra the coalescence parameter, B_2 , was investigated. The increase of B_2 with transverse momentum is inconsistent with a simple model and indicates a decreasing source size with increasing momentum, which is indicative of an expanding source.

Future analysis work would, of course, be to analyse data with higher statistics to improve the results for the (anti-)deuterons and also allow for a search and measurements of heavier anti-nuclei, for example, anti-triton or anti-helium. However, an analysis of (anti-)deuterons in data from proton-proton collisions, where no collective transverse flow is expected, may also provide valuable information. The results obtained in such measurements should yield a smaller source size compared to that obtained from gold-gold collisions.

The second part of the thesis discusses lifetime measurements of excited states of atomic nuclei and illustrates how such measurements are utilized to access and determine effective transition operators. In particular, the lifetime of the analogue $27/2^-$ states in the $A = 51$ mirror pair have been measured. This allow to determine the corresponding $B(E2; 27/2^- \rightarrow 23/2^-)$ values, which are employed in a unique investigation of the effective nucleon charges near the doubly magic nucleus ^{56}Ni . A detailed comparison with large-scale shell-model calculations yields the effective charges of $\varepsilon_n \sim 0.80$ and $\varepsilon_p \sim 1.15$ for the neutron and proton, respectively. A more extensive study on the phenomenon of effective charges requires additional experimental data on nuclei in the fp shell. A similar study may be performed in the $A = 54$ mirror pair with the long-lived 10^+ state in ^{54}Fe and the corresponding, so far unknown, analogue state in ^{54}Ni .

An analysis based on data from two different experiments aiming at identification of γ -ray transitions in the ^{54}Ni isotope has been performed. No such γ -rays are, however, observed. Hence, in future experiments, which aim to investigate the ^{54}Ni isotope, the trigger conditions need to be optimised for the very long-lived predicted state. Furthermore, if such an analysis is to employ the same reaction as in the present analysis, a careful handling of the targets to minimize the contamination is necessary.

A largely extended level scheme of ^{53}Fe has been constructed as presented in PAPER V. The lifetimes of a few of the newly observed excited states have been measured and are presented in the thesis. The excitation energies and decay properties of these states are reproduced in large-scale shell-model calculations performed in the full fp shell. Also a limited investigation on effective g -factors has been performed. This study employs large-scale shell-model calculations, using the previously derived effective nucleon charges, and attempts to reproduce the experimentally determined branching ratios. However, no quantitative estimations on the effective g -factors can be derived from this investigation. A more extensive study using more experimental data is required.

Future work must extend the amount of experimental data for nuclei in the fp shell. Similar studies of electromagnetic properties as discussed in the present thesis should be employed to other mirror pair systems. This would provide additional information on the phenomenon of effective transition operators. In particular, an experiment dedicated to investigate the properties of the ^{54}Ni isotope has been proposed and accepted. This will take place within the RISING stopped beam campaign at Gesellschaft für Schwerionenforschung, GSI, in Germany, probably during the year 2005.

Chapter 6

Popularised Summary in Swedish

De atomer och molekyler som utgör materian i dagens universum, såsom vi känner det, är uppbyggda av många olika komponenter. Dessa komponenter har under årens lopp upptäckts genom diverse olika experiment. I början av 1900-talet upptäcktes att atomen har en inre struktur och består av en liten positivt laddad atomkärna omgiven av ett moln av elektroner. Senare experiment visade att atomkärnan i sig själv är uppbyggd av protoner och neutroner, gemensamt kallade nukleoner, vilka hålls sammans via den starka kärnkraften. Nukleonerna i sin tur uppvisar även de en inre struktur i form av kvarkar. Kvarkarna antas vara de fundamentala byggstenarna i materian omkring oss. De har sitt ursprung miljarder år tillbaka i tiden vid tidpunkten för universums skapelse.

Dagens forskning inom kärn- och partikelfysik strävar efter att försöka förstå och förklara de fundamentala egenskaper och förändringar som materian och dess olika byggstenar uppvisar under givna förhållanden. Exempelvis försöker vetenskapsmän återskapa det tillstånd som universums materia antas ha befunnit sig i strax efter Big Bang, vilket kräver extrema förhållanden vad gäller temperatur och densitet. I detta tillstånd antas kvarkarna, vilka normalt är bundna inne i nukleonerna, kunna röra sig fritt över en större volym. Under mer "normala" förhållanden undersöks de parametrar som används för att beskriva atomkärnan. Utifrån dessa studier hoppas forskarna exempelvis på att få en djupare förståelse för de krafter som påverkar de individuella nukleonerna. De förhållanden som krävs för att genomföra studierna skapas vid stora anläggningar runt om i världen. Vid dessa anläggningar accelereras atomkärnor till höga hastigheter och tillåts kollidera med en annan atomkärna, vilket skapar det system av materia man önskar undersöka. De komponenter och signaler som bildas vid kollisionen registreras med avancerad detektorutrustning och därefter analyseras den insamlade datamängden.

I denna avhandling diskuteras olika aspekter av kärnreaktioner inducerade med tunga atomkärnor. En beskrivning av de experiment, detektorer och metoder som har använts återfinns tillsammans med en utförlig redogörelse av analysarbetet. De resultat som presenteras är baserade på dels experimentella data men även från simu-

leringar och teoretiska beräkningar.

Avhandlingen redogör för mätningarna av deuteroner och anti-deuteroner producerade vid acceleratoren RHIC (Relativistic Heavy-Ion Collider) på Brookhaven National Laboratory i USA. Vid tidpunkten för dessa mätningar accelererades guldkärnor upp till en hastighet väldigt nära ljusets innan de tilläts kollidera med varandra. Resultaten från dessa mätningar, vilka är de första för deuteroner och anti-deuteroner vid denna hastighet, presenteras och diskuteras.

Vidare i avhandlingen diskuteras mätningar av livstider av exciterade tillstånd i atomkärnor. Dessa mätningar baserar sig på data från experiment utförda vid LNL (Legnaro National Laboratory) i Italien där atomkärnor accelererades upp till ett par procent av ljusets hastighet innan kärnreaktionerna ägde rum. De uppmätta livstiderna kan användas för att undersöka fundamentala elektromagnetiska egenskaper hos kärnorna. Speciellt redogörs för hur livstidsmätningar i så kallade spegelkärnor, vilka är par av kärnor där antalet protoner och neutroner är det omvända, kan användas för att bestämma effektiva nukleonladdningar. Dessa introduceras i gängse teoretiska modeller för att ge en bättre överensstämmelse mellan teori och experiment. Speciellt fokuserar avhandlingen på livstidsresultat för spegelkärnorna ${}_{26}^{51}\text{Fe}_{25}$ och ${}_{25}^{51}\text{Mn}_{26}$. Metodiken och de erhållna resultaten från denna studie diskuteras utförligt.

Acknowledgements

I would like to express my gratitude to everyone who has, in one way or another, been involved in the present thesis. All colleagues and friends at the Division of Nuclear Physics and the former Division of Cosmic and Subatomic Physics are acknowledged for their help and support over the years. In particular, I would like to thank the persons I have been working closest with:

Claes Fahlander, for giving me the contingency to continue and complete my thesis work within his research group. I thank him for his encouragement and motivation in this work as well as the introduced poker sessions, which enriched my life in several different aspects.

My supervisor, Dirk Rudolph, mainly for his excellent guidance, valuable advice, and expertise in nuclear physics, but also for introducing me to "Doppelkopf".

Hans-Åke Gustafsson, together with Anders Oskarsson and Evert Stenlund, for their knowledge, encouragement, and guidance during the time I spent working within the group for Relativistic Heavy-Ion Physics.

Joakim Nystrand, for encouraging and introducing me to search for deuterons and anti-deuterons. His help and guidance in the analysis work is greatly appreciated.

My fellow students and moreover roommates over the years, Henrik Tydesjö and Jörgen Ekman, for their assistance and support on various issues as well for sharing great fun, not only within the walls of the physics department, and for being good friends.

Lennart Österman for countless small favours, discussions and help with computers whenever needed.

I also wish to thank the rest of the Nuclear Structure Group; Lise-Lotte Andersson, Joakim Cederkäll, Andreas Ekström, Emma Johansson, Margareta Hellström, Milena Mineva, and Hans Ryde for valuable discussions and for creating a nice and friendly atmosphere to work in. The former students Pavel Golubev, Paul Nilsson, and David Silvermyr are acknowledged for their help on various issues. Furthermore, I also would like to thank my friends for their support and for all good moments shared over the years.

I gratefully acknowledge the financial support from Lund University, the Swedish House of Nobility, NORDITA (Nordic Institute for Theoretical Physics), Legnaro National Laboratory, and Kungliga Fysiografiska Sällskapet i Lund.

Finally, I would like to express my sincere gratitude to my family for their encouragement and support throughout the years.

Appendix A

Parameterization of the cross sections

Due to the limited amount on experimental data on total cross sections for deuteron and anti-deuteron induced interactions, a direct parameterization of the cross section on a nucleus A is not possible. Instead, a method has been developed, which calculates the inelastic deuteron (anti-deuteron) cross section from the inelastic cross sections for protons (anti-protons), $\sigma_{p,A}$ ($\sigma_{\bar{p},A}$), and neutrons (anti-neutrons), $\sigma_{n,A}$ ($\sigma_{\bar{n},A}$). The parameterization for $\sigma_{p,A}$, $\sigma_{\bar{p},A}$, $\sigma_{n,A}$, and $\sigma_{\bar{n},A}$ is taken from Ref. [44], where the inelastic (anti-)helium cross section is calculated using

$$\begin{aligned}
 \sigma_{p,A}(E) &= 45 \cdot A^{0.7} \cdot [1 + 0.016 \sin(5.3 - 2.63 \ln A)] \cdot \\
 &\quad \cdot [1 - 0.62 \exp(-5E) \sin(1.58 \cdot E^{-0.28})], \\
 \sigma_{\bar{p},A}(E) &= A^{2/3} \cdot [48.2 + 19 \cdot (E - 0.02)^{-0.55} - 0.106 \cdot A^{0.927} \cdot E^{-1.2} + \\
 &\quad + 0.059 A^{0.927} + 0.00042 A^{1.854} \cdot E^{-1.5}], \\
 \sigma_{n,A} &= (43.2 \pm 2.3) \cdot A^{0.719 \pm 0.012}, \\
 \sigma_{\bar{n},A} &= A^{2/3} \cdot (51 + 16 \cdot E^{-0.4}).
 \end{aligned} \tag{A.1}$$

The cross sections are given in mb and the parameter E is the kinetic energy of the nucleon in GeV. The effective nucleon-nucleus cross section, $\sigma_{N,A}$, is calculated as the average of the neutron- and proton-nucleus cross section,

$$\sigma_{N,A} = \frac{\sigma_{p,A} + \sigma_{n,A}}{2}, \tag{A.2}$$

and similarly for anti-nucleons.

The parameterization of the inelastic deuteron cross section, $\sigma_{d,A}$, on nuclei is derived as follows. The cross section on a nucleus A can be written as

$$\sigma_{d,A} = \sigma_{N,A} + \Delta\sigma_{d,A}, \tag{A.3}$$

where $\Delta\sigma_{d,A}$ is the difference in cross section compared to the nucleon-nucleus cross section. A geometric picture of the nuclear collisions is illustrated in Fig. A.1. Based

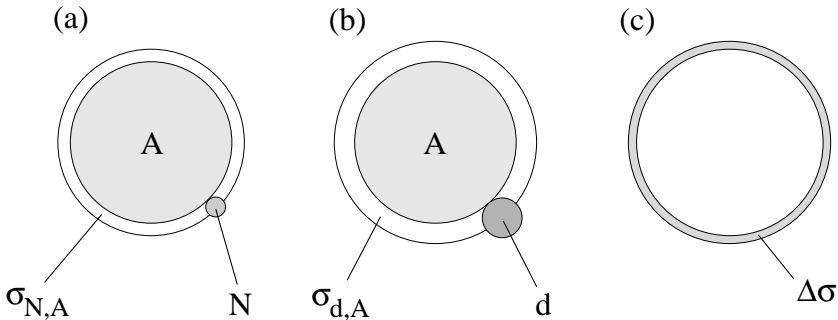


Figure A.1: *Geometric picture used for the parameterization of the (anti-)deuteron cross section. Panels (a) and (b) illustrate the nucleon-nucleus, $\sigma_{N,A}$, and the deuteron-nucleus, $\sigma_{d,A}$, cross section, respectively. The cross section difference, $\Delta\sigma$, is illustrated in panel (c).*

on this geometry the deuteron cross section can be written as

$$\sigma_{d,A} = [\sqrt{\sigma_{N,A}} + \Delta_d(A)]^2, \quad (\text{A.4})$$

from which $\Delta_d(A)$ can be expressed as

$$\Delta_d(A) = \sqrt{\sigma_{d,A}} - \sqrt{\sigma_{N,A}}. \quad (\text{A.5})$$

$\Delta_d(A)$ corresponds to the average difference in radius between a nucleon and a deuteron, which can be expected to be largely independent of the nuclear mass number and the collision energy. Comparison with experimental deuteron data [45, 46] gives that $\Delta_d(A) = 3.51(25) \text{ mb}^{1/2}$ independent of A .

In Ref. [44] it is assumed that the anti-helium cross section can be written in the same way as the helium cross section. Following this approach, the inelastic anti-deuteron cross section, $\sigma_{\bar{d},A}$, can be written as

$$\sigma_{\bar{d},A} = [\sqrt{\sigma_{\bar{N},A}} + \Delta_{\bar{d}}(A)]^2, \quad (\text{A.6})$$

where

$$\sigma_{\bar{N},A} = \frac{\sigma_{\bar{p},A} + \sigma_{\bar{n},A}}{2}. \quad (\text{A.7})$$

The difference in radius between an anti-nucleon and an anti-deuteron, $\Delta_{\bar{d}}(A)$, is assumed identical to the difference between a nucleon and a deuteron. Hence, the constant value $\Delta_{\bar{d}}(A) = 3.51(25) \text{ mb}^{1/2}$ is used.

Bibliography

- [1] K.S. Krane, "Introductory Nuclear Physics", John Wiley & Sons, New York (1988).
- [2] K.L.G. Heyde, "The Nuclear Shell Model", Springer Verlag, Heidelberg (1994).
- [3] J. Ekman, Ph.D. thesis, Lund University (2004), ISBN 91-628-6061-5.
- [4] J.D. Bjorken, Phys. Rev. D **27** (1983) 140.
- [5] J.W. Harris and B. Müller, Ann. Rev. Nucl. Part. Sci. **46** (1996) 71.
- [6] U. Heinz and B.V. Jacak, Ann. Rev. Nucl. Part. Sci. **49** (1999) 529.
- [7] GAMMASPHERE, The Beginning ... 1993-1997, Science Highlights booklet, Ed. M.A. Riley, (1998); <http://nucalf.physics.fsu.edu/~riley/gamma>
- [8] G.D. Westfall *et al.*, Phys. Rev. Lett. **37** (1976) 1202.
- [9] C. Rossi Alvarez, Nuclear Physics News, Vol. 3, 3 (1993).
- [10] A. Dewald *et al.*, Nucl. Phys. **A545**, 822 (1992).
- [11] A. Dewald *et al.*, Z. Phys. A **334** (1989) 163-175.
- [12] G. Böhm *et al.*, Nucl. Inst. Meth. A **329** (1993) 248-261.
- [13] <http://www.ikp.uni-koeln.de>
- [14] I.Y. Lee, Nucl. Phys. A **520** 641c (1990).
- [15] D.G. Sarantites *et al.*, Nucl. Inst. Meth. A **383** 506 (1996).
- [16] D.G. Sarantites *et al.*, to be published.
- [17] C. Andreiou, Ph.D. thesis, Lund University (2002), ISBN 91-628-5308-2.
- [18] <http://www.phenix.bnl.gov>
- [19] D.P. Morrison *et al.*, (PHENIX Collaboration), Nucl. Phys. A **638** (1998) 565.
- [20] F. Sauli, CERN preprint 77-09 (1977).
- [21] S.T. Butler and C.A. Pearson, Phys. Rev. **129** (1963) 836.
- [22] A.Z. Mekjian, Phys. Rev. C **17** (1978) 1051.

- [23] L.P. Csernai and J.I. Kapusta, Phys. Rep. **131** (1986) 223.
- [24] W.R Leo, "Techniques for Nuclear and Particle Physics Experiments", Springer-Verlag, New York, (1994).
- [25] T. Chujo *et al.*, (PHENIX Collaboration), Nucl. Phys. **A715** (2003).
- [26] A. Polleri, J.P. Bondorf and I.N. Mishustin, Phys. Lett. B **419** (1998) 19.
- [27] H. Morinaga and T. Yamazaki, "In-Beam Gamma-Ray Spectroscopy" North-Holland Publishing Company, Amsterdam, New York, Oxford, 1976.
- [28] K. Heyde, "Basic Ideas and Concepts in Nuclear Physics", Institute of Physics Publishing, Bristol (1994).
- [29] A. Bohr and B.R. Mottelson, "Nuclear Structure Vol. 2", Benjamin Inc., New York, 1975.
- [30] E. Caurier, shell model code ANTOINE, IRES, Strasbourg 1989-2002.
- [31] E. Caurier, F. Nowacki, Acta Phys. Pol. **30**, 705 (1999).
- [32] M.A. Bentley *et al.*, Phys. Rev. C **62**, 051303(R) (2000).
- [33] J. Ekman *et al.*, Eur. Phys. J. A **9**, 13 (2000).
- [34] J. Ekman *et al.*, Phys. Rev. C **70**, 014306 (2004).
- [35] A. Poves, J. Sanchez-Solano, E. Caurier, and F. Nowacki, Nucl. Phys. **A694**, 157 (2001).
- [36] W.A. Richter *et al.*, Nucl. Phys. A **523**, 325 (1991).
- [37] S.J. Williams, Ph.D. thesis, Keele University (2003).
- [38] J. Huo, H. Sun, W. Zhao and Q. Zhou, Nucl. Data Sheets **68** 887 (1993).
- [39] D. Rudolph *et al.*, Eur. Phys. J. A **4**, 115 (1999).
- [40] A. Gadia *et al.*, private communications.
- [41] J. Ekman, "Isospin Symmetry Breaking in the A=51 Mirror Nuclei", Licentiate thesis, Department of Physics, Lund University (2002).
- [42] M. Weiszflog *et al.*, Eur. Phys. J. A **11**, 25 (2001).
- [43] S.J. Williams, Phys. Rev. C **68**, 011301 (2003).
- [44] A.A. Moiseev and J.F. Ormes in Astroparticle Physics 6(1997) 379-386.
- [45] J. Jaros *et al.*, Phys. Rev. C **18**(1978)2273.
- [46] E.O. Abdurakhmanov *et al.*, Z. Phys. C **5**(1980)1.

Paper I

Construction and performance of the PHENIX pad chambers

K. Adcox^a, J. Ajitanand^b, J. Alexander^b, J. Barrette^c, R. Belkin^d, D. Borland^a,
W.L. Bryan^e, R. du Rietz^f, K. El Chenawi^a, A. Cherlin^g, J. Fellenstein^a,
K. Filimonov^{c,1}, Z. Fraenkel^g, D. Gan^{c,2}, S. Garpman^{f,*}, Y. Gil^g, S.V. Greene^a,
H.-Å. Gustafsson^f, W. Holzmann^b, M. Issah^b, U. Jagadish^e, R. Lacey^b,
J. Lauret^{b,d}, W. Liccardi^d, S.K. Mark^c, J. Milan^b, T.E. Miller^a, A. Milov^{g,3},
J.T. Mitchell^d, P. Nilsson^{f,4}, L. Nikkinen^c, J. Nystrand^f, E. O'Brien^d,
A. Oskarsson^{f,*}, L. Österman^f, I. Otterlund^f, Y. Qi^{c,5}, B. Pasmantirer^g,
C. Pinkenburg^{b,d}, I. Ravinovich^g, M. Rosati^{c,6}, A. Rose^a, D. Silvermyr^{f,7},
M. Sivertz^d, M.C. Smith^e, N. Starinsky^{c,8}, E. Stenlund^f, O. Teodorescu^{c,9},
I. Tserruya^g, H. Tydesjö^f, W. Xie^{g,10}, G.R. Young^e, V. Yurevich^{g,11}

^a Vanderbilt University, Nashville, TN 37235, USA

^b Chemistry Department, State University of New York - Stony Brook, Stony Brook, NY 11794, USA

^c McGill University, Montreal, Que., Canada H3A 2T8

^d Brookhaven National Laboratory, Upton, NY 11973-5000, USA

^e Oak Ridge National Laboratory, Oak Ridge, TN 37831, USA

^f Department of Physics, Lund University, Box 118, SE-221 00 Lund, Sweden

^g Weizmann Institute of Science, Rehovot 76100, Israel

Received 5 September 2002; accepted 10 September 2002

Abstract

We present the Pad Chamber detector system in the PHENIX experiment at the Relativistic Heavy Ion Collider (RHIC) at Brookhaven National Laboratory. The three station system provides space points along each track in the

*Corresponding author. Tel.: +46-46-222-0000; fax: +46-46-222-4015.

E-mail address: anders.oskarsson@kosufy.lu.se (A. Oskarsson).

¹ Present address: Lawrence Berkeley Nat. Laboratory, Berkeley, CA 94720, USA.

² Present address: Dept. of Electrical Engineering, Cornell University, Ithaca, NY 14853-7501, USA.

³ Deceased.

⁴ Present address: State University of New York-Stony Brook, Stony Brook, NY 11794, USA.

⁵ Present address: CERN, EP-division, CH-1211 Geneva 22, Switzerland.

⁶ Present address: Dept. of Biomedical Engineering, University of North Carolina, Chapel Hill, NC 27599, USA.

⁷ Present address: Iowa State University, Ames, IA 50011, USA.

⁸ Present address: Los Alamos National Laboratory, Los Alamos, NM 87545, USA.

⁹ Present address: Dept. of Physics and Astronomy, Queen's University, Kingston, ON, Canada K7L 3N6.

¹⁰ Present address: Dept. of Computer Science, Cornell University, Ithaca, NY 14853-7316, USA.

¹¹ Present address: University of California-Riverside, Riverside, CA 92521, USA.

¹² On leave from the Joint Inst. for Nuclear Res. JINR, Moscow.

spectrometer arms at mid-rapidity and covers a total area of 88 m². Its main functions are to provide the track coordinate along the beam and to ensure reliable pattern recognition at very high particle multiplicity. A new concept for two dimensional wire chamber readout via its finely segmented cathode was developed. The full readout system, comprising 172 800 electronic channels, is described together with the challenging design of the chambers. The electronics, mounted on the outer chamber face, together with the chamber itself amounts to 1.2% of a radiation length. Results from cosmic ray tests, showing an average efficiency better than 99.5% for all chambers are presented. The experiences from the full scale operation in the first run are reported.

© 2002 Elsevier Science B.V. All rights reserved.

PACS: 29.40.CS; 29.40.GX

Keywords: PHENIX; RHIC; Tracking; Wire chamber; Cathode pixels; Readout electronics

1. Introduction

Collider experiments with beams of heavy nuclei at very high energy, are now possible at the Relativistic Heavy Ion Collider (RHIC), at Brookhaven National Laboratory, and in the future at the Large Hadron Collider (LHC) at CERN. Heavy ion collisions, introduce additional experimental challenges compared to collider experiments with protons. Whereas the luminosities with heavy ions are low (at best $10^{27} \text{ s}^{-1}/\text{cm}^{-2}$), the number of charged particles emitted per central Au–Au collision is about 4800 at the highest RHIC energy [1–3] and may be as large as 50 000 at LHC. At the time of design of the RHIC experiments, the expected multiplicities ranged up to a factor two larger than what has now been measured.

Detector systems, aiming at observing individual particles under such conditions must cope with the high multiplicities by using a very fine granularity to reduce the occupancy. The large channel count makes it necessary to place the amplifying and digitizing electronics in specialized integrated circuits, on the detector. Transfer of digitized data from the detector profits from advances in broadband technology, allowing serial transfer from a large number of channels via fiber optic links.

This paper describes the design, construction, testing and performance of the Pad Chambers which form part of the particle tracking system at mid rapidity of the PHENIX detector [4,5]. Three layers of Pad Chambers define three space points

along the straight line tracks through the tracking spectrometers which also include specialized detectors for momentum and particle identification.

2. The PHENIX experiment

The main objectives of the PHENIX experiment at RHIC are to measure rare observables like leptonic decays of light (ω, ρ, ϕ) and heavy ($J/\Psi, \Psi'$ and Υ) vector mesons and phenomena at high p_T , all requiring maximal collision rate. PHENIX is thus only using tracking detectors with short drift times. The leptonic decays are observed in the $\mu^+\mu^-$ channel at large rapidity and in the e^+e^- channel at mid-rapidity.

The PHENIX detector is built (Fig. 1) around a central, circular dipole magnet with a vertical gap producing a radially varying axial field with about 2 m radius. Two spectrometer arms, named east and west, located in the field free region, view the collisions from opposite sides. The arms cover the mid-rapidity region $|\eta| < 0.35$, each one with a 90° coverage in azimuth. The arms are positioned with a 67.5° opening at the top (and 112.5° at the bottom) rather than 90° both up and down, in order to obtain a finite acceptance for all relative azimuthal angles within particle pairs and thus a smooth acceptance in transverse momentum for the parent particles.

Several stations of tracking detectors (Fig. 2), including the Pad Chambers are complemented by a Ring Imaging Čerenkov detector (RICH) and an Electromagnetic Calorimeter (EMCal) for

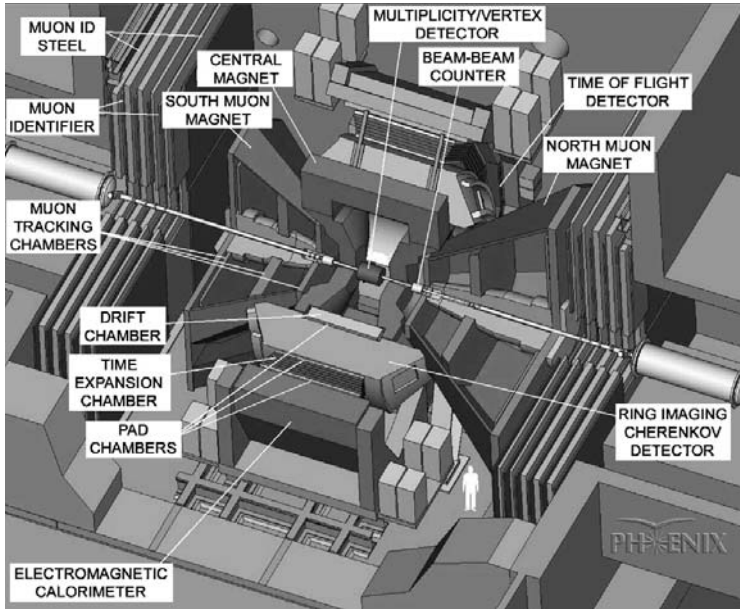


Fig. 1. The baseline PHENIX detector.

electron identification and photon detection. Hadron identification is possible in the full aperture by time of flight measurements using the good time resolution of the calorimeters. In addition, specialized high resolution Time-of-Flight (TOF) detectors cover a subset of the mid-rapidity acceptance. The start time is determined by the Beam–Beam Counters (BBC), which also provide a coarse determination of the vertex position.

Conically shaped magnets surround the beams in the forward and backward directions, forming radial magnetic fields for the muon tracking spectrometers which end with muon identifiers. The muon detection is less affected by the large number of produced hadrons since these are absorbed in the iron of the central magnet.

Three detector systems characterize the collisions with regards to global properties related to the impact parameter. The signal from the BBC reflects the particle density at large pseudorapidity ($3.1 < |\eta| < 3.9$). The MVD (Multiplicity and Vertex

Detector), close to the vertex, measures the multiplicity ($|\eta| < 2.6$) and the interaction coordinate, while the dual Zero Degree Calorimeters (ZDC) view the collision along a tangent through the interaction region, thus integrating the non-interacting energy carried by single spectator neutrons.

2.1. The central arms

The design of the spectrometer arms at mid-rapidity was driven by the strict requirements of electron identification, arising from the expected ratio of 10^3 or larger between the number of hadrons and electrons. Another mandatory concern was to reduce the photon conversion by pair production in various materials in the spectrometer, i.e. to minimize the radiation thickness of the detectors. The main source of high energy photons is π^0 decay and such photons are almost as numerous as charged hadrons.

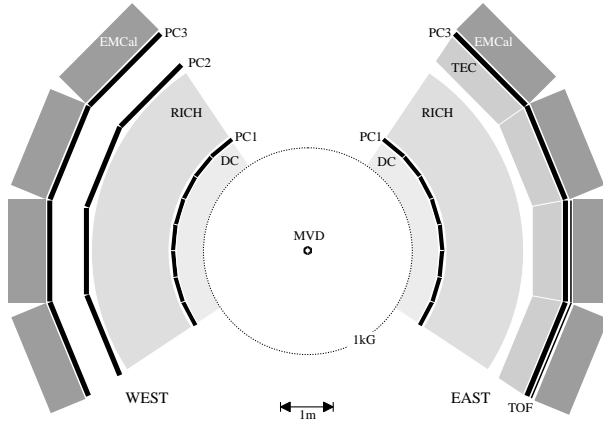


Fig. 2. A schematic illustration of the two mid-rapidity spectrometer arms. The cut is made by a plane, perpendicular to the beams, through the average collision point at the center of the magnet gap. The dotted circle represents the radius at which the magnetic field is approximately 1 kG which is about $\frac{1}{10}$ of the central field strength at the full field setting.

The main detector system (Fig. 2) for electron identification is the RICH (Cherenkov threshold). The momentum is obtained from the Drift Chambers (DC). Combining the information from the EMCal (measured energy and flight time) and/or the Time Expansion Chambers (TEC) provides additional electron identification in certain momentum ranges.

All these means of identification are needed to obtain the required hadron rejection factor of 10^4 over a wide momentum range. This condition requires however that no errors are made when correlating the momentum measured in the DC placed between 2.0 and 2.5 m from the interaction region with the identifying information obtained at twice that distance. This means that a track has to be followed with very high reliability from detector to detector through the whole spectrometer, and this has to be achieved when several hundred particles pass through a spectrometer arm in a central collision. Reliable pattern recognition is the most important role of the Pad Chamber (PC) detector system.

The mid-rapidity spectrometers as they are visualized in Fig. 1, with the east and west arm tracking detectors being identical, was the original

design. This plan was changed due to financial reasons, and the spectrometer arms have a TEC only in the east arm and PC2 only in the west arm as shown in Fig. 2. The mechanical design however, still allows the original version to be implemented.

2.2. Specifications of the Pad Chambers

As part of the requirements of the tracking system in the PHENIX central arms, the Pad Chambers must fulfill the following roles and have the following specifications:

- Provide reliable track information with accurate coordinate in the z direction (parallel to the beams) and good position resolution in the other (ϕ) direction.
- Provide redundancy for the drift chamber measurements (though with poorer azimuthal resolution).
- Very high detection efficiency.
- Low occupancy of individual channels.
- Define entry and exit coordinates of the particle identification subsystems, mainly the TEC, RICH and the EMCal.

- Minimum radiation thickness to minimize conversions.
- Provide fast position information to be used as input to the second-level trigger.

For a detector system, covering almost 100 m² in a cylindrical geometry, wire chambers with 2-dimensional cathode readout, are best suited to obtain the required functions of the Pad Chambers.

The DC and the TEC determine the track coordinate in the plane perpendicular to the beams (r - ϕ) with high resolution. Several close points are measured and the information can be put together to determine direction vectors in r - ϕ . This information alone would lead to combinatorial ambiguities when tracing particles through the spectrometer, i.e. connecting distant points, when the multiplicity is high. Another complication is that the occupancy of these systems is fairly high in the most central collisions.

Reliable pattern recognition through the spectrometer requires resolving the tracks in three dimensions. The three layers of Pad Chambers, located at the radial distances of 2.5 m (PC1), 4.2 m (PC2) and 4.9 m (PC3) from the interaction region, serve this purpose. Since they provide the coordinates of three space points on each track, the Pad Chamber information defines reliably the straight line particle tracks in the field free region. The transverse coordinates do not need to be precise, since the transverse momentum is determined by the DC.

The DC has some of the wires oriented at a small stereo angle (i.e. a small angle relative to the beam) providing a measurement also of the z -coordinate. However, the small stereo angle, the low number of wires and the high occupancy makes this z -measurement less reliable. The z -measurement provided by PC1 (placed immediately behind the DC), is thus the most accurate measurement of the z -coordinate, in particular at high multiplicity. To fulfill this crucial role in the tracking, the highest possible detection efficiency is required.

Tracking simulations, at the charged particle multiplicity expected in central Au + Au collisions, motivate an angular resolution in ϕ corresponding

to a wire spacing in the pad chambers (at the PC1 position) of approximately 8 mm. Tentatively this results in a position resolution across the wires of $8/\sqrt{12} = 2.3$ mm. From the point of view of pattern recognition one would require to the same resolution along the wire (z). This z -resolution also satisfies the minimum requirements imposed by parallel momentum measurements and invariant mass reconstruction, which both are important measurements at the PC1 location. Reliable matching of tracks throughout the spectrometer motivates the same angular resolution for PC2 and PC3 as for PC1. Thus a doubled position resolution is acceptable for PC3, situated at approximately the double radial distance compared to PC1.

PC2 and PC3 also fulfill important roles in some of the particle identification sub-systems. For example, PC3, placed in front of the EMCal, allows tagging of charged particles entering the EMCal.

A mandatory concern was also to minimize the radiation thickness of the chambers, in particular PC1, in order to reduce the number of electron-positron pairs from conversion of high energy photons. Conversions further out can be eliminated in the offline analysis since these electrons cannot be traced back to the DC. Such electrons can however be a complication for the online electron trigger.

3. Pad readout of wire chambers

Two-dimensional readout of wire chambers is normally done by using a cathode segmented into readout pads. Different types of cathode segmentation have been used, such as the cathode strip chamber in which narrow strips are oriented at an angle relative to the wire [6], or the interpolating pad chamber [7] which uses Chevron shaped pads. Both solutions provide very good position resolution along the wire if the signal is spread over several pads/strips. For the tracking system in PHENIX, it was found that the granularity needed to master the high multiplicities made these types of solutions less suitable.

Instead, a new scheme for 2-dimensional readout of wire chambers was developed, based on readout cells having a size similar to the required position resolution. The simplest digital readout, i.e. just comparing the signal with a discriminator threshold, would then be adequate to meet the requirements on position resolution and one would have a system with very low occupancy, due to the fine granularity.

3.1. The pad geometry

A short presentation of the principles of the cell readout is given. Consider a detector with a square shaped readout cell with side w , i.e. a wire chamber with a wire spacing of w and anode-cathode distance of $w/2$. This would potentially result in a position resolution of $w/\sqrt{12}$ (the standard deviation of a rectangular distribution with total width w) across the wires. Along the wire a somewhat better resolution can be expected due to the continuous position sensitivity. The discussion can be generalized to any cell size as long as the ratio between cell width and anode-cathode distance is kept constant.

A straightforward segmentation of the cathode into $8 \times 8 \text{ mm}^2$ sensor cells (as needed for the required position resolution in PC1) with an electronic readout channel connected to each, leads to such a low occupancy that it is not economically justified. Thus we adopt a pad geometry which effectively saves a factor 3 in the number of electronic channels while maintaining the position resolution of the original cell size

$8 \times 8 \text{ mm}^2$. The basics of the concept are described in Fig. 3.

3.2. The principle

The size of the cell is shown in Fig. 3a. Assume that we make three separate layers of pad chambers (individual wire chambers) each with the pad size equal to 3×3 cells. By shifting the three layers by one cell relative to each other in both dimensions, one would be able to reconstruct in which cell the hit is, since each cell means a unique combination of a hit pad from each of the three layers (Fig. 3b). In Fig. 3c, each pad has been cut into nine parts, called pixels, one in each cell covered by the pad, such that the three planes of pixels can be projected onto one single plane without any geometrical overlap. Since the avalanche (i.e. the signal) is always located on a wire, the sharing of the charge between the three pixels in the cell is only governed by the pixel geometry. The width of a pixel is thus chosen such that the same amount of charge is sensed, irrespective of the location of the pixel (position R, M or L) relative to the wire. Hence the pixel in position M (centered over the wire) has the smallest area while the pixels in positions R and L, located symmetrically with respect to the wire, have equal (and slightly larger) area. In panel Fig. 3d, the electrical connections between the nine pixels of a pad have been added.

The three layers of pads can thus be printed on one plane and this plane constitutes one cathode of a wire chamber. A pad is part of nine cells, but

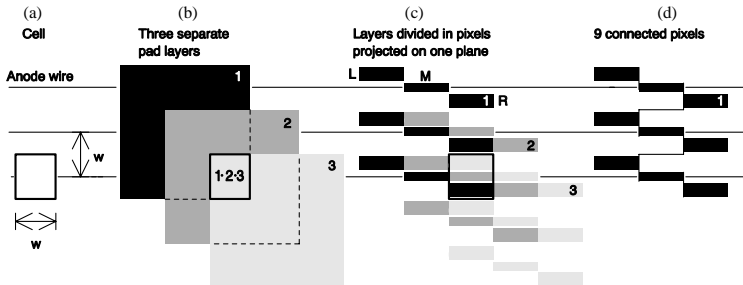


Fig. 3. Principles of the pad geometry.

from the observed pad triplet is however straightforward in software. Each cell is given a (z_c, x_c) coordinate, where z_c is the position along the wire and x_c is the wire number. Each pad also has a coordinate (z_p, x_p) which coincides with the coordinate of the cell located at the center of the pad. When the hit pattern is reconstructed from the information of fired pads, one has to move from pad-space to cell-space. To find out, in which nine cells a certain pad is present, is a trivial task, but to find out which three pads belong to a given cell is not as easy. A general transformation between pad space and cell space has the form:

$$z_p = z_c + \delta_z,$$

$$x_p = x_c + \delta_x$$

where δ_z and δ_x take the values $-1, 0$ or 1 . If we number the three pixels of a cell $0, 1$ and 2 (from top to bottom) a general expression is

$$z_p(i) = z_c + 1 - i$$

$$x_p(i) = x_c + (k - x_c \pm (i - z_c)) \bmod 3 - 1$$

for $i = 0, 1$ and 2 . The two signs in the expression for x_p correspond to the two different possible orientations of the global pattern (the two mirror images). The value of k (either $0, 1$ or 2) corresponds to the three possible different boundary conditions imposed by the plane edges, i.e. the pad configuration at the corner where the pattern starts. In this particular design, we have a $+$ sign and the value of k is 0 .

There is of course also a possibility to use the mirror image of an individual pad (or to look at the plane from the opposite direction). This, however, gives the same formulae if we instead count the i -value from bottom to top in each cell.

4. The wire chambers

This section describes the mechanical design and construction of the chambers using PC1 as an example. Specific features of PC2/3 are mentioned where they differ significantly from PC1. Table 1 summarizes the most important design parameters of the three chamber types.

4.1. Mechanical design

As indicated in Section 2, the basic requirements of the Pad Chambers are to achieve the highest possible efficiency and to minimize the amount of material used in the chamber construction. Both requirements are particularly important for PC1. In order to achieve the highest possible efficiency, dead or inactive areas due to frames etc., must be avoided. Thus a frameless construction was chosen for PC1, in which the wire tension is counteracted by the rigidity of honeycomb sandwich structures, building up the cathode planes.

Table 1
Design parameters of the individual chambers. The radiation thicknesses for PC2 and PC3 are for the sensitive area only

Parameter	PC1	PC2	PC3
Gas gap (mm)	6.0	10.0	12.0
Number of wires	58	116	116
Wire pitch (mm)	8.4	13.6	16.0
Length (cells)	212	106	106
Cell pitch (mm)	8.45	14.2	16.7
Dimensions L × W × H (cm)	198 × 50 × 6.0	151 × 157 × 7.2	177 × 185 × 9.0
Total weight (kg)	7	60	80
Maximal vertical sag (mm)	<1	<1	<1
FR4 thickness (mm)	0.25	0.75	0.75
Honeycomb thickness (mm)	24.5	32	38
Copper thickness (μm)	5	16	16
Radiation thickness (% X_0)	1.2	2.38	2.37
Dead area by design (%)	<0.7	7.6	7.6

The scale for the acceptable amount of material in PC1 is set by the Dalitz decay $\pi^0 \rightarrow e^+e^-\gamma$ which has a branching ratio of 1.2%. The goal of the PC1 design was to keep the photon conversion rate comparable to, or below, the Dalitz decay rate. The largest source of conversions would normally be the copper cladding (usually 36 μm thick) on each side of the (FR4 fiberglass) circuit boards. This is unacceptable and in cooperation with the manufacturer [10] the copper cladding was reduced to only 5 μm for the ($0.5 \times 2 \text{ m}^2$) PC1 boards. The amount of glue used in the construction was carefully measured so as to minimize its contribution to the overall radiation budget of the chambers.

The boards with etched pixel pattern also have copper plated feedthrough holes bringing the signals to the opposite face of the board (named spider board due to the spider-like, etched trace pattern). The copper plating process would by standard methods add about 30 μm copper to each face of the board. After refining the plating process by the manufacturer [10], the additional copper deposit was reduced to 1–2 μm , with maintained quality of the electrical connection through the hole.

PC1 is subdivided into 2×8 sectors, each one with a trapezoidal profile in order to follow the arc shape of the Drift Chamber with a minimum of dead areas. Special care was taken in the tolerances of the global dimensions allowing the mounting of the 8 sectors on each of the two central arms with only 1 mm clearance between two adjacent sectors. Fig. 5 shows a vertical cut through a Pad Chamber and Fig. 6 shows an exploded view of the individual parts of PC1.

Each sector is an independent chamber 1974 mm long, 495 mm wide at the middle plane of the trapezoid and 58 mm thick. It is made out of two flat panels, the pixel panel and the cathode panel, and an anode wire electrode between them.

Each panel consists of two 0.25 mm thick FR4 facesheets glued to a 25.4 mm thick honeycomb core. The solid cathode panel has a copper layer on its inner side, which serves as ground electrode. Gas is fed through recesses made in the

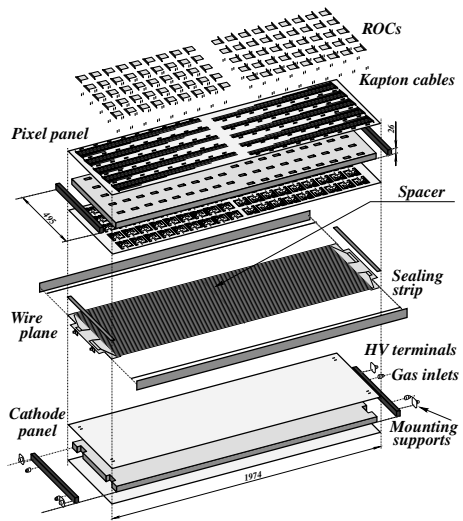


Fig. 6. Exploded view of a PCI chamber.

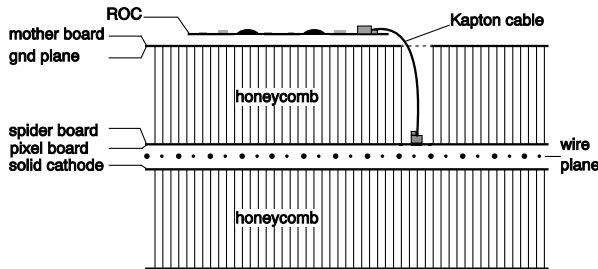


Fig. 5. Vertical cut through a chamber. Copper coated facesheet surfaces are named.

panel heads, the honeycomb and the facesheet to provide flow from one side of the detector to the other.

The two facesheets of the pixel panel are the pixel board and the motherboard. The pixel board is a double sided printed circuit board with the pixel pattern on its inner side (not visible in the sketch) and the signal traces on the other side. Approximately 4500 plated-through holes in each pixel board connect the pads to the traces. The traces are bunched in groups of 24 traces to a total of 180 microconnectors soldered to the ends of the traces. The signals are taken through the panel by flexible Kapton cables plugged into the microconnectors and the readout cards (ROCs) on the motherboard. See Section 5.

The motherboard has 2×5 signal busses on the outer side bringing the signals to and from the ROCs to the front-end electronic module (FEM) connected to the PHENIX DAQ by optical links. The inner side of the motherboard is copper clad to screen the signal traces from the noise coming from the communications in the busses. Several power lines on the motherboard were later reinforced with wires to reduce the resistivity along the 90 cm long traces made of very thin copper.

The anode wires are made of a tungsten–rhenium alloy with gold coating with a diameter of 25 μm . The field wires are gold-coated copper–beryllium of 75 μm diameter. The wire tension is 60 g for the anode wires and 120 g for the field wires, which is less than $\frac{2}{3}$ of their elastic limit. The spacing between the anode wires, the field wires and the anode-to-cathode gap for all chambers are given in Table 1.

The wires are glued and soldered to two terminal boards located at the edges of the chambers. The terminal boards distribute the high voltage through individual RC filters to each anode wire. The wires are grouped into four independent HV sectors limiting the loss to a part of a chamber in case of a broken wire. The wires are also glued on a 1 mm wide spacer bar located in the center of the chamber (“Spacer” in Fig. 6). The height of the bar is equal to half of the gas gap. The spacer holds the wires in position when the chamber sags due to its own weight. The

sagitta of a PC1 chamber, freely supported at the four corners, is about 1 mm. The gravitational sag of the wires themselves is less than 80 μm . Another purpose of the spacer is to avoid possible electrostatic staggering of the wires.

As mentioned above, the PC1 sectors are sealed by gluing. This has the advantage of considerably reducing both the dead area and the amount of material. However the price we pay is that repairing a chamber, once sealed, is practically impossible. The sealing is ensured by gluing two 3 mm thick end beams to the two panels along the short sides. Along the long sides the chamber is sealed with a 6 mm high C-shape strip. In addition, this element plays an important role in holding the two panels together making them as a single mechanical unit. There is an additional 0.2 mm thick protective sealing strip running on both sides of the chamber covering the gap and the sides of the panels. This design gives the chamber sufficient mechanical rigidity while minimizing the thickness of the materials used for the construction. The radiation budget of the chamber, specified in Table 2, does not exceed 1.2% of a radiation length including the electronics. In part, this is achieved by moving the more massive parts of the chamber such as mechanical supports, gas fitting, and high voltage connections to the edges of the detector, outside of the PHENIX acceptance. The total inactive area of PC1 is 0.7% of the whole acceptance of a PHENIX central arm.

The large area to be covered by the PC2 and PC3 layers, requires very large chambers. The outer detector in the spectrometer, EMCAL, is segmented in 22.5° sectors in ϕ compared to 11.25° for PC1. All detector systems outside the RICH (e.g. PC2/3), which is shaped like an arc, follow the sector geometry of EMCAL. These chambers are divided in two separate halves at the median plane of the spectrometer (i.e. at $z = 0$).

For PC2 and PC3, the requirement of minimum mass is less crucial (since they are located after the RICH detector which provides the main electron identification). The chambers are also four times larger in area (about $2 \times 2 \text{ m}^2$ for PC3). Thicker honeycomb sheets (32 mm for PC2 and 38 mm in PC3) in the panels provide enough mechanical rigidity to these large chambers. Also the

Table 2
PC1 radiation budget

PC1 element	Material	X_0	Thickness	Area (%)	Rad. length (%)
Traces	Copper	1.43 cm	5 μm	~40	0.014
Facesheet $\times 4$	FR4	17.1 cm	0.25 mm $\times 4$	100	0.580
Screen	Copper	1.43 cm	5 μm	100	0.035
Glue joint $\times 4$	Epoxy	25 cm	~50 μm $\times 4$	100	0.080
Panel core $\times 2$	Honeycomb	81.7 m	25.4 mm $\times 2$	100	0.060
Traces	Copper	1.43 cm	5 μm	~10	0.005
Pads	Copper	1.43 cm	5 μm	~90	0.030
Wires	W/Au Cu/Be	0.35, 1.4 cm	25, 75 μm	0.3, 0.8	0.005
Gas	Air Ar/ethane	304, 165 m	2 \times 25.6 mm	100	0.020
Cathode	Copper	1.43 cm	5 μm	100	0.035
Hole sealing	Epoxy	25 cm	~10 μm	100	0.005
Gap sealing	FR4	17.1 cm	6 mm	0.4	0.015
Sealing strip	FR4	17.1 cm	56 mm	0.08	0.025
Edge finish	Epoxy	25 cm	~40 μm	100	0.015
Solder joint	Pb/Sn/Flux	~1 cm	0.2 mm	1.4	0.028
Connectors	Nylon/brass	20 cm	~2 mm	—	0.080
Kapton cables	Kapton + copper	17 cm	Undefined	—	0.020
ROCs	Polyimide + comp.	18 cm	Undefined	30	0.110
Total			65 mm		1.16

FR4-fiberglass face sheets (760 μm) and the copper cladding (16 μm) were thicker compared to PC1. Most of the mechanical strength relies on honeycomb sandwich structures as for PC1. A thin frame construction housing an O-ring provides the gas seal.

PC2 is very similar to PC3 in design. The linear dimensions are however scaled down by approximately 0.85 due to the closer radial position of PC2. Of the two, PC3 was the most challenging to build due to the large size. Circuit boards of this size were too large to manufacture in one piece. However, a $1 \times 2 \text{ m}^2$ board area was feasible and a square profile S2-glass tube with the same thickness as the honeycomb was used as a joint piece (along z) when gluing two circuit boards together to form the full plane. The etched pad pattern, was cut at the seam in the same way as at the chamber edges. The seam does not introduce any dead areas. In terms of data readout, PC2 and PC3 are segmented identically to PC1 and the same readout architecture and software treatment can be used all over the Pad Chamber system.

The board size needed for PC3-chambers proved to be at the limit of what was possible. Even after optimization of line spacing, line width

and hole diameter, the manufacturing did not reach a quite predictable state and a careful testing and inspection was needed, followed by some repair by hand. The slightly smaller boards for PC2 had considerably fewer errors.

Around the edge of the honeycomb sandwich, a solid frame was glued. In the fiducial volume of the spectrometer it is as thin as possible. Bolts through the frames hold the pixel- and cathode panels together, pressing the panels against the O-ring seal. The edges of the chamber are cut at a right angle to the plane of the detector. The dead area imposed by the frames is 7.6% and coincides to a large extent with the sector edges of neighboring detector systems. Localized, thick material, like the frames, have proven by simulations to be acceptable at the radial positions of PC2 and PC3.

A thin wire support is placed along the pixel surface at the centerline of the chamber. Close to the center point of the chamber, the distance between the two panels is fixed by a small spacer and a nylon screw, preventing bulging due to the slight overpressure in the chamber.

The material thickness of PC2/3 is less critical than for PC1. The radiation thickness compares to the PC1 values as in Table 2 as follows: The

contribution from copper is a factor 3.2 larger than on PC1 and a factor 3 larger from the FR4 facesheets. All other materials covering 100% of the area have about the same radiation thickness as on PC1. Materials with less than 100% coverage have a factor 2 to 4 lower radiation thickness than on PC1. This comparison applies to the sensitive parts of the detector. The frames, placed in insensitive parts have a considerable local thickness.

4.2. Pixel board test

A critical and challenging step before starting the construction of the chambers is the testing of the pixel boards. Once glued together with the honeycomb, repairs are practically impossible. The pixel electrode and signal transport to the ROCs form a complex structure: on the wire side it consists of 36 888 pixels connected into groups of nine pixels by narrow 150 μm wide copper traces (and similar minimum line spacing) forming 4320 pads. These connect to traces on the other side of the board by plated-through holes. These traces bring the signals to 180 microconnectors, one for each group of 24 pads. Flexible Kapton cables 36 mm long (41 mm on PC2 and 49 mm on PC3) transport the signals to microconnectors on the ROCs.

A trace pitch of this order is a challenge even on small boards and here it has to be etched, with uniform quality, on a $0.5 \times 2 \text{ m}^2$ board. The twice as large boards for PC2/3 have only slightly larger minimum trace pitch and the need for board tests was as large as for PC1. The whole assembly of pixel board, microconnectors and Kapton cables must be checked for electrical conductivity from the pixel to the end of the Kapton cable and for shorts between neighboring traces. Standard tools are inadequate for this task. A reliable, efficient and fast test method was developed, together with the necessary tooling (including mechanics and a dedicated electronic unit) to test the pixel structure.

The tests consisted of: (i) ohmic connection, i.e. check electrical continuity from the pixels up to the end of the Kapton cable and (ii) ohmic insulation, i.e. find all possible shorts between

neighboring channels. The work with a prototype chamber allowed us to identify the main error types in the pixel boards and to develop methods to repair them. Based on that experience, a three step test procedure was worked out.

The first test searched for connections between neighboring pads due to mistakes in the board production. It used a small test device consisting of an insulator board on which a number of spring-loaded test pins are mounted in a specific two dimensional pattern fitting the pixel geometry. A part of a pixel board together with the pin pattern is shown in Fig. 7. The spring loaded test pins (INGUN GKS-422-0123) with round heads made a reliable contact without destroying the fragile 5 μm copper layer of the pads.

The pins were set at different voltages in the range of 1–5 V. A simple electronic circuit checked the contact between pins. In order to scan the board quickly and efficiently, the contact pins and the electronic unit are attached to an x – y positioning system.

The pad in black in Fig. 7, could potentially have been shorted to any of its six neighbors shown in grey in the panel “Step 0”. During the test, the pattern of pins was moved through the pad structure in steps, each step corresponding to a pad column. In “Step 1” only one pin touched the black pad, and the hatched pads were tested against shorts to the black pad. By moving the pin pattern further, all neighboring pads (“Steps 2 and 3”) were checked.

The microconnectors were then soldered and the Kapton cables were inserted. As the second test, the soldering and cables were checked for shorts between neighboring leads. Legs corresponding to neighboring electrical lines are on opposite sides of the connector. Thus, every second trace could be contacted by shorting all the traces on one side of the microconnector with a conductive rubber. Using a probe pin, connected to a beeper every other lead in the connector and cable was then checked for shorts to its neighbors.

The final test controlled the continuity of the whole chain. The pixel board was placed with pixel side up, and the open end of all Kapton cables were shorted to ground on the opposite side of the board. A pattern of pins connect to the outmost

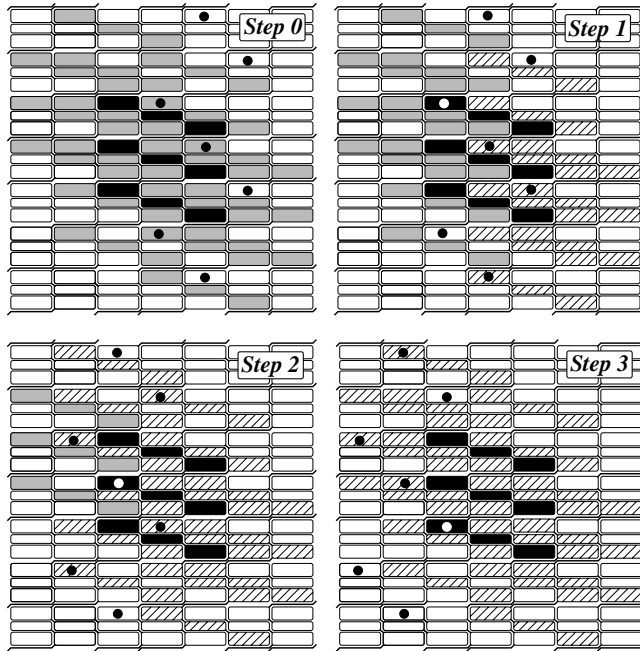


Fig. 7. The pad structure together with the pattern of test pin positions (circles) used in the first test. An arbitrary chosen pad is shown in black with its six neighbors in grey (Step 0). The pins are moved from right to left in steps of one column. Neighboring pads checked in each step (1–3) are hatched.

pixel in each pad in a way similar to what was done in the first test and the connection to the grounded far end of the Kapton cable was verified.

4.3. Chamber construction

The first step in the chamber production was the soldering of the microconnectors. A procedure based on surface mount techniques was developed which allowed very high soldering quality, minimum amount of soldering material as well as speeding up the soldering process. The solder paste was applied at the soldering places through a 0.2 mm thick stainless steel mask. The connectors were then installed in place and the joints were heated with hot air.

After soldering the microconnectors, the pixel board was tested using the procedure described above and repaired if needed. The sandwiches consisting of the honeycomb between two fiberglass boards were then glued together. The circuit board material, used in the construction, is one-sided copper-clad FR-4 fiberglass boards for the solid cathode and double-sided copper-clad board for the pixel board and motherboard, whereas the fourth board has no copper cladding. Gluing was done on a flat granite table using a vacuum bag pressing the pieces together. Special care was taken to minimize the amount of epoxy used for the gluing of the large surfaces. An average epoxy layer thickness of approximately 50 μm was used, controlled by weighing the amount of glue prepared before and remaining after the operation.

Each one of the ~ 4500 plated-through holes in the pixel board must be filled by epoxy for gas tightness. Every PC1 panel was checked for its deformation due to gravity and due to intrinsic tensions in the structure of the panels. Cathode and pixel panels with similar intrinsic deformations were selected in pairs in order to allow the deformations to compensate each other.

Before the assembly of the anode wire plane, the terminal boards were equipped with the electronics components and tested for HV. Terminal boards and wire support were glued to the pixel panels. The PC1 wire planes with the two types of wires were prepared on a winding machine in advance and moved to the detector using transfer frames. The wires, aligned to the pixel pattern using optical systems, were glued to the terminal boards and then soldered. A simplifying construction feature of the pixel readout system is its moderate demand on alignment between the wires and the etched pixel pattern. The measured alignment between wires and pixels is always better than $100\ \mu\text{m}$, well within the requirements.

Before the permanent glue sealing of PC1, a preliminary test was performed to verify the chamber functionality. The chamber was closed in a gas box filled with P10. After demonstrating clear anode signals from cosmic rays in all four HV-sectors, the chamber was permanently sealed. After sealing, deformation and gas leak rates were measured. The total leak rate of all 16 PC1 chambers was less than 1 ml per min. The chamber, suspended at the four corners showed typically less than 1 mm sag due to its own weight. Intrinsic deformations were substantially smaller than that. Tests showed that even a 3 mm deformation does not significantly affect the chamber performance due to the robustness of the pixel readout concept.

In order to build a pixel panel for PC2/3, two pixel boards with microconnectors were placed face down on a tooling plate. The two pixel boards were joined by gluing to the S2-glass frame and the S2 joint tube. The honeycomb was glued to the back of the pixel boards (inside the frames). Finally the motherboard was added. The entire panel was placed under vacuum until the epoxy had cured. The plain panels were constructed

similarly, except that there were no Kapton cables and the plain copper surface was placed next to the flat surface.

On the PC2/3 pixel panel the wire terminal boards were glued to the pixel panel and the wires were strung onto the panel, placed on a rotating winding table. The wires were fixed by epoxy at both ends before cutting them to allow the wound panel to be removed from the winding table. After soldering the wires to the traces on the terminal boards, S2 bars, housing the O-ring were glued around the edge of the gas volume. As the final assembly step, the plain panel was bolted together with the pixel panel and the chamber could be tested for gas tightness and HV performance. Typically, leak rates of a few ml per minute were obtained for PC2/3.

Finally the connector cards (cf. Section 5) were soldered on the motherboards (~ 2500 contacts per chamber) using the same surface mount technique which was developed for soldering the microconnectors. Other details permanently mounted on the motherboard are pin headers for the flat cable connections from the motherboard and termination resistors at the far end of the communication busses.

When the ROCs had been connected to the connector card and the Kapton cables, the chamber was ready for the cosmic test which was the final stage before mounting the chambers on the spectrometer carriage. Typical results of the cosmic tests are reported in Section 6.

4.4. PC1 chamber mounting

The PC1 chambers were mounted directly onto the back of the DC (Fig. 8). No mounting material is placed in the active region. Mounting brackets with a cylindrical rod extend out from each of the four corners of a chamber. These rods attach to four couplers which stand off the outer radius of the DC. The couplers allow position adjustments in all directions. Survey marks on each PC1 chamber allow the chambers positions to be determined relative to survey targets on the DC. This is crucial because there is no point on PC1 that can be viewed once it is installed and all

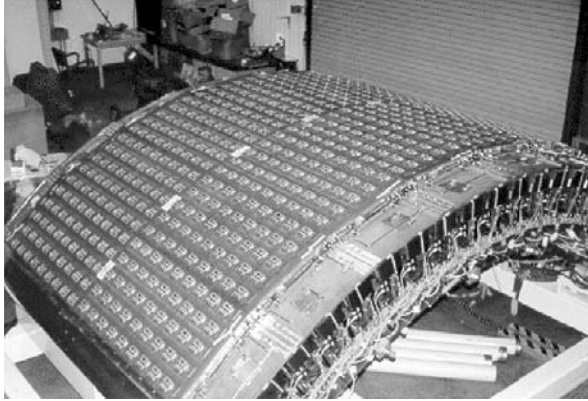


Fig. 8. PC1 chambers mounted on a drift chamber.

position information must be related to secondary targets.

DC and PC1 can be separated electrically from each other, but experience showed that the best common performance was achieved if the DC (being most sensitive) and PC1 were grounded together. The PC1 chambers have the ROCs on the outer surface, away from the DC due to safety and noise considerations. A flame-proof vinyl window protects the RICH in case of a component failure causing overheating on a ROC.

4.5. PC2/3 chamber mounting

Two PC3 (or PC2) chambers were mounted together to form a 22.5° sector, separated at the $z = 0$ plane. The two chambers were held together with an H-frame construction using an aluminum I-beam. The H-frame does not extend into the active area of the chambers as it covers only the chamber frames. The H-frame serves like a pair of rails, allowing the PC2/3 chambers to be slid into the frame. The H-frame is held together at $z = 0$ by a pair of stainless steel threaded rods which keep the two rails from separating in the center. At the outer edge, the H-frame is bolted directly to the PC3 chamber. This gives the H-frame rigidity.

The entire package of two PC3 chambers in their H-frame were mounted on the outer surface of a TEC sector. The H-frame is bolted to the TEC at each of the four corners, and at the middle of the two rails. This keeps the inner surface of the PC3 chambers spaced a uniform 2.5 mm away from the TEC frame. The PC3 chambers also serve to keep the thin TEC window from ballooning out because the window is pressed up against the PC3 panel by the slight gas overpressure in the TEC.

PC3 is mounted with the ROCs facing away from the TEC for safety and noise reasons. The TEC and PC3 can be operated isolated from each other but the best common noise performance has been achieved by grounding them together. The EMCal situated next to the ROCs has been shown to be insensitive to possible digital noise from PC3.

In the west arm, both PC2 and PC3 are present but there is no TEC, an aluminum box construction constitutes a mockup for the TEC and provides a structure for PC mounting.

Like PC1, there are survey marks on the PC3 chambers which allow the PC3 positions to be determined relative to survey marks on the TEC. No survey of the PC3 chambers is possible after it has been installed on the east arm.

5. The readout electronics

A unique property of the electronics for the Pad Chamber system is that a substantial part of it is mounted on the chamber planes in the path of the particles. A minimal amount of material in the electronics circuits was therefore a major design goal. Since it was to be built in several hundred thousand channels, it was necessary to incorporate all functions in two new Application Specific Integrated Circuits (ASICs) named TGLD and DMU. These are mounted on ultra thin readout cards (ROCs), the part of the front end electronics mounted in the fiducial volume.

On the detector, but outside the fiducial volume, the FEM circuit (Front End Module) handles the communication and power distribution to the ROCs, collects the data from the ROCs and formats the data for transport off the detector. Global timing synchronization is provided by the Timing and Control system (T&C) as well as trigger requests and other fast instructions which may change from one cycle to another. Together, the ROCs and the FEM constitute the Front End Electronics (FEE). The FEM communicates via

fiber optics with the data collection module (DCM) and the T&C-system in the counting house. Programmable configuration control of the FEM and the TGLD chip is provided by a slow control line using the ARCNet protocol. The block scheme in Fig. 9 illustrates the architecture of the readout system. In this section we describe the function of the readout electronics and its performance.

5.1. The charge sensitive amplifier/discriminator chip, TGLD

An electronics channel for the Pad Chamber detector compares the amplified input signal with a threshold. The block diagram in Fig. 10 illustrates the main components in one channel of the amplifier/discriminator chip [11]. Each channel consists of a charge sensitive preamplifier (CSA), a voltage amplifier, a test pulse generator, a CR differentiator, a leading edge (LE) threshold discriminator, a one-shot generator and a voltage to current output stage. The design sensitivity of the readout system was determined by the requirements imposed by PC1 which has the

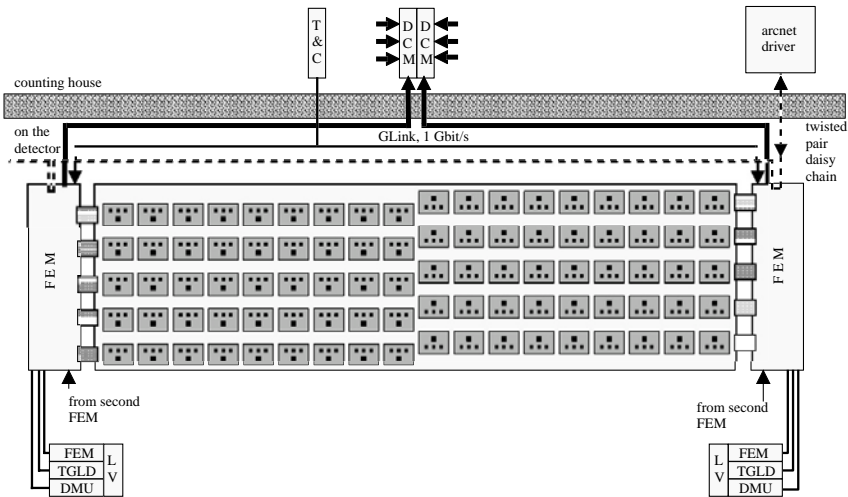


Fig. 9. Full system architecture, handling 4320 channels on a PC1 chamber.

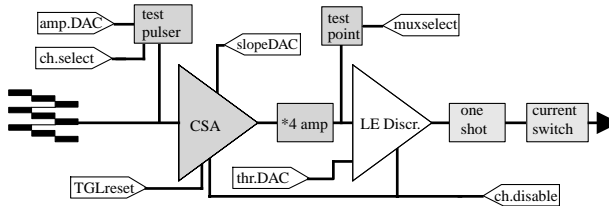


Fig. 10. Block scheme of a single channel.

thinnest gas gap. The most probable signal on a pad is 18 fC corresponding to the most probable anode charge at the nominal gain setting (50 000). In order to obtain full plateau efficiency one should be able to set the threshold at 10% of the most probable charge, i.e. about 2 fC.

The CSA has a charge to voltage conversion gain of 2.5 mV/fC and an adjustable time for return to baseline. For reliable restoring of the baseline after saturation, the preamplifier needs to be reset on a 100 Hz basis. A voltage amplifier provides further amplification by a factor 4 resulting in an overall sensitivity of the amplifier stage of 10 mV/fC. The AC coupled, input signal to the discriminator can be attenuated by a factor 3 or a factor 9 for a larger dynamic range. For normal operation, the setting with no attenuation is used, giving a threshold interval of 1.5 to 10 fC with ± 0.25 fC maximum channel to channel variation. The one-shot ensures that the current output is always a 75 μ A, 150 ns wide pulse. A reference output current of 25 μ A (common to all 16 channels in a chip) defines the on/off switching level for safe interpretation of the signal levels by the receiver stage of the DMU. Current mode is preferred to voltage mode for these digital signals as it gives robustness against crosstalk and common-mode pickup noise.

The simulated value of the preamplifier noise corresponds to 590 electrons at 0 pF input capacitance with an additional 32 electrons per picofarad of pad input capacitance (23 pF for PC1, 36 pF for PC2, 43 pF for PC3). This noise is a factor 5 lower than the minimum settable discriminator threshold. Oscilloscope studies have qualitatively verified these noise values by obser-

ving the test point after the voltage amplifier, where the analog signal of a selected channel can be connected to an output pin by an analog multiplexer. The test pulse generator can inject a selectable test charge (0–127 fC) at the preamplifier input.

Each chip has 16 parallel channels. The discriminators have a common threshold. Careful control of low voltage distribution and decoupling among the three main stages was needed to avoid crosstalk between channels at the lowest thresholds. Many functional characteristics can be controlled remotely, through a serial communication where each TGLD has its own 5-bit address. The most important programmable features are the on-chip digital to analog converters by which thresholds and test pulse amplitudes are set. Individual channels can be disabled as well as selected for test pulsing. Downloaded serial control information can be read back for consistency check.

The preamplifier reset is in itself a source of noise, internally in the chip as well as over the full system, due to induced charge from the reset switching. The internal reset sequence was carefully timed, in order to minimize these effects and in addition, the discriminator function was gated off, thus avoiding simultaneous firing of all discriminator channels in the system in conjunction with the reset.

No special attention needs to be paid to radiation hardness. This CMOS chip, designed for the 1.2 μ m CMOS process at Orbit semiconductor (now Supertex), has an area of 3.7 \times 3.7 mm². The power consumption is in total about 50 mW, i.e. about 3 mW per channel.

5.2. The digital memory and derandomizer unit, DMU

The main functions of the digital memory unit, DMU (Fig. 11), are:

- To sample the discriminator output signals from three TGLD chips (48 channels) for each clock pulse (RHIC beam crossing).
- To store all data until the first level trigger arrives.
- In case the first level trigger arrives, to provide storage of the corresponding event until readout is completed.
- To provide storage of at most five events, to accommodate the random occurrence of events.

Filling of data into the DMU is driven by the clock while emptying of events is controlled by the readiness of the readout chain. The clock frequency, equal to the beam crossing frequency of RHIC, is 9.38 MHz (the circuit is operational up to 40 MHz).

The communication between TGLD and DMU is specially designed to minimize the noise

generated by this digital activity. When a TGLD output is in a TRUE state (channel fired), it delivers a 75 μ A current (equivalent DC current). This is sensed as TRUE by the input circuit of the DMU if the current is larger than a reference current (25 μ A) also provided by the TGLD chip. By this automatic signal normalization we obtain transfer reliability, in spite of the extremely low signal levels.

The delay memory stores data for each beam crossing until a possible receipt of a first level trigger. The memory is 48 bits wide (one for each channel) and the depth address (i.e. what beam crossing the data belongs to) is determined by the beam clock counter. The memory is a dual arrangement where writing and reading is performed in an alternating sequence between the two. Reading and writing can be done in the same cycle, however in opposite banks. The total depth until data is overwritten is 44 clock cycles, determined by the time it takes to produce the first level trigger in PHENIX. The depth is selectable up to the hardware limit (64) by a

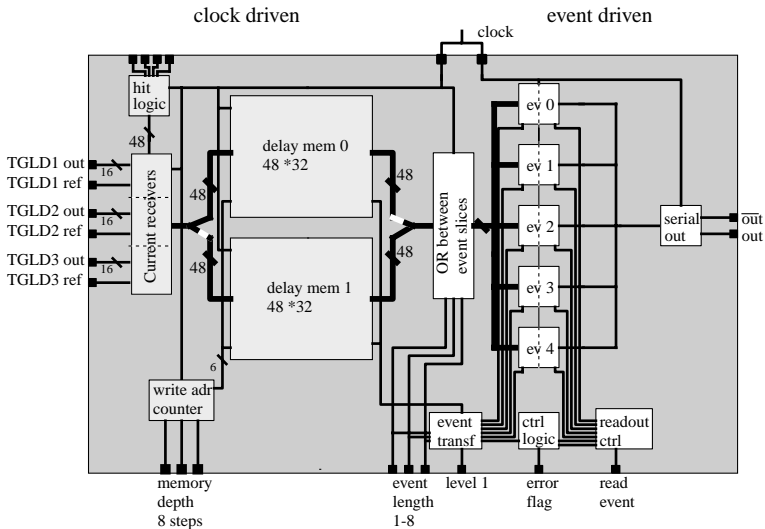


Fig. 11. Block scheme of the DMU chip.

three-bit binary code, strapped via external pins at the time of ROC assembly.

If a trigger arrives, the data fed into the DMU 44 clock ticks earlier is moved from the delay memory to one of five event memories. Data belonging to the same collision can be spread out in time by several hundred nanoseconds due to: flight time of the particles, drift time in the wire chambers and timing walk in the leading edge discriminator. Collecting the data in four time slices (the number of slices is selectable by strapping) is sufficient to catch all data belonging to an event. It is not worthwhile to keep the information which of the four time slices the bit belongs to. Thus a bitwise OR is made between the four slices before data is stored in the event memory.

Upon receipt of a READ.EVENT signal, data is read from the event memory. Data is sent serially as complementary CMOS signals thus allowing reliable transfer over the long distances to the FEM (2 m on PC3). The address of the event memory, accounts for the first three bits, followed by the 48 data bits and a trailing parity bit as a final check of the data transfer.

The DMU chip was designed¹² for the 1 μ m CMOS process at AMS (Austria Mikro Systeme Int.).

5.3. The readout card and the connector card

The large number of channels per unit area, a major merit of this detector, made it necessary to mount the part of the electronics where all channels are treated in parallel i.e. up to the DMU output, on the backplane of the wire chamber. A problem to solve in this context was to reduce the amount of material in the electronics in order to minimize the effects of secondary interactions by particles passing through. A potential difficulty would also be the presence of digital signals close to the highly sensitive charge inputs. On the other hand, a short distance from pad to preamplifier is an advantage from a noise point of view.

¹²The DMU chip was developed by SiCon AB, Linköping, Sweden.

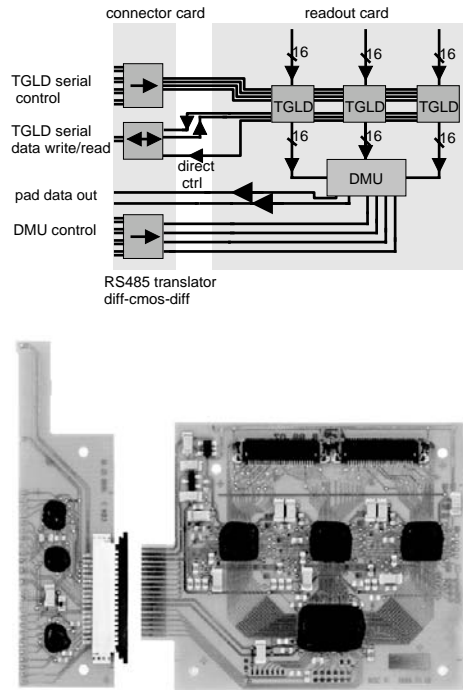


Fig. 12. Block scheme of the connector and readout cards and a photograph showing how they look in reality. The ROC area is 20 cm².

Fig. 12 shows the block diagram of the circuits on the readout card (ROC) and the connector card. A ROC receives the input signals from 48 pads via two flexible Kapton cables and distributes them to the three TGLD chips. The discriminator results are transferred in parallel and stored in the DMU.

The chips on the connector card translate the differential control signals bussed through a row of nine ROCs to a single ended CMOS signal standard. The well defined functions on the connector card are obtained by commercially available chips. It was convenient, both from development and manufacturing point of view to separate this part of the design from the more critical, custom made chips placed on the ROC.

The TGLD and DMU chips on the readout card and the translator chips on the connector card are mounted with the chip-on-board technique on fiberglass reinforced polyimide circuit boards of 100 μm thickness¹³. In this assembly technique, the naked silicon dice are glued to the circuit board and the electrical connections are done by ultrasonic wire bonding from the connector pad on the silicon, directly to the circuit board. Besides the minimal amount of material, this technique has advantages of low cost and excellent signal performance due to the extremely short connections. Passive components are surface mounted with conductive epoxy. After functional test, the chips are covered by a glob of hard epoxy, which protects the chip and the bondwires mechanically and stiffens the flexible card in the bonding area. The black epoxy also protects the chip from ambient light. An option, to cover the glob by conductive (grounded) paint for RF-shielding, proved to be unnecessary.

The connector card was soldered onto traces on the motherboard, which is the outer fiberglass board of the cathode sandwich. The ROC can easily be dismantled since it plugs into a 1 mm pitch Flexible Printed Circuit (FPC) connector on the connector card. The Kapton cables from the pads connect to FPC connectors (0.5 mm pitch) on the ROC.

Together, the connector card and the ROC (including the Kapton cables and connectors for pad connection) weigh 4.8 g. On PC1, where the density of ROCs is one per 100 cm^2 , this amounts to 0.2% of a radiation length when averaged out over the detector surface. On PC3 the corresponding value is 0.05% due to the factor 4 lower ROC density.

5.4. The motherboard and the system noise

The upper fiberglass board of the cathode panel is also the electronics motherboard where all signals and DC-voltages are distributed from the FEM at the side of the detector to the ROCs and output data is sent from the ROCs to the FEM.

The opposite side of the motherboard is a continuous ground plane, to which the analog ground of each ROC is tied locally. This ground plane provides an efficient shielding of the noise sensitive pads from the continuous digital activity on the motherboard traces and in the DMU. In order to reduce the noise generated by digital signals on the motherboard, these are distributed as differential RS485 standard, with which we achieve reliable communication over long distances (about 2 m on PC3), even using as low signal amplitudes as 0.7 V. As a compromise with timing accuracy, amplitudes of 1.4 V are used.

The DC-supply to the analog and digital chips on the ROCs suffer from the long distances and thin copper on the motherboard, although these traces were made extra wide. Thus the ROCs are equipped with low dropout voltage regulators for the TGLD power while the DMU is tolerant enough to accept the variation in supply voltage over the length of the trace.

During regular data taking the thresholds are set at 5.4 fC for PC1 and 7.2 fC for PC2/3. With these thresholds, no channel ever fired either on random noise or on pickup noise from the digital activity. The lowest common threshold for the whole system that was usable, with totally noise free operation, was 2.5 fC for PC1 and slightly higher on PC2/3.

5.5. The FEM and the data transfer to the DCM

The Front End Module (FEM) [12] is placed at the side of the detector and connects to the motherboard via short flat ribbon cables, one for each ROC row. Each FEM handles the control and data collection from five rows of nine ROCs each (Figs. 9, 13), i.e. 2160 channels. On PC1 there is one FEM card at each end of the chamber, while PC2 and PC3 have two FEMs on the same side of each chamber.

The FEM card has a programmable readout and control module (called the heap manager), implemented in a Xilinx 4020 field-programmable gate array (FPGA). This provides control signals to the ROCs, collects and transmits data, and manages the command interface (timing and control). A second FPGA of the same type

¹³The chip on board assembly on thin flexible boards was developed by XICON AB, Malmö, Sweden.

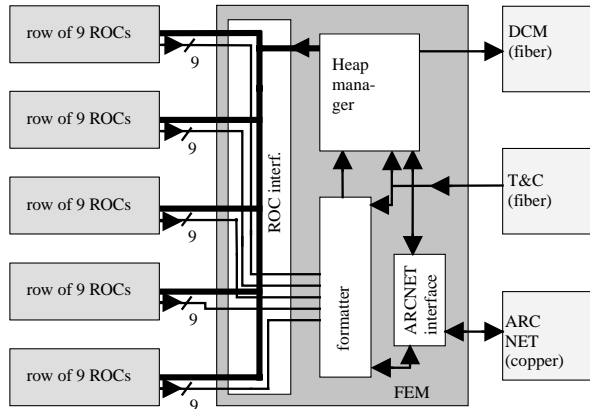


Fig. 13. Block scheme of the Front End Module (FEM) card.

controls the serial data readout from each DMU and serial-to-parallel data conversion. Additionally, an embedded controller is included for transmission of slow serial data and control information to the FEM and the ROCs via ARCNet protocol. Fig. 13 shows the generalized architecture and the data flow path associated with the FEM and its interfaces.

The signal interface to an individual ROC row includes separate voltage regulators for TGLD power, DMU power and RS485 chip power (signals to DMU only). All signals from the FEM to a ROC row are sent by RS485 transmitter chips. Receiving of data from ROCs is done by RS485 receiver chips on the FEM.

Each FEM receives system clocks and mode control signals directly from PHENIX Timing and Control (T&C) via a GLink fiber at 37.5 MHz, i.e. four times the beam clock frequency. Serial data from each DMU is clocked out to the FEM, all 45 in parallel. Data is converted into 20-bit words by the data formatter for transmission by the heap manager over the GLink fiber. The data format reflects the pad location such that a 20-bit word contains the result from 20 pads across five ROC rows on the chamber. Twelve such words contain the data from five ROCs, one from each row. A full event produces 108 (9×12) such 20-bit words

per FEM, and this data block is a direct image of the pattern of hit pads on the chamber with the bit position in a word being the location across the wires (ϕ) while the word number is the position along the wires (z -direction). This format is useful for later data handling and analysis speed.

The ARCNet interface provides slow serial communication to the front end electronics from the high level control of PHENIX. Its functions include programming of the FPGAs after a cold start or hard system reset, loading of the ROC/TGLD control bits (channel enables, threshold settings, calibration enables, multiplexer controls), resetting the GLink interfaces, and controlling the heap manager self-test function. Readback capability exists at every level allowing readback of FPGA 'done' condition, GLink synchronization status, and complete readback of heap manager and ROC/TGLD programmable parameters.

The FEM also includes a built in self-test (BIST) function which produces a set of known packets. Use of BIST mode helps certify FEM operation independently of the ROCs' status.

The data collection module (DCM) receives the data through the 1 Gbit/s GLink. Together with the data words, a few words at the beginning are reserved for event header, event number, clock counter, FEM address etc. At the end of the buffer

additional words like parity check of the FEM-DCM communication are found. The 20-bit result words are restored in the DCM and here zero suppression can be done. A simple zero suppression, just skipping 20-bit words which are zero, gives an average reduction to four 20-bit words per particle hit. The DCMs are read out to the event builder, together with DCMs for other Pad Chamber FEMs and other PHENIX detectors, where the data is assembled into full events which are sent to archiving and software analysis.

5.6. FEM mounting and cabling

The FEM cards are housed in aluminum boxes which are fixed to the chambers. The boxes provide electrical shielding and an additional safety barrier against overheated components. Five short, 50 conductor ribbon cables bring the ROC signals out from the motherboard to each FEM where they enter the aluminum FEM housing through narrow slits.

Optical fibers are used to bring timing signals to the FEMs and data from the FEMs. The FEMs are read out in duplex mode, with one FEM passing its data along to the other FEM which communicates with the DCM. Each FEM requires a timing signal brought in on a fiber, while a readout fiber is only needed on the first FEM of a pair. Data transfer from the second to the first FEM goes via a pair of RG174 coaxial cables, using the GLink protocol at 800 Mbits/s.

In addition each FEM only requires one low voltage cable (with 3 pairs of power and ground in each) and the daisy chained twisted pair ARCNet cable.

6. Performance of the Pad Chambers

Each fully instrumented Pad Chamber was tested with cosmic rays before installation. The purpose of the test was to verify the gas gain at running conditions i.e. an argon–ethane 1:1 mixture at atmospheric pressure. By sensing the produced charge at the wire, the signal connection from each pixel to the input of the preamplifier was reconfirmed. The operation of the electronics

alone was also tested by the internal test pulse in the TGLD chip and the self test of the FEM.

One chamber each of PC1, PC2 and PC3 was extensively tested with cosmics for efficiency calibration and determination of the position resolution (only PC1 and PC2). Fig. 14 shows the setup used for the cosmic measurements. Two large area plastic scintillator planes (SL1, SL2) of approximately the size of a PC1 chamber, were placed above and below the chamber under study. The chamber was placed on a thick granite table, acting as an absorber of low energy particles. Each scintillator plane consisted of five scintillator bars, read out at both ends by photomultiplier tubes. A triggering particle required coincidence between the two photomultipliers of a scintillator bar. A

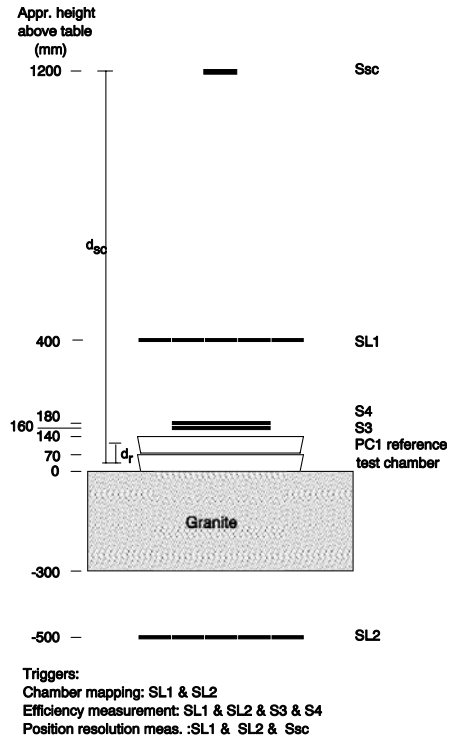


Fig. 14. The cosmic trigger arrangement.

coincidence between a hit scintillator bar in each layer constituted a cosmic trigger with about 1% random coincidence rate.

For the efficiency measurements, an additional scintillator (S3) of size $33 \times 58 \text{ cm}^2$, was placed right on top of the chamber under study, thus defining a large area but still well within the sensitive area of the chamber. Cherenkov light, produced in the lightguide between the scintillator and the photomultiplier, produced triggers outside the well defined area and thus a fourth scintillator (S4, identical to S3) was placed right on top of the third scintillator but oriented with the lightguide in the opposite direction, thus avoiding hits in the lightguides to trigger the system. This four-fold coincidence provided a cosmic trigger with negligible random rate. It was used in all measurements described below, except for the studies of the position resolution.

6.1. The charge gain on the anode wires

The anode wires of the Pad Chambers had no wire readout installed, but for a few wires of each chamber type, the wire signal was extracted over a capacitor to an ORTEC 142B preamplifier followed by a spectroscopy amplifier system. The pulse height distribution was recorded on a LeCroy QVT multichannel analyzer, and the peak of the pulse height distribution (representing the most probable energy loss by a minimum ionizing particle) was determined. Fig. 15 summarizes the anode charge measurements for different high voltage settings for the three chamber types. The measured charge, relies on the absolute calibration of the spectroscopy amplifier readout chain. The absolute uncertainties due to the calibration and due to the determination of the peak position of the Landau distribution, add up to $\pm 25\%$.

The charge gain was determined by dividing the charge corresponding to the peak with the most probable initial ionization by a minimum ionizing particle. This was calculated to be 95 electrons per cm for this gas mixture using tabulated values for the average energy needed to liberate an electron ion pair in argon and ethane. The average for the two gases is 26.4 eV. The energy loss for the gas mixture was weighted by the elemental composi-

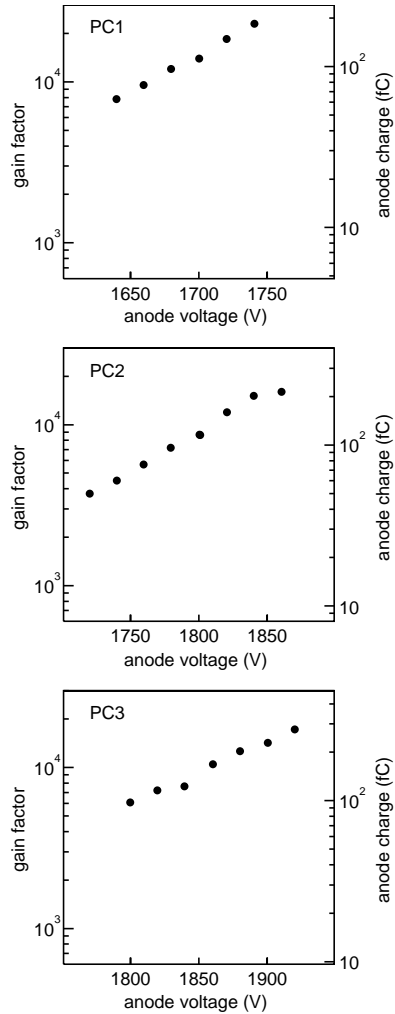


Fig. 15. Gain curves for PC1/2/3.

tion of the gas [13]. This calculation reveals the average number of initial electrons. Since the quantity measured is the most probable (peak position) charge, the value was modified to the most probable value of the Landau distribution.

The HV-ranges used are safely below the onset of sparking and all chambers built are operational at gains up to at least 50 000.

6.2. Efficiency measurements

The chamber efficiency was studied as a function of high voltage and threshold setting. The cosmic trigger in the four-fold coincidence mode was used. The area defined by the trigger involves fifteen ROCs on PC1 and eight on PC3. The area selected for the studies was typical for the performance in those parts of the detector which were unaffected by the central wire support. The charge gain was recorded for each efficiency measurement for gain normalization.

In addition to the efficiency, these measurements reveal the cluster size distribution, i.e. the number of pads and cells fired for each detected particle. On the level of 5%, a trigger particle is accompanied by another particle hitting the chamber. This second particle must coincide with the trigger particle in a window of about 400 ns in order to be

detected in the chamber. Its origin is therefore most probably the same cosmic air shower as the trigger particle. Such events were omitted from the analysis if the two hits were easily distinguishable. Only if the distance between the two hits was less than 3 cm was there a risk not to be able to recognize them as two. Less than 0.1% of the events are estimated to be unresolved double hits.

Fig. 16 shows the number of pads for which the discriminator has fired, at different high voltage settings on the anode wires. The threshold setting for all studies except when the threshold is the varying parameter corresponds to 5.4 fC collected charge on the cathode pad for PC1 and 7.2 fC for PC2/3. These thresholds are the same as those used during real data taking and it never happens that a channel fired due to electronics or pickup noise. We show only the result for PC1 but very similar results were obtained for PC2/3 at corresponding high voltage settings.

When the chamber gain is too low (HV below 1700 V) a fraction of the events have no pads fired. At 1680 V, it never happens that only one pad

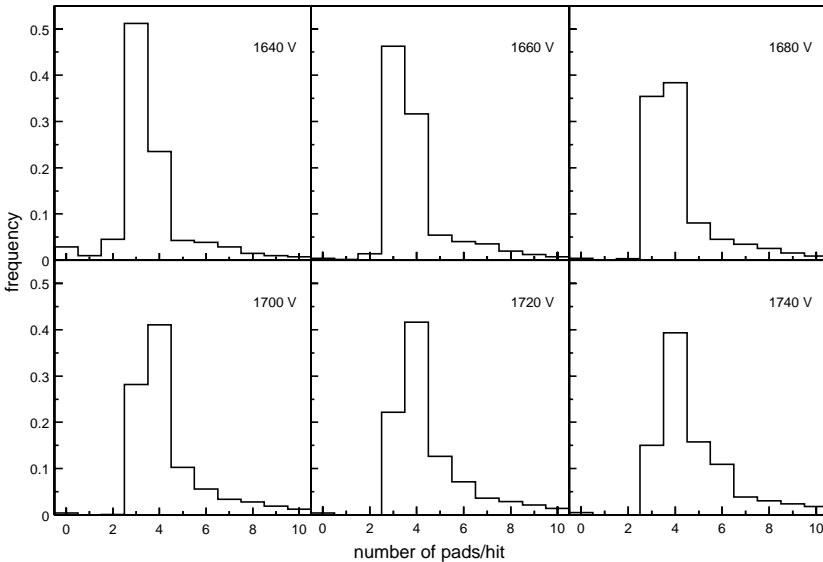


Fig. 16. Pad multiplicity distributions for PC1.

fired while it does happen that only two pads fire when the voltage is too low. At 1700 V and higher, the fraction of two pad events is also negligible. The fraction of completely empty events levels out at the higher voltages, indicating that a plateau efficiency has been reached. This small fraction (less than 0.5%) is interpreted as a real inefficiency as it cannot be reduced by further gain increase.

For Fig. 17 the results have been transformed from pad space to cell space, i.e. all cells for which the three neighboring pads have fired have been labelled as fired cells. The number of fired cells per hit is displayed. The fraction of events with no cell fired is exactly the sum of no-pad and two-pad events in Fig. 16. Our basic criterion of a detected particle is that at least one cell must have fired. At 1700 V and higher the fraction of events with no reconstructed cell is very small and basically constant. It is also noticeable that the fraction of one cell clusters compared to two-cell clusters depends sensitively on the high voltage, indicating that it can be used for efficiency monitoring. It is also clear that three fired cells is a rather unlikely

situation as expected from symmetry arguments, while four cells (two by two) is more probable.

The results for PC2 and PC3, corresponding to Figs. 16 and 17, are quite comparable to the PC1 results.

The efficiency is calculated as the number of events producing at least one fired cell divided by the number of cosmic events as defined by the 4-fold coincidence in the cosmic setup (Fig. 14). In Fig. 18 we summarize the efficiency information as a function of high voltage for the three chamber types. Clearly a plateau efficiency is reached for all chambers. The plateau is 99.6% for PC1 and 99.8% for PC2 and PC3.

The filled circles represent the basic “fired cell” definition, i.e. three adjacent pads fired. The open squares are obtained if also two adjacent pads fired are accepted as a valid hit. The plateau efficiency is then reached at a lower (by about 20 V) voltage. The probability that two neighboring pads could fire on noise is negligible and one could operate the system at somewhat lower sensitivity if one accepts two fired neighbor pads as a fired cell for the

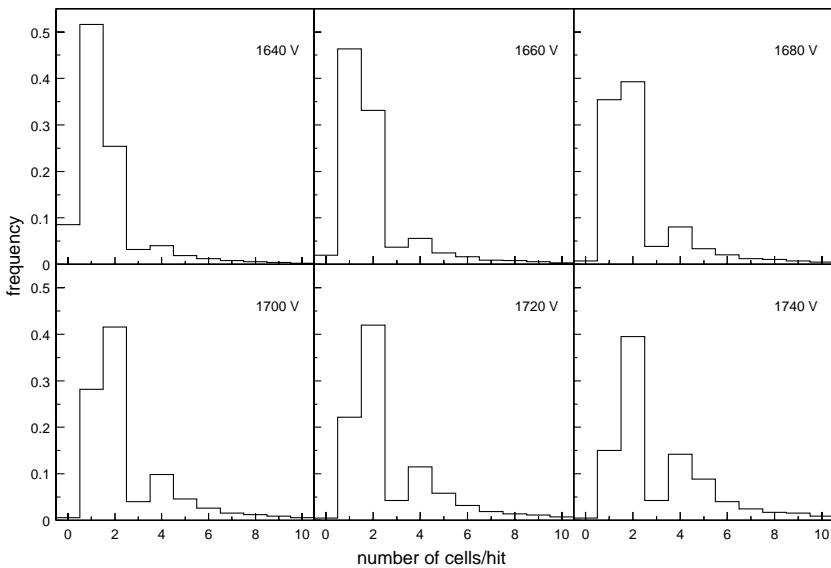


Fig. 17. Cell multiplicity distributions for PC1.

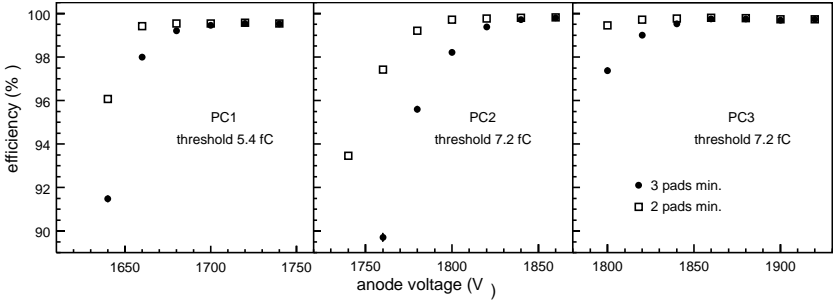


Fig. 18. Efficiency curves for PC1/2/3 with varying high voltage at the operation thresholds.

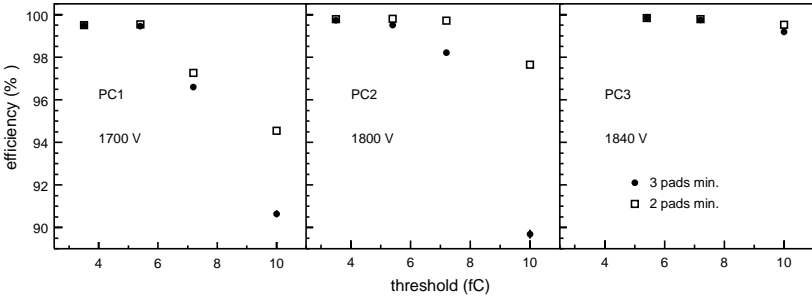


Fig. 19. Efficiency curves for PC1/2/3 with varying threshold at the operation HV.

weakest avalanches. This would result in reduced cluster sizes which is beneficial for operation at high multiplicity.

In Fig. 19 the HV was kept constant and the discriminator thresholds were instead varied from 3.5 to 10 fC. The lowest threshold was completely noise-free for PC1 and PC2 while on PC3 the lowest, noise-free threshold was 5 fC (limited by coherent noise on a few pads). Changing the sensitivity by adjusting the threshold is equivalent to changing the gain of the chamber as long as the thresholds are well above the noise level.

As a summary of the efficiency studies we use as a sensitivity parameter, the normalized threshold expressed as its fraction of the anode charge [14] at the peak as can be seen in Fig. 15. If the pad geometry as seen from the wire (i.e. the charge pickup properties) are the same for the three

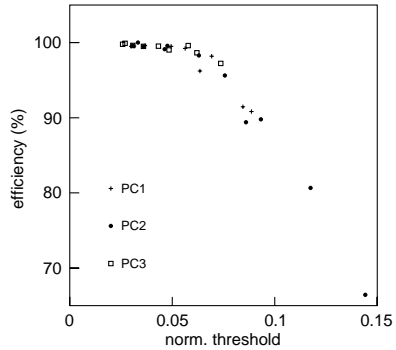


Fig. 20. Efficiency vs. threshold, normalized to the anode charge.

chamber types, all efficiency data should fall on a unique curve when displayed versus the normalized threshold. This is clearly the case as displayed in Fig. 20, where the efficiency data for all settings of HV and threshold and all three chamber types are included.

6.3. Efficiency monitoring

Usually the gain in wire chambers is monitored by reading out the wire signals. In our case, this would require a complete parallel signal and data processing path with analog readout. Instead, we exploit the fact, already indicated, that the ratio between the fraction of two-cell and one-cell clusters in the cell multiplicity distribution in Fig. 17 varies sensitively, in a monotonic way with the efficiency. This variation is displayed in Fig. 21 showing that at a ratio of about 1 one would have optimal conditions. Monitoring this ratio for each chamber has sufficed to ensure the operation of the pad chamber system at plateau efficiency.

The ratio above can to some small extent be influenced by the angle of incidence of the particles. In particular the angles change depending on the magnetic field. Differences between magnet on and off were studied with the data from the first run. No noticeable effects were observed in the 2 cell to 1 cell ratio.

As an additional efficiency monitor we also studied the fraction of hits resulting in only two pads fired, which appeared in the pad multiplicity distribution in Fig. 16. These are due to hits

located right between two cells along the wire. Here, two of the four pads involved collect only 50% as much charge, compared to the two pads that are members of both cells. This is the situation in which the weakest avalanches start to influence the efficiency. The ratio of three-pad hits to two-pad hits is basically governed by the pad geometry and provides an additional handle on the intrinsic chamber efficiency. As seen in Fig. 22, this ratio depends sensitively on the efficiency.

With these two complementary methods one can safely re-establish the calibrated operating point of the system, providing plateau efficiency at a minimal cluster size.

6.4. Position resolution

Minimal cluster sizes are required in order to obtain the best performance at high multiplicity as well as to achieve the best position resolution. Lacking a beam test, we have not been able to study the position resolution in the way one would like to, i.e. with beam and a reference chamber of better resolution. Since all aspects of the chamber performance studied so far have followed the simulations extremely well, one may expect that the position resolution should follow the simulated values as well.

We have performed a study of the position resolution using cosmic rays and two Pad Chambers placed, on top of each other in the cosmic test stand. One of the two chambers was used as the reference chamber and tracks were projected into

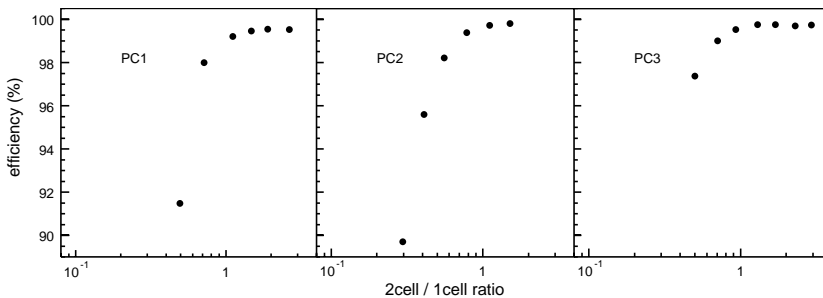


Fig. 21. Efficiency vs. two-cell/one-cell ratio.

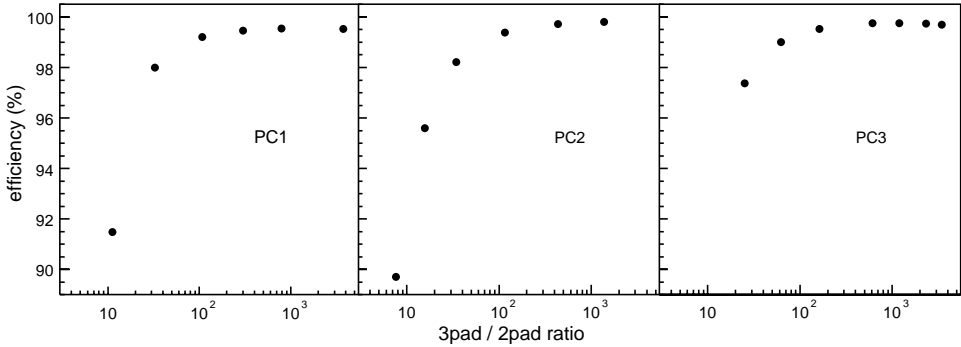


Fig. 22. Efficiency vs. three-pad/two-pad ratio.

the chamber under study by including a smaller scintillator placed at a distance of 1.2 m above the table (S_{sc} in Fig. 14). If the position resolution of the reference chamber is known as well as the position resolution of the small scintillator, one is able to calculate the position error (σ_e) in the track projection into the chamber studied. This error can then be subtracted from the measured position spread (σ_m) in this chamber to obtain the intrinsic (σ_i) chamber resolution.

$$\sigma_i^2 = \sigma_m^2 - \sigma_e^2$$

where σ_e is calculated from the inaccuracies of the scintillator and the reference chamber as

$$\sigma_e^2 = \left(\frac{d_r \sigma_{sc}}{d_{sc} - d_r} \right)^2 + \left(\frac{d_{sc} \sigma_r}{d_{sc} - d_r} \right)^2.$$

The distances $d_r = 70$ mm and $d_{sc} = 1165$ mm are indicated in Fig. 14. The position resolution of the small scintillator (σ_{sc}) is known since it is governed by its size. The resolution (σ_r) of the reference chamber is on the other hand unknown. But for the case where the reference chamber and the studied chamber are identical (in our case 2 PC1's) we have $\sigma_i = \sigma_r$ and we can solve the equations.

The procedure is as follows: First determine the position resolution of PC1, by using two PC1 chambers, one being the reference chamber. Once this is done we use the PC1 reference chamber also

for determining the position resolution of PC2 and PC3.

Fig. 23 shows the result of the position resolution measurement along the wire for PC1 and PC2. The position resolution result along the wire (z -direction) is most straightforward to interpret as the measured distribution, i.e. the difference between projected hit position and the reconstructed position is a nice symmetric Gaussian. σ_m is obtained by fitting a Gaussian to the distribution and the intrinsic resolution in z (σ_i) is obtained from the formulae above.

The measured position resolutions (σ_i) along the wire are 1.7 mm in PC1 and 3.1 mm in PC2. This compares well with the simulated values 1.6 and 2.7 mm, respectively. One may expect that PC3 should relate to the simulations in a similar way with an actual position resolution slightly larger than the simulated 3.2 mm.

Across the wires one does not expect a Gaussian distribution but rather a rectangular one since positions can only be reconstructed to either wire. This is the case for tracks traversing perpendicular to the wire plane. Inclined tracks can however produce avalanches on two wires if traversing right between the two wires. In that case we could quite correctly reconstruct the hit to this middle position. Thus one can expect the measured distribution to be flat, with a rather sharp peak representing very accurately, the reconstructed positions, just at the field wire. These features are

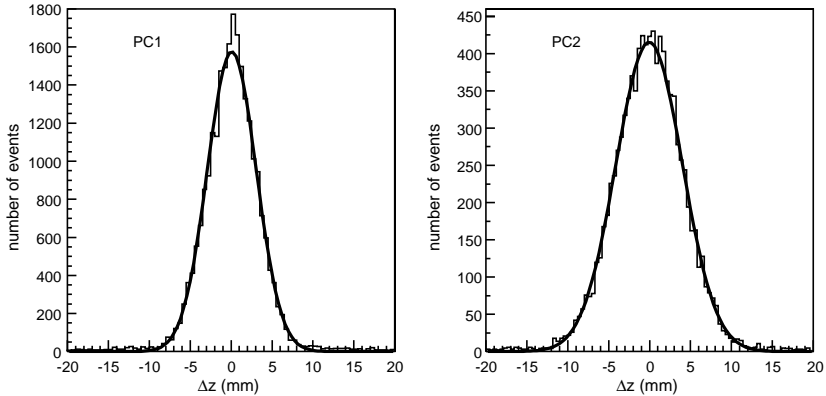


Fig. 23. Reconstructed hit position along the wire direction (z) in a PC1 and a PC2 chamber relative to the intercept of a track, projected from the center of the scintillator and the position in the reference chamber. The widths (σ_m) of the gaussian fits are 3.0 mm for PC1 and 4.1 mm for PC2.

similar to conventional wire readout, i.e. one can determine on which wire an avalanche was situated. With the pad readout, there is a complication since an unusually high charge avalanche may also fire cells that are located above the neighboring wires. In the unlikely event that this crosstalk would only be between two cells on neighboring wires, one would reconstruct this as a hit right between the two wires since this is the most probable cause of this type of 2-cell cluster. But if the cluster was due to crosstalk, one has at most made a position error equal to the wire spacing. One can reduce the crosstalk by decreasing the anode-pad distance. This reduces the extension of the induced charge on the pad plane. By choosing an anode-cathode distance of $\frac{3}{4}$ of the anode-field wire spacing, the crosstalk is a minor problem in the Pad Chambers and the position determination across the wires resembles the wire readout very well.

7. Utilities for Pad Chamber operation

7.1. High voltage system

The high voltage for a chamber is segmented into four groups with separate HV channels

supply. A group contains 29 wires on PC3, 24 or 34 on PC2 and 9 or 20 on PC1. The current requirement during normal operation can be kept quite low; typically less than 100 nA for a group of anode wires. This configuration limits a possible high voltage problem to a smaller region of the chamber than if we had used a single channel for all anode wires.

The HV bus which distributes the HV to the wires has a 22 nF filter capacitor to ground, and a 10 k Ω series resistor to the bus. In order to provide noise immunity, the HV ground and detector ground are isolated through a 100 k Ω resistor. The distribution to each wire goes through a 2 M Ω resistor and a 100 pF capacitor to ground to provide an excellent charging rate without causing a HV sag during high rate operation. Should the need arise, a single wire can be removed from the HV bus by cutting the trace feeding HV to that wire.

The HV is supplied by a LeCroy 1469P module in remotely controlled LeCroy mainframes placed in racks on the spectrometer carriage. Operating voltages are 1700 V for PC1, 1840 V for PC2 and 1880 V for PC3. Trip currents during data taking are set to 10 μ A for each channel controlling a group of wires, and 100 μ A for the bulk supplies which feed eight channels. When turning on the

HV, the voltages are ramped up at 10 V per second, taking about 3 min to reach operating voltage. Voltages are ramped down at 100 V per second.

At the operating voltages chosen, breakdown does not occur during normal data taking. However at beam injection or when the beam is dumped, breakdown can occur due to a large number of tracks traversing at small angle relative to the wire plane. Thus, the HV is reduced to a standby voltage of 1000 V, at filling and whenever a planned dumping of beam occurs.

7.2. Low voltage system

Crates, located in racks on the movable spectrometer carriages, house the custom made low voltage supply modules. A channel in this system, provides the necessary power to one FEM. This includes three separate voltages, one for the FEM itself and two for the analog and digital parts of the ROCs. Each channel is remotely controlled and supervised through a serial bus.

Cabling between LV-supply and the FEM is an eight-conductor twelve-gauge cable. It is necessary to use such heavy gauge wire because of the long distance (approximately twenty meters) from the low voltage supply to the chambers. Although only three independent voltages are supplied, power from the most heavily loaded supply is divided between two pairs of cables to reduce resistive losses in the cable. The low voltage grounds are tied together on the FEM cards. This configuration gives the best noise immunity.

The PC1 FEMs are required to operate in a relatively high magnetic field of approximately 400 G. This necessitates an additional cable supplying a bias voltage to the differential ARCNet receivers on the FEM. PC2 and PC3 use a transformer internal to the ARCNet receiver to draw the ARCNet power from the FEM bias. This transformer would not function in the PC1 FEM location due to the residual magnetic field.

A dozen thermocouples were distributed across the PC1 FEMs and chambers, recording the temperature on the hottest part of the FEMs (voltage regulators) and at the center of the chambers themselves. During data taking these

thermocouples are monitored for indications of unusual performance of the FEMs.

7.3. Gas system

The operating gas chosen for the PC is a mixture of argon and ethane in the ratio 1:1. This mixture has a long history of use in wire chambers, giving good gain with a broad safe plateau of operating voltage.

The gas sources are cryogenic liquid argon and high pressure liquid ethane. Gas from these sources are regulated to 20 psi and mixed using a Hastings Gas System Controller. Gas to each of the chambers is delivered at approximately 100 ml/min per chamber. This is verified by checking flow meters placed on the exhaust of each chamber. Needle valves on the supply pipes to the chambers allow individual flows to be adjusted, equalizing the flow through each chamber. Pressure at the chamber is typically 1 Torr above atmospheric pressure. This is maintained by placing a mineral oil bubbler in parallel with the chamber supply. If pressure at the chamber supply were to exceed 2 Torr, the bubbler would vent to the outside. In normal operation this bubbler did not bubble. Instead, the gas is returned to the mixing house where it is vented outside.

A monitoring system keeps gas flowing to the chambers within our selected operating parameters. Any fluctuations causes an alarm and a safe shutdown of the gas system, protecting the chambers and leaving the system in no danger from the flammable gas.

Gas is delivered in parallel to all chambers. The needle valves and flow meters allow us to shut off gas to an individual chamber, should the need arise, without disturbing the flow to any of the other chambers. Inside the PC1 chambers, the gas inlet is in one side of each chamber with the exhaust port on the other. This ensures that the gas is flowing throughout the entire chamber. The PC2/3 chambers have a gas inlet which travels through the S2 tube in the pixel panel and opens into the gas volume at the far end of the chamber. The exhaust ports are a pair of 1.5 mm slots which collect the gas at the near end of the chamber. This

gives the best distribution of gas inside the PC2 and PC3 chambers.

The gas is delivered to the Pad Chambers through about 100 m of copper pipes. The piping was assembled primarily by soldering, with Swagelok fitting making the final connections to the chambers. The pipes were cleaned with phosphoric acid followed by rinsing with water and drying with ethanol. Moisture levels in the piping were measured to be 25 ppm after drying.

8. Summary: The first full system experience under running conditions

For the first run with the PHENIX experiment at RHIC, a large number of Pad Chambers were put in operation. In total 16 PC1 chambers (69 120 channels) and eight PC3 chambers (34 560 channels) were installed and operated. The commissioning of this system was quite straightforward and only minor problems were encountered in the chambers and the electronic readout system. Once commissioned, operation was maintained by non-expert shift personnel. The performance of the tracking system as a whole, during the first run, has been described in detail in a separate paper [15].

For the second run (2001-02), another eight PC3 chambers and eight PC2 chambers have been installed and the Pad Chamber system now comprises 172 800 channels.

Analysis of the data is in progress and all results indicate that the performance, obtained in bench tests as well as in simulations is well reproduced in the full scale system with the large multiplicity of particles passing through the chambers. The first published physics results from the PHENIX experiment, concerning the charged particle multiplicity distribution, were based on measurements with the Pad Chamber subsystem [16].

Acknowledgements

This development and construction project is a part of the PHENIX project at RHIC. The support from the PHENIX collaboration is gratefully acknowledged. We also thank the technical staffs of the participating institutions for their vital contributions. The supports from RHIC staff and the personnel in the PHENIX experimental halls are also gratefully acknowledged. We are indebted to the Vanderbilt University for providing excellent clean room facilities. The detector construction project is supported by the Department of Energy (USA), VR and the Wallenberg Foundation (Sweden), MIST and NSERC (Canada). The research was supported by Grant No. 97-00088 from the United States-Israel Binational Science Foundation (BSF), Jerusalem, Israel and by the Benozio Center of high energy physics at the Weizmann Institute.

References

- [1] B.B. Back, et al., Phys. Rev. Lett. 87 (2001) 102303.
- [2] B.B. Back, et al., Phys. Rev. Lett. 88 (2002) 022302.
- [3] I.G. Bearden, et al., Phys. Rev. Lett. 88 (2002) 202301.
- [4] D.P. Morrison, et al., Nucl. Phys. A 638 (1998) 565c.
- [5] K. Adcox, et al., PHENIX central arm tracking detectors, Nucl. Instr. and Meth. A (2003), in press. PII: S0168-9002(02)01952-6.
- [6] B. Yu, G.C. Smith, V. Radeka, E. Mathieson, IEEE Trans. Nucl. Sci. NS-38 (1991) 454.
- [7] B. Yu, Ph.D. Thesis, University of Pittsburgh, Pittsburgh, 1991, pp. 69–94.
- [8] L. Carlén, et al., Nucl. Instr. and Meth. A 396 (1997) 310.
- [9] A. Milov et al., PHENIX technical note no. 379.
- [10] Ditron S.R.L. Cerano, Italy.
- [11] W.L. Bryan, et al., IEEE Trans. Nucl. Sci. NS-45 (1998) 754.
- [12] M.C. Smith, et al., IEEE Trans. Nucl. Sci. NS-46 (1999) 1998.
- [13] F. Sauli, CERN preprint 77-09, 1977.
- [14] O. Teodorescu, Master Thesis, McGill University, Montreal, 1998.
- [15] J.T. Mitchell, et al., Nucl. Instr. and Meth. A 482 (2002) 498.
- [16] K. Adcox, et al., Phys. Rev. Lett. 86 (2001) 3500.

Paper II

Deuteron and antideuteron production in Au+Au collisions at $\sqrt{s_{NN}} = 200$ GeV

S.S. Adler,⁵ S. Afanasiev,¹⁷ C. Aidala,⁵ N.N. Ajitanand,⁴³ Y. Akiba,^{20,38} J. Alexander,⁴³ R. Amirikas,¹² L. Aphecetche,⁴⁵ S.H. Aronson,⁵ R. Averbeck,⁴⁴ T.C. Awes,³⁵ R. Azmoun,⁴⁴ V. Babintsev,¹⁵ A. Baldisseri,¹⁰ K.N. Barish,⁶ P.D. Barnes,²⁷ B. Bassalleck,³³ S. Bathe,³⁰ S. Batsouli,⁹ V. Baublis,³⁷ A. Bazilevsky,^{39,15} S. Belikov,^{16,15} Y. Berdnikov,⁴⁰ S. Bhagavatula,¹⁶ J.G. Boissevain,²⁷ H. Borel,¹⁰ S. Borenstein,²⁵ M.L. Brooks,²⁷ D.S. Brown,³⁴ N. Bruner,³³ D. Bucher,³⁰ H. Buesching,³⁰ V. Bumazhnov,¹⁵ G. Bunce,^{5,39} J.M. Burward-Hoy,^{26,44} S. Butsyk,⁴⁴ X. Camard,⁴⁵ J.-S. Chai,¹⁸ P. Chand,⁴ W.C. Chang,² S. Chernichenko,¹⁵ C.Y. Chi,⁹ J. Chiba,²⁰ M. Chiu,⁹ I.J. Choi,⁵² J. Choi,¹⁹ R.K. Choudhury,⁴ T. Chujo,⁵ V. Ciaciolo,³⁵ Y. Cobigo,¹⁰ B.A. Cole,⁹ P. Constantin,¹⁶ D.G. d'Enterria,⁴⁵ G. David,⁵ H. Delagrèe,⁴⁵ A. Denisov,¹⁵ A. Deshpande,³⁹ E.J. Desmond,⁵ O. Dietzsch,⁴¹ O. Drapier,²⁵ A. Drees,⁴⁴ R. du Rietz,²⁹ A. Durum,¹⁵ D. Dutta,⁴ Y.V. Efremenko,³⁵ K. El Chenawi,⁴⁹ A. Enokizono,¹⁴ H. En'yo,^{38,39} S. Esumi,⁴⁸ L. Ewell,⁵ D.E. Fields,^{33,39} F. Fleuret,²⁵ S.L. Fokin,²³ B.D. Fox,³⁹ Z. Fraenkel,⁵¹ J.E. Frantz,⁹ A. Franz,⁵ A.D. Frawley,¹² S.-Y. Fung,⁶ S. Garpman,^{29,*} T.K. Ghosh,⁴⁹ A. Glenn,⁴⁶ G. Gogiberidze,⁴⁶ M. Gonin,²⁵ J. Gosset,¹⁰ Y. Goto,³⁹ R. Granier de Cassagnac,²⁵ N. Grau,¹⁶ S.V. Greene,⁴⁹ M. Grosse Perdekamp,³⁹ W. Guryn,⁵ H.-Å. Gustafsson,²⁹ T. Hachiya,¹⁴ J.S. Haggerty,⁵ H. Hamagaki,⁸ A.G. Hansen,²⁷ E.P. Hartouni,²⁶ M. Harvey,⁵ R. Hayano,⁸ X. He,¹³ M. Heffner,²⁶ T.K. Hemmick,⁴⁴ J.M. Heuser,⁴⁴ M. Hibino,⁵⁰ J.C. Hill,¹⁶ W. Holzmann,⁴³ K. Homma,¹⁴ B. Hong,²² A. Hoover,³⁴ T. Ichihara,^{38,39} V.V. Ikonnikov,²³ K. Imai,^{24,38} D. Isenhower,¹ M. Ishihara,³⁸ M. Issah,⁴³ A. Isupov,¹⁷ B.V. Jacak,⁴⁴ W.Y. Jang,²² Y. Jeong,¹⁹ J. Jia,⁴⁴ O. Jinnouchi,³⁸ B.M. Johnson,⁵ S.C. Johnson,²⁶ K.S. Joo,³¹ D. Jouan,³⁶ S. Kametani,^{8,50} N. Kamihara,^{47,38} J.H. Kang,⁵² S.S. Kapoor,⁴ K. Katou,⁵⁰ S. Kelly,⁹ B. Khachaturov,⁵¹ A. Khanzadeev,³⁷ J. Kikuchi,⁵⁰ D.H. Kim,³¹ D.J. Kim,⁵² D.W. Kim,¹⁹ E. Kim,⁴² G.-B. Kim,²⁵ H.J. Kim,⁵² E. Kistenev,⁵ A. Kiyomichi,⁴⁸ K. Kiyoyama,³² C. Klein-Boesing,³⁰ H. Kobayashi,^{38,39} L. Kochenda,³⁷ V. Kochetkov,¹⁵ D. Koehler,³³ T. Kohama,¹⁴ M. Kopytine,⁴⁴ D. Kotchetkov,⁶ A. Kozlov,⁵¹ P.J. Kroon,⁵ C.H. Kuber,^{1,27} K. Kurita,³⁹ Y. Kuroki,⁴⁸ M.J. Kweon,²² Y. Kwon,⁵² G.S. Kyle,³⁴ R. Lacey,⁴³ V. Ladygin,¹⁷ J.G. Lajoie,¹⁶ A. Lebedev,^{16,23} S. Leckey,⁴⁴ D.M. Lee,²⁷ S. Lee,¹⁹ M.J. Leitch,²⁷ X.H. Li,⁶ H. Lim,⁴² A. Litvinenko,¹⁷ M.X. Liu,²⁷ Y. Liu,³⁶ C.F. Maguire,⁴⁹ Y.I. Makdisi,⁵ A. Malakhov,¹⁷ V.I. Manko,²³ Y. Mao,^{7,38} G. Martinez,⁴⁵ M.D. Marx,⁴⁴ H. Masui,⁴⁸ F. Matathias,⁴⁴ T. Matsumoto,^{8,50} P.L. McGaughey,²⁷ E. Melnikov,¹⁵ F. Messer,⁴⁴ Y. Miake,⁴⁸ J. Milan,⁴³ T.E. Miller,⁴⁹ A. Milov,^{44,51} S. Mioduszewski,⁵ R.E. Mischke,²⁷ G.C. Mishra,¹³ J.T. Mitchell,⁵ A.K. Mohanty,⁴ D.P. Morrison,⁵ J.M. Moss,²⁷ F. Mühlbacher,⁴⁴ D. Mukhopadhyay,⁵¹ M. Muniruzzaman,⁶ J. Murata,^{38,39} S. Nagamiya,²⁰ J.L. Nagle,⁹ T. Nakamura,¹⁴ B.K. Nandi,⁶ M. Nara,⁴⁸ J. Newby,⁴⁶ P. Nilsson,²⁹ A.S. Nyanin,²³ J. Nystrand,²⁹ E. O'Brien,⁵ C.A. Ogilvie,¹⁶ H. Ohnishi,^{5,38} I.D. Ojha,^{49,3} K. Okada,³⁸ M. Ono,⁴⁸ V. Onuchin,¹⁵ A. Oskarsson,²⁹ I. Otterlund,²⁹ K. Oyama,⁸ K. Ozawa,⁸ D. Pal,⁵¹ A.P.T. Palounek,²⁷ V.S. Pantuev,⁴⁴ V. Papavassiliou,³⁴ J. Park,⁴² A. Parmar,³³ S.F. Pate,³⁴ T. Peitzmann,³⁰ J.-C. Peng,²⁷ V. Peresodov,¹⁷ C. Pinkenburg,⁵ R.P. Pisani,⁵ F. Plasil,³⁵ M.L. Porschke,⁵ A.K. Purwar,⁴⁴ J. Rak,¹⁶ I. Ravinovich,⁵¹ K.F. Read,^{35,46} M. Reuter,⁴⁴ K. Reygers,³⁰ V. Riabov,^{37,40} Y. Riabov,³⁷ G. Roche,²⁸ A. Romana,²⁵ M. Rosati,¹⁶ P. Rosnet,²⁸ S.S. Ryu,⁵² M.E. Sadler,¹ N. Saito,^{38,39} T. Sakaguchi,^{8,50} M. Sakai,³² S. Sakai,⁴⁸ V. Samsonov,³⁷ L. Sanfratello,³³ R. Santo,³⁰ H.D. Sato,^{24,38} S. Sato,^{5,48} S. Sawada,²⁰ Y. Schutz,⁴⁵ V. Semenov,¹⁵ R. Seto,⁶ M.R. Shaw,^{1,27} T.K. Shea,⁵ T.-A. Shibata,^{47,38} K. Shigaki,^{14,20} T. Shiina,²⁷ C.L. Silva,⁴¹ D. Silvermyr,^{27,29} K.S. Sim,²² C.P. Singh,³ V. Singh,³ M. Sivertz,⁵ A. Soldatov,¹⁵ R.A. Soltz,²⁶ W.E. Sondheim,²⁷ S.P. Sorensen,⁴⁶ I.V. Sourikova,⁵ F. Staley,¹⁰ P.W. Stankus,³⁵ E. Stenlund,²⁹ M. Stepanov,³⁴ A. Ster,²¹ S.P. Stoll,⁵ T. Sugitate,¹⁴ J.P. Sullivan,²⁷ E.M. Takagui,⁴¹ A. Taketani,^{38,39} M. Tamai,⁵⁰ K.H. Tanaka,²⁰ Y. Tanaka,³² K. Tanida,³⁸ M.J. Tannenbaum,⁵ P. Tarján,¹¹ J.D. Tepe,^{1,27} T.L. Thomas,³³ J. Tojo,^{24,38} H. Torii,^{24,38} R.S. Towell,¹ I. Tserruya,⁵¹ H. Tsuruoka,⁴⁸ S.K. Tuli,³ H. Tydesjö,²⁹ N. Tyurin,¹⁵ H.W. van Hecke,²⁷ J. Velkovska,^{5,44} M. Velkovsky,⁴⁴ L. Villatte,⁴⁶ A.A. Vinogradov,²³ M.A. Volkov,²³ E. Vznuzdaev,³⁷ X.R. Wang,¹³ Y. Watanabe,^{38,39} S.N. White,⁵ F.K. Wohn,¹⁶ C.L. Woody,⁵ W. Xie,⁶ Y. Yang,⁷ A. Yanovich,¹⁵ S. Yokkaichi,^{38,39} G.R. Young,³⁵ I.E. Yushmanov,²³ W.A. Zajc,^{9,†} C. Zhang,⁹ S. Zhou,⁷ S.J. Zhou,⁵¹ and L. Zolin¹⁷

(PHENIX Collaboration)

¹Abilene Christian University, Abilene, TX 79699, USA

²Institute of Physics, Academia Sinica, Taipei 11529, Taiwan

³Department of Physics, Banaras Hindu University, Varanasi 221005, India

⁴Bhabha Atomic Research Centre, Bombay 400 085, India

⁵Brookhaven National Laboratory, Upton, NY 11973-5000, USA

⁶University of California - Riverside, Riverside, CA 92521, USA

⁷China Institute of Atomic Energy (CIAE), Beijing, People's Republic of China

- ⁸Center for Nuclear Study, Graduate School of Science, University of Tokyo, 7-3-1 Hongo, Bunkyo, Tokyo 113-0033, Japan
- ⁹Columbia University, New York, NY 10027 and Nevis Laboratories, Irvington, NY 10533, USA
- ¹⁰Dapnia, CEA Saclay, F-91191, Gif-sur-Yvette, France
- ¹¹Debrecen University, H-4010 Debrecen, Egyetem tér 1, Hungary
- ¹²Florida State University, Tallahassee, FL 32306, USA
- ¹³Georgia State University, Atlanta, GA 30303, USA
- ¹⁴Hiroshima University, Kagamiyama, Higashi-Hiroshima 739-8526, Japan
- ¹⁵Institute for High Energy Physics (IHEP), Protvino, Russia
- ¹⁶Iowa State University, Ames, IA 50011, USA
- ¹⁷Joint Institute for Nuclear Research, 141980 Dubna, Moscow Region, Russia
- ¹⁸KAERI, Cyclotron Application Laboratory, Seoul, South Korea
- ¹⁹Kangnung National University, Kangnung 210-702, South Korea
- ²⁰KEK, High Energy Accelerator Research Organization, Tsukuba-shi, Ibaraki-ken 305-0801, Japan
- ²¹KFKI Research Institute for Particle and Nuclear Physics (RMKI), H-1525 Budapest 114, POBox 49, Hungary
- ²²Korea University, Seoul, 136-701, Korea
- ²³Russian Research Center "Kurchatov Institute", Moscow, Russia
- ²⁴Kyoto University, Kyoto 606, Japan
- ²⁵Laboratoire Leprince-Ringuet, Ecole Polytechnique, CNRS-IN2P3, Route de Saclay, F-91128, Palaiseau, France
- ²⁶Lawrence Livermore National Laboratory, Livermore, CA 94550, USA
- ²⁷Los Alamos National Laboratory, Los Alamos, NM 87545, USA
- ²⁸LPC, Université Blaise Pascal, CNRS-IN2P3, Clermont-Fd, 63177 Aubiere Cedex, France
- ²⁹Department of Physics, Lund University, Box 118, SE-221 00 Lund, Sweden
- ³⁰Institut für Kernphysik, University of Muenster, D-48149 Muenster, Germany
- ³¹Myongji University, Yongin, Kyonggido 449-728, Korea
- ³²Nagasaki Institute of Applied Science, Nagasaki-shi, Nagasaki 851-0193, Japan
- ³³University of New Mexico, Albuquerque, NM, USA
- ³⁴New Mexico State University, Las Cruces, NM 88003, USA
- ³⁵Oak Ridge National Laboratory, Oak Ridge, TN 37831, USA
- ³⁶IPN-Orsay, Université Paris Sud, CNRS-IN2P3, BP1, F-91406, Orsay, France
- ³⁷PNPI, Petersburg Nuclear Physics Institute, Gatchina, Russia
- ³⁸RIKEN (The Institute of Physical and Chemical Research), Wako, Saitama 351-0198, JAPAN
- ³⁹RIKEN BNL Research Center, Brookhaven National Laboratory, Upton, NY 11973-5000, USA
- ⁴⁰St. Petersburg State Technical University, St. Petersburg, Russia
- ⁴¹Universidade de São Paulo, Instituto de Física, Caixa Postal 66318, São Paulo CEP05315-970, Brazil
- ⁴²System Electronics Laboratory, Seoul National University, Seoul, South Korea
- ⁴³Chemistry Department, Stony Brook University, SUNY, Stony Brook, NY 11794-3400, USA
- ⁴⁴Department of Physics and Astronomy, Stony Brook University, SUNY, Stony Brook, NY 11794, USA
- ⁴⁵SUBATECH (Ecole des Mines de Nantes, CNRS-IN2P3, Université de Nantes) BP 20722 - 44307, Nantes, France
- ⁴⁶University of Tennessee, Knoxville, TN 37996, USA
- ⁴⁷Department of Physics, Tokyo Institute of Technology, Tokyo, 152-8551, Japan
- ⁴⁸Institute of Physics, University of Tsukuba, Tsukuba, Ibaraki 305, Japan
- ⁴⁹Vanderbilt University, Nashville, TN 37235, USA
- ⁵⁰Waseda University, Advanced Research Institute for Science and Engineering, 17 Kikui-cho, Shinjuku-ku, Tokyo 162-0044, Japan
- ⁵¹Weizmann Institute, Rehovot 76100, Israel
- ⁵²Yonsei University, IPAP, Seoul 120-749, Korea
- (Dated: January 18, 2005)

The production of deuterons and antideuterons in the transverse momentum range $1.1 < p_T < 4.3$ GeV/c at mid-rapidity in Au + Au collisions at $\sqrt{s_{NN}} = 200$ GeV has been studied by the PHENIX experiment at RHIC. A coalescence analysis comparing the deuteron and antideuteron spectra with that of proton and antiproton, has been performed. The coalescence probability is equal for both deuterons and antideuterons and it increases as a function of p_T , which is consistent with an expanding collision zone. Comparing (anti)proton yields : $\bar{p}/p = 0.73 \pm 0.01$, with (anti)deuteron yields: $\bar{d}/d = 0.47 \pm 0.03$, we estimate that $\bar{n}/n = 0.64 \pm 0.04$. Using the coalescence measurement, the nucleon phase space density is estimated and found to be below 1.

PACS numbers: 25.75.Dw

Keywords: relativistic, heavy ion, collisions, deuteron

*Deceased

†PHENIX Spokesperson:zajc@nevis.columbia.edu

Ultrarelativistic heavy ion collisions are used to study the behavior of nuclear matter at extreme conditions of temperature and density, similar to those that existed in the universe a few microseconds after the Big Bang. Previous measurements indicate that high particle multiplicities [1] and large \bar{p}/p ratios prevail at the Relativistic Heavy-Ion Collider (RHIC), which is expected for a nearly net baryon free region [2]. As the hot, dense system of particles cools, it expands and the mean free path increases until the particles cease interacting (“freeze-out”). At this point, light nuclei like deuterons and antideuterons (d and \bar{d}) can be formed, with a probability proportional to the product of the phase space densities of its constituent nucleons [3, 4]. Thus, invariant yield of deuterons, compared to the protons [5, 6] from which they coalesce, provides information about the size of the emitting system and its space-time evolution.

PHENIX [7] at RHIC, is a versatile detector designed to study the production of leptons, photons, and hadrons over a wide momentum range. In this Letter, results on d and \bar{d} production in Au+Au interactions at $\sqrt{s_{NN}} = 200$ GeV are presented. For the sake of brevity, in the rest of this Letter, our statements will generally apply to both particles and antiparticles.

The East central tracking spectrometer in the PHENIX detector [5, 7, 8] is used in this analysis. The information from the PHENIX Beam-Beam Counters (BBC) and Zero-Degree Calorimeters (ZDC) is used for triggering and event selection. The BBCs are Čerenkov-counters surrounding the beam pipe in the pseudorapidity interval $3.0 < |\eta| < 3.9$, and provide the start timing signal. The ZDCs are hadronic calorimeters 18 m downstream of the interaction region and detect spectator neutrons in a narrow forward cone. Particle identification in the central rapidity region is achieved by measuring momentum (by drift chamber) and time of flight (by time-of-flight detector). The drift chamber (DC) and two layers of pad chambers (PC) are used for tracking and momentum reconstruction [8]. The time-of-flight detector (TOF) spans the pseudorapidity range $|\eta| < 0.35$ and $\Delta\phi = \pi/4$ azimuthally. The TOF consists of plastic scintillators, with a combined time resolution of ≈ 115 ps. The TOF thus provides identification of d and \bar{d} in the transverse momentum (p_T) range $1.1 < p_T < 4.3$ GeV/ c . For $p_T < 1.1$ GeV/ c , the signal to background ratio suffers due to multiple scattering and energy loss effects.

The dataset for this analysis includes 21.6 million minimum bias events. The minimum bias cross section corresponds to $92.2^{+3.5}_{-3}$ % of the total inelastic Au+Au cross section (6.9 b) [9]. Using the momentum determined by the DC, which has a resolution of $\delta p/p \approx 0.7\% \oplus 1\% p$ GeV/ c , and the time of flight from the event vertex provided by the TOF, the mass of the particle is determined. The d and \bar{d} yields are obtained by fitting the mass squared distributions to the sum of a Gaussian signal and an exponential background. Examples of mass

squared distributions with fits for antideuterons in minimum bias collisions are shown in Fig. 1.

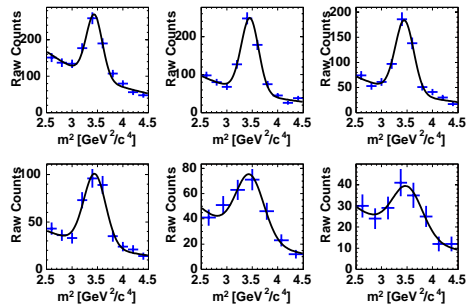


FIG. 1: (color online). Histograms of the mass squared for identified antideuterons in the transverse momentum range $1.1 < p_T < 3.5$ GeV/ c (in 400 MeV/ c increments), with Gaussian fits including an exponential background.

The raw yields are corrected for effects of detector acceptance, reconstruction efficiency and detector occupancy. Corrections are determined by reconstructing single deuterons simulated using GEANT [10] and a detector response model of PHENIX, using the method described in [6]. The track reconstruction efficiency decreases in high multiplicity events because of high detector occupancy. This effect can be slightly larger for slower, heavier particles, due to detector dead times between successive hits. Occupancy effects on reconstruction efficiency ($\approx 83.5\%$ for 0-20% most central events) are evaluated by embedding simulated single particle Monte Carlo events in real events. Since the hadronic interactions of nuclei are not treated by GEANT, a correction needs to be applied to account for the hadronic absorption of d and \bar{d} (including annihilation). The d - and \bar{d} -nucleus cross sections are calculated from parameterizations of the nucleon and anti-nucleon cross sections:

$$\sigma_{d/\bar{d},A} = [\sqrt{\sigma_{N/\bar{N},A}} + \Delta_d]^2 \quad (1)$$

The limited data available on deuteron induced interactions [11] indicate that the term Δ_d is independent of the nuclear mass number A and that $\Delta_d = 3.51 \pm 0.25$ mb $^{1/2}$. The hadronic absorption varies only slightly over the applicable p_T range and is $\approx 10\%$ for d and $\approx 15\%$ for \bar{d} . The background contribution from deuterons knocked out due to the interaction of the produced particles with the beam pipe is estimated using simulations and found to be negligible in the momentum range of our measurement.

Figure 2 shows the corrected d and \bar{d} invariant yields as a function of transverse mass (m_T in the range $1.1 < p_T < 4.3$ GeV/ c , for minimum bias events, and two centrality bins: 0-20% (most central), 20-92% (non-central).

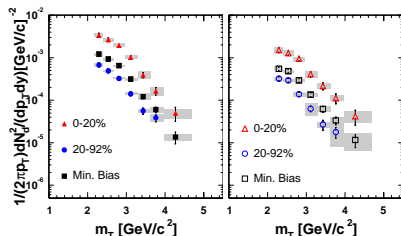


FIG. 2: (color online). Corrected spectra for deuterons (left panel) and anti-deuterons (right panel) for different centralities are plotted vs m_T . Error bars indicate statistical errors and grey bands the systematic errors. Values are plotted at the “true” mean value of m_T of each bin, the extent of which is indicated by the width of the grey bars along x-axis.

TABLE I: The inverse slope parameter T_{eff} obtained from a m_T exponential fit to the spectra along with multiplicity dN/dy and mean transverse momentum $\langle p_T \rangle$ obtained from a Boltzman distribution for different centralities:

T_{eff} [MeV]	Deuterons	Anti-deuterons
Minimum Bias	519 ± 27	512 ± 32
0-20%	536 ± 32	562 ± 51
20-92%	475 ± 29	456 ± 35
dN/dy		
Minimum Bias	$0.0250 \pm_{0.0006(stat.)}^{0.005(sys.)}$	$0.0117 \pm_{0.002(sys.)}^{0.0003(stat.)}$
0-20%	$0.0727 \pm_{0.0141(sys.)}^{0.0022(stat.)}$	$0.0336 \pm_{0.0057(sys.)}^{0.0013(stat.)}$
20-92%	$0.0133 \pm_{0.0029(sys.)}^{0.0004(stat.)}$	$0.0066 \pm_{0.0015(sys.)}^{0.0002(stat.)}$
$\langle p_T \rangle$ [GeV/c]		
Minimum Bias	$1.54 \pm_{0.13(sys.)}^{0.04(stat.)}$	$1.52 \pm_{0.12(sys.)}^{0.05(stat.)}$
0-20%	$1.58 \pm_{0.13(sys.)}^{0.05(stat.)}$	$1.62 \pm_{0.11(sys.)}^{0.07(stat.)}$
20-92%	$1.45 \pm_{0.15(sys.)}^{0.05(stat.)}$	$1.41 \pm_{0.15(sys.)}^{0.06(stat.)}$

The 20-92% centrality bin is dominated by mid-central events, due to larger track multiplicities relative to peripheral events.

Systematic uncertainties have several sources: errors in particle identification, DC-TOF hit match efficiency, the uncertainty in momentum scale, d and \bar{d} hadronic interaction correction, and uncertainty in occupancy corrections. All the systematic uncertainties are added in quadrature, depicted by grey bars in Fig. 2.

The p_T spectra $E d^3N/d^3p$ are fitted in the range $1.1 < p_T < 3.5$ GeV/c to an exponential distribution in $m_T = \sqrt{p_T^2 + m^2}$. The inverse slopes (T_{eff}) of the spectra are tabulated in Table I. The deuteron inverse slopes of $T_{eff} = 500$ -520 MeV are considerably higher than the $T_{eff} = 300$ -350 MeV observed for protons [5, 6]. The invariant yields and the average transverse momenta ($\langle p_T \rangle$) are obtained by summing the data over p_T and using a

Boltzmann distribution: $\frac{d^2N}{2\pi m_T dm_T dy} \propto m_T e^{-m_T/T_{eff}}$, to extrapolate to low m_T regions where we have no data. The extrapolated yields constitute $\approx 42\%$ of our total yields. The rapidity distributions, dN/dy , and the mean transverse momenta, $\langle p_T \rangle$, are compiled in Table I for three different centrality bins. Systematic uncertainties on dN/dy and $\langle p_T \rangle$ are estimated by using an exponential in p_T and a “truncated” Boltzmann distribution (assumed flat for $p_T < 1.1$ GeV/c) for alternative extrapolations.

With a binding energy of 2.24 MeV, the deuteron is a very loosely bound state. Thus, the observed deuterons can be formed only at a later stage in the collision. The proton and neutron must be close in space and tightly correlated in velocity to coalesce. As a result, d and \bar{d} yields are a sensitive measure of correlations in phase space at freeze-out and can provide information about the space-time evolution of the system. If deuterons are formed by coalescence of protons and neutrons, the invariant deuteron yield can be related [12] to the primordial nucleon yields by:

$$E_d \frac{d^3N_d}{d^3p_d} \Big|_{p_d=2p_p} = B_2 \left(E_p \frac{d^3N_p}{d^3p_p} \right)^2 \quad (2)$$

where B_2 is the coalescence parameter, with the subscript implying that two nucleons are involved in the coalescence. The above equation includes an implicit assumption that the ratio of neutrons to protons is unity. The proton and antiproton spectra [6] are corrected for feed-down from Λ and $\bar{\Lambda}$ decays by using a MC simulation tuned to reproduce the particle ratios: $(\Lambda/p$ and $\bar{\Lambda}/\bar{p})$ measured by PHENIX at 130 GeV [13].

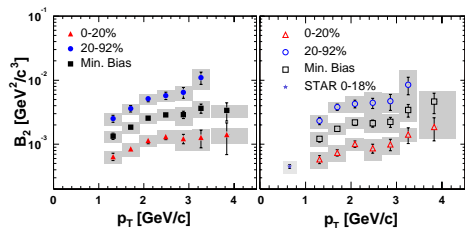


FIG. 3: (color online). Coalescence parameter B_2 vs p_T for deuterons (left panel) and anti-deuterons (right panel). Grey bands indicate the systematic errors. Values are plotted at the “true” mean value of p_T of each bin, the extent of which is indicated by the width of the grey bars along x-axis.

Figure 3 displays the coalescence parameter B_2 as a function of p_T for different centralities. Thermodynamic models [4] predict that B_2 scales with the inverse of the effective volume V_{eff} ($B_2 \propto 1/V_{eff}$). The lower B_2 in more central collisions may thus reflect the increase in the participant volume with centrality. We also observe that B_2 increases with p_T . This is consistent with an expanding source because position-momentum correlations

lead to a higher coalescence probability at larger p_T . The p_T -dependence of B_2 can provide information about the density profile of the source as well as the expansion velocity distribution. It has been shown [14, 15] that an increase of B_2 with p_T can be achieved if the source density when squared does not lose weight in the region of large flow. This condition is satisfied by a flat distribution, whereas a Gaussian source density gives greater weight to the center of the system leading to a constant B_2 with p_T . This is not supported by our data, which shows a rise in B_2 with p_T .

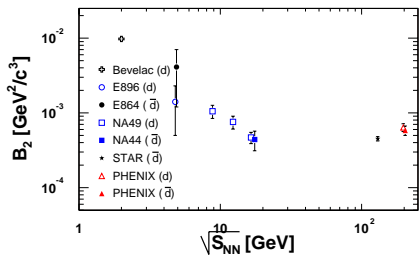


FIG. 4: (color online). Comparison of the coalescence parameter for deuterons and anti-deuterons ($p_T = 1.3$ GeV/c) with other experiments at different values of \sqrt{s} .

Figure 4 compares B_2 for most central collisions to results at lower \sqrt{s} [16–21]. Note that B_2 is nearly independent of \sqrt{s} , indicating that the source volume does not change appreciably with center-of-mass energy (with the caveat that B_2 varies as a function of p_T , centrality and rapidity). Similar behavior is seen for B_2 for deuterons [19] as a function of \sqrt{s} . This observation is consistent with what has been observed in Bose-Einstein correlation Hanbury-Brown Twiss (HBT) analysis at RHIC [22] for identified particles. The coalescence parameter B_2 for d and \bar{d} , is equal within errors, indicating that nucleons and antinucleons have the same temperature, flow and freeze-out density distributions.

The \bar{d}/d ratio is independent of centrality, and p_T within errors. The average value of \bar{d}/d is 0.47 ± 0.03 , consistent with the square of the ratio $\bar{p}/p = 0.73 \pm 0.01$ [6] within statistical and systematic uncertainties. This is expected if deuterons are formed by coalescence of comoving nucleons and $\bar{p}/p = \bar{n}/n$. The ratio \bar{n}/n can, however, be estimated from the data based on the thermal chemical model. Assuming thermal and chemical equilibrium, the chemical fugacities are determined from the particle/anti-particle ratios [14]:

$$\frac{E_A(d^3 N_A / d^3 p_A)}{E_{\bar{A}}(d^3 N_{\bar{A}} / d^3 p_{\bar{A}})} = \exp\left(\frac{2\mu_A}{T}\right) = \lambda_A^2 \quad (3)$$

Using the ratio p/\bar{p} , the extracted proton fugacity is $\lambda_p = \exp(\mu_p/T) = 1.17 \pm 0.01$. Similarly, using

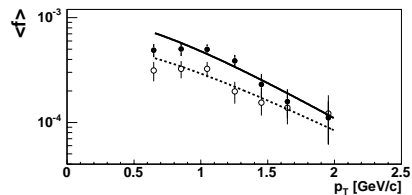


FIG. 5: Average nucleon phase space density as a function of p_T for central collisions. Filled circles correspond to nucleons and open circles correspond anti-nucleons. The curves are fits to a Boltzmann function, $C \exp(-m_T/T)$.

the d/\bar{d} ratio, the extracted deuteron fugacity is $\lambda_d = \exp[(\mu_p + \mu_n)/T] = 1.46 \pm 0.05$. From this, the neutron fugacity can be estimated to be $\lambda_n = \exp(\mu_n/T) = 1.25 \pm 0.04$, which results in $\bar{n}/n = 0.64 \pm 0.04$. The extracted \bar{p}/p and \bar{n}/n ratios are in agreement with what one would expect from the initial neutron excess in the Au nucleus if the same number of (anti-)neutrons and (anti-)protons are produced in the collision. Thermal models predict [23] $\bar{d}/d = 0.52$ and $\bar{n}/n = 0.73$ for $T = 177$ MeV and $\mu_B = 29$ MeV.

Finally, the coalescence requirement allows us estimate the nucleon phase space distribution, i.e. the average number of nucleons per cell ($d^3 p d^3 x$)/ h in phase space. We define the phase space distribution averaged over the source volume as

$$\langle f(p) \rangle = \frac{1}{2S+1} \frac{(2\pi\hbar)^3 d^3 N}{V dp^3} \quad (4)$$

where $2S+1$ is the spin degeneracy factor. From the coalescence equation[15], $f_A(\vec{r}, \vec{p}) = [f(\vec{r}, \vec{p}/A)]^A$, we can thus calculate $\langle f \rangle$ as function of p_T from the measured invariant yields, if we assume that the protons, neutrons and deuterons are emitted from the same volume. The results is shown in Fig. 5. The phase space density is well below 1 in the range of our measurement, and much lower than what has been found for pions produced in Au+Au collisions previously[24].

To summarize, the transverse momentum spectra of d and \bar{d} in the range $1.1 < p_T < 4.3$ GeV/c, have been measured at mid-rapidity in Au+Au collisions at $\sqrt{s_{NN}} = 200$ GeV, and are found to be less steeply falling than proton (and antiproton) spectra. The extracted coalescence parameter B_2 increases with p_T , which is indicative of an expanding source. The results rule out a Gaussian source density distribution combined with a linear flow velocity profile and seem to favor a flat density distribution. The B_2 measured in nucleus-nucleus collisions is independent of $\sqrt{s_{NN}}$ above 12 GeV, consistent with the energy dependence of the source radii extracted from Bose-Einstein correlation measurements. B_2 is equal within errors for both deuterons and anti-deuterons. From the measurements, it is estimated that $\bar{n}/n = 0.64 \pm 0.04$.

We thank the staff of the Collider-Accelerator and Physics Departments at BNL for their vital contributions. We acknowledge support from the Department of Energy and NSF (U.S.A.), MEXT and JSPS (Japan), CNPq and FAPESP (Brazil), NSFC (China), CNRS-IN2P3 and CEA (France), BMBF, DAAD, and AvH

(Germany), OTKA (Hungary), DAE and DST (India), ISF (Israel), KRF and CHEP (Korea), RMIST, RAS, and RMAE, (Russia), VR and KAW (Sweden), U.S. CRDF for the FSU, US-Hungarian NSF-OTKA-MTA, and US-Israel BSF.

-
- [1] K. Adcox *et al.*, Phys. Rev. Lett. **86**, 3500 (2001); B. B. Back *et al.*, Phys. Rev. Lett. **88**, 022302 (2002).
 - [2] K. Adcox *et al.*, Phys. Rev. Lett. **88**, 242301 (2002); B. B. Back *et al.*, Phys. Rev. **C67**, 021901 (2003); C. Adler *et al.*, Phys. Rev. Lett. **86**, 4778 (2001).
 - [3] L. P. Csernai and J. I. Kapusta, Phys. Rep. **131**, 223 (1986).
 - [4] A. Z. Mekjian, Phys. Rev. **C17**, 1051 (1978).
 - [5] K. Adcox *et al.*, Phys. Rev. **C69**, 024904 (2004).
 - [6] S. S. Adler *et al.*, Phys. Rev. **C69**, 034909 (2004).
 - [7] K. Adcox *et al.*, Nucl. Instrum. Methods **A499**, 469 (2003) and references therein.
 - [8] J. T. Mitchell *et al.*, Nucl. Instrum. Methods **A482**, 491 (2002).
 - [9] S. S. Adler *et al.*, Phys. Rev. Lett. **91**, 072301 (2003).
 - [10] GEANT 3.21, CERN program library.
 - [11] J. Jaros *et al.*, Phys. Rev. **C18**, 1978 (2273); E. O. Abdurakhmanov *et al.*, Z. Phys. **C5**, 1980 (1).
 - [12] S. T. Butler and C. A. Pearson, Phys. Rev. **129**, 836 (1963).
 - [13] K. Adcox *et al.*, Phys. Rev. Lett. **89**, 092302 (2002).
 - [14] R. Scheibl, and U. Heinz, Phys. Rev. **C59**, 1585 (1999).
 - [15] A. Polleri, J. P. Bondorf, and I. N. Mishustin, Phys. Lett. **B419**, 19 (1998).
 - [16] S. Wang *et al.*, Phys. Rev. Lett. **74**, 2646 (1995).
 - [17] S. Albergo *et al.*, Phys. Rev. **C65**, 034907 (2002).
 - [18] T. A. Armstrong *et al.*, Phys. Rev. Lett. **85**, 2685 (2000).
 - [19] T. Anticic *et al.*, Phys. Rev. **C69**, 024902 (2004).
 - [20] I. G. Bearden *et al.*, Phys. Rev. Lett. **85**, 2681 (2000).
 - [21] C. Adler *et al.*, Phys. Rev. Lett. **87**, 262301 (2001).
 - [22] K. Adcox *et al.*, Phys. Rev. Lett. **88**, 192302 (2002); C. Adler *et al.*, Phys. Rev. Lett. **87**, 082301 (2001).
 - [23] P. Braun-Munzinger, D. Magestro, K. Redlich and J. Stachel, Phys. Lett. **B518**, 41 (2001); J. Stachel private communication.
 - [24] F. Laue *et al.*, Nucl. Phys. **A698**, 177c (2002).

Paper III

Effective Charges in the fp Shell

R. du Rietz,¹ J. Ekman,¹ D. Rudolph,¹ C. Fahlander,¹ A. Dewald,² O. Möller,² B. Saha,² M. Axiotis,³ M. A. Bentley,⁴ C. Chandler,⁴ G. de Angelis,³ F. Della Vedova,⁵ A. Gadea,³ G. Hammond,⁴ S. M. Lenzi,⁵ N. Märginean,³ D. R. Napoli,³ M. Nespolo,⁵ C. Rusu,³ and D. Tonev³

¹Department of Physics, Lund University, S-22100 Lund, Sweden

²Institut für Kernphysik der Universität zu Köln, D-50937 Köln, Germany

³Instituto Nazionale di Fisica Nucleare, Laboratori Nazionali di Legnaro, I-35020 Legnaro, Italy

⁴School of Chemistry and Physics, Keele University, Keele, Staffordshire ST5 5BG, United Kingdom

⁵Dipartimento di Fisica dell'Università and INFN, Sezione di Padova, I-35141 Padova, Italy

(Received 16 August 2004; published 22 November 2004)

Following the heavy-ion fusion-evaporation reaction $^{32}\text{S} + ^{24}\text{Mg}$ at 95 MeV beam energy the lifetimes of analogue states in the $T_z = \pm 1/2 A = 51$ mirror nuclei ^{51}Fe and ^{51}Mn have been measured using the Cologne plunger device coupled to the GASP γ -ray spectrometer. The deduced $B(E2; 27/2^- \rightarrow 23/2^-)$ values afford a unique opportunity to probe isoscalar and isovector polarization charges and to derive effective proton and neutron charges, ϵ_p and ϵ_n , in the fp shell. A comparison between the experimental results and several different large-scale shell-model calculations yields $\epsilon_p \sim 1.15e$ and $\epsilon_n \sim 0.80e$.

DOI: 10.1103/PhysRevLett.93.222501

PACS numbers: 21.10.Tg, 21.60.Cs, 27.40.+z

In the isospin formalism the proton and neutron are treated as two different quantum states of the same particle, the nucleon. The assumption of isospin symmetry relies on the fact that the nucleon-nucleon interaction is charge independent. In reality, however, the symmetry is broken by the Coulomb force between protons [1].

Nuclei in the vicinity of the doubly magic $N = Z$ nuclei ^{40}Ca and ^{56}Ni as well as $N \sim Z$ nuclei near the middle of the $1f_{7/2}$ shell are well described by large-scale shell-model calculations [2]. They are well suited for isospin symmetry studies since the $1f_{7/2}$ shell is relatively isolated in energy. Together with significant theoretical effort the understanding and interpretation of Coulomb effects in mirror nuclei, which are pairs of nuclei with the number of protons and neutrons interchanged, has increased substantially during recent years [3–5]. However, almost all studies so far have been limited to the comparison of excitation energies in so called Mirror Energy Difference diagrams. Other spectroscopic quantities, such as lifetimes of excited states and related electromagnetic properties of mirror nuclei, have only recently been looked upon [6].

Electromagnetic properties of nuclei give information on core polarization effects due to the valence particles outside closed shells, if the configurations of the valence particles are taken care of by large-scale shell-model calculations. In practice, the polarization effects are accounted for in nuclear models by using effective nucleon charges and gyromagnetic factors instead of those of the bare nucleons. The polarization charge, which is the difference between the effective and bare charge, is believed to arise from virtual excitations of isoscalar and isovector giant resonances of the nucleus. As the wave functions of analogue states in mirror nuclei are to first

order identical under the exchange of protons and neutrons, the study of mirror nuclei offers a unique opportunity to access, probe, and pin down the effective charges.

The $A = 51$ mirror nuclei ^{51}Fe and ^{51}Mn have well established level schemes [7–9], which are shown in Fig. 1. The lifetimes of the nanosecond isomeric $17/2^-$ states are known in both nuclei, and a lifetime of $\tau = 130(25)$ ps has been suggested for the terminating $27/2^-$ state in ^{51}Mn [10]. In this Letter, we present a refined number for this state and the first measurement of the lifetime of its analogue state in ^{51}Fe . A unique study, based on large-scale shell-model calculations, is performed and for the first time a quantitative estimate of effective charges near ^{56}Ni is derived.

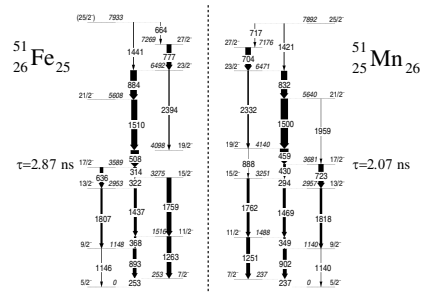


FIG. 1. Level schemes of the $A = 51$ mirror nuclei [7–9]. Energy labels are in keV and the widths of the arrows correspond to the relative intensities of the transitions.

The experiment was performed at the Legnaro National Laboratory using the heavy-ion fusion-evaporation reaction $^{32}\text{S} + ^{24}\text{Mg}$ with a beam energy of 95 MeV. The 99.92% isotopically enriched and on average 0.95 mg/cm² thick ^{24}Mg target was mounted inside the Cologne plunger device [11] in front of a stretched 13 mg/cm² gold stopper foil. Data were taken at 21 target-stopper distances ranging from electric contact to 4.0 mm.

The mass $A = 51$ mirror nuclei ^{51}Fe and ^{51}Mn were produced via the evaporation of one α particle and one neutron ($1\alpha 1n$ channel) and one α particle and one proton ($1\alpha 1p$ channel), respectively. The γ rays were detected with the GASP detector array [12] using its 40 HPGe detectors (distributed in seven rings at 34.6°, 59.4°, 72.0°, 90.0°, 108.0°, 120.6°, and 145.4°) and 74 BGO elements. Events with at least one BGO element and two HPGe detectors firing in coincidence were accepted by the event trigger. At the end of the experiment, ^{56}Co , ^{133}Ba , and ^{152}Eu standard sources were used to calibrate the detector system.

The method used to determine the lifetimes of the $27/2^-$ states in the $A = 51$ mirror pair is based on very specific features of their decay schemes. They consist of essentially three regimes: the transitions below the isomeric $17/2^-$ states, those feeding into the long-lived (~ 100 ps) $27/2^-$ states, and the short-lived states in between (see Fig. 1). Thus it is possible to apply the recoil distance Doppler shift (RDDS) method to the 777 and 704 keV (or 884 and 832 keV) transitions in spectra taken in coincidence with low-lying transitions, which are essentially always emitted from stopped residues.

Therefore, for each distance the events were sorted offline into $\gamma\gamma$ coincidence matrices with γ rays detected in one given detector ring placed along one axis and γ rays detected anywhere in the array along the second axis of the matrix. Clean spectra of ^{51}Fe and ^{51}Mn are shown in Fig. 2. They are obtained by gating on the low-energy 253 and 237 keV $7/2^- \rightarrow 5/2^-$ transitions, respectively. A RDDS analysis is performed using the two most forward and the two most backward detector rings of GASP, where the shifted and unshifted components of the coincident transitions are well separated.

The analysis of the same transition for different distances requires a normalization of its intensity due to, e.g., different beam currents or measuring times. To obtain these normalization coefficients for each distance, the intensities of the unshifted and Doppler shifted components for the 459 and 832 keV transitions observed in all detector rings were summed up in spectra in coincidence with the 237 keV ground-state transition in ^{51}Mn . The (mainly systematic) uncertainty for the normalization coefficients was estimated to be 2%.

The normalization coefficients are also used as weighting factors when different measurements at about the

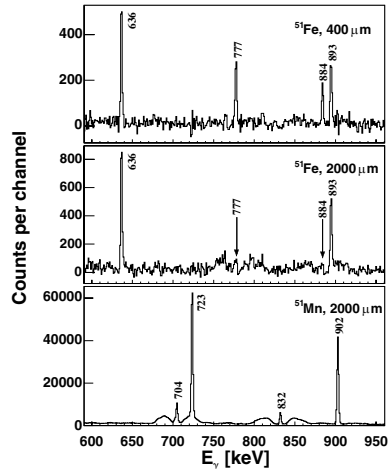


FIG. 2. Gamma-ray spectra taken at different distances in the GASP detector rings at 34.6°, 59.4°, 120.6°, and 145.4°. They are in coincidence with the $7/2^- \rightarrow 5/2^-$ 253 keV transition in ^{51}Fe (top, middle) and the 237 keV mirror transition in ^{51}Mn (bottom). Energy labels of the peaks are in keV. Note the significant reduction of statistics when moving from ^{51}Mn to the more exotic isotope ^{51}Fe .

same distance were combined. This is necessary for the analysis of the transitions from the very weakly populated nucleus ^{51}Fe . For each of the 21 target-distance combinations the recoil velocity was derived from the positions of the stopped and Doppler shifted components of the intense $1500 \text{ keV } 21/2^- \rightarrow 19/2^-$ transition in ^{51}Mn . The velocities range from 3.7% to 4.1% of the speed of light for the three different targets used during the experiment. Using these velocities the 21 distances can be converted into 21 flight times, which are then combined in nine effective flight times used in the analysis: 0.537(7), 1.45(1), 3.42(5), 10.3(2), 34.8(9), 61.2(14), 105(3), 175(5), and 354(9) ps.

The top two spectra of Fig. 2 illustrate how the target-stopper distance affects the intensities of the stopped and Doppler shifted components. For the short distance (400 μm) the four transitions at 636, 777, 884, and 893 keV in ^{51}Fe are clearly seen as stopped peaks. When increasing the distance to 2000 μm the stopped components of the two transitions at 777 and 884 keV are significantly reduced and Doppler shifted and broadened peaks arise on each side of the stopped peaks. The 636 and 893 keV transitions are still observed as stopped peaks, because they are situated below the isomeric $17/2^-$ state and the flight distance is still rather short with respect to its lifetime.

The comparison of the ^{51}Fe and ^{51}Mn spectra for the same distance in Fig. 2 shows a difference in statistics of some 2 orders of magnitude. The large amount of statistics in the ^{51}Mn spectrum allows us to discriminate Doppler shifted components even for the transitions below the $17/2^-$ state (723 and 902 keV). Additionally, it enables both a thorough investigation of possible systematic errors and a proper normalization in the course of the analysis.

Figure 3 illustrates the decay curves of the 777 keV $27/2^- \rightarrow 23/2^-$ transition in ^{51}Fe and the 832 keV $27/2^- \rightarrow 21/2^-$ transition in ^{51}Mn . The analysis of the $27/2^- \rightarrow 23/2^-$ 704 keV transition was hampered due to Doppler shifted components of the 723 keV $17/2^- \rightarrow 13/2^-$ and 717 keV $25/2^- \rightarrow 27/2^-$ transitions (cf. Figure 2) as well as background radiation at 701 keV from the decay of the $19/2^-$ isomer in ^{53}Fe . To account for possible side feeding (<10%) directly into the $23/2^-$ state, the decay curve of the 832 keV line was least-squares fitted with a short ($\tau < 10$ ps) and a long lifetime component. The result is $\tau = 100.7 \pm 1.2 \pm 3$ ps for the $27/2^-$ state in ^{51}Mn , i.e., $B(E2) = 46.7(14) e^2 \text{fm}^4$. The systematic uncertainty of ± 3 ps is related to the normalization, the exact determination of the yield of the stopped component at large distances, possible short-lived ($\tau < 1$ ps cf. [9]) feeding into the $27/2^-$ state, and combining the yields of measurements at several distances.

To increase statistics in the case of ^{51}Fe , spectra in coincidence with the 253, 314, and 636 keV transitions from the two most forward and the two most backward detector rings were summed. Since a stopped component of the 777 keV line was absent in the spectrum taken at the largest distance, it was excluded from the analysis. The resulting lifetime of the $27/2^-$ state in ^{51}Fe is found to be $\tau = 69.7 \pm 1.6 \pm 3$ ps, i.e., $B(E2) = 41.3(24) e^2 \text{fm}^4$. The ratio, R , between the $B(E2)$ values of the mirror transitions in ^{51}Fe and ^{51}Mn amounts to $R = 0.884(22)$.

To study the consequences of the lifetime results on polarization and effective charges, large-scale shell-

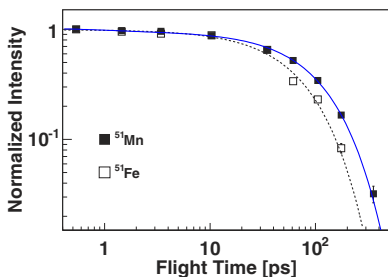


FIG. 3 (color online). Decay curves for the 832 keV transition in ^{51}Mn (solid line) and the 777 keV transition in ^{51}Fe (dashed line) for nine effective flight distances.

model calculations were performed using the shell-model code ANTOINE [13,14]. The calculations employ the full fp space containing the $1f_{7/2}$ orbit below and the $2p_{3/2}$, $1f_{5/2}$, and $2p_{1/2}$ orbits above the $N, Z = 28$ shell closure. The configuration space was truncated to allow for excitations of up to five particles across the shell closure. This configuration space provides predictions more or less indistinguishable from calculations using the full fp space [2]. Three interactions have been studied: The standard KB3G interaction without any Coulomb interaction, with theoretical harmonic-oscillator Coulomb matrix elements (Coulomb HO), and with the $1f_{7/2}$ Coulomb matrix elements replaced with the experimental values from the $A = 42$ mirror pair (Coulomb A42).

The predicted reduced $E2$ -transition probabilities are generally expressed as a sum over all nucleons,

$$B(E2; J_i \rightarrow J_f) = \frac{1}{2J_i + 1} \left| \left\langle J_f \left| \left| \sum_{i=1}^A \varepsilon_i r_i^2 Y_{20} \right| \right| J_i \right\rangle \right|^2, \quad (1)$$

where ε_i denote the effective nucleon charges and $\langle r^2 \rangle = b_0^2 A^{1/3} (N + 3/2)$ in the case of harmonic-oscillator wave functions. Note that the principle quantum number N and thus $\langle r^2 \rangle$ is constant within the fp shell. The harmonic-oscillator parameter, b_0 , is commonly set to 1.01.

The effective proton and neutron charges, ε_p and ε_n , are introduced to account for polarization effects of the valence nucleons on the otherwise inert core of the shell-model calculation. The isoscalar and isovector polarization charges, $e_{\text{pol}}^{(0)}$ and $e_{\text{pol}}^{(1)}$, arise from the virtual excitation of the isoscalar and isovector giant quadrupole resonances (GQR) of the core. Thus,

$$\varepsilon_p = 1 + e_{\text{pol}}^{(0)} - e_{\text{pol}}^{(1)}, \quad \varepsilon_n = e_{\text{pol}}^{(0)} + e_{\text{pol}}^{(1)}, \quad (2)$$

where it is predicted that $e_{\text{pol}}^{(0)} = Z/A \sim 0.5$ and $e_{\text{pol}}^{(1)} \sim 0.32$ in the case of $N \sim Z$ nuclei [15].

In the absence of Coulomb effects, the wave functions of analogue states are identical with respect to the exchange of protons and neutrons. Therefore, the $B(E2)$ values of mirror transitions and their ratio are sensitive to the effective charges according to Eq. (1) and, consequently, to the isovector polarization charge [cf. Eq. (2)].

Assuming identical orbital radii, i.e., the same b_0 for ^{51}Mn and ^{51}Fe , the $B(E2)$ values for the two $27/2^- \rightarrow 23/2^-$ transitions were calculated. The experimental values and their ratio are reproduced simultaneously for different combinations of the three parameters b_0 and the isoscalar and isovector polarization charges. Figure 4 illustrates this dependency for two different sets of Coulomb matrix elements and one set without any Coulomb interaction. Table I summarizes the results for $b_0 = 1.01$. The uncertainties in $e_{\text{pol}}^{(0)}$ and $e_{\text{pol}}^{(1)}$ are determined by reproducing the maximum (minimum)

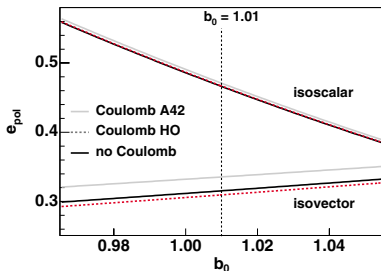


FIG. 4 (color online). Polarization charges, necessary to reproduce the $B(E2; 27/2^- \rightarrow 23/2^-)$ values in the $A = 51$ mirror nuclei, as a function of b_0 for three different shell-model calculations. The top three lines correspond to the isoscalar component, $e_{\text{pol}}^{(0)}$, while the bottom three lines represent the isovector component, $e_{\text{pol}}^{(1)}$.

$B(E2; 27/2^- \rightarrow 23/2^-)$ value in ^{51}Mn and the minimum (maximum) $B(E2; 27/2^- \rightarrow 23/2^-)$ value in ^{51}Fe , respectively. It is intriguing that the numbers in Table I result in effective charges similar to recently refined estimates in the ^{100}Sn region (cf. Ref. [16], and references therein). Most interestingly, however, is that the present results are in very good agreement with Eq. 6-386b in Ref. [15], where the effective charge phenomenon is treated as a weak coupling of the valence nucleons to the GQR of the core. This coupling gives rise to a mixing of the GQR components into the shell-model states, which results in an increase of the transition matrix elements. The isoscalar and isovector GQRs originate from the particle-hole states with excitation energies of about $2\hbar\omega_0 \sim 22$ MeV for $A = 51$.

From Fig. 4 it is seen that the isoscalar $e_{\text{pol}}^{(0)}$ component is much more sensitive to changes in nuclear radii than the isovector $e_{\text{pol}}^{(1)}$ component. In turn, the isoscalar part is rather independent of the choice of $1f_{7/2}$ Coulomb matrix elements, whereas the isovector part shows a more pronounced dependence. It is interesting to note that the $e_{\text{pol}}^{(1)}$ results obtained using the two sets of Coulomb matrix elements are situated on opposite sides of the line originating from the calculation without any Coulomb interaction. The major differences between the two sets are the $1f_{7/2} J = 2$ and $1f_{7/2} J = 6$ Coulomb matrix elements. A detailed investigation reveals that mainly the latter is responsible for this effect.

The effective charges given above are extracted under the assumption that the radii of the two mirror partners are identical (b_0 is the same for both members). However, it is reasonable to assume that the Coulomb interaction pushes the proton wave functions towards larger radii with respect to the neutron wave functions. Following

TABLE I. Isoscalar and isovector polarization charges, which simultaneously reproduce the $B(E2; 27/2^- \rightarrow 23/2^-)$ values in the $A = 51$ mirror nuclei, for three different shell-model calculations using $b_0 = 1.01$.

	No Coulomb	Coulomb HO	Coulomb A42
$e_{\text{pol}}^{(0)}$	0.466(3)	0.466(3)	0.471(2)
$e_{\text{pol}}^{(1)}$	0.316(26)	0.310(37)	0.336(37)

this argument, the radius of ^{51}Fe should be slightly larger than the radius of ^{51}Mn . But, since this adds extra degrees of freedom, more experimental data are required.

In summary, the lifetimes of the $27/2^-$ states in the $A = 51$ mirror nuclei have been measured. Utilizing the results provides an unique way to investigate the effective charges near ^{56}Ni . A detailed comparison with large-scale shell-model calculations gives effective charges of $\varepsilon_n \sim 0.80$ and $\varepsilon_p \sim 1.15$ for the neutron and proton, respectively.

We would like to express our gratitude to I. Hamamoto for valuable discussions. We thank the accelerator crew at LNL for the excellent support. This research was supported in part by the Swedish Research Council, the European Commission under Contract No. HPRI-1999-CT-00083, and the European Community programme IHP under Contract No. HPMF-CT-2002-02018.

- [1] *Isospin in Nuclear Physics*, edited by D.H. Wilkinson (North-Holland Publishing Company, Amsterdam, 1969).
- [2] A. Poves, J. Sanchez-Solano, E. Caurier, and F. Nowacki, Nucl. Phys. **A694**, 157 (2001).
- [3] A. P. Zuker *et al.*, Phys. Rev. Lett. **89**, 142502 (2002).
- [4] S. J. Williams, Ph.D. thesis, Keele University, 2003 (unpublished).
- [5] J. Ekman, Ph.D. thesis, Lund University, 2004, ISBN 91-628-6061-5.
- [6] D. Tonev *et al.*, Phys. Rev. C **65**, 034314 (2002).
- [7] M. A. Bentley *et al.*, Phys. Rev. C **62**, 051303(R) (2000).
- [8] J. Ekman *et al.*, Eur. Phys. J. A **9**, 13 (2000).
- [9] J. Ekman *et al.*, Phys. Rev. C **70**, 014306 (2004).
- [10] J.W. Noe and P. Gural, *Proceedings of the International Conference on Medium-Light Nuclei, Florence, Italy, 1978*, edited by P. Blasi and R.A. Ricci (Editrice Compositori, Bologna, 1978), p. 459.
- [11] A. Dewald *et al.*, Nucl. Phys. **A545**, 822 (1992).
- [12] C. Rossi Alvarez, Nucl. Phys. News **3**, 3 (1993).
- [13] E. Caurier, shell-model code ANTOINE, IRES, Strasbourg, 1989.
- [14] E. Caurier and F. Nowacki, Acta Phys. Pol. **30**, 705 (1999).
- [15] A. Bohr and B.R. Mottelson, *Nuclear Structure* (Benjamin Inc., New York, 1975), Vol. 2, Chap. 6.
- [16] A. Blazhev *et al.*, Phys. Rev. C **69**, 064304 (2004).

Paper IV

LIFETIME MEASUREMENTS IN THE $A = 51$ MIRROR NUCLEI

R. DU RIETZ*, J. EKMAN, C. FAHLANDER, and D. RUDOLPH

Department of Physics, Lund University, S-22100 Lund, Sweden

*rickard.du_rietz@nuclear.lu.se

Following the heavy-ion fusion-evaporation reaction $^{32}\text{S} + ^{24}\text{Mg}$ at 95 MeV beam energy the lifetimes of analogue states in the $T_z = \pm 1/2$ $A=51$ mirror nuclei ^{51}Fe and ^{51}Mn have been measured using the Cologne plunger device coupled to the GASP γ -ray spectrometer. The deduced $B(E2; 27/2^- \rightarrow 23/2^-)$ values allow to probe isoscalar and isovector polarization charges and to derive effective proton and neutron charges, ϵ_p and ϵ_n , in the fp shell. A comparison between the experimental results and several different large-scale shell-model calculations yields $\epsilon_p \sim 1.15 e$ and $\epsilon_n \sim 0.80 e$.

Keywords: effective charges, lifetimes, mirror nuclei, nuclear shell model

In the isospin formalism the proton and neutron are treated as two different quantum states of the same particle, the nucleon. The assumption of isospin symmetry relies on the fact that the nucleon-nucleon interaction is charge symmetric and charge independent. In reality, however, the isospin symmetry is broken by the Coulomb interaction between protons [1]. Effects of isospin symmetry breaking can be differences in excitation energies or electromagnetic properties in mirror nuclei, which are pairs of nuclei with the number of protons and neutrons interchanged. The electromagnetic properties can give information on core polarization effects due to the valence particles outside closed shells, if the configurations of valence particles are taken care of by large-scale shell-model calculations. To account for the polarization effect in theoretical models effective nucleon charges, which are the sum of the bare charges and the polarization charge, are introduced. As the wave functions of analogue states in mirror nuclei are to first order identical under the exchange of protons and neutrons, the study of mirror nuclei offers a unique opportunity to access, probe, and pin down the effective charges. In this contribution we present novel results on effective charges for the $A=51$ mirror nuclei ^{51}Fe and ^{51}Mn [2].

The results are based on determined lifetimes of analogue states in the $A=51$ mirror nuclei in combination with theoretical large-scale shell-model calculations. The lifetimes were measured in an experiment performed at the Legnaro National Laboratory utilizing a heavy-ion fusion-evaporation reaction $^{32}\text{S} + ^{24}\text{Mg}$ with a beam energy of 95 MeV. The ^{24}Mg target was mounted inside the Cologne plunger device [3] in front of a stretched gold stopper foil and data were collected at 21 target-stopper distances ranging from electric contact to 4.0 mm. The two mirror nuclei, ^{51}Fe and ^{51}Mn , were produced via the evaporation of one α particle and one neutron ($1\alpha 1n$ channel) and one α particle and one proton ($1\alpha 1p$ channel), respectively. The γ -rays were detected with the GASP detector array [4] using its 40 HPGe detectors (distributed in seven rings at 34.6° , 59.4° , 72.0° , 90.0° , 108.0° , 120.6° and 145.4°) and 74 BGO elements. The event trigger accepted events with at least one BGO element and two HPGe detectors firing in coincidence. At the end of the experiment ^{56}Co , ^{133}Ba , and ^{152}Eu standard sources were used to calibrate the detector system.

The lifetime analysis is based on coincidence spectroscopy using data sorted into $\gamma\gamma$ coincidence matrices. For each distance the events were sorted with γ rays detected in one or several given detector rings placed along one axis and γ rays detected anywhere in the array along the second axis of the matrix. Coincidence spectra are obtained by defining a γ -energy gate on one of the axes. The width and placement of the γ -energy gate can be determined by inspecting the total projection, i.e. the projection of the whole $\gamma\gamma$ matrix onto one axis. Figure 1 shows the total projection (a) and a spectra gated on the 237 keV transition in ^{51}Mn (b) using all detector rings for data taken at a target-stopper

distance of 1200 μm . Due to the relatively long distance Doppler shifted components can be observed for some of the transitions in the gated ^{51}Mn spectra. The quality of the gated spectra strongly depends on the gate conditions, i.e. how the peak and background is chosen, and the setting of the γ -energy gate was reworked several times to optimize the result.

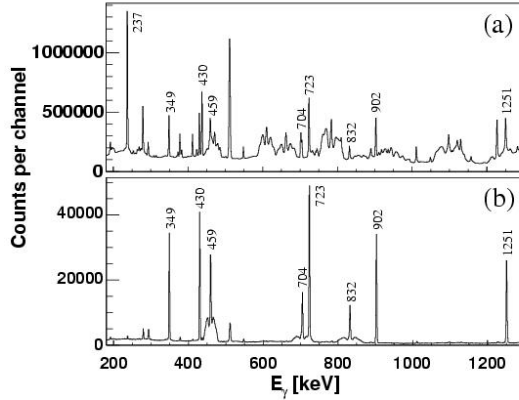


Fig 1: (a) Total projection of a gg coincidence matrix for data taken at a target-stopper distance of 1200 μm . Panel (b) is in coincidence with the 237 keV transition in ^{51}Mn . Energy labels of the peaks are in keV and correspond to transitions in ^{51}Mn .

The method used to determine the lifetimes of the analogue $27/2^-$ states in the $A=51$ mirror pair is based on the very specific features of their level schemes [5]. They consist of essentially three regimes: the transitions below the isomeric $17/2^-$ states ($\tau \sim 3$ ns), those feeding into the long-lived ($\tau \sim 100$ ps) $27/2^-$ states, and the short-lived states in between. Due to the isomeric $17/2^-$ states low-lying transitions are essentially always emitted from stopped residues independently of the target-stopper distance used. Thus for spectra taken in coincidence with these low-lying transitions it is possible to apply the Recoil Distance Doppler Shift method to the transitions between the $27/2^-$ and the $17/2^-$ states. To avoid that Doppler shifted and unshifted components interfere only the two most forward and two most backward detector rings are used, for which the two components of the coincident transitions are well separated. This interference effect is mostly observed for the larger target-stopper distances due to that relatively more γ -rays are emitted in-flight than as stopped. Figure 2 illustrate how the target-stopper distance affects the intensities of the stopped and Doppler shifted components. The spectra are obtained by gating on the low-energy 253 keV $7/2^- \rightarrow 5/2^-$ transition in ^{51}Fe for distances of 400 μm (Fig. 2a) and 2000 μm (Fig. 2b). For the short distance the four transitions at 636, 777, 884, and 893 keV in ^{51}Fe are clearly seen as stopped peaks. When increasing the distance to 2000 μm the stopped components of the two transitions at 777 and 884 keV are significantly reduced and Doppler shifted components arise on each side of the stopped peaks. The 636 and 893 keV transitions are still observed as stopped peaks, because they are situated below the isomeric $17/2^-$ state and the flight distance is still rather short with respect to its lifetime.

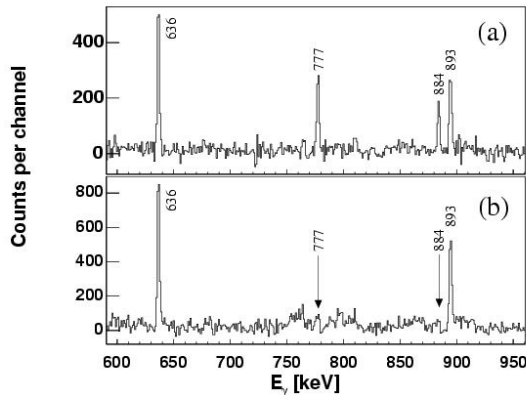


Fig 2: Spectra taken in coincidence with the $7/2^- \rightarrow 5/2^-$ 253 keV transition in ^{51}Fe for the two most forward and two most backward detector rings of GASP. Panel (a) shows a spectrum obtained with target-stopper distance 400 μm and panel (b) for the distance 2000 μm . Energy labels of the peaks are in keV.

The analysis of the same transition for different distances requires a normalization of its intensity due to, e.g., different beam currents or measuring times. To obtain these normalization coefficients for each distance, the intensities of the unshifted and Doppler shifted components for the 459 and 832 keV transitions observed in all detector rings were summed up in spectra in coincidence with the 237 keV ground-state transition in ^{51}Mn . As the relative statistics of ^{51}Mn and ^{51}Fe in the collected data is the same for different distances the same normalization coefficients can be used for both nuclei, i.e. used to normalize the intensities of transitions from both ^{51}Mn and ^{51}Fe . Furthermore, to perform an analysis of the very weakly populated ^{51}Fe nucleus the measured distances were needed to be recombined into nine effective distances: 6.5(1), 17.7(1), 42.7(7), 125(3), 404(11), 701(16), 1198(29), 1984(60), and 4000(100) μm . This merge was done using the extracted normalization coefficients as weighting factors and the effect on the result from nine distances compared to all 21 distances was investigated using the ^{51}Mn sample where each individual distance can be used in the analysis. Each target-distance was converted to flight time using the recoil velocity derived from the positions of the stopped and Doppler shifted components of the intense 1500 keV $21/2^- \rightarrow 19/2^-$ transition in ^{51}Mn . The velocities range from 3.7% to 4.1% of the speed of light for the three different targets used during the experiment. The resulting lifetimes of the $27/2^-$ states in ^{51}Mn and ^{51}Fe with the corresponding $B(E2; 27/2^- \rightarrow 23/2^-)$ are listed in Table 1. The $B(E2)$ values are calculated as

$$B(E2) = \frac{816.2}{\tau \cdot E_\gamma^5},$$

using the extracted lifetimes and $E_\gamma = 704.4(5)$ keV and $E_\gamma = 777.1(5)$ keV for ^{51}Mn and ^{51}Fe , respectively. The ratio, R, between the $B(E2)$ values of the mirror transitions in ^{51}Fe and ^{51}Mn amounts to $R = 0.884(22)$.

Table 1: Values for the extracted lifetimes and the corresponding $B(E2)$ values for the $27/2^-$ analogue states in the mirror nuclei ^{51}Mn and ^{51}Fe

	Lifetime [ps]	$B(E2)$ [$e^2\text{fm}^4$]	$B(E2)$ [W.u.]
^{51}Mn	$100.7 \pm 1.2 \pm 3$	46.7(14)	4.16(12)
^{51}Fe	$69.7 \pm 1.6 \pm 3$	41.3(24)	3.68(21)

The systematic uncertainties in the lifetimes are related to the normalization and the exact determination of the yield of the stopped component at large distances. Other contributions are the possible short-lived ($\tau < 1$ ps, cf. [5]) feeding into the $27/2^-$ state and the combination of the measured distances into nine effective distances, which is necessary for the analysis of ^{51}Fe .

To study the consequences of the lifetime results on polarization and effective charges large-scale shell-model calculations were performed using the shell-model code ANTOINE [6, 7]. The calculations employ the full fp space containing the $1f_{7/2}$ orbit below and the $2p_{3/2}$, $1f_{5/2}$, and $2p_{1/2}$ orbits above the $N, Z=28$ shell closure. The configuration space was truncated to allow for excitations of up to five particles across the shell closure. This configuration space provides predictions more or less indistinguishable from calculations using the full fp space [8]. Three interactions have been studied: The standard KB3G interaction without any Coulomb interaction, with theoretical harmonic-oscillator Coulomb matrix elements (Coulomb HO), and with the $1f_{7/2}$ Coulomb matrix elements replaced with the experimental values from the $A=42$ mirror pair (Coulomb A42). The effective proton and neutron charges, ε_p and ε_n , are introduced to account for polarization effects of the valence nucleons on the otherwise inert core of the shell-model calculation. The effective nucleon charges are expanded in terms of isoscalar and isovector polarization charges, $e_{\text{pol}}^{(0)}$ and $e_{\text{pol}}^{(1)}$, such as

$$\varepsilon_p = 1 + e_{\text{pol}}^{(0)} - e_{\text{pol}}^{(1)} \quad \text{and} \quad \varepsilon_n = e_{\text{pol}}^{(0)} + e_{\text{pol}}^{(1)},$$

for protons and neutrons, respectively. The isoscalar and isovector polarization charges arise from the virtual excitation of the isoscalar and isovector giant quadrupole resonances of the core and it is predicted that $e_{\text{pol}}^{(0)} \sim 0.5$ and $e_{\text{pol}}^{(1)} \sim 0.32$ in the case of $N \sim Z$ nuclei [9]. The polarization charges are used as input parameters to the simulations and are varied to reproduced the experimental $B(E2)$ values (see Table 1). It was found that $e_{\text{pol}}^{(0)} \approx 0.47$ and $e_{\text{pol}}^{(1)} \approx 0.32$ by en large independently of the used interaction, which is in good agreement with the predicted values. This corresponds to the effective nucleon charges $\varepsilon_p \sim 1.15 e$ and $\varepsilon_n \sim 0.80 e$ for protons and neutrons, respectively. It is intriguing that the numbers result in effective charges similar to recently refined estimates in the ^{100}Sn region (cf. Ref. [10], and references therein). A more detailed description of the performed investigation on effective charges can be found in Ref. [2].

We would like to thank all colleagues participating in the experiment and the accelerator crew at LNL for the excellent support. Especially we thank the people in Cologne for their help with the lifetime analysis. Furthermore, we would like to express our gratitude to I. Hamamoto for valuable discussions. This research was supported in part by the Swedish Research Council, the European Commission under contract number HPRI-1999-CT-00083, and the European Community programme IHP under contract number HPMF-CT-2002-02018.

References

- [1] Isospin in Nuclear Physics, edited by D. H. Wilkinson (North-Holland Publishing Company, Amsterdam, 1969).
- [2] R. du Rietz *et al.*, Phys. Rev. Lett. **93**, 222501 (2004).
- [3] A. Dewald *et al.*, Nucl. Phys. **A545**, 822 (1992).
- [4] C. Rossi Alvarez, Nuclear Physics News, Vol. **3**, 3 (1993).
- [5] J. Ekman *et al.*, Phys. Rev. C **70**, 014306 (2004).
- [6] E. Caurier, shell model code ANTOINE, IRES, Strasbourg 1989-2002.
- [7] E. Caurier, F. Nowacki, Acta Phys. Pol. **30**, 705 (1999).
- [8] A. Poves, J. Sanchez-Solano, E. Caurier, and F. Nowacki, Nucl. Phys. **A694**, 157 (2001).
- [9] A. Bohr and B.R. Mottelson, Nuclear Structure Vol. 2 (Benjamin Inc., New York, 1975), chap 6.
- [10] A. Blazhev *et al.*, Phys. Rev. C **69**, 064304 (2004).

Paper V

A Shell-Model Study of ^{53}Fe

R. du Rietz¹, D. Rudolph¹, J. Ekman¹, C. Fahlander¹, C. Andreoiu¹, M. Axiotis², M.A. Bentley³, M.P. Carpenter⁴, C. Chandler³, R. Charity⁵, R. M. Clark⁶, M. Cromaz⁶, A. Dewald⁷, G. de Angelis², F. Della Vedova⁸, P. Fallon⁶, A. Gadea², G. Hammond³, E. Ideguchi⁵, S.M. Lenzi⁸, A. O. Macchiavelli⁶, N. Mărginean², M. N. Mineva¹, O. Möller⁷, D.R. Napoli², M. Nespolo², W. Reviol⁵, C. Rusi², B. Saha⁷, D. G. Sarantites⁵, D. Seweryniak⁴, D. Tonev², and S. J. Williams³

¹*Department of Physics, Lund University, S-22100 Lund, Sweden*

²*Instituto Nazionale di Fisica Nucleare, Laboratori Nazionali di Legnaro, I-35020 Legnaro, Italy*

³*School of Chemistry and Physics, Keele University, Keele, Staffordshire ST5 5BG, United Kingdom*

⁴*Physics Division, Argonne National Laboratory, Argonne, IL 60439*

⁵*Chemistry Department, Washington University, St. Louis, MO 63130*

⁶*Nuclear Science Division, Lawrence Berkeley National Laboratory, Berkeley, CA 94720*

⁷*Institut für Kernphysik der Universität zu Köln, D-50937 Köln, Germany*

⁸*Dipartimento di Fisica dell'Università and INFN, Sezione di Padova, I-35141 Padova, Italy*

(Dated: January 19, 2005)

The fusion-evaporation reactions $^{28}\text{Si}(^{32}\text{S},1\alpha2p1n)^{53}\text{Fe}$ at 125 MeV and $^{24}\text{Mg}(^{32}\text{S},2p1n)^{53}\text{Fe}$ at 95 MeV beam energy were used to investigate excited states in ^{53}Fe . The combination of the Gammasphere Ge-detector array and ancillary devices led to the construction of an extensive level scheme comprising some 90 transitions connecting 40 states. Lifetimes of a number of states were derived using the Cologne plunger device coupled to the GASP γ -ray spectrometer. The experimental results are compared to large-scale shell-model calculations using different sets of two-body matrix-elements. In particular, the influence of effective charges and effective gyromagnetic factors on the predictions concerning electromagnetic decay properties such as lifetimes, branching ratios, and mixing ratios is studied.

PACS numbers: 21.60.Cs, 23.20.En, 23.20.Lv, 27.40.+z

I. INTRODUCTION

Nuclei in the vicinity of the doubly magic $N = Z$ nuclei ^{40}Ca and ^{56}Ni as well as $N \sim Z$ nuclei near the middle of the $1f_{7/2}$ shell are well described by large-scale shell-model calculations within the full fp model space [1]. These nuclei offer the possibility for detailed investigations of a large variety of phenomena through the comparison between comprehensive and concise experimental data and theoretical predictions. Examples range from 'complete' spectroscopy via the subject of band termination to the possible influence of isospin $T = 0$ or $T = 1$ neutron-proton pairing and isospin symmetry studies in pairs of $T_z = \pm 1/2$ or $T_z = \pm 1$ mirror nuclei.

The latter investigations are always based on a comparison of excitation energies of analogue states in so-called Mirror Energy Difference diagrams, which require well established level schemes of both mirror partners. Such an investigation has recently been presented for the yrast structures in the $A = 53$ mirror pair [2]. While the experimental information on the neutron-deficient partner often is limited to excitation energies and spins and parities of the excited states, detailed spectroscopy including electromagnetic decay properties can be derived — and thus probed — in the less exotic member of the mirror pair. In turn, these more detailed tests of the interactions and Coulomb effects included in the large-scale shell-model calculations may help to obtain a better understanding of the origin and importance of certain isospin breaking contributions.

This work presents a largely extended level scheme for the ^{53}Fe nucleus including lifetimes of a few excited states. Previously known low-lying excited states in ^{53}Fe [3] are either adopted or confirmed in the final level scheme. A preliminary analysis of the present data set is described in Ref. [4], which includes also additional information from the experiment described in Ref. [2]. The experimental results are compared to large-scale shell-model calculations using four different interactions common for the fp model space. In these calculations the effective charges in the mass $A \sim 50$ –60 region derived in Ref. [5] are employed, and an investigation of effective g factors is performed. In particular, the agreement between experimental and calculated electromagnetic properties such as lifetimes, branching ratios, and mixing ratios is studied.

II. EXPERIMENTS

The present work is based on data from three experiments, of which two experiments were performed under nearly identical conditions using the Argonne Tandem-Linac Accelerator System at Argonne National Laboratory and the 88-inch cyclotron at Lawrence Berkeley National Laboratory. These two experiments employed the $^{28}\text{Si}(^{32}\text{S},1\alpha2p1n)^{53}\text{Fe}$ fusion-evaporation reaction at an effective beam energy on target of 125 MeV. The ^{28}Si targets were enriched to 99.90% and had a thickness of 0.5 mg/cm^2 . They were supported with a 1 mg/cm^2 Au

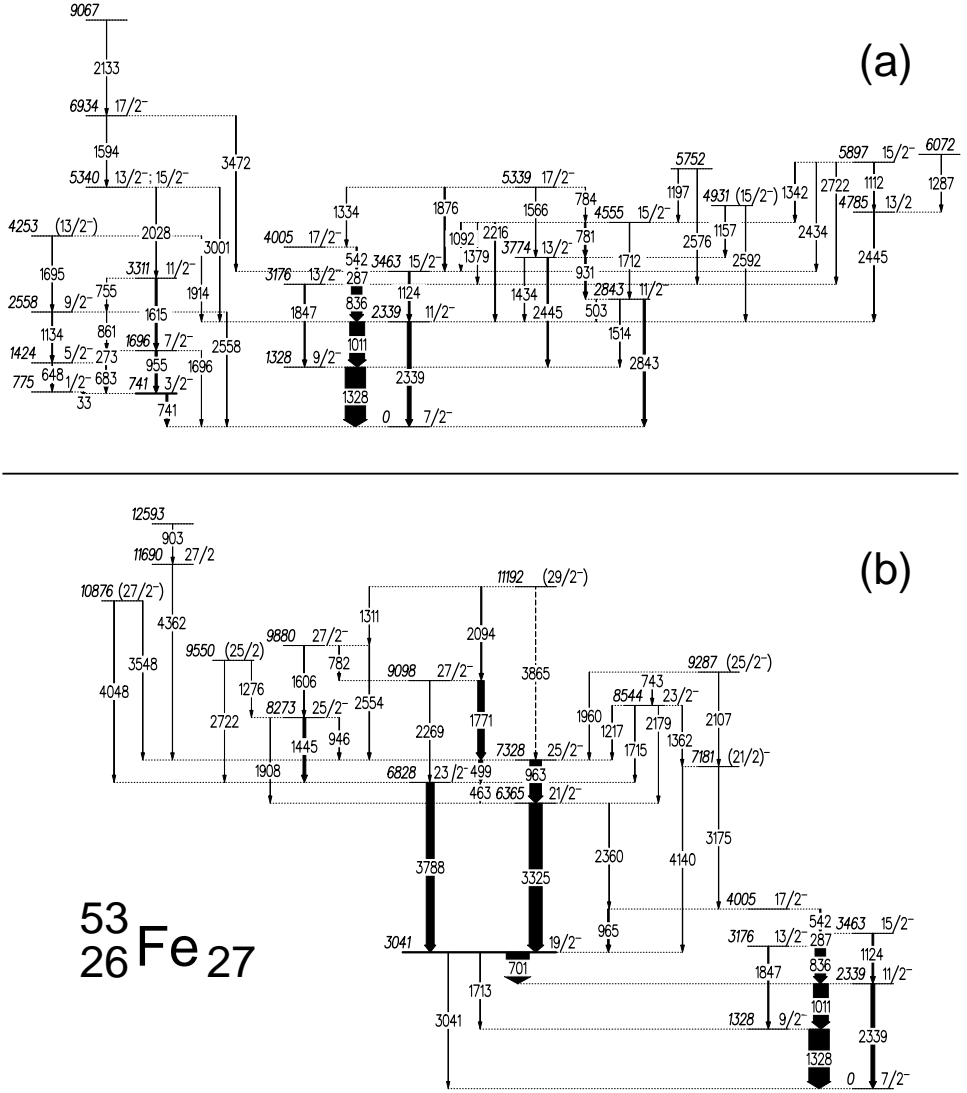


FIG. 1: The proposed level scheme of ^{53}Fe . The top panel (a) provides the 'low-spin' regime, which was in part known from previous studies [3], while the bottom panel (b) focuses on the 'high-spin' part, which is build upon the 3041 keV $19/2^-$ spin gap isomer. Energy labels are in keV. The thickness of the arrows corresponds to the relative intensities of the transitions. Tentative transitions are dashed.

TABLE I: The energies of excited states in ^{53}Fe , the transition energies and relative intensities of the γ rays placed in the level scheme, angular distribution ratios, DCO ratios, the spins and parities of the initial and final states of the γ rays.

E_x (keV)	E_γ (keV)	I_{rel} (%)	R_{150-97}	R_{DCO} 150°-97°	$Mult.$ Ass.	I_i^π (\hbar)	I_f^π (\hbar)
741.1(1) ^a	741.1(1) ^a	^b			<i>E2</i>	3/2 ^{-a}	7/2 ⁻
775.4(4) ^a	33.3(1) ^a	^b			<i>M1</i>	1/2 ^{-a}	3/2 ⁻
1328.3(4)	1328.4(6)	100(3)	0.56(2)	0.81(7) ^c	<i>E2/M1</i>	9/2 ⁻	7/2 ⁻
1423.7(2)	648.3(2)	1.8(2)	1.26(17)		<i>E2</i>	5/2 ^{-a}	1/2 ⁻
	682.6(2)	5.2(2)	1.08(8)		<i>E2/M1</i>	5/2 ⁻	3/2 ⁻
1696.4(2)	272.8(1)	0.9(2)	0.60(7)		<i>E2/M1</i>	7/2 ^{-a}	5/2 ⁻
	955.3(5)	11(1)	1.13(8)		<i>E2</i>	7/2 ⁻	3/2 ⁻
	1696(1)	0.6(1)			$\Delta I = 0$	7/2 ⁻	7/2 ⁻
2339.4(3)	1010.5(5)	72(2)	0.62(3)	0.86(8) ^c	<i>E2/M1</i>	11/2 ⁻	9/2 ⁻
	2339(1)	15(2)	1.18(7)	1.58(28) ^c	<i>E2</i>	11/2 ⁻	7/2 ⁻
2557.9(4)	861.3(4)	1.6(3)	0.75(9)		<i>M1</i>	9/2 ⁻	7/2 ⁻
	1134.2(6)	4.8(4)	1.26(17)		<i>E2</i>	9/2 ⁻	5/2 ⁻
	2558(1)	1.5(3)			<i>E2/M1</i>	9/2 ⁻	7/2 ⁻
2842.6(4)	503.1(4)	1.8(3)			$\Delta I = 0$	11/2 ⁻	11/2 ⁻
	1514(1)	1.2(2)	0.69(14)		<i>M1</i>	11/2 ⁻	9/2 ⁻
	2843(1)	12(1)	1.22(9)		<i>E2</i>	11/2 ⁻	7/2 ⁻
3040.6(3)	701.1(1) ^a	^b			<i>E4</i>	19/2 ^{-a}	11/2 ⁻
	1712.6(3) ^a	^b			<i>M5</i>	19/2 ⁻	9/2 ⁻
	3040.6(5) ^a	^b			<i>E6</i>	19/2 ⁻	7/2 ⁻
3175.8(4)	836.4(4)	50(2)	0.66(3)	0.50(9)	<i>E2/M1</i>	13/2 ⁻	11/2 ⁻
	1847(1)	6.2(6)	1.32(10)	1.36(31) ^c	<i>E2</i>	13/2 ⁻	9/2 ⁻
3311.2(6)	755.2(5)	2.2(5)			<i>E2/M1</i>	11/2 ⁻	9/2 ⁻
	1614.9(8)	10(1)	1.13(8)	0.92(14)	<i>E2</i>	11/2 ⁻	7/2 ⁻
3463.0(4)	287.1(1)	38(1)	0.74(3)	0.64(12)	<i>M1</i>	15/2 ⁻	13/2 ⁻
	1123.6(6)	8.7(8)	1.39(11)		<i>E2</i>	15/2 ⁻	11/2 ⁻
3773.8(5)	931.0(5)	7.8(5)	0.57(5)	0.45(10)	<i>E2/M1</i>	13/2 ⁻	11/2 ⁻
	1434(1)	2.5(3)	0.68(9)		<i>M1</i>	13/2 ⁻	11/2 ⁻
	2445(1)	7.7(9)	1.17(16)		<i>E2</i>	13/2 ⁻	9/2 ⁻
4005.2(4)	542.2(2)	6.6(3)	0.70(5)	1.25(27) ^c		17/2 ⁻	15/2 ⁻
	965.0(6)	8.0(8)			<i>E2/M1</i>	17/2 ⁻	19/2 ⁻
4253.2(8)	1695(1)	2.6(4)	1.29(14)		(<i>E2</i>)	(13/2 ⁻)	9/2 ⁻
	1914(1)	1.8(4)	0.91(15)		(<i>E2/M1</i>)	(13/2 ⁻)	11/2 ⁻
4554.8(4)	780.7(4)	8.2(5)	0.76(8)		<i>M1</i>	15/2 ⁻	13/2 ⁻
	1091.8(6)	2.9(4)	1.41(15)		$\Delta I = 0$	15/2 ⁻	15/2 ⁻
	1244(1) ^d	0.6(2)			<i>E2</i>	15/2 ⁻	11/2 ⁻
	1379.1(7)	1.4(2)			<i>E2/M1</i>	15/2 ⁻	13/2 ⁻
	1712(1)	2.6(3)			<i>E2</i>	15/2 ⁻	11/2 ⁻
	2216(1)	4.9(4)			<i>E2</i>	15/2 ⁻	11/2 ⁻
4784.7(8)	2445(1)	4.5(9)	0.82(10)		$\Delta I = 1$	13/2 ⁻	11/2 ⁻
4930.9(9)	1157(1)	3.2(5)	0.94(14)		(<i>E2/M1</i>)	(15/2 ⁻)	13/2 ⁻
	2592(2)	1.9(3)	1.47(21)		(<i>E2</i>)	(15/2 ⁻)	11/2 ⁻
5339.3(5)	784.4(5)	1.4(4)			<i>M1</i>	17/2 ⁻	15/2 ⁻
	1334(1)	1.2(4)			$\Delta I = 0$	17/2 ⁻	17/2 ⁻
	1566(1)	2.3(4)			<i>E2</i>	17/2 ⁻	13/2 ⁻
	1876(1)	6.8(3)	0.66(5)	0.85(21) ^c	<i>E2/M1</i>	17/2 ⁻	15/2 ⁻
5339.6(9)	2028(1)	2.9(5)				13/2 ⁻ ; 15/2 ⁻	11/2 ⁻
	3001(2)	3.0(7)				13/2 ⁻ ; 15/2 ⁻	11/2 ⁻
5751.5(7)	1196.7(6)	1.3(3)					15/2 ⁻
	1746(1) ^d	2.2(4)					17/2 ⁻
	2576(2)	0.8(2)					13/2 ⁻
5896.9(7)	1112(1)	1.0(3)			$\Delta I = 1$	15/2 ⁻	13/2 ⁻
	1342.1(7)	2.3(5)			$\Delta I = 0$	15/2 ⁻	15/2 ⁻
	1892(1) ^d	1.5(3)			$\Delta I = 1$	15/2 ⁻	17/2 ⁻
	2434(2)	1.0(2)	1.14(21)		$\Delta I = 0$	15/2 ⁻	15/2 ⁻
	2722(2)	1.6(2)	0.33(8)		<i>E2/M1</i>	15/2 ⁻	13/2 ⁻
6071.8(11)	1287.1(7)	1.3(2)					13/2 ⁻
6365.1(11)	2360(2)	0.8(2)	1.51(33)		<i>E2</i>	21/2 ⁻	17/2 ⁻
	3325(2)	64(2)	1.70(7)	1.33(9)	<i>E2/M1</i>	21/2 ⁻	19/2 ⁻

TABLE I: Continued.

E_x (keV)	E_γ (keV)	I_{rel} (%)	R_{150-97}	R_{DCO} 150°-97°	Mult. Ass.	I_π^π (h)	I_π^π (h)
6689.0(20)	3226(2) ^d	2.4(5)	0.18(5)		<i>E2/M1</i>	17/2 ⁻	15/2 ⁻
6828.3(11)	463.2(4)	0.6(1)			<i>M1</i>	23/2 ⁻	21/2 ⁻
	3788(2)	39(1)	1.36(6)		<i>E2</i>	23/2 ⁻	19/2 ⁻
6933.8(13)	1594(1)	2.2(6)				17/2 ⁻	13/2 ⁻ ; 15/2 ⁻
	3472(3)	1.2(3)	0.36(12)		<i>E2/M1</i>	17/2 ⁻	15/2 ⁻
7139.0(30)	3676(3) ^d	1.8(4)	1.20(24)		(<i>E2</i>)	(19/2 ⁻)	15/2 ⁻
7181.0(12)	3175(2)	2.0(4)	1.47(19)		(<i>E2</i>)	(21/2 ⁻)	17/2 ⁻
	4140(3)	2.2(2)			(<i>E2/M1</i>)	(21/2 ⁻)	19/2 ⁻
7214.0(30)	3751(3) ^d	1.4(3)					15/2 ⁻
7327.5(11)	499.3(2)	20(1)	1.09(5)	0.79(7)	<i>E2/M1</i>	25/2 ⁻	23/2 ⁻
	962.6(5)	57(2)	1.26(5)		<i>E2</i>	25/2 ⁻	21/2 ⁻
8273.4(11)	945.8(6)	3.4(3)	1.47(10)	1.12(27)	$\Delta I = 0$	25/2 ⁻	25/2 ⁻
	1445(1)	14(1)	1.01(6)	0.65(9)	<i>E2/M1</i>	25/2 ⁻	23/2 ⁻
	1908(1)	0.5(2)	1.13(23)		<i>E2</i>	25/2 ⁻	21/2 ⁻
8543.8(11)	1217(1)	0.5(2)	0.51(11)		<i>E2/M1</i>	23/2 ⁻	25/2 ⁻
	1362(1)	0.6(3)			(<i>E2/M1</i>)	23/2 ⁻	(21/2 ⁻)
	1715(1)	0.6(2)	1.27(37)		$\Delta I = 0$	23/2 ⁻	23/2 ⁻
	2179(2)	0.6(2)	1.70(39)		<i>E2/M1</i>	23/2 ⁻	21/2 ⁻
9066.8(16)	2133(1)	1.4(2)					17/2 ⁻
9098.0(13)	1771(1)	32(2)	0.95(4)	0.77(7)	<i>E2/M1</i>	27/2 ⁻	25/2 ⁻
	2269(2)	0.3(1)			<i>E2</i>	27/2 ⁻	23/2 ⁻
9287.4(12)	743(1)	0.6(3)			(<i>M1</i>)	(25/2 ⁻)	23/2 ⁻
	1960(1)	1.0(2)	1.14(27)		($\Delta I = 0$)	(25/2 ⁻)	25/2 ⁻
	2107(1)	1.1(3)			(<i>E2</i>)	(25/2 ⁻)	(21/2 ⁻)
9549.6(14)	1276(1)	0.4(2)			($\Delta I = 0$)	(25/2 ⁻)	25/2 ⁻
	2722(2)	0.6(2)	0.72(22)		($\Delta I = 1$)	(25/2 ⁻)	23/2 ⁻
9880.3(13)	782.3(5)	0.7(2)			$\Delta I = 0$	27/2 ⁻	27/2 ⁻
	1606(1)	3.4(4)	0.99(11)	0.68(19)	<i>E2/M1</i>	27/2 ⁻	25/2 ⁻
	2554(2)	3.5(3)	1.59(15)		<i>E2/M1</i>	27/2 ⁻	25/2 ⁻
10875.8(26)	3548(3)	0.6(2)			(<i>E2/M1</i>)	(27/2 ⁻)	25/2 ⁻
	4048(4)	0.8(3)	1.17(50)		(<i>E2</i>)	(27/2 ⁻)	23/2 ⁻
11191.7(14)	1311(1)	0.4(2)			(<i>E2/M1</i>)	(29/2 ⁻)	27/2 ⁻
	2094(1)	6.0(5)	1.43(10)	1.02(26)	(<i>E2/M1</i>)	(29/2 ⁻)	27/2 ⁻
	3865(3)	0.5(2)			(<i>E2</i>)	(29/2 ⁻)	25/2 ⁻
11689.5(32)	4362(3)	1.4(2)	0.54(11)		$\Delta I = 1$	27/2	25/2 ⁻
12592.9(32)	903.4(6)	0.8(2)					27/2

^aAdopted from Ref. [3].

^bCannot be determined in the present experiment due to the long lifetime of the initial state.

^cThe pure, stretched 287 keV 15/2⁻ → 13/2⁻ *M1* transition is used for gating.

^dNot included in the level scheme displayed in Fig. 1.

and Ta foil, respectively, which was directed towards the beam. The γ rays were detected in the Gammasphere array [6], which comprised 78 Ge-detectors. The Heavimet collimators were removed to allow for γ -ray multiplicity and sum-energy measurements [7]. For the detection of light charged particles the 4 π CsI-array Microball [8] was used, and evaporated neutrons were measured in the Neutron Shell [9], which consists of 30 liquid-scintillator detectors replacing the 30 most forward Ge-detectors of Gammasphere. Events with four or more Ge detectors in coincidence or more than three Ge detectors and one neutron in coincidence were written to magnetic tape. At

the end of the experiments data were taken with ⁵⁶Co, ¹³³Ba, and ¹⁵²Eu standard sources to calibrate the Ge detectors.

The third experiment was conducted at Legnaro National Laboratory, Italy, using the ²⁴Mg(³²S,2p1n)⁵³Fe fusion-evaporation reaction with a beam energy of 95 MeV. The 99.92% isotopically enriched and on average 0.95 mg/cm² thick ²⁴Mg target was mounted inside the Cologne plunger device [10] in front of a stretched 13 mg/cm² gold stopper foil. Data were taken at 21 target-stopper distances ranging from electric contact to 4.0 mm. The γ rays were detected with the GASP detec-

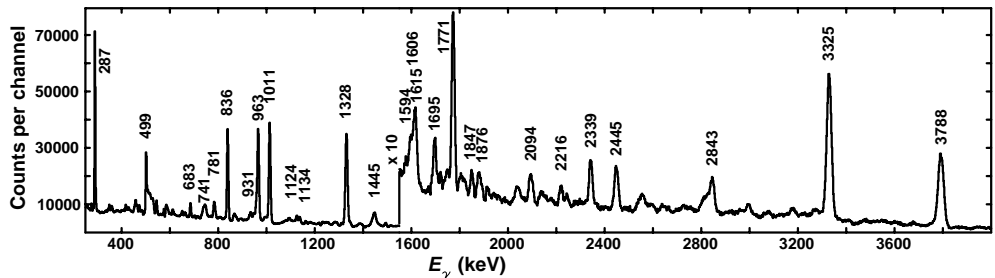


FIG. 2: Gamma-ray spectrum in coincidence with one α particle, two protons, and one neutron from the two Gammasphere experiments. Small contaminations from ^{52}Mn , $^{54,55}\text{Fe}$, and ^{56}Co were carefully subtracted (see text for details). The most intense transitions are labelled with their energies in keV.

tor array [11] using its 40 HPGe detectors (distributed in seven rings at $r_0 = 34.6^\circ$, $r_1 = 59.4^\circ$, $r_2 = 72.0^\circ$, $r_3 = 90.0^\circ$, $r_4 = 108.0^\circ$, $r_5 = 120.6^\circ$ and $r_6 = 145.4^\circ$) and 74 BGO elements. Events with at least one BGO element and two HPGe detectors firing in coincidence were accepted by the event trigger. At the end of the experiment ^{56}Co , ^{133}Ba , and ^{152}Eu standard sources were used to calibrate the detector system.

III. DATA ANALYSIS

A. The Gammasphere experiments

The details of the data analysis of the two Gammasphere experiments have been described earlier [4, 12–14]. In short, clean particle gated γ -ray spectra are obtained by employing pulse-shape discrimination techniques to distinguish between protons and α particles detected in Microball and to discriminate between neutrons and γ rays detected in the Neutron Shell. The detection efficiencies for the evaporated particles amount to some 65% for protons, 50% for α particles, and 25% for neutrons. In addition, an event-by-event kinematic reconstruction method was applied to reduce the effect of the Doppler broadening caused by the evaporated particles.

The $1\alpha 2p 1n$ reaction channel leads to ^{53}Fe . In the course of the analysis E_γ projections and E_γ - E_γ matrices in coincidence with one α particle, two protons, and one neutron were studied by means of the Radware software package and the spectrum-analysis code TV [15, 16] to construct the level scheme and derive the relative intensities of the transitions. Weak contaminations in the $1\alpha 2p 1n$ -gated spectra arose from the $1\alpha 3p 1n$ channel ^{52}Mn , i.e., when a proton escaped detection, from the $3p 1n$ and $4p 1n$ channels ^{56}Co and ^{55}Fe , i.e., when one or two protons were misidentified as an α particle, and from ^{54}Fe , which represents the $1\alpha 2p 1n$ channel for reactions on small ^{29}Si target impurities. These contaminants can be suppressed considerably by applying the total energy

plane selection method [17] and by eventually subtracting corresponding spectra in coincidence with, for example, one α particle, three protons, and one neutron.

Multipolarity assignments of γ -ray transitions were based on two methods, and we refer to Refs. [12, 14, 18] for further details. The first method is based on efficiency-corrected intensity ratios, R_{150-97} , of γ -ray transitions detected in the three most backward oriented Ge-detector rings of Gammasphere and Ge detectors placed in the central section of Gammasphere. The ratios were evaluated from γ -ray spectra in coincidence with proper subsets of intense transitions known to belong to ^{53}Fe . These transitions were detected at an average angle of $\bar{\theta} = 124^\circ$, where the relative intensities from different multipolarities are roughly the same. Stretched $E2$ transitions are predicted to have $R_{150-97} \approx 1.2$ whereas stretched $\Delta I = 1$ transitions should have $R_{150-97} \approx 0.8$. $\Delta I = 0$ transitions have values similar to $E2$ transitions, and, of course, all these estimates depend somewhat on the spin alignment of the respective nuclear state.

Directional correlations of oriented states (DCO-ratios) defined as

$$R_{DCO}(150-97) = \frac{I(\gamma_1 \text{ at } 150^\circ; \text{gated with } \gamma_2 \text{ at } 97^\circ)}{I(\gamma_1 \text{ at } 97^\circ; \text{gated with } \gamma_2 \text{ at } 150^\circ)},$$

were deduced as well. If possible, known stretched $E2$ transitions were used for gating. In this case one expects $R_{DCO} = 1.0$ for observed stretched $E2$ transitions and ≈ 0.6 for stretched $\Delta I = 1$ transitions. Again, non-stretched $\Delta I = 0$ transitions have values similar to $E2$ transitions. If, however, stretched $M1$ transitions were used for gating, $R_{DCO} = 1.0$ and ≈ 1.6 is expected for observed stretched $\Delta I = 1$ and $E2$ transitions, respectively.

Deviations from these estimates for $\Delta I = 1$ transitions indicate a non-zero mixing ratio of the respective transition, namely $\delta(E2/M1) > 0$ (< 0) for numbers smaller (larger) than expected for R_{150-97} and $R_{DCO}(150-97)$, respectively. The sign convention of Rose and Brink is applied [19]. Finally, even though stretched $E2$ and

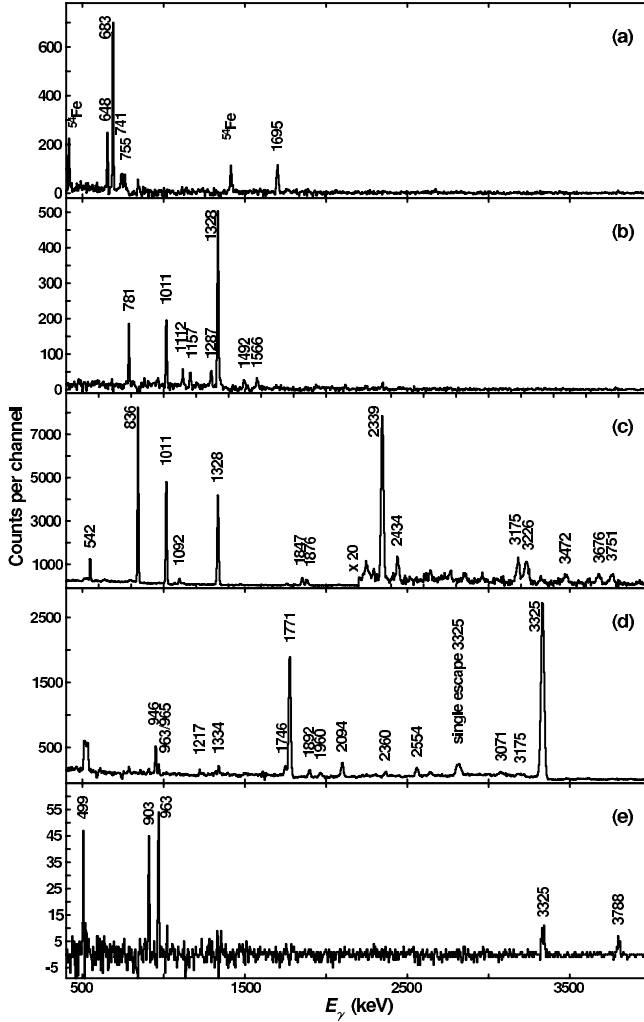


FIG. 3: Gamma-ray spectra in coincidence with one α particle, two protons, and one neutron from the two Gammasphere experiments. Panel (a) is in coincidence with the 1134 keV $9/2^- \rightarrow 5/2^-$ transition, panel (b) is in coincidence with the 2445 keV doublet decaying from the 3774 keV and 4785 keV levels, respectively, and panel (c) is in coincidence with the intense 287 keV $15/2^- \rightarrow 13/2^-$ yrast transition. These three spectra provide examples for the data quality of the low-spin part of the level scheme of ^{53}Fe shown in Fig. 1(a). Panels (d) and (e) are in coincidence with the 963 keV $25/2^- \rightarrow 21/2^-$ yrast transition and the high-energy 4362 keV $27/2^- \rightarrow 25/2^-$ transition. They illustrate the newly established high-spin part of the level scheme of ^{53}Fe displayed in Fig. 1(b). The energy labels next to the peaks are in keV.

$\Delta I = 0$ transitions provide similar angular distribution and correlation ratios, a distinction is usually straight forward because of yrast arguments — in fusion-evaporation reactions the most intense transitions denote the yrast line — and the combination of the numbers of several feeding, decaying, or parallel transitions. A few examples are going to be mentioned in the following section.

B. The GASP experiment

The lifetimes of the yrast $21/2^-$ and $25/2^-$ states in ^{53}Fe are derived by means of the recoil distance Doppler shift (RDDS) technique. The intensities of the unshifted components of the 963 keV $25/2^- \rightarrow 21/2^-$ and the 3325 keV $21/2^- \rightarrow 19/2^-$ transitions are determined in coincidence with the shifted component of the 1771 keV $27/2^- \rightarrow 25/2^-$ transition [cf. Fig.1(b)]. The RDDS analysis requires shifted and unshifted components of the transitions to be well separated. Therefore, only the two most forward (r_0, r_1) and the two most backward (r_5, r_6) detector rings of GASP are used. For each distance the events were sorted offline into $\gamma\gamma$ coincidence matrices with γ rays detected in one of the given detector rings placed along the axis. In total, 16 matrices ($\gamma_{r_0}\gamma_{r_0}, \gamma_{r_0}\gamma_{r_1}, \dots, \gamma_{r_6}\gamma_{r_5},$ and $\gamma_{r_6}\gamma_{r_6}$) per distance were created.

At first, the position of the shifted components of the 1771 keV transition in rings $\gamma_{r_0}, \gamma_{r_1}, \gamma_{r_5},$ and γ_{r_6} is determined in respective γ -ray spectra in coincidence with the 3325 keV transition. In turn, this information is used for producing for each distance 16 spectra in coincidence with the shifted component of the 1771 keV transition. Four times of these 16 spectra are taken at the same detector ring, i.e., they can be added together. An example are the four γ_{r_0} spectra from the $\gamma_{r_0}\gamma_{r_0}, \gamma_{r_0}\gamma_{r_1}, \gamma_{r_0}\gamma_{r_5},$ and $\gamma_{r_0}\gamma_{r_6}$ matrices, whereby the 1771 keV coincidence condition is imposed on the $\gamma_{r_0}, \gamma_{r_1}, \gamma_{r_5},$ and γ_{r_6} axes, respectively. The intensities of the unshifted components of the 963 keV and the 3325 keV transitions can now be measured in these four spectra and are subsequently summed together resulting in one number for each transition and each measured target-stopper distance.

The analysis of the same transition for different distances requires a normalization of its intensity due to, e.g., different beam currents or measuring times. The normalization coefficients employed in the current analysis have been determined for each target-stopper distance as described in Ref. [5]. The normalization coefficients are also used as weighting factors when different measurements at about the same distance are combined. Also the recoil velocity for the 21 target-distance combinations has been settled in the previous analysis. The velocities range from 3.7% to 4.1% of the speed of light for the three different targets used during the experiment. Using these velocities the 21 distances can be converted into 21 flight times, which are combined to 14 effective flight times: 0.339(12), 0.506(12), 0.675(10), 1.09(1), 1.70(2), 2.61(6),

3.99(8), 8.5(9), 14.7(3), 34.8(9), 61.2(14), 105(3), 175(5), and 354(9) ps. Since unshifted components of the 963 and 3325 keV transitions were not visible in the spectra taken at the largest distance, it was excluded from the analysis.

IV. RESULTS

The experimental results are summarized in the deduced excitation scheme of ^{53}Fe shown in Fig. 1 and Tables I and III. For clarity, the deduced level scheme of ^{53}Fe is split in two parts, each of which comprises the $17/2^- \rightarrow 15/2^- \rightarrow 13/2^- \rightarrow 11/2^- \rightarrow 9/2^- \rightarrow 7/2^-$ yrast cascade as a reference. Figure 1(a) shows the levels and transitions directly connected to this yrast cascade, while Fig. 1(b) focuses on a high-spin sequence built upon the 3041 keV $19/2^-$ isomer ($T_{1/2} = 2.526(24)$ min [3]). Two weak transitions at 2360 and 3175 keV were found to feed the 4005 keV $17/2^-$ yrast state and thus connect the two parts. Due to the long half-life of the isomer it is impossible to observe the depopulating 701, 1713, and 3041 keV transitions in prompt coincidence with the transitions feeding the isomer. They are included in Fig. 1(b) and Table I for completeness. Similarly, the 33 keV $1/2^- \rightarrow 3/2^-$ transition cannot be observed in the present experiment due to our low-energy threshold of some 60 keV, and the spectroscopy of the 741 keV $3/2^- \rightarrow 7/2^-$ ground-state transition is hampered by the relatively long half-life of the $3/2^-$ state ($T_{1/2} = 63.5(14)$ ns [3]).

Figure 2 provides a prompt γ -ray spectrum from the two Gammasphere experiments, which is in coincidence with one α particle, two protons, and one neutron detected in Microball and the Neutron Shell, respectively. The contaminations from the above mentioned reaction channels were carefully subtracted, i.e., the spectrum provides a necessary and sufficient condition for transitions belonging to ^{53}Fe . The spectrum served also as the basis for the relative intensities in Table I. Next to the well-known 287, 836, 1011, 1328, and 2339 keV transitions, which connect the low-spin yrast states, intense transitions at 499, 963, 1771, 3325, and 3788 keV are visible. They form the skeleton of the high-spin part of the level scheme in Fig. 1(b). With a few exceptions, all transitions in Figure 2 with relative intensities of about 1% of the intensity of the 1328 keV line could be placed in the present level scheme of ^{53}Fe .

The low-spin part of the decay scheme of ^{53}Fe in Fig. 1(a) is by and large in agreement with the most recent data evaluation [3]. The single difference is a change of the spin value of the 2843 keV state from $7/2^-$ in Ref. [3] to $11/2^-$ in the present decay scheme. The assignment is based on angular distributions and correlations of both populating and depopulating transitions of the 2843 keV state (cf. Table I). Figure 3(b) provides a γ -ray spectrum in the respective region of the level scheme. It is in coincidence with the 2445 keV dou-

blet. The 2445 keV transition connecting the 4785 and 2339 keV levels sees both the 1011 and 1328 keV transitions in the yrast cascade, and is responsible for the peaks at 1112 and 1287 keV in Fig. 3(b). The 2445 keV transition between the 3774 and 1328 keV levels adds statistics to the 1328 keV ground-state transition in Fig. 3(b), and is responsible for the 781, 1157, and 1566 keV lines in the spectrum. The weak transition at 1492 keV could not be placed in the level scheme.

Figure 3(a) focuses on the low-spin portion of the level scheme on the left hand side of Fig. 1(a). The spectrum is in coincidence with the new 1134 keV $9/2^- \rightarrow 5/2^-$ transition. The 648 and 683 keV lines, which depopulate the known 1424 keV state are clearly seen as well as the continuation of the sequence via the 755 and 1695 keV lines. The peaks at 411 and 1408 keV arise from the ^{54}Fe yrast cascade, namely via the 1130 keV $4^+ \rightarrow 2^+$ transition [18]. Figure 3(c) is in coincidence with the intense 287 keV $15/2^- \rightarrow 13/2^-$ transition. Besides the transitions belonging to the yrast sequence, peaks are visible at 1092, 1876, 2434, 3175, 3226, 3472, 3676, and 3751 keV. With the exception of the 3175 keV line, which populates the 4005 keV $17/2^-$ state, all of them are found to feed the 3463 keV 15^- level and connect to non-yrast $15/2^-$, $17/2^-$, and $19/2^-$ states. For the sake of clarity, the transitions at 3226, 3676, and 3751 keV have not been included in Fig. 1.

Figure 3(e) provides a spectrum in coincidence with the high-energy 4362 keV γ ray, which has been placed in the new high-spin regime. The yrast transitions between the 7328 keV $25/2^-$ state and the $19/2^-$ isomer at 499, 963, 3325, and 3788 keV are clearly visible, as well as a peak at 903 keV, which thus is placed on top of the 11690 keV level. The angular distribution ratio of the 4362 keV line, $R_{150-97} = 0.54(11)$, is a clear indication for the dipole character of that transition.

The spectrum in Fig. 3(d) has been measured in coincidence with the 963 keV $25/2^- \rightarrow 21/2^-$ and 965 keV $17/2^- \rightarrow 19/2^-$ doublet, the existence of which is apparent through the appearance of the 'self-coincident' peak at 964 keV. The most intense transitions at 1771 and 3325 keV as well as the line at 2094 keV mark the yrast sequence within this high-spin part of the level scheme. The angular distribution and correlation results of the 1771 keV line point at an almost pure dipole transition, while the values for the high-energy 3325 keV line require a considerable quadrupole admixture, $\delta(E2/M1) \sim -1$. Due to the relatively large uncertainties, the multipole character of the 2094 keV transition cannot be fixed. However, its relative intensity hints towards a yrast transition, and the tentative existence of the 3865 keV transition provides further confidence in a $(29/2^-)$ assignment to the 11192 keV level. The 946, 1217, 1960, and 2554 keV peaks in Fig. 3(d) connect to non-yrast structures. Several combinations of angular distribution and correlation values in conjunction with the plain existence of certain transitions allow for firm spin and parity assignments to the states at 8273, 8544, and 9880 keV and

tentative assignments to the levels at 7181, 9287, 9550, and 10876 keV.

The lines at 1334, 1746, 1892, 2360, and 3175 keV in Fig. 3(d) relate to the 965 keV $17/2^- \rightarrow 19/2^-$ transition. While the former three belong to the low-spin region of the ^{53}Fe level scheme, the latter two form important connections between the two parts of the level scheme, namely between the yrast and (tentative) yrare $21/2^-$ states towards the 4005 keV yrast $17/2^-$ state. Though associated with large uncertainties, the angular distribution ratios of the 2360 and 3175 keV transitions are consistent with stretched $E2$ character.

Finally, in the thin target experiments, the 1445, 1606, 1771, and 2094 keV transitions reveal significant additional Doppler shifts with respect to the applied generic event-by-event Doppler correction. This correction is based on recoils, which are supposed to have left the thin target foil before the γ -ray emission occurred, and thus includes a slowing down process inside the target foil. If, however, the γ -rays were emitted while the recoils are slowing down inside the thin target foil, they would be emitted with on average higher velocities, i.e., yield additional Doppler shifts. Therefore, the time it takes for the recoils to pass through the thin target foil, $t_{\text{pass}} \sim 0.2$ ps, represents an upper limit for the effective lifetimes of the states at 8273, 9098, 9880, and 11192 keV.

The lifetimes of the 6365 keV and 7328 keV states are determined from the GASP experiment using the RDDS technique as described in the previous section. Figure 4 illustrates the decay curve of the unshifted portion of the 963 keV $25/2^- \rightarrow 21/2^-$ transition in ^{53}Fe . The data

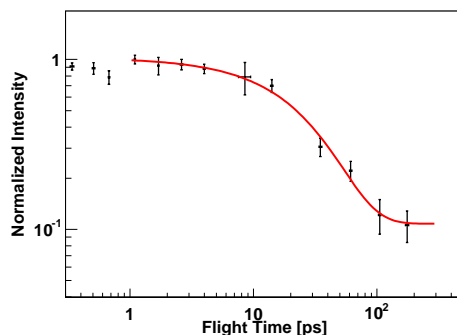


FIG. 4: Decay curve of the unshifted component of the 963 keV transition in ^{53}Fe for 13 effective flight distances measured in coincidence with the shifted component of the 1771 keV transition.

points were least-squares fitted to an exponential with a constant background. The result is $\tau = 26.2(32)$ ps for the 7328 keV $25/2^-$ state. To avoid any influence from the short-lived 9098 keV state ($\tau < 0.2$ ps), the

TABLE II: Mean level deviations, binding energy shifts, and mean branching deviations of the yrast sequence in ^{53}Fe , for the four different shell-model calculations performed.

Interaction	MLD [keV]	BES [keV]	MBD
kb3g	268	-146	0.15
kb3g_coul	249	-64	0.14
gxpf1	193	71	0.18
gxpf1_coul	206	144	0.18

starting point for the fits was set to 1 ps. This is five times the estimated upper limit of the 9098 keV level, and the 1771 keV line should effectively have no stopped components anymore, i.e., full statistics are seen in the coincidence spectra used in the analysis.

Since the intensity of the unshifted part of the 3325 keV $21/2^- \rightarrow 19/2^-$ transition is measured in coincidence with the shifted part of the 1771 keV transition, its decay curve represents an effective lifetime of the $25/2^-$ and $21/2^-$ states. Therefore, the decay curve of the 3325 keV line was least-squares fitted with two lifetime components, which allows to estimate an upper limit for the lifetime of the 6365 keV $21/2^-$ state. One of the lifetime components used in the fit was fixed to a value corresponding to the lower limit of the lifetime of the $25/2^-$ state. Like for the analysis of the 963 keV transition, the starting point for the fit was set to 1 ps. The result indicates $\tau < 4$ ps for the 6365 keV $21/2^-$ state.

TABLE III: Lifetimes of excited states in ^{53}Fe determined in the present study.

I^π (\hbar)	E_γ (MeV)	τ (ps)
$21/2^-$	6.365	< 4
$25/2^-$	7.328	26.2(32)
$25/2^-$	8.273	$< 0.2^a$
$27/2^-$	9.098	$< 0.2^a$
$27/2^-$	9.880	$< 0.2^a$
$29/2^-$	11.192	$< 0.2^a$

^aEffective lifetime.

V. SHELL-MODEL INTERPRETATION

To interpret the excited negative-parity states in ^{53}Fe large-scale shell-model calculations were performed using the shell-model code ANTOINE [21, 22]. The calculations employ the full fp space comprising the $1f_{7/2}$ orbit below and the $2p_{3/2}$, $1f_{5/2}$, and $2p_{1/2}$ orbits above the $N, Z = 28$ shell closure. The configuration space was truncated to allow for five particle excitations from the $1f_{7/2}$ shell into the upper fp shell. Calculations performed on the $1f_{7/2}$ yrast structure in ^{51}Mn using this configuration space have been shown to give results more or less indistinguishable from calculations performed in the full fp configuration space [1]. Four interactions have

been studied: The standard KB3G [1] and GXPF1 [23] interactions without any Coulomb interaction (kb3g, gxpf1) and with theoretical harmonic-oscillator Coulomb matrix elements (kb3g_coul, gxpf1_coul). The calculations are done with bare g factors and effective nucleon charges taken from Ref. [5], i.e. $\varepsilon_p = 1.16e$ and $\varepsilon_n = 0.78e$ for protons and neutrons, respectively. The experimental γ -ray energies were used to compute transition strengths and deduce branching ratios and mixing ratios of the transitions and lifetimes of the nuclear states.

In Fig. 5 the calculated energy values are compared with the observed excitation energies for the yrast structure starting at spin $I^\pi = 7/2^-$ and up to spin $29/2^-$. The agreement for these states is overall very good, which is manifested by the rather small values of mean level deviations (MLD) and binding energy shifts (BES) presented in Table II.

The BES is chosen to minimize the MLD and enables a quantitative comparison of states at different excitation energies. While there is no major difference between the calculations with and without the basic Coulomb interaction, there are two obvious differences between the different interactions. KB3G predicts a too large gap just above the $19/2^-$ level, which is almost perfectly reproduced with GXFP1. On the other hand, GXFP1 seems to have some problems with the distance between the $27/2^-$ and $29/2^-$ states, for which KB3G yields preferred numbers. Since the latter minor disagreement affects only two states, while the former acts on three levels, the MLD values for GXFP1 turn out to be somewhat smaller than those for KB3G.

To better estimate the quality of the predicted wave functions one should compare the electromagnetic properties rather than the excitation energies. Therefore, the experimental and calculated branching ratios for the yrast cascade are compared and the corresponding mean branching deviations (MBD) [24] are calculated. They are also included in Table II. Like for the level energies, the branching ratios are overall very well reproduced. One problem common to all parametrisations is the decay of the $17/2^-$ state. Experimentally an almost 50:50 distribution towards the $15/2^-$ and $19/2^-$ levels is observed, while the calculations predict an almost exclusive branch into the $19/2^-$ isomer, probably based upon an $M1$ spin-flip transition within the seniority $\nu = 3$ scheme. In reality, however, the $17/2^-$ state may comprise more core-excited components. While this problem is the only one for KB3G, GXFP1 also fails to describe the experi-

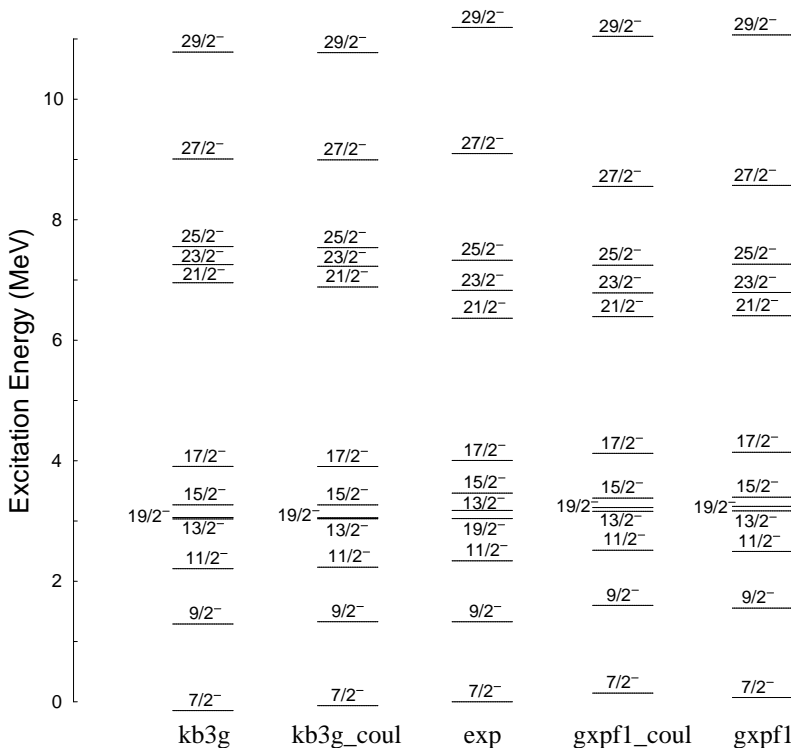


FIG. 5: Experimental and calculated excitation energies for the observed yrast sequence between $I^\pi = 7/2^-$ and $I^\pi = 29/2^-$ states. For all calculated states the binding energy shift (cf. Table II) has been added to the excitation energies.

mentally well-established branching ratios of the 499 and 963 keV transitions depopulating the $25/2^-$ state. Here, GXFP1 favors the 499 keV branch approximately 60:40, while the experiment demands 25:75. This additional disagreement explains the somewhat higher MBD value of the two GXFP1 calculations in Table II.

Table IV exemplifies a comparison of the measured and predicted electromagnetic decay properties for one of the four parametrisations, namely kb3g_coul. The calculations were performed only for the two lowest negative parity states for angular momentum up to $29/2^-$. Thus, in Table IV there are no theoretical branching ratios given for transition decaying to higher lying non-yrast states. For the sake of completeness, the low-lying $1/2^-$, $3/2^-$, and $5/2^-$ states are included. Even for the yrast states, the agreement between experimental and calculated branching ratios is pretty good, even though being somewhat worse than for the yrast sequence. This implies that even the previously unknown states in ^{53}Fe are

generally well described in the present shell-model calculations. The shell-model predictions for the lifetimes of the 6365 keV $21/2^-$ and 7328 keV $25/2^-$ states are in good agreement with the present experiment.

Finally, the effective g factors, g_{eff} , which enter as parameters in the predictions of electromagnetic decay properties were investigated. In a first attempt, the predicted branching ratios of the yrast cascade were compiled using effective g factors of 70%, 80%, 90%, and 100% of the bare g -factors, g_0 , while keeping the effective charges constant at the numbers mentioned above. The result from this study is inconclusive: For some states the best agreement with experiment is achieved for $g_{\text{eff}} = 0.7 \cdot g_0$, whereas other states are best reproduced for, e.g., $g_{\text{eff}} = 0.9 \cdot g_0$. It is concluded that a more extensive investigation is required to obtain quantitative best estimates for the effective g factors in the mass region based on electromagnetic decay data from more than one nucleus.

TABLE IV: Comparison of experimental branching ratios b of γ rays depopulating negative parity states in ^{53}Fe with predictions from shell-model calculations as described in the text. The calculated mixing ratios δ and lifetimes τ are provided as well and compared to experimental values.

E_x (MeV)	I_i	I_f	E_γ (MeV)	b_{exp}	b_{theo}	δ_{exp}^a	δ_{theo}	τ_{exp}^a	τ_{theo}
0.741	3/2	7/2	0.741	1.00	1.00			91.6(20) ns	20.3 ns
0.775	1/2	3/2	0.033	1.00	1.00			2.9(3) ns	
1.328	9/2	7/2	1.328	1.00	1.00	-0.11(2)	0.18	25(10) fs	33 fs
1.424	5/2	9/2	0.096	n.o.	0.00			4.0(10) ps	16.6 ps
		1/2	0.648	0.22(2)	0.46				
		3/2	0.683	0.78(2)	0.53	+0.36($\frac{5}{2}$)	-0.68		
		7/2	1.424	n.o.	0.01		$-\infty$		
1.696	7/2	5/2	0.273	0.07(2)	0.18		0.02	2($\frac{3}{1}$) ps	2.9 ps
		9/2	0.368	n.o.	0.01		0.03		
		3/2	0.955	0.88(1)	0.70				
		7/2	1.696	0.05(1)	0.11		1.89		
2.339	11/2	7/2	0.643	n.o.	0.00			76(17) fs	43 fs
		9/2	1.010	0.79(1)	0.88	+0.11(2)	0.10		
		7/2	2.339	0.21(1)	0.12				
2.558	9/2	11/2	0.219	n.o.	0.00		0.06		1.0 ps
		7/2	0.861	0.20(4)	0.06		-0.41		
		5/2	1.134	0.61(3)	0.66				
		9/2	1.230	n.o.	0.04		0.50		
		7/2	2.558	0.19(4)	0.24		1.31		
2.843	11/2	9/2	0.285	n.o.	0.00		0.03	48(17) fs	216 fs
		11/2	0.503	0.13(2)	0.00		-0.12		
		7/2	1.147	n.o.	0.08				
		9/2	1.514	0.09(2)	0.00		∞		
		7/2	2.843	0.79(2)	0.91				
3.176	13/2	11/2	0.198	n.o.	0.00		0.02		94 fs
		9/2	0.483	n.o.	0.00				
		11/2	0.836	0.89(1)	0.91		0.06		
		9/2	1.847	0.11(1)	0.09				
3.463	15/2	11/2	0.152	n.o.					1.7 ps
		13/2	0.287	0.81(2)	0.82		0.01		
		19/2	0.422	n.o.	0.00				
		11/2	0.620	n.o.	0.00				
		11/2	1.124	0.19(2)	0.18				
3.774	13/2	15/2	0.311	n.o.	0.00		-0.03		0.3 ps
		11/2	0.463	n.o.					
		13/2	0.598	n.o.	0.00		∞		
		11/2	0.931	0.43(3)	0.51		0.05		
		9/2	1.216	n.o.	0.18				
		11/2	1.434	0.14(2)	0.00		$-\infty$		
		9/2	2.445	0.43(3)	0.31				
4.005	17/2	13/2	0.231	n.o.	0.00				55 fs
		15/2	0.542	0.45(3)	0.08		0.01		
		13/2	0.829	n.o.	0.00				
		19/2	0.965	0.55(3)	0.92		0.00		
4.555	15/2	13/2	0.302	n.o.					1.3 ps
		17/2	0.550	n.o.	0.01		0.35		
		13/2	0.781	0.41(2)	0.22		0.07		
		11/2	1.244	0.03(1)					
		15/2	1.092	0.14(2)	0.31		-0.07		
		13/2	1.379	0.07(1)	0.14		0.08		
		19/2	1.514	n.o.	0.04				
		11/2	1.712	0.13(2)	0.22				
		11/2	2.216	0.25(2)	0.06				
5.339	17/2	15/2	0.784	0.11(3)	0.22		0.12		47 fs
		13/2	1.086	n.o.					
		17/2	1.334	0.16(7)	0.33		-0.03		
		13/2	1.566	0.18(4)	0.02				
		15/2	1.876	0.54(5)	0.25		0.05		
		13/2	2.163	n.o.	0.00				
		19/2	2.299	n.o.	0.17		0.30		

^aValues for $I_i < 13/2$ are adopted from Ref. [3].

^bEffective lifetime.

TABLE IV: Continued.

E_x (MeV)	I_i	I_f	E_γ (MeV)	b_{exp}	b_{theo}	δ_{exp}^a	δ_{theo}	τ_{exp}^a	τ_{theo} (ps)
6.365	21/2	17/2	1.026	n.o.	0.00			< 4 ps	35 fs
		17/2	2.360	0.01(1)	0.02				
		19/2	3.325	0.99(1)	0.98	~ -1	-3.58		
6.828	23/2	21/2	0.463	0.02(1)	0.02		-0.00	37 fs	
		19/2	3.788	0.98(1)	0.98				
7.181	21/2	19/2	0.042	n.o.	0.00		0.00	7 fs	
		23/2	0.353	n.o.	0.00		0.21		
		17/2	0.492	n.o.					
		21/2	0.816	n.o.	0.01		-0.10		
		17/2	1.842	n.o.	0.01				
		17/2	3.175	0.48(6)	0.02				
		19/2	4.140	0.52(6)	0.96		-0.87		
7.328	25/2	21/2	0.147	n.o.	0.00			26.2(32) ps	25.4 ps
		23/2	0.499	0.26(1)	0.39		0.09		
		21/2	0.963	0.74(1)	0.61				
		25/2	0.946	0.19(2)	0.11		0.05		
8.273	25/2	21/2	1.092	n.o.	0.00			< 0.2 ps ^b	39 fs
		23/2	1.445	0.78(2)	0.85		-0.12		
		21/2	1.908	0.03(1)	0.04				
		25/2	0.271	n.o.	0.00		0.06		
8.544	23/2	25/2	1.217	0.22(9)	0.21		-0.00	14 fs	
		21/2	1.362	0.26(12)	0.10		0.06		
		19/2	1.405	n.o.	0.00				
		23/2	1.715	0.26(9)	0.07		0.10		
		21/2	2.179	0.26(9)	0.14		0.30		
		19/2	5.503	n.o.	0.48				
		23/2	0.554	n.o.	0.00				
9.098	27/2	25/2	0.825	n.o.	0.01		0.06	< 0.2 ps ^b	31 fs
		25/2	1.771	0.99(1)	0.96		-0.20		
		23/2	2.269	0.01(1)	0.03				
		27/2	0.593	n.o.					
9.880	27/2	27/2	0.783	0.09(3)	0.09		-0.01	< 0.2 ps ^b	44 fs
		23/2	1.336	n.o.	0.00				
		25/2	1.606	0.45(4)	0.87		-0.17		
		25/2	2.554	0.46(4)	0.04		5.57		
		23/2	3.051	n.o.	0.00				
		27/2	2.094	0.92(3)	0.77		-0.52		
11.192	29/2	25/2	1.905	n.o.				< 0.2 ps ^b	65 fs
		27/2	2.094	0.92(3)	0.77		-0.52		
		25/2	2.919	n.o.					
		25/2	3.865	0.08(3)	0.23				
		25/2	3.865	0.08(3)	0.23				

^aValues for $I_i < 13/2$ are adopted from Ref. [3].

^bEffective lifetime.

VI. SUMMARY AND CONCLUSIONS

A new extensive level scheme of the even-odd nucleus ^{53}Fe is presented. The lifetime of the yrast $25/2^-$ state and an upper limit for the lifetime of the yrast $21/2^-$ state has been determined via the RDDS method. A thorough and detailed comparison of excitation energies and electromagnetic decay properties with large-scale shell-model calculations in the fp shell has been performed. Four different interactions have been studied using effective charges taken from Ref. [5] and bare g factors. The comparison indicates an overall very good agreement, even though some distinct local disagree-

ments remain.

Acknowledgments

We would like to thank the accelerator crews and the Gammasphere and GASP support staff at Argonne, Berkeley, and Legnaro for their supreme efforts. This work is supported in part by the Swedish Research Council, the European Commission under contract number HPRI-1999-CT-00083, the European Community programme IHP under contract number HPMF-CT-2002-02018, and the U.S. Department of Energy under grants No. DE-AC03-76SF00098 (LBNL), DE-FG05-88ER-40406 (WU), and W-31-109-ENG38 (ANL).

-
- [1] A. Poves *et al.*, Nucl. Phys. **A694**, 157 (2001).
- [2] S.J. Williams *et al.*, Phys. Rev. C **68**, 011301(R) (2003).
- [3] J. Huo, Nucl. Data Sheets **87**, 507 (1999).
- [4] S.J. Williams, PhD thesis, Keele University, unpublished.
- [5] R. du Rietz *et al.*, Phys. Rev. Lett. **93**, 222501 (2004).
- [6] I.-Y. Lee, Nucl. Phys. **A520**, 641c (1990).
- [7] M. Devlin *et al.*, Nucl. Instr. Meth. A **383**, 506 (1996).
- [8] D.G. Sarantites *et al.*, Nucl. Instr. Meth. A **381**, 418 (1996).
- [9] D.G. Sarantites *et al.*, Nucl. Instr. Meth. A **530**, 473 (2004).
- [10] A. Dewald *et al.*, Nucl. Phys. **A545**, 822 (1992).
- [11] C. Rossi Alvarez, Nuclear Physics News, Vol. 3, 3 (1993).
- [12] J. Ekman *et al.*, Phys. Rev. C **70**, 014306 (2004).
- [13] C. Andreiou, PhD thesis, Lund University (2002), ISBN 91-628-5308-2.
- [14] J. Ekman, PhD thesis, Lund University (2004), ISBN-91628-6061-5.
- [15] D.C. Radford, Nucl. Instr. Meth. Phys. Res., Sect A **386**, 297 (1995).
- [16] J. Theuerkauf, S. Esser, S. Krink, M. Luig, N. Nicolay, O. Stuch, and H. Wolters, program TV, University of Cologne, unpublished.
- [17] C.E. Svensson *et al.*, Nucl. Instr. Meth. A **396**, 228 (1997).
- [18] D. Rudolph *et al.*, Eur. Phys. J. A **4**, 115 (1999).
- [19] H.J. Rose and D.M. Brink, Rev. Mod. Phys. **39**, 306 (1967).
- [20] C. Andreiou *et al.*, Eur. Phys. J. A **14**, 317 (2002).
- [21] E. Caurier, shell model code ANTOINE, IRES, Strasbourg 1989-2002.
- [22] E. Caurier, F. Nowacki, Acta Phys. Pol. **30**, 705 (1999).
- [23] M. Honma, T. Otsuka, B. A. Brown, and T. Mizusaki, Phys. Rev. C **65**, 061301 (2002).
- [24] D. Rudolph, K.P. Lieb, and H. Grawe, Nucl. Phys. **A 597**, 298 (1996).